# X-ray spectroscopy of high ionisation outflows in Suzaku observed type I active galaxies

**Jason Gofford**

A thesis submitted to Keele University
for the Degree of Doctor of Philosophy

Department of Physics, Keele University.

July 2013

# Abstract

In this thesis I present the culmination of my research into the phenomenon of AGN winds in the X-ray regime using the *Suzaku* X-ray telescope. There are two studies described in this thesis. In the first I perform a deep broad-band spectral analysis of radio-quiet quasar MR 2251-178 and outline the evidence which suggests that its X-ray continuum is partially-covered by ionised gas along the line of sight, possibly in the form of a disc-wind.

In the second study I perform a survey for Fe XXV He$\alpha$ and Fe XXVI Ly$\alpha$ absorption lines in a large sample of 51 *Suzaku*-observed AGN (99 observations). These absorption lines are unambiguously detected in $\sim$ 40% of the sample (20/51 AGN), consistent with recent results from *XMM-Newton*, with peak and mean absorber parameters of $\log(N_{\rm H}/{\rm cm}^{-2}) \approx 23$ and $\log(\xi/{\rm erg\,cm\,s}^{-1}) \approx 4.5$. Their velocities cover a continuous range, from $v_{\rm out} < 1500\,{\rm km\,s}^{-1}$ to $\sim 100,000\,{\rm km\,s}^{-1}$, with a median of $\sim 0.056\,{\rm c}$. The winds are located on sub-parsec scales ($< 0.1\,{\rm pc}$, typically), placing them in the vicinity of the inner accretion disc. A correlation analysis shows that more powerful AGN launch more powerful winds which implies their being accelerated by radiation pressure. Indeed, the overall energetics of the outflows are quantitatively consistent with continuum-driving via Compton-scattering, although a magnetic origin cannot be ruled out on the basis of the available data. I find that the mean kinetic power of the outflows is $\sim 1\%\,L_{\rm bol}$, suggesting a possible feedback effect in their host galaxies could be important. Finally, I show that the measured outflow velocity distribution bares a striking resemblance to one inferred using the $M_{\rm BH} - \sigma_*$ relation for local quiescent galaxies which suggests that the observed $M_{\rm BH} - \sigma_*$ relation may be an artefact of wind-induced feedback.

Overall, these results are consistent with the view that highly-ionised Fe K winds may represent an important addition to the currently held AGN paradigm, and further enforce the hypothesis that they may be important for galaxy evolution.

# Acknowledgements

I would like to extend my utmost gratitude to my supervisor, Dr. James Reeves, who has been an indispensable source of guidance and reassuring humour over the last 4 years of my Ph.D, and without whom this thesis would simply not have been possible. It was his infectious enthusiasm and enjoyment of his research which compelled me to study active galaxies and X-ray astronomy in the first place, and for that I am deeply indebted. I would also like to thank my secondary supervisor, Dr. Dean McLaughlin, for his help with the more theoretical side of my research. The frequent-but-not-regular 'James Dean' curries have been one of the highlights of my Ph.D, and have always been a great way end to the week (particularly during write-up!). Similarly, I would also like to thank my numerous scientific collaborators whose input, suggestions and good ideas have proved extremely valuable over the last few years; in no particular order, this includes Valentina Braito, Jane Turner, Lance Miller, Francesco Tombesi and Massimo Cappi.

I would not have made it this far if it were not for my excellent friends and colleagues who have helped me over the years: the Lindsay A-block lads (Peter Hallam, Mark Pakula, Like Whitehead, Andy Brown, Matt Bowling, Simon Boyle, Anthony Davies, Miles Majstorovic and Laz Majstorovic — Keele just hasn't been the same since you guys graduated!), Katy Warner, Krishan Gohel, Adam Snitch, Deepak Mahtani, and especially Andrew "why do bad things keep happening to me?" Lobban for helping me find a towel that time in Utrecht. I would also like to extend a very special and heartfelt thank you to Amy Dobson for putting up with me whilst I have been writing up this research, and for just generally being pretty awesome.

Lastly, and by certainly no means least, I would like to express my deep and undying gratitude to my close family for all of their love and support during my studies; in particular, my parents, Julie and Alan, my sister, Paula, and the entire Denny family. I've spent a long 8 years at Keele and they have stood by me on every step of the journey. Thank you, all.

# Contents

# List of Figures

# List of Tables

# 1 Introduction

That almost every massive galaxy in the universe harbours a super-massive black hole (SMBH) at its centre, with a mass of many millions of solar masses ($M_\odot$), is one of the most remarkable conclusions of modern extra-galactic astrophysics (Kormendy & Richstone 1995; Kormendy & Gebhardt 2001). In the majority of galaxies the central black holes are themselves invisible — silently lurking at the heart of the host galaxy, their presence only being revealed by studying the orbits of nearby stars — but in some of them the hole is voraciously feeding on in-falling material from the surrounding inter-stellar medium. These galaxies, which comprise only about $10 - 20\%$ of the total population, are called '*active galaxies*'.

The feeding gas and dust inevitably possesses a certain amount of angular momentum and so spins faster and faster as it falls towards the black hole, eventually forming a rapidly spinning disc-like body termed an *accretion disc*. Various forces acting within the disc gradually remove energy and angular momentum from the material, which allows it to slowly spiral towards, and eventually into, the black hole. The energy released in this process is tremendous and much of it is radiated away, ultimately appearing as a bright point-like source of radiation in the nucleus of the active galaxy. These bright sources, which are the brightest continuously emitting objects in the universe, are termed '*active galactic nuclei*' (hereafter, AGN).

The study of AGN is a vibrant and active area of research. Because they are so luminous, AGN, and specifically quasars (§1.1), can be seen out to extremely high red-shifts, e.g., $z \gtrsim 7$ (Mortlock et al. 2011), corresponding to a time when the universe was only $\sim 6\%$ of its current age. This makes them excellent probes of the early universe, and for studying how both it and galaxies have evolved over cosmic time. The light from AGN can pass through many clouds of gas before it reaches us, and so by studying their spectra we can glean information about both the chemical make-up of the intra-galactic medium and about the AGN–host-galaxy ecosystem.

In this thesis I present the results of my research which has focused on the

spectroscopic study of AGN at X-ray wavelengths using observations from the *Suzaku* space observatory. As I will explain in this chapter, radiation emitted at X-ray energies carries with it information about the properties of material deep inside the AGN. The principle motivator of my work has been to find observational evidence for material outflowing from the AGN at X-ray energies, and to determine whether the energy associated with these outflows could plausibly influence the evolution of an AGNs host galaxy.

This chapter begins with a general overview of active galaxies in which I introduce the various different classes of AGN and the proposed unified scheme (§1.1). I then go on to outline how black hole mass is measured (§1.2), describe the various physical processes which are important at X-ray energies (§1.3) and give a summary of a typical AGN X-ray spectrum (§1.4). Next, I set the wider context for my work by briefly reviewing both the evidence for AGN–host-galaxy co-evolution and the observational evidence for AGN winds / outflows (§1.5). Finally, §1.6 outlines the structure of the remaining chapters in this thesis.

## 1.1 Observational overview of active galaxies

AGN are split into two main classes based on the ratio of their radio (5 GHz) to optical (B-band) luminosity. If $L_\nu(5\,\mathrm{Ghz})/L_\nu(\mathrm{B}) \geq 10$ then an object is classified as *radio-loud*, otherwise it is *radio-quiet* (Kellermann et al. 1989). Another important distinction can be made on the basis of their optical luminosity, leading to two further luminosity-based sub-groups; those more luminous than $M_\mathrm{B} = -23$ (where $M_\mathrm{B}$ is the absolute B-band magnitude; Schmidt & Green 1983) are termed *quasars*, while those less luminous are called *Seyferts*. They are then even further categorised depending upon both their spectral & temporal variability, and the widths of emission lines present in their optical / UV spectra. In the remainder of this section I briefly describe the various classes of object which make up the veritable 'zoo' of AGN, with a particular emphasis on those which are important in the context of the work presented in this thesis.

### 1.1.1 Seyfert galaxies

Seyfert galaxies have relatively low X-ray luminosities of $L_{2-10\,\mathrm{keV}} \simeq 10^{41} - 10^{43}\,\mathrm{erg\,s^{-1}}$, and are typically only seen in the local universe (i.e. $z < 0.05$). At such distances the host galaxy is spatially resolved and they are generally found in spiral galaxies. Most Seyfert galaxies are radio-quiet and are further sub-divided into two main groups based upon their emission-line spectra (Khachikian & Weedman 1974). Seyfert 1 galaxies (Sy 1) have bright continua superposed with both broad permitted and narrow forbidden emission lines. The narrow lines typically have a full-width half-maximum (FWHM) of $< 1000\,\mathrm{km\,s^{-1}}$ and, due to the association with forbidden transitions such as [O III], are believed to originate in low-density gas so as to avoid collisional de-excitation (Peterson 1997; Beckmann & Shrader 2012). In contrast, the FWHM of the broad H$\alpha$, H$\beta$ and C IV lines, for example, can be Doppler-broadened up to $\sim 10^4\,\mathrm{km\,s^{-1}}$. The lack of broad forbidden lines indicates that the forbidden emission originates from low density gas (i.e., $n_e \gtrsim 10^9\,\mathrm{cm^{-3}}$; Peterson 1997; Beckmann & Shrader 2012). A virial argument suggests that the broad lines are emitted from a region closer to the black hole (the 'broad-line region'; BLR) than the narrow lines (which originate from the 'narrow-line region'; NLR). Seyfert 2 galaxies (Sy 2) differ from their type-1 counterparts in that they have weak continua and show only narrow emission lines. This means that either they have no high velocity gas, or, as we now believe, that their gas is obscured from view by a thick wall of obscuring material which is colloquially referred to as the 'obscuring torus' (c.f. §1.1.4). Some Seyfert galaxies have properties intermediate between type-1 and type-2, showing both broad and narrow components in their permitted lines; these are commonly classified as Seyfert 1.5, 1.8 or 1.9 galaxies depending on the relative strength of the broad lines with respect to the narrow lines (Osterbrock 1981). In this scheme a Seyfert 1.9 galaxy will have weaker broad lines relative to the narrow ones than, for example, a Seyfert 1.5 or a Seyfert 1.8.

#### Narrow-line Seyfert 1 galaxies

Narrow-line Seyfert 1 (NLSy1) galaxies, a subset of the Seyfert 1 galaxies, are now recognised as a class of AGN in their own right (Osterbrock & Pogge 1985). These are essentially Seyfert 1 galaxies in which the broad permitted optical emission lines have only FWHM $\leq 2,000\,\mathrm{km\,s^{-1}}$ (Osterbrock & Pogge 1987), making them only marginally broader than the forbidden lines, but with a ratio of permitted to forbidden line flux which is more reminiscent of bona-fide Seyfert 1 rather than Seyfert 2 galaxies (e.g., Osterbrock & Pogge 1985). NLSy1s also show strong blends of Fe II lines in their optical spectra which are rarely seen in Seyfert 2 spectra (Goodrich 1989). Observationally, NLSy1s are further distinguished from Seyfert 2s in that they tend to have strong soft X-ray excesses (e.g., Dewangan et al. 2007; see §1.4.3), and rapid temporal variability at X-ray energies (e.g., Vaughan et al. 1999, 2011; Lobban et al. 2011). In general, NLSy1s are found to have low black hole masses, of the order $\sim 10^6 M_\odot$, and are accreting at an appreciable fraction of their Eddington rate.

### 1.1.2 Quasars

Quasars are far brighter than Seyferts with luminosities of $L_{2-10\,\mathrm{keV}} \simeq 10^{44} - 10^{47}\,\mathrm{erg\,s^{-1}}$ and can be seen out to beyond $z \sim 7$ (e.g. Mortlock et al. 2011). Quasars are capable of outshining their host galaxy by a factor of $10^2 - 10^3$ or more which, when combined with their high red-shift, leads to a star-like point-source appearance which caused them to initially be classified as Quasi-Stellar Objects (QSOs). Despite the terms QSO and Quasar originally being reserved for radio-quiet and radio-loud objects respectively, they are now both used interchangeably. As a result, I use the nomenclature of radio-quiet quasar (RQQ) and radio-loud quasar (RLQ) to differentiate between the sub-classes in this thesis. As is the case with Seyferts, there are both type-1 and type-2 quasars the latter only being detected relatively recently (Stern et al. 2002; Norman et al. 2002; Martínez-Sansigre et al. 2006; Severgnini et al. 2006).

### 1.1.3 Radio galaxies

Radio Galaxies have point-like optical nuclei and emit a significant fraction of their luminosity at radio wavelengths. This radio emission is frequently observed as jets or lobes which emanate from the optical nucleus. In essence, they can be considered the radio-loud equivalent of Seyfert galaxies and, analogously, there are two types: narrow-line radio galaxies (NLRG) and broad-line radio galaxies (BLRG). In contrast to Seyferts, however, radio galaxies are typically found in elliptical galaxies and therefore appear to share a closer relation to quasars.

Depending on their jet–lobe morphology, radio-loud AGN are frequently further sub-divided into two broad classes according to the criteria described by Fanaroff & Riley (1974). Fanaroff-Riley Class I (FR 1) are weaker radio sources where the radio emission is brighter in the centre and the surface brightness decreases outwards. FR 2 sources, on the other hand, show limb-brightening, i.e., they are brighter away from the core and often show enhanced emission around the edge of the radio structure.

### 1.1.4 Unified models

The so-called 'Unified model' of AGN (Antonucci & Miller 1985; Antonucci 1993) represents an effort to describe the different types of AGN using the same intrinsic nuclear structure. In this paradigm, it is thought that at a given luminosity there are no intrinsic differences between the broad- and narrow-line classes of AGN / quasars; the observed differences arise solely due to orientation effects. Besides the central engine, which comprises a central SMBH and accretion disc, an AGN is thought to consist of three other regions: the narrow line region (NLR), the broad line region (BLR) and a parsec-scale dusty 'torus' of optically-thick material which encircles nuclear regions along the accretion disc axis. A schematic of the proposed structure is shown in Fig. 1.1.

If the observers; sight-line intercepts the toroidal material the central regions (i.e., the SMBH, accretion disc and the BLR) are all obscured from direct view, and the only nuclear emission observed is that reprocessed by the dusty torus and the NLR. As

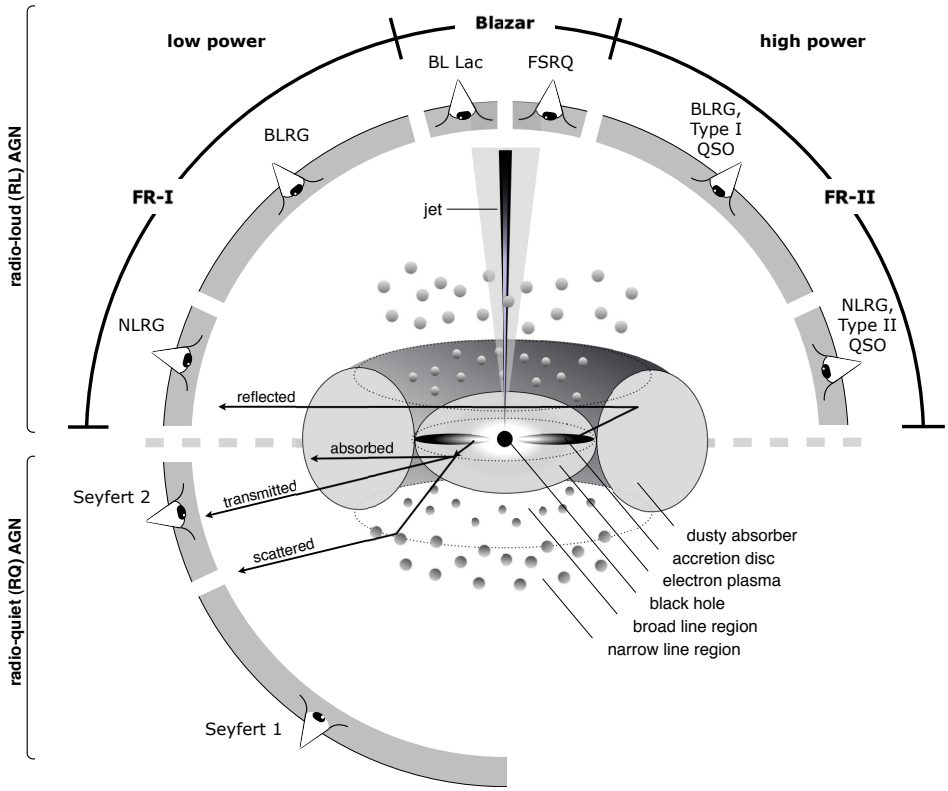


Figure 1.1: Cartoon depicting the various components which are believed to make up an AGN. The central engine consists of a super-massive black hole which is actively accreting from a surrounding accretion disc. Further out on sub-pc scales, there is the Broad Line Region (BLR) which is responsible for the broad permitted emission lines. The Narrow Line Region (NLR) is then located further out still, likely on pc-kpc scales, and is responsible for the narrow permitted and forbidden emission lines. Encompassing the nuclear regions along the accretion disc axis an optically-thick torus-like structure is invoked on pc-scale distances which, from certain viewing angles, obscures different parts of the nucleus and gives rise to type-1 and type-2 objects. In radio-loud objects, a relativistic jet is also present which is emitted perpendicularly to the accretion disc rotation axis. Figure credit: Beckmann & Shrader (2012).

such, the observed spectrum will be dominated by narrow emission lines, and the source classified as type-2. Type-1 sources can then be explained if the AGN is viewed from higher latitudes and through the polar hole in the obscuring material. This will allow both the BLR and NLR to be seen together with emission from the accretion disc, giving rise to both broad and narrow lines in the optical continuum. Important evidence in favour of this model was first obtained by Antonucci & Miller (1985), who detected broad Sy1-like emission lines in the polarised light of the Seyfert 2 galaxy NGC 1068. Since then, 'hidden BLRs' have also been found in several other classical Sy2s (e.g., Tran 1995a,b; Heisler, Lumsden & Bailey 1997). The large column densities of X-ray obscuring gas seen obscuring the central source in type-2 AGN (Risaliti, Maiolino & Salvati 1999), and their corresponding weaker luminosities (Mushotzky 1982; Pounds et al. 1990; Singh, Rao & Vahia 1992), are also consistent with obscuration by an optically-thick absorber on the accretion disc axis which lends further weight in favour of this simple model.

Orientation based schemes have also been proposed to explain the differing radio properties in radio-loud sources (Urry & Padovani 1995). In addition to the angle dependent obscuration, Doppler boosting renders the jet and nuclear radio emission also angle dependent in radio-loud AGN. In this context, when a radio-loud AGN is observed at acute angles relative to the jet axis (or even directly down it), a rapidly variable blazar is observed. At the other extreme, i.e., when an AGN is viewed at an angle perpendicular to the jet emission, the toroidal absorber obscures the central regions and a NLRG is observed which has extended radio lobes on the plane of the sky. At intermediate viewing angles, a core-dominated FR1 radio galaxy will be observed at angles closer to the jet, and lobe-dominated FR2s and BLRGs will be observed at angles closer to the torus.

However, while an obscuration based unified scheme is clearly effective and almost universally accepted throughout the field, there are aspects that orientation alone cannot explain. The most obvious problem is the clear differences between un-obscured AGN which, according to an orientation based unified model, should not show significant differences. For example, it does not account for why some AGN are radio-loud, whilst most are radio-quiet. Nor does it explain why quasars are so much more luminous than Seyfert galaxies, despite their showing very similar spectra at a phenomenological

level. These issues suggest that a more complex scheme is required. It is likely that any new 'grand unification scheme' will need to account for differences in black hole mass (e.g., Boroson 2002), the mass accretion rate (e.g., Wang, Biermann & Wandel 2000; Boroson 2002; Marinucci et al. 2012), and black hole spin (e.g., Punsly & Coroniti 1990; Meier 2002; Narayan & McClintock 2012; Narayan et al. 2012) if it is to explain the multitude of observable spectral properties. Even so, the obscuration based model remains a remarkably effective one given its simplicity.

## 1.2 Estimating SMBH mass

The mass of a black hole, $M_{\rm BH}$, is one of its two fundamental properties (the other being its spin) and methods of accurately establishing it are constantly being developed. This is not a trivial task; black hole masses can cover approximately nine or ten orders of magnitude, ranging from the small stellar-mass black holes in the Milky Way through to the largest super-massive black holes, and so no single method can be universally applied across the mass spectrum. For black holes in the local universe (such as nearby stellar-mass ones and the SMBHs in nearby AGN) the mass can be measured by studying its effect on the dynamics of nearby material, such as stars. Measuring both the rotational velocity and the velocity dispersion of the stars as a function of radius in the galaxy provides a proxy for studying the underlying potential and hence draw an estimate for the mass of the SMBH.

Dynamical methods are most accurate if the information comes from stellar material at the inner radii of the galaxy, hence close to the central black hole, and lose their precision when applied to material further out. To date, measuring the orbits of stars caught in the potential of the black hole in Sgr A — the Galactic centre of the Milky Way — has provided the best evidence for a SMBH. Due to its close proximity, instruments are able to resolve individual stars caught in the central potential which allows the black hole mass to be measured (Genzel et al. 1996; Schödel et al. 2002; Ghez et al. 2008; Gillessen et al. 2009). Fig. 1.2 shows the orbits of stars in the Galactic centre as

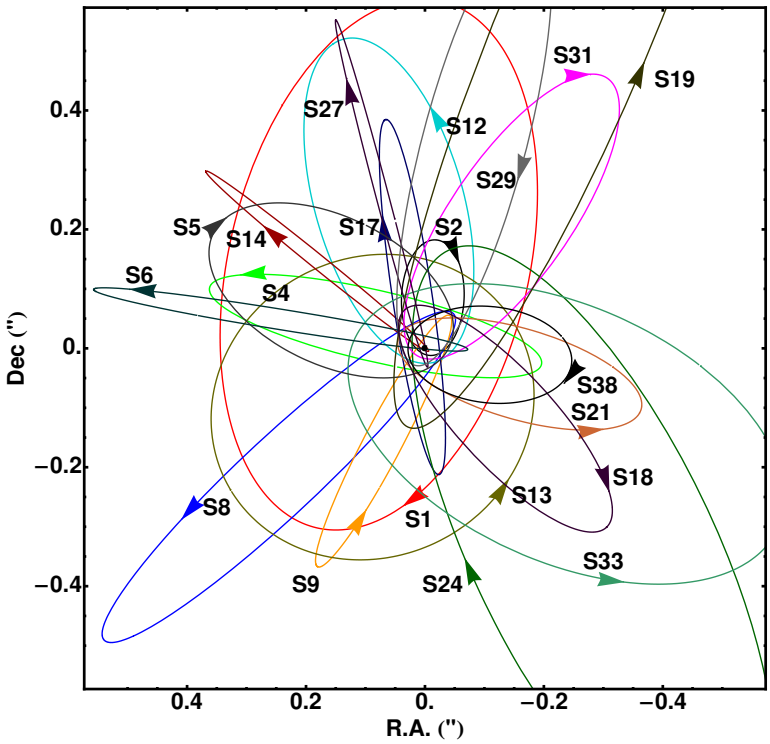


Figure 1.2: Plot highlighting how the gravitational potential at the Galactic centre of the Milky Way affects the orbits of nearby stars. The stellar mechanics can be used to infer the mass of the central body, which in this case turns out to be a super-massive black hole with $M_{\rm BH} = (4.31 \pm 0.38) \times 10^6 M_\odot$. Figure reproduced from Gillessen et al. (2009).

presented by Gillessen et al. (2009); the inferred value for the black hole mass in Sgr A* is $(4.31 \pm 0.38) \times 10^6 M_\odot$.

Theoretically, dynamical mass measurements can be made for every SMBH, but in practice its application has been limited to only a handful of nearby objects because the current generation of instruments are unable to resolve stellar components caught within a black holes' sphere of influence in more distant galaxies. Therefore, alternative methods designed to indirectly measure the black hole mass have been developed. These are briefly described below.

- **Reverberation Mapping**

  The continuum emission in AGN has long been known to exhibit short time-scale variability. The broad emission lines seen in broad-line AGN also exhibit variability, and in some cases these variations can trace those seen in the continuum. This implies that the BLR gas is reprocessing photons emitted by the ionising continuum, and means that the BLR gas provides indirect information about the primary emitting region. Reverberation mapping is the process through which black hole masses are estimated by measuring the response of broad emission lines to variations of the primary continuum. Assuming that the BLR gas is predominantly accelerated by the gravitational force exerted by the black hole, the virial theorem (i.e., $E_{\rm kin} = \frac{1}{2}E_{\rm gra}$) can be applied. The black hole mass $M_{\rm BH}$ is then given by:

$$M_{\rm BH} = \frac{R_{\rm BLR}(\Delta v)^2}{G} = \frac{f c\tau (\Delta v)^2}{G} \tag{1.1}$$

  where $\Delta v$ is the velocity dispersion of the BLR cloud as determined by the Doppler broadened emission line width, $R_{\rm BLR}$ is the distance (size) of the BLR as measured from the light travel time $c\tau$, $G$ is the Gravitational constant, and $f$ is a dimensionless factor of order unity which allows for variations due to specific kinematics, structure and inclination in the BLR.

  This method was first developed by Blandford & Payne (1982) but the first sample of successfully reverberation mapped AGN was only achieved relatively recently by Kaspi et al. (2000). Since then, there have been numerous reverberation mapped samples (e.g., Peterson et al. 2004; Bentz et al. 2009a,b), yielding of order $\sim 50$ AGN with reverberation mapped black hole estimates in the local Universe.

- **The $R_{\rm BLR}$–Luminosity relationship**

  Theoretically, reverberation mapping is applicable to all AGN. However, the reverberation time-delay scales with source luminosity and this, coupled with

time-dilation effects, make it difficult and time consuming to make such measurements in sources at high red-shifts (e.g., Kaspi et al. 2007). The scaling of the reverberation time-delay with luminosity yields a relationship of the form $R_{\rm BLR} \propto L^{\delta}$, with $\delta \simeq 0.5$ (e.g., Bentz et al. 2009a,b) and $L$ is the monochromatic luminosity at a given wavelength, typically $\lambda = 5100$Å in the AGN rest-frame (e.g., Kaspi et al. 2000, 2005). This provides a far simpler, but correspondingly less precise, method of estimating black hole masses directly from the observed luminosity and the velocity dispersion of a broad emission line. The adopted line is dependent on the red-shift of the object. Most work has been done using the $H\beta$ line to calibrate $M_{\rm BH}$ estimates to reverberation mapped samples in the local universe (e.g., Vestergaard & Peterson 2006). At higher red-shifts, the broad components of Mg II (e.g., Wang et al. 2009) and C IV can be used, although the presence of inhomogeneities such as non-virial outflowing components leads to the C IV relationships being notably less precise (e.g., see Denney 2012). In the case of the H$\beta$ line, Vestergaard & Peterson (2006) measure $R_{\rm BLR}$ from reverberation mapping and derive that $M_{\rm BH}$ can be determined from the relation:

$$\frac{M_{\rm BH}}{10^6 M_{\odot}} = 8.3 \left[\frac{\rm FWHM(H\beta)}{10^3\,{\rm km\,s^{-1}}}\right]^2 \left[\frac{\lambda L_{\lambda}(5100\,{\rm \AA})}{10^{44}\,{\rm erg\,s^{-1}}}\right]^{0.5}, \tag{1.2}$$

where FWHM(H$\beta$) is the full-width at half-maximum velocity width of the H$\beta$ emission line and $\lambda L_{\lambda}(5100\,{\rm \AA})$ is the monochromatic source flux at 5100 Å. The $R_{\rm BLR} - L$ relationship applies to all red-shifts for which a broad-line AGN spectrum can be obtained. This makes it a particularly attractive means of estimating black hole masses in large samples of objects (e.g., Kollmeier et al. 2006; Shen et al. 2008; Vestergaard et al. 2008).

- **Black hole–host galaxy correlations**

  In the last decade or so it has become apparent that the properties of the host galaxy are intimately linked to the mass of the central black hole. The $M_{\rm BH} - \sigma_*$ relation indicates that black hole mass and stellar velocity dispersion are strongly

correlated, with $M_{\rm BH} \propto \sigma_*^y$ and $y \simeq 4-5$ (Ferrarese & Merritt 2000; Gebhardt et al. 2000; Merritt & Ferrarese 2001; Tremaine et al. 2002; Ferrarese & Ford 2005; Gültekin et al. 2009; Bennert et al. 2011), which appears to hold regardless of whether the host galaxy is active or quiescent (Gültekin et al. 2009; see §1.5). The black hole mass is also correlated with the mass of stellar material in the galaxy bulge (e.g., Marconi & Hunt 2003; Häring & Rix 2004), and also with its luminosity (e.g., Magorrian et al. 1998; Gültekin et al. 2009). These correlations suggest a symbiotic relationship between the black hole and the hot spheroidal stellar component of the host galaxy, and in principle their existence allows the black hole mass to be estimated where direct observations of the galactic centre and BLR are not possible (e.g., in type-2 sources). However, it is currently unclear whether these relations hold at all red-shifts, or whether there are subtly different relationships in different types of galaxy, e.g., see Zubovas & King (2012b) and discussion therein. In general, black hole mass estimates obtained through host galaxy scaling relations are often used when the more direct and reliable methods, such as reverberation mapping and the $R_{\rm BLR} - L$ relationship, are not viable.

## 1.3 Physical processes

As I have already discussed, AGN are typically broken down into different sub-classes based on their luminosity in different energy bands and on the width of their principle optical emission lines. However, despite their clearly differing observational properties it is now almost universally agreed upon that all AGN are powered by the same physical process: the accretion of matter onto a SMBH (e.g., Salpeter 1964; Lynden-Bell 1969). In this section I begin by describing the physics which underlay the AGN accretion process. I then outline the radiation and atomic processes which are important in the X-ray regime, with a particular focus on those which are important in the context of the work presented in this thesis.

### 1.3.1 Accretion

Accretion is the physical process through which a gravitational body aggregates matter from its surroundings. If the accreting matter possesses angular momentum — a quantity which must be conserved from the basic laws of physics — it is unable to fall directly onto the central mass, and it instead assumes Keplerian orbits of varying radii. The resultant body is referred to as an accretion disk (Shakura & Sunyaev 1973), and is the body through which material dissipates its angular momentum before accreting onto the central mass. In a Keplerian system the rotational velocity at radius $r$ is given by $v_{\rm kep} = (GM/r)^{0.5}$, with specific angular momentum $l_{\rm kep} = \sqrt{GMr}$. This means that material closer to the central mass will orbit it at a higher velocity than that further out. The differential rotation creates a viscous shear between the layers which, as well as increasing the temperature of the disk through the dissipation of gravitational potential energy, transports angular momentum outwards and allows matter to slowly spiral towards, and eventually accrete onto, the central object. In AGN, that central object is the SMBH (Rees 1984).

The two most important parameters when it comes to describing an accreting black hole system are the black hole's mass, $M_{\rm BH}$, and the rate at which it accretes matter, $dm/dt = \dot{M}_{\rm acc}$. The black hole mass determines the typical size scale of the system through the *Schwarzschild radius*, the radius to the event-horizon in a non-spinning black hole system,

$$r_{\rm s} = \frac{2GM_{\rm BH}}{c^2} \simeq 3 \left( \frac{M_{\rm BH}}{10^7 M_\odot} \right) \times 10^{12}\,{\rm cm}. \tag{1.3}$$

The light crossing-time from black hole to radius $r$ is then given by

$$t_{\rm L} = \frac{r}{c} \simeq 100 \left( \frac{M_{\rm BH}}{10^7 M_\odot} \right) \left( \frac{r}{r_{\rm s}} \right)\,{\rm s}. \tag{1.4}$$

The energy released through accretion is that due to the loss of gravitational potential energy, i.e., a mass $dm$ flowing from infinity down to radius $r$ will release potential energy

$$dE = \frac{GMdm}{r}. \tag{1.5}$$

This then corresponds to an accretion luminosity of

$$dL = \frac{dE}{dt} = \frac{GM\dot{M}}{2r}, \tag{1.6}$$

where the factor of 2 arises from the virial theorem which states that only half of the gravitational potential energy lost through accretion is thermalised (i.e., radiated away as heat). The rest goes towards increasing the kinetic energy of particles which hence allows them to occupy consecutively smaller orbits.

This process occurs with a characteristic efficiency and, in general, the amount of energy which is able to be released depends on how close to the black hole the accreted matter can move before plunging into it. By the conservation of energy, the closer to the black hole a particle can get the more energy it must radiate away before it can accrete; the *Innermost Stable Circular Orbit* (ISCO) is the last stable orbit that a particle can achieve before this occurs. In the simplest case, that of a non-spinning Schwarzschild black hole, the ISCO occurs at $r_{\rm isco} = 3\,r_{\rm s}$. A rigorous estimation of the accretion efficiency, i.e., one which takes into account general relativistic effects such as the curvature of space-time close to the black hole, gives an efficiency of $\eta = 0.057$ (Salpeter 1964) in the Schwarzschild metric. However, the value of $\eta$ can increase significantly if the black hole is spinning. In this case, space-time is described by the Kerr metric and $r_{\rm isco}$ moves inward by an amount proportional to the spin of the black hole. For a maximally spinning black hole, $a = J/M = 0.998\,GM_{\rm BH}/c$ (where $J$ is the angular momentum of the hole), $r_{\rm isco} = 0.62\,r_{\rm s}$, and $\eta \approx 0.32$ (Thorne 1974).

While accretion is clearly a highly efficient process there is a finite limit to the maximum luminosity that it can generate. This limit is known as the *Eddington Luminosity*, $L_{\rm edd}$, and is reached when the outward radiative momentum flux is equal to the gravitational force of the central object. For a spherically symmetric distribution of fully ionised, pure hydrogen gas, the forces due to radiation pressure and gravity are balanced when the following relation is satisfied

$$\frac{L\sigma_{\rm T}}{4\pi r^2 c} = \frac{GMm_p}{r^2}, \tag{1.7}$$

where $L$ is the luminosity released by accretion, $m_p$ is the proton mass, and $\sigma_T =$

$8\pi e^4/3m_e^2c^4 \simeq 6.65 \times 10^{-24}\,\mathrm{cm}^{-2}$ is the Thomson cross-section for electron scattering. Only the gravitational attraction of the proton is important, as it dominates over that of the electron; likewise, the scattering of photons by electrons dominates the radiation force. In both cases, the other particle is carried along through its Coulomb attraction. The Eddington luminosity — the critical luminosity which can halt accretion — is hence

$$L_{\mathrm{edd}} = \frac{4\pi GMm_pc}{\sigma_T} = 1.26 \times 10^{45} \left(\frac{M}{10^7 M_\odot}\right) \mathrm{erg\,s}^{-1}. \tag{1.8}$$

This critical luminosity has a corresponding critical accretion rate, the *Eddington accretion rate*, which is the mass required for an object to maintain its Eddington luminosity to a steady state,

$$\dot{M}_{\mathrm{edd}} = \frac{L_{\mathrm{edd}}}{\eta c^2}. \tag{1.9}$$

Therefore, in the limit that $\dot{M}_{\mathrm{acc}} > \dot{M}_{\mathrm{edd}}$ the momentum associated with the emergent radiation would be so great that any additional in-falling material would be blown back. The ratio of the source bolometric luminosity, $L_{\mathrm{bol}}$, and the Eddington luminosity is called the 'Eddington ratio', $\lambda$ ($\equiv L_{\mathrm{bol}}/L_{\mathrm{edd}}$). The Eddington ratio represents the relative importance of radiation pressure with respect to gravity. Sources with $\lambda > 0.01$ are usually regarded as relatively high accretion-rate AGN, and are thus expected to have a non-negligible contribution from radiation pressure, while sources below this threshold are dominated by gravity.

### The Shakura-Sunyaev disc

Standard disc theory (e.g., Shakura & Sunyaev 1973; Novikov & Thorne 1973) considers an optically-thick and geometrically thin disc (i.e., the ratio of disc scale height $H$ to its radius $r$ is $\ll 1$ at all radii), where the orbital velocity of material in the disc is much faster than its inward flow speed. Material in the disc drifts inward by losing energy and angular momentum through the action of the internal disc viscosity $\alpha$. The lost angular momentum is then transported through the disc to larger radii, and the excess energy heats the gas and ultimately gets radiated away. Since the radial velocity in such a system is small compared to the rotational one, the energy is dissipated locally without

being advected further inward. The disc is thus radiatively efficient with each annuli of gas thermalising to a black body. From standard physics, the luminosity $dL$ emitted from a specific disc annulus of thickness $dr$ is related to its effective temperature by

$$dL = A\sigma T^4 = 2 \times 2\pi r dr \sigma T^4, \tag{1.10}$$

where $A$ is the area of the emitting annulus (multiplied by 2 because the disc has two sides), $T$ is the temperature of the black body emission and $\sigma$ is the Stefan-Boltzmann constant. The luminosity of a given annulus in the disc can also be represented as

$$dL = \frac{GM\dot{M}}{2r^2} dr, \tag{1.11}$$

which hence implies that

$$T = \left( \frac{GM\dot{M}}{8\pi r^3 \sigma} \right)^{\frac{1}{4}}. \tag{1.12}$$

However, this rather simple derivation over-simplifies the situation in that it only conserves energy and neglects the conservation of momentum. A derivation which conserves this second quantity yields an additional factor of 3, and a new term (Frank, King & Raine 2002):

$$T(r) \approx \left[ \frac{3GM\dot{M}}{8\pi r^3 \sigma} \right]^{\frac{1}{4}} \left( 1 - \sqrt{\frac{r_{\rm in}}{r}} \right)^{\frac{1}{4}} \tag{1.13}$$

where $r_{\rm in}$ is the inner radius of the accretion disc. In the limit that $r \gg R_{\rm in}$ this can be expressed in more convenient units as:

$$T(r) \approx 3.5 \times 10^7 \eta^{-\frac{1}{4}} \left( \frac{\dot{M}}{\dot{M}_{\rm edd}} \right)^{\frac{1}{4}} \left( \frac{M_{\rm BH}}{M_\odot} \right)^{-\frac{1}{4}} \left( \frac{r}{r_{\rm s}} \right)^{-\frac{3}{4}} K \tag{1.14}$$

From this, it is clear that $T(r) \propto r^{-3/4}$ and so the inner annuli of the accretion disc will be much hotter and emit thermal radiation at subsequently higher energies than those further out. The resultant superposition of blackbodies creates a so-called 'multi-colour disc black-body', which is the simplest way of visualising the intrinsic emission spectrum. It is also apparent that at a given radius, the temperature increases with accretion rate but will decrease with increasing mass. In the fiducial case of a $M_{\rm BH} \sim 10^7 M_\odot$

Schwarzschild black hole accreting at its Eddington rate, the accretion disc temperature at, say, $r = 10\,r_{\rm s}$, is $kT \sim 50\,{\rm eV}$, where $k$ is Boltzmann's constant. Therefore, the thermal black-body emission for an accretion disc around an AGN black hole is expected to be observed in the extreme ultraviolet. The question then arises: how and why can AGN be so bright in the X-rays? I discuss this topic in the next section.

### 1.3.2 Comptonisation

Compton scattering, or the Compton effect, is the process through which energy is exchanged between photons and electrons. In the standard case it describes how high-energy photons (e.g., an X-ray or a $\gamma$-ray) are scattered when they collide with non-relativistic electrons. In a collision a portion of the incident photons' energy and momentum are transferred to the electron (which recoils from the collision), with the photon being scattered in a new direction with a reduced energy and a change of momentum. The energy (wavelength) shift between the in–out photon is proportional to the change in momentum caused by the primary photon–electron collision. In wavelength space, Compton scattering is described by:

$$\lambda' - \lambda = \Delta\lambda = \frac{h}{m_{\rm e}c}(1 - \cos\theta), \tag{1.15}$$

where $\lambda$ is the wavelength of the incident photon, $\lambda'$ is the post-scattering wavelength of the photon and $\theta$ is the scattering angle. The other constants have their standard definitions.

Inverse Compton scattering (or Comptonisation) is the reverse of this process and occurs when the electrons are relativistic and have more energy than the incident photon field. In this case the photons scattered by the electron field gain energy and momentum rather than lose it. The more photon–electron collisions that occur the more energy is given to the photons, which decreases their wavelength. However, the limit to this 'upscattering' is reached when the photons and electrons reach a state of energetic equilibrium at the 'Compton temperature'. Relative to this, Compton scattering and

Comptonisation can then be considered heating and cooling mechanisms for the electron field by virtue of increasing / reducing the electron temperature.

### 1.3.3 Photoelectric effect

The observed spectral features in a spectrum are the product of an interaction between bound electrons in an atom and incident photons. When a bound electron absorbs a photon the energy state of the atom is changed such that the electron makes either a bound-free or a bound-bound transition. Which of these occurs is dependent upon the energy of the incident photon. If the photon has an energy exceeding the binding energy of the electron it is able to escape the system via a bound-free transition and the atom becomes ionised. Alternatively, if the photon energy is less than the binding energy the absorbed energy may still allow the electron to transit between energy levels via a bound-bound transition and the atom enters an excited state, which then de-excites by emitting another photon. In both cases, a photon is removed from the continuum and a characteristic spectral feature is imprinted into the spectrum.

#### Bound-free absorption

The amount of absorption which is observed is governed by the optical depth of the absorbing gas along the line of sight. In X-ray astronomy it is convention to represent this as $\tau = \sigma(E)N_{\mathrm{H}}$, where $\sigma(E)$ and $N_{\mathrm{H}}$ are the photo-electric cross-section and equivalent column density of hydrogen, respectively. The cross-section itself is in turn a complex function of energy state, atomic number and ionisation state. The simplest exploratory case to consider is that of a neutral absorber of pure hydrogen gas, where each atom has only one bound electron with a binding energy of 13.6 eV. For bound-free absorption to occur the atom must absorb a photon with energy in excess of the binding energy. The cross-section for the ionisation event is zero below 13.6 eV, increases sharply at $E_{\mathrm{edge}} = 13.6\,\mathrm{eV}$ and then slowly declines as $\sim (E/E_{\mathrm{edge}})^{-3}$ at higher energies. The

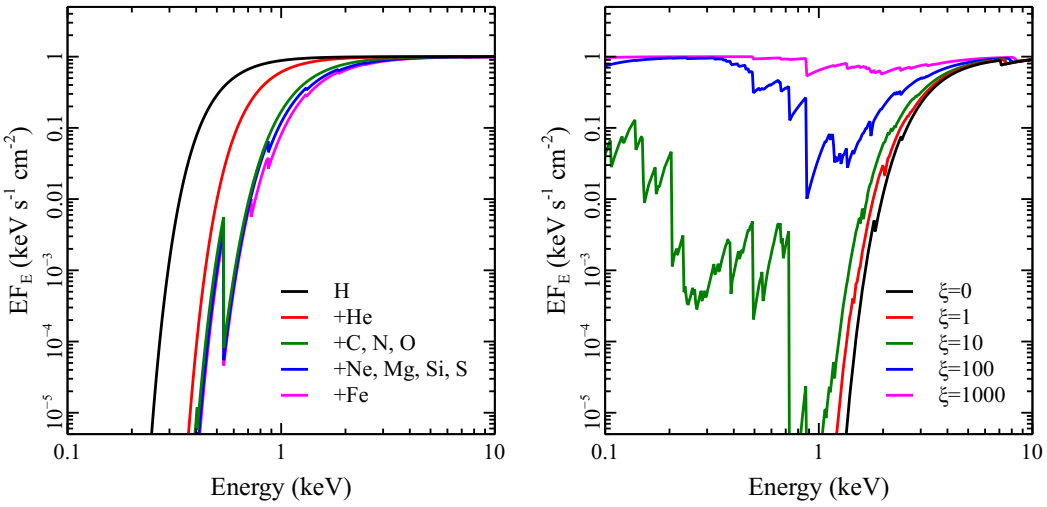


Figure 1.3: Example models showing how changes in the photo-electric absorption cross-section affect the transmitted spectrum. The *left* panel shows how the inclusion of subsequently heavier metals affects the flux transmitted through a fiducial $\log(N_{\rm H}/{\rm cm}^{-2}) = 22$ layer of neutral gas. The *right* panel shows how increasing the ionisation state of a $\log(N_{\rm H}/{\rm cm}^{-2}) = 23$ layer of gas alters the transmitted flux. Note that whilst it is not explicitly stated, the Energy scale is in units of keV on the right-hand panel. Both of these figures are adapted from Done (2010).

reprocessed (absorbed) and intrinsic continuum emission are then related by:

$$S_{\rm obs}(E) = S_{\rm int}(E) \times e^{-\tau} \tag{1.16}$$

where $S_{\rm obs}$ is the observed reprocessed spectrum, $S_{\rm int}$ is the intrinsic spectrum and $\tau = \sigma(E)N_{\rm H}$ is the optical depth of the absorbing material. The increased opacity at 13.6 eV imparts a characteristic 'edge' of absorption in the spectrum. In reality, the total photo-electric absorption cross-section is a sum of abundance weighted cross-sections for each element. Additional elements cause more photoelectric edges to appear in the spectrum, and the total cross-section increases in proportion to the metals' astrophysical abundance (see Fig. 1.3, left).

Bound-free absorption turns an atom into an ion and this can have an important

effect on the photo-electric cross section. In an ion the nuclear charge is not balanced (i.e., protons in the nucleus outnumber the orbiting electrons) which means that the remaining electrons are more tightly bound than before. This increases the energy needed to un-bind them and shifts $E_{\rm edge}$ to even higher energies. In principle, any ion can recombine with any free electrons but if the photon field is sufficiently intense there can be many photon absorption events before the ions are able to recombine, and the total cross-section becomes dominated by ions rather than neutral atoms. This has the effect of making the gas more transparent to continuum radiation. For example, in a (solar abundances) gas where every element has on average one electron removed, hydrogen would not contribute to the total cross-section because it has an effective optical depth of zero as there are no more electrons for an ionisation event. Helium then has one electron, and its edge moves to higher energies as the remaining electron is bound more tightly due to increased effective nuclear charge. At even higher ionisations Helium will become completely ionised, so it also no longer contributes to the total cross-section, and so-on and so-forth for subsequently higher ionisation states. Thus, the higher the average ionisation state the lower the total cross-section for absorption, and the more transparent the material. Ultimately, if the ionisation state is high enough there will be no photo-electric absorption at all because every atom will be stripped of all of their electrons. The ionisation state of the gas can be parametrised by the ionisation parameter $\xi = L_{\rm ion}/nr^2$ (Tarter, Tucker & Salpeter 1969), where $L_{\rm ion}$ is the ionising source luminosity integrated between $1 - 1000$ Rydberg, $n$ is the hydrogen number density and $R$ is the distance of the ionising source from the absorbing clouds. Fig. 1.3 (right) shows the flux transmitted through a $\log(N_{\rm H}/{\rm cm}^{-2}) = 23$ column of gas at various ionisation stages, ranging from $\xi = 0 - 1000$, highlighting the decreasing absorption cross-section (and therefore more transmitted flux) at higher ionisations.

At X-ray energies any intervening gas is typically in a high ionisation state which means that the opacity is dominated by ions rather than neutral atoms. Throughout this thesis I use a naming convention which labels an ion according to which neutral atom would have the same number of electrons. For example, should an atom have only one or two of its electrons left, its electronic configuration resembles that of hydrogen or

helium, and I then refer to it as Hydrogen-like (H-like) or Helium-like (He-like). I also extended this scheme to configurations involving larger numbers of electrons by referring to ions as Li-like, Be-like, etc., for increasing numbers of electrons, and also to specific electron transitions as well. Specifically, I refer to the $1s \leftrightarrow np$ transitions in H-like ions as Lyman lines due their resemblance of the hydrogen Lyman series, e.g., a $1s \rightarrow 2p$ in H-like oxygen will be referred to as O VIII Ly$\alpha$. Atoms ionised to their H-like and He-like electron configurations are prevalent in the X-ray regime, and so this naming convention is used frequently throughout this thesis.

### Bound-bound absorption & spectral lines

If there are sufficient vacancies in an outer electron shell the absorption of photons can cause an atom or ion to become photo-excited via line (bound-bound) transitions. These occur if the absorbed photon has an energy equal to the quantised energy separation between different electron orbital shells. As before, the probability of this occurring is still a function of energy and the cross-section, with the cross-section again peaking when the photon has *just* enough energy to excite the electron between orbitals and declining rapidly to higher and lower energies. Atomic lines can occur for every bound electron in an atom or ion which has sufficient outer-shell vacancies and the resultant absorption line has a unique energy which depends on both the element and the specific electron transition. As the system relaxes back to the ground state, the absorbed energy is re-emitted as either a single photon of the same frequency as the original (i.e., equal to the energy separation between the shells), or, if there are many electrons present, in a cascade of photons where the total sum of the energies will equal that which was absorbed. These constitute discrete bound-bound emission lines. As the characteristic energy differences between the electron levels are unique to each type of atom, observations of these line features can unlock information relating to the constituents and abundances of these elements within the material that is being observed. They can also provide information about the density and temperature of the material (e.g., Porquet & Dubau 2000; Porquet et al. 2001; Porquet, Dubau & Grosso 2010).

In general, and regardless of whether a line is seen in absorption or emission, the standard metric for measuring the strength of a profile is its *equivalent width* ($EW$). The $EW$ is defined as the width of a rectangular box of continuum (down to zero intensity) centred at the measured line energy, which contains the same flux as the area of the observed profile, i.e.,

$$EW = \int \left(1 - \frac{F_{\rm line}}{F_{\rm cont}}\right) dE, \tag{1.17}$$

where $F_{\rm line}$ is the flux (intensity) contained in the observed line profile (in units of $\mathrm{ph\,cm^{-2}\,s^{-1}}$) and $F_{\rm cont}$ is the integrated continuum flux beneath the line (in units of $\mathrm{ph\,cm^{-2}\,s^{-1}\,eV^{-1}}$).

### Fluorescence

In addition to the standard bound-bound transitions in ions and atoms, there is a special bound-bound transition which is specific to neutral material: *fluorescence emission*, which occurs when an incoming high-energy photon has sufficient energy to directly remove an inner-shell electron from the K-shell in neutral material. When this occurs, an electron from a higher energy level — for example, the L- or M-shells — drops down to fill the vacancy in the K-shell via the emission of a fluorescent line photon. Alternatively, if there is another L-shell electron present, the energy released can instead remove another L-shell electron from the atom in a process known as auto-ionisation or the Auger effect. The probability that a fluorescence line photon is emitted rather than an auto-ionisation event occurring is given by the fluorescence yield of the material, which has a $\sim Z^3$ dependence (where $Z$ is the proton number; e.g., Krolik 1999). This means that while fluorescent lines can in principle be observed in all elements, those from heavier elements (e.g., iron) will be much stronger than those of lighter ones. Fluorescence is a very important physical process in AGN and, as I will discuss in more detail later, is a key identifiable characteristic of the X-ray reflection continuum seen around accreting black holes.

## 1.4 The complex X-ray spectrum

AGN are prodigious emitters at X-ray energies, with the X-ray radiation constituting of order a thirtieth of their bolometric luminosity (e.g., Elvis et al. 1994; Marconi et al. 2004; Barger et al. 2005). The X-ray radiation is also rapidly variable, down to time-scales as short as ∼hours in some cases (e.g., Giustini et al. 2011). Causality arguments therefore suggest that the primary X-ray emitting region is location close to the black hole, on the order of $t_{\rm L} \lesssim c\Delta t \sim 10^{-3}\,{\rm pc}$, while gravitational lensing studies have resolved the emitting region to be on the order of tens of Schwarzschild radii in radius (e.g., Morgan et al. 2008; Chartas et al. 2009; Dai et al. 2010). This means that studying AGN at X-ray wavelengths is of fundamental importance when it comes to both probing the inner-most regions of active galaxies, and to studying the details of the accretion process which power them. A toy model of a typical X-ray spectrum for a type-1 Seyfert galaxy, highlighting the various spectral components, is shown in Fig. 1.4. In the remainder of this section I will briefly discuss the various components which make up this composite model.

### 1.4.1 Producing the X-ray continuum

As I showed in §1.3.1 the accretion disc around a SMBH emits the bulk of its thermal radiation at ∼EUV wavelengths and so cannot be responsible for the observed X-ray emission; at least not directly. The currently accepted model is that the X-ray emission is produced in a 'corona' of hot (i.e., relativistic) electrons which envelope the inner regions of the accretion disc (e.g., Haardt & Maraschi 1991, 1993). Optically-thick UV photons from the disc enter the corona which allows the hot electrons to cool by Compton (up)scattering the UV seed photons into a hard X-ray power-law. In such a power-law the number of photons per energy bin is given by $N(E) = N_0 E^{-\Gamma}$, where $\Gamma$ is the photon index or 'slope' of the power-law and $N_0$ is its normalisation (Done 2010). This then

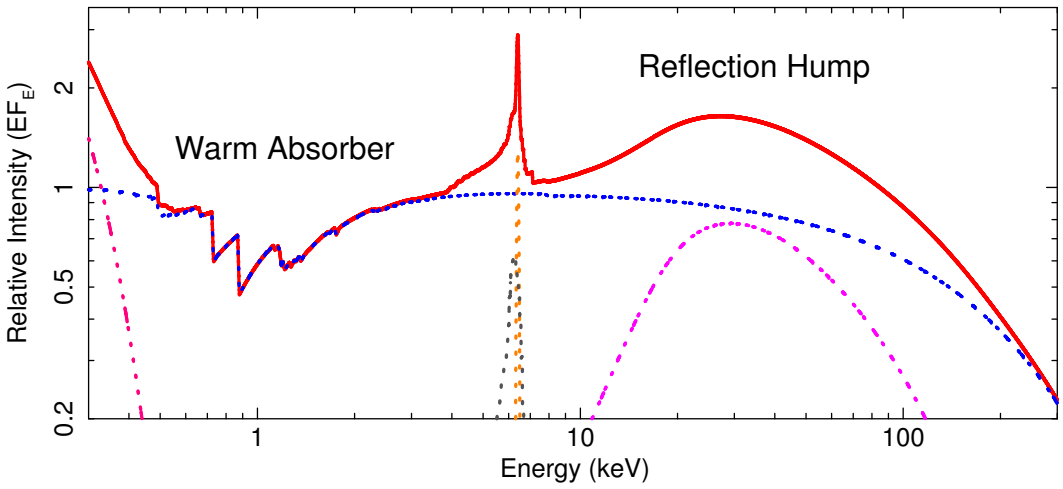


Figure 1.4: Plot showing a toy model of a typical Seyfert 1 X-ray spectrum designed to highlight the various spectral model components which are frequently observe at X-ray wavelengths. As such, not all of these components are present in every X-ray spectrum. The total integrated (observed) spectrum is shown by the *red* line. The other components shown are (1) the primary power-law continuum [*blue* line], (2) the soft-excess [*magenta* line], (3) the Compton reflection component [*pink* line], (4) the neutral Fe K$\alpha$ fluorescence line at $\sim 6.4\,\mathrm{keV}$ [*yellow* line], and (5) broadened Fe K$\alpha$ line [*gray* line]. The typical spectrum can also show strong atomic features from photo-ionised material at $E \lesssim 2-3\,\mathrm{keV}$, known as the 'warm absorber'. The components are described in further detail in the text.

corresponds to an energy flux of

$$F(E) = E \cdot N(E) = N_0 E^{-\Gamma+1}. \tag{1.18}$$

The scattered photons cannot obtain energies in excess of the thermal energy of the corona so the Comptonisation model predicts an exponential cut-off of the power-law at $E > E_{\mathrm{corona}}$ which is proportional to $\exp[-(E/E_{\mathrm{corona}})]$. To date cut-offs have been measured in a number of AGN leading to inferred corona temperatures ranging from $50-200\,\mathrm{keV}$ (e.g., Perola et al. 2002; Dadina 2008).

As an aside it is important to note that while the primary continuum is approximated by a power-law it is commonplace to plot spectra in $\log(EF_{\mathrm{E}})$ versus $\log(E)$ format.

These plots are useful in AGN because a $\Gamma = 2$ power-law, which has equal energy output over all wavelengths and is fairly typical of local AGN (e.g. Reeves & Turner 2000), will appear as a flat horizontal line (i.e., $EF_{\rm E} \propto E$). This allows the energy output at different points of the spectrum to be compared directly which makes it immediately obvious where the majority of the energy output is taking place.

### 1.4.2 The reflection component

Comptonisation is an isotropic process. This means that around half of the flux emitted from the corona will be scattered into the ambient medium whilst the remainder is scattered back towards the disc and undergoes further reprocessing. This gives rise to a spectral phenomenon known as *Compton reflection*, which is most apparent at hard X-ray energies (Lightman & White 1988; Guilbert & Rees 1988; Pounds et al. 1990; Nandra & Pounds 1994; George & Fabian 1991; Matt, Perola & Piro 1991). In the simplest case, the modelling of this component supposes that the accretion disc is a semi-infinite slab of uniform density covering $2\pi$ steradian (from the view of the source) which is irradiated by the X-ray continuum produced in the disc corona. In the slab, hydrogen and helium are completely ionized while the other elements are either effectively neutral or only lowly ionised (i.e., Fe XVII and below).

An X-ray photon incident upon the disc can undergo one of two principal reprocessing interactions. Firstly, the photon can be Compton down-scattered out of the slab by free electrons in the plasma. Secondly, the photon can be photo-electrically absorbed by one of the neutral or lowly ionised atoms resulting in spectral line emission. Which of these occurs is governed by the energy of the incident photon and the interplay between the scattering and absorption cross-sections. Fig. 1.5 (left) compares the total opacity of a $\log(N_{\rm H}/{\rm cm}^{-2}) = 24$ column of 'neutral' medium (with H and He fully-ionised, as per the standard reflection models) against the electron scattering cross-section. The two are equal at around 10 keV, with absorption and scattering becoming dominant at lower and higher energies, respectively. This means that softer X-rays are far more likely to be absorbed than to be scattered due to the larger photo-electric cross-section at

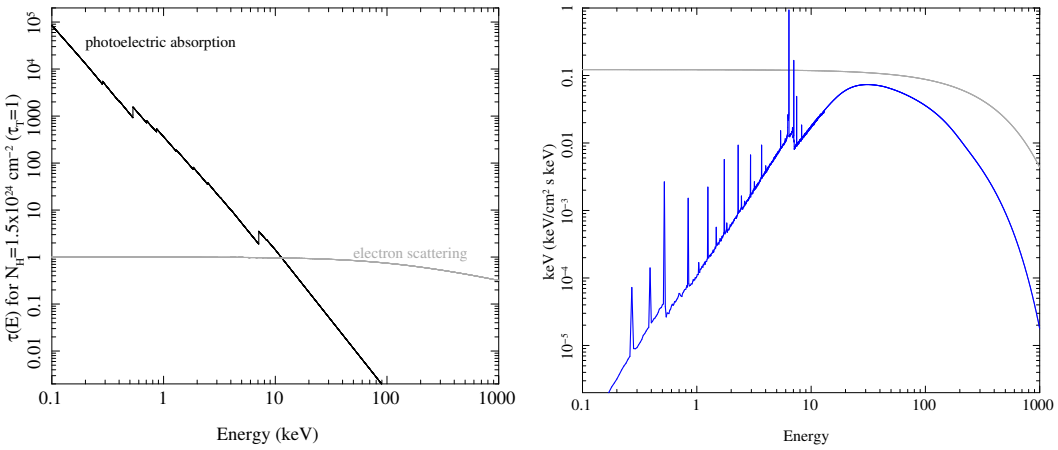


Figure 1.5: The *left* panel compares the photo-electric absorption cross-section in a $\log(N_{\rm H}/{\rm cm}^{-2}) \sim 24.18$ 'neutral' absorber (i.e., every element neutral except for helium and hydrogen, which are fully ionised) with the electron scattering cross-section. The two are ∼equal at $\sim 10\,{\rm keV}$, with absorption and scattering becoming dominant towards higher and lower energies, respectively. The *right* panel shows an example reflection continuum which occurs when a Compton-thick accretion disc is illuminated by a flat power-law continuum. There are numerous fluorescent lines present, with the most prominent being that due to Fe K$\alpha$ at 6.4 keV. Both of these figures are taken directly from Done (2010).

lower energies. As the photon energy increases, the cross-section for absorption decreases, leading to a larger reflection fraction towards higher energies. High energy X-rays, on the other hand, are rarely absorbed and will instead lose a large fraction of their energy through one or more Compton down-scattering interactions before being 'reflected' at lower energies. Therefore, if the X-ray radiation incident on the disc is a flat power-law, the reflection radiation will be most intense in the $5 - 50\,{\rm keV}$ range, with a 'peak' at around 30 keV. The peak is termed the 'reflection hump' (Pounds et al. 1990; Nandra & Pounds 1994; George & Fabian 1991; Matt, Perola & Piro 1991) and is the characteristic signature of a reflected continuum.

In addition to the above, it is possible that an absorbed soft X-ray photon will result in either fluorescent line emission or the ejection of an Auger electron. Due to its

large cosmic abundance and high fluorescence yield the most prominent fluorescent lines seen in AGN spectra are those from iron, with Fe K$\alpha$ at $E \sim 6.4\,\mathrm{keV}$ being an almost ubiquitous feature of the X-ray spectrum (Nandra et al. 2007; Shu, Yaqoob & Wang 2010). Fluorescent emission from other heavier elements, such as argon, calcium or nickel, can also be observed. However, the fluorescence yield scales as $\sim Z^3$ and this combined with the relative solar abundances means that iron is always the strongest. The Fe K$\alpha$ line is actually a doublet, consisting of two separate components: Fe K$\alpha_1 = 6.404\,\mathrm{keV}$ Fe K$\alpha_2 = 6.391\,\mathrm{keV}$, with a branching ratio of 2 : 1. But the individual components are indistinguishable with the current generation of X-ray telescopes and the observed line is therefore a blend of the two. Whenever fluorescent emission is present, an accompanying absorption edge is theoretically expected at the binding energy of the inner-shell (K) electron. For neutral iron, this edge occurs at 7.1 keV and the line at 6.4 keV is the energy emitted when an $n = 2$ (L-shell) electron drops down to fill the hole left behind in the inner K-shell. The Fe K$\beta$ fluorescence line, which the result of an $n = 3$ (M-shell) electron dropping to fill the K-shell vacancy, is also sometimes detected at $E \sim 7.06\,\mathrm{keV}$ with a K$\beta$ : K$\alpha$ flux ratio of $\sim 13\%$.

While not the primary topic of this thesis it is worth noting that should the reflecting region be close to the SMBH, e.g., from the surface of the accretion disc, then the Fe K$\alpha$ fluorescent line can become broadened by a combination of disc rotation, the transverse Doppler effect and the gravitational red-shift induced by the black hole (see Fabian et al. 2000a for a review). In principle, a distorted Fe K$\alpha$ line profile offers a very powerful diagnostic of the state of the accretion flow and also provides a means of measuring the spin of the central black hole. However, it has recently been highlighted that broadened Fe K$\alpha$ fluorescence line profiles can be mimicked by absorption and scattering effects (e.g., Sim et al. 2010; Tatum et al. 2012) associated with outflowing nuclear material, which suggests that a number of the reported spin estimates in the literature may be model dependent.

### 1.4.3 The soft-excess

Relative to the low-energy extrapolation of the power-law continuum in the $2-10\,\mathrm{keV}$ band the X-ray spectra of AGN often show a smooth increase in emitted flux below $\sim 1\,\mathrm{keV}$ (Turner & Pounds 1988; Porquet et al. 2004a). Historically, this feature was initially explained as a separate soft continuum component such as a thermalised disc black-body, with temperatures of the order $kT \sim 0.1-0.3\,\mathrm{keV}$ (e.g., Walter & Fink 1993; Czerny et al. 2003). However, it was soon remarked that this is much too hot to be the direct emission from an accretion disc around a SMBH (see §1.3.1), although it could plausibly be Comptonised disc emission (e.g., Czerny & Elvis 1987; Wang & Netzer 2003). In this scenario the electrons in the Comptonising corona could be 'quasi-thermal', having both a thermal and non-thermal component (e.g., Coppi 1999). Even so, explaining the soft excess through this mechanism would require a very narrow range of electron temperatures over a very wide range of black hole mass (Gierliński & Done 2004), which makes this origin for the soft-excess unlikely. That being said, recent studies by Done et al. (2012, see also Jin et al. 2012; Jin, Ward & Done 2012a,b) have shown that Comptonisation models are plausible for high accretion-rate and low black-hole-mass AGN such as NLSy1s, although it is unclear how, or even if, these models extend to the wider lower accretion-rate AGN population.

Another possibility is that the soft-excess has a direct atomic origin. Plausible explanations in this context include blurred reflection (e.g., Crummy et al. 2006; Nardini et al. 2011; Brenneman et al. 2011; Nardini, Fabian & Walton 2012) or smeared absorption (e.g., Middleton, Done & Gierliński 2007). Both of these scenarios would require a portion of the continuum to be re-processed in partially-ionised gas located close to the black hole. In the reflection case, the re-processor is likely to be the inner accretion disc, where relativistic and gravitational light-bending effects smear the reflected emission lines into a smooth pseudo-continuum which manifests itself as the soft-excess (e.g., Miniutti & Fabian 2004). For smeared absorption, on the other hand, the smearing could feasibly be achieved via intervening gas along the line of sight being subjected to a large velocity shear which Doppler broadens the atomic features into a smooth shape

(Gierliński & Done 2004; Middleton, Done & Gierliński 2007). However, the velocity needed for sufficient smearing is prohibitively large, i.e., of the order $v \sim c$ (Schurch & Done 2007; Schurch, Done & Proga 2009), which rules out an identification with a radiatively or thermally driven disc-wind, although a jet origin could be plausible.

Another absorption-based explanation for the soft-excess is that it may not actually be an 'excess' at all, but could instead just be the result of a complex / partially-covering absorption geometry. In this scenario, the gas does not require a large shear velocity but instead simply consists of one or more partially-covering fractions of neutral or ionised gas. Different combinations of ionisation state and column density in the absorber conspire to suppress the intrinsic continuum through scattering effects. At moderate ionisation states and column, i.e., $\log(\xi/\mathrm{erg\,cm\,s^{-1}}) \sim 2$ and $\log(N_{\mathrm{H}}/\mathrm{cm^{-2}}) \sim 22$, the lighter elements are fully ionised which allows more continuum to be transmitted at lower energies, giving rise to the observed 'pseudo-excess'. To date, this interpretation has been used to describe the broad-band X-ray continua in a number of objects, e.g., Mrk 766 (Miller et al. 2007; Turner et al. 2007), MCG 6-30-15 (Miller, Turner & Reeves 2008, 2009; Miyakawa, Ebisawa & Inoue 2012), NGC 3516 (Turner et al. 2007, 2011) and MR 2251-178 (see Chapter 3) which suggests that, at least in some cases, the soft-excess could have an origin in complex absorption. An advantage of this interpretation is that the complex absorption geometries can also be invoked to describe complicated spectral variability patterns (e.g., Miller et al. 2007; Turner et al. 2011; Risaliti et al. 2011; Nardini, Fabian & Walton 2012), although reflection-based models can sometimes fit the spectrum equally well.

In any case, and while multiple plausible scenarios have been proposed, there is no consensus as to what causes the soft-excess phenomenon. In the majority of objects it is extremely difficult to unambiguously distinguish between these interpretations on a statistical basis, and vastly differing models can fit the same data equally well. Ultimately, it is clear that there remains a lot of work to be done when it comes to understanding what causes the soft-excess phenomenon.

### 1.4.4 X-ray absorption

Absorption is also important elsewhere in the X-ray spectrum. Below $E \lesssim 2-3\,\mathrm{keV}$ the X-ray spectrum of Seyfert 1 galaxies is often absorbed by circum-nuclear gas in the vicinity of the AGN. Numerous spectroscopic studies have established that such absorption, as revealed through the presence of discrete bound-bound and bound-free absorption lines from astrophysically abundant elements such as C, N, O, Ne, Mg, Si, S and Fe, is a characteristic of at least $\sim 50\%$ of AGN in the local universe (e.g., Reynolds 1997; Blustin et al. 2005; McKernan, Yaqoob & Reynolds 2007). More recently, absorption from He- and H-like iron has also been found at $E \gtrsim 6.7\,\mathrm{keV}$ in a similar fraction of objects (e.g., Tombesi et al. 2010a). Generally, these absorption lines are blue-shifted with respect to the AGN rest-frame, thereby indicating an association with gas outflowing along the line of sight. These outflows are capable of expelling large quantities of energy into the host galaxy and it is thought that this energy can play a role in shaping the host galaxy via self-regulated negative feedback (e.g., Di Matteo, Springel & Hernquist 2005; Hopkins & Elvis 2010). In the next section I will describe the physical properties of AGN outflows in more detail and outline their possible importance when it comes to feedback.

## 1.5 The AGN–host-galaxy connection

Whilst AGN have always been considered interesting objects of study in their own right, it is now apparent that feedback from AGN may also play an important role in the evolution of their host galaxies. In particular, there is compelling evidence that the properties of both the central AGN and those of the host galaxy are inextricably linked. The mass of the SMBH is now known to be correlated with several of the host galaxies bulge properties, e.g., the stellar velocity dispersion[1] ($M_{\mathrm{BH}} - \sigma_*$, Ferrarese & Merritt

[1]The velocity dispersion denotes the standard deviation of stellar rotational velocities relative to the mean. From the virial theorem, the kinetic energy (and thus rotational velocity) is directly related to the potential energy of the system. The stellar velocity hence provides an indirect estimate of the depth of the galaxies' gravitational potential well, which is a proxy for how massive the galaxy is.

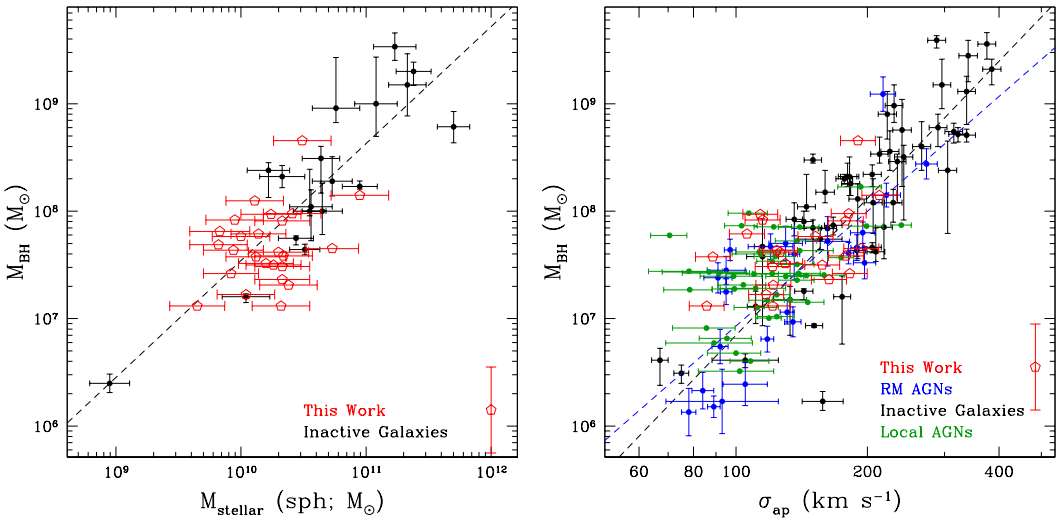


Figure 1.6: Plots highlighting two of the numerous linear correlations which exist between the properties of the host galaxy and the mass of the central SMBH. The *left* panel shows the $M_{\rm BH} - M_{\rm stellar}$ relation, while the *right* panel shows a compendium of recent results in relation to the $M_{\rm BH} - \sigma_*$ relation. 'RM AGNs' refers to AGN with a reverberation mapped black-hole mass available in the literature. The $M_{\rm BH} - \sigma_*$ relation currently represents one of the strongest evidences for their being self-regulating feedback at play in AGN. 'This work' refers to Bennert et al. (2011), from which both figures are taken.

2000; Gebhardt et al. 2000; Merritt & Ferrarese 2001; Tremaine et al. 2002; Ferrarese & Ford 2005; Gültekin et al. 2009), bulge luminosity ($M_{\rm BH} - L_{\rm bulge}$, e.g., Magorrian et al. 1998; Gültekin et al. 2009), the bulge binding energy (Aller & Richstone 2007), and the mass of stellar material ($M_{\rm BH} - M_{\rm bulge}$, Marconi & Hunt 2003; Häring & Rix 2004). Moreover, recent results have found that the inferred rate of SMBH growth in $z \sim 1 - 2$ star-forming galaxies is essentially linearly proportional to the star formation rate, with a constant ratio between the two of $\sim 10^{-3}$ (Mullaney et al. 2012). An almost identical ratio is found for $M_{\rm BH}/M_{\rm bulge}$ in quiescent galaxies (e.g., Marconi & Hunt 2003; Häring & Rix 2004), which suggests a close coupling between the evolution of the central black hole and that of the host galaxies' stellar content.

To first order, the existence of these relationships in both active and quiescent

galaxies, implies that (1) nearly every galaxy harbours a SMBH which goes through an active AGN phase where it accrues mass, and that (2) a feedback or self-regulation mechanism is present which (i) prevents the SMBH mass from growing at a rate independent of its local environment, and (ii) ensures that the star formation rate is proportional to the SMBH mass. In this sense, galaxies and their AGN can largely considered be coeval, although the precise details of the feedback mechanism acting to lock-in this co-evolution remains elusive.

### 1.5.1 The role of feedback

AGN feedback takes place when the energy and radiation emitted as a by-product of the accretion process interacts with the gas of the host galaxy. During a given phase of nuclear activity there are two principle mechanisms through which an AGN can interact with its environment: radiative feedback and mechanical energy injection. Given the intense electromagnetic emission which is characteristic of AGN, the interactions between the emergent AGN photon field and the ambient gas in both the inter-stellar and intra-cluster medium (ISM and ICM, respectively) are a logical source of feedback. Indeed, high energy continuum emission from the AGN (e.g., X-rays) is thought to be capable of providing the necessary Compton heating to counteract the expected baryonic cooling flow in galaxy spheroids, and to thus potentially quench local star formation (Ciotti & Ostriker 2001; Sazonov et al. 2005); however, this mechanism alone is unable to account for the more fundamental relationships, e.g., the $M_{\rm BH} - \sigma_*$ relation, and a source of mechanical feedback still needs to be invoked to explain the observations (Ciotti, Ostriker & Proga 2009).

In this context the term 'mechanical feedback' refers to the in-situ deposition of kinetic energy and momentum via the coupling of radiation with ambient gas. Two modes of mechanical feedback have been identified in AGN. Formally, these are known as (1) the *radio mode* (also known as 'kinetic' or 'maintenance' mode) and (2) the *quasar mode* (alternatively, 'radiative' or 'wind' mode), and the two are differentiated by the coupling mechanism of the energy flow.

The radio-mode is typified by the presence of powerful relativistic jets and as such is a characteristic of the radio-loud sub-population of AGN. Jets, which are presumably driven by magnetic forces (e.g., Blandford & Znajek 1977) and emanate close to the SMBH, inject heat into the intra-galactic medium (IGM) by inflating huge lobes of intense radio emission which can extend up to $\sim$ Mpc scales from host galaxy (e.g., 3C 236, Willis, Strom & Wilson 1974). The mechanical heating associated with this emission is argued to be the regulatory mechanism which brings the high mass end of the observed galaxy luminosity function, which is otherwise over-predicted (Croton et al. 2006), in line with the expected $\Lambda$CDM dark matter distribution (e.g., Croton et al. 2006; Bower et al. 2006). The heating of the IGM reduces the efficiency with which gas can cool in the most massive dark matter haloes, thus preventing the formation of too many massive galaxies (see Croton et al. 2006 and references therein). The hot bubbles inflated in the ICM can also quench the cooling flow in gas rich clusters of galaxies (e.g., Fabian et al. 2000b, 2006; Sanders, Fabian & Taylor 2009) which further implies that jets can be an important source of self-regulation and feedback on the large scale. Even so, the fraction of explicitly radio-loud AGN is relatively low, at around 10%, and therefore the jet phenomenon apparently has a similarly low incidence in active galaxies. This, compounded by their highly collimated nature (hence low covering fraction) which disfavours efficient energy coupling over large solid angles, suggests that the so-called 'radio-mode' feedback is not the main form of feedback at play over the Hubble time.

The other — likely more dominant — means of exerting mechanical feedback is through mass outflows (hereafter 'winds'). Radiatively driven wide-angle winds are naturally expected in high accretion rate systems (i.e., $\lambda > 0.1$, where outwards radiation pressure is an appreciable fraction of the gravitational force, King & Pounds 2003; Proga & Kallman 2004; Sim et al. 2008, 2010) and during gas-rich galaxy mergers (e.g., Hopkins et al. 2006). As such, they are likely to have been prominent at the peak of quasar activity and (currently) represent the most promising forms of feedback when it comes to explaining, for example, the observed downsizing problem (Scannapieco, Silk & Bouwens 2005), the metal enrichment of the ISM/IGM (Germain, Barai & Martel 2009; Barai, Martel & Germain 2011) and the black hole–host galaxy relations (Di Matteo,

Springel & Hernquist 2005). In principle, then, winds could play an important role, if not a fundamental one, in both setting up the black hole–host galaxy relationships and explaining the red-shift evolution of AGN.

However, the precise mechanism through which these winds are accelerated — be it radiation pressure (King & Pounds 2003; Proga & Kallman 2004; Sim et al. 2008) or magneto-centrifugal forces (Ohsuga et al. 2009; Kazanas et al. 2012; Narayan et al. 2012) — is a matter of debate. This is in contrast to the relativistic jets which are almost certainly driven by magneto-centrifugal forces close to the black hole. Of the two proposed mechanisms, those pertaining to radiative driving are both the most developed, and the most successful in describing observations because they give quantitative predictions which can be compared to real data (e.g., King 2005, 2010; Sim et al. 2010). Models describing magneto-centrifugally driven winds, on the other hand, are at a relatively young stage of development and give mainly qualitative predictions at this stage (e.g., Kazanas et al. 2012). This makes magnetic models difficult to test observationally. Even so, and independent of principle driving mechanism, the presence of AGN winds as revealed through blue-shifted absorption lines in the emergent continuum is almost ubiquitous. Blue-shifted lines at UV and X-ray wavelengths are particularly interesting as they correspond to winds very close to the central black hole, most likely from the accretion disc itself (e.g., Proga & Kallman 2004; King 2010). In the next section I give a brief phenomenological review of the properties of these AGN winds.

### 1.5.2 Spectral signatures of winds

The majority of the evidence for the existence of strong nuclear winds in AGN comes from the UV spectra of quasars which were the first class of object known to harbour them. UV spectroscopy of optically selected quasars at high red-shift has shown that ionised outflows are prevalent amongst the quasar population at high red-shift. The so-called Broad Absorption Line quasars (BALQSOs) were the first sources known to harbour strong winds (e.g., PHL 5200, Lynds 1967; Weymann et al. 1991). These sources, which comprise around $10 - 20\%$ of quasars (Hamann, Korista & Morris 1993; Hewett &

Foltz 2003), are characterised by strongly blue-shifted C IV, N V and Si IV absorption profiles with FWHM (full-width at half-maximum) velocity widths $> 2,000\,\mathrm{km\,s^{-1}}$. The inferred velocities for BALQSO troughs cover a wide range, from $\sim 10^3\,\mathrm{km\,s^{-1}}$ through to several $\times 10^4\,\mathrm{km\,s^{-1}}$ (Gibson et al. 2009), which seemingly indicates a substantial momentum coupling between the absorbing gas and the local radiation field (e.g., Arav, Li & Begelman 1994). Other intrinsic absorption features, narrower than the BALs but comprising the same ionic species and covering the same velocity space, are also frequently observed in the UV spectra of quasars. Depending on the FWHM velocity width of the observed troughs, quasars hosting these lines are classified as either Narrow Absorption Line quasars (NALQSOs, FWHM $< 500\,\mathrm{km\,s^{-1}}$) or mini-Broad Absorption Line quasars (mini-BALQSO, $500\,\mathrm{km\,s^{-1}} <$ FWHM $< 2,000\,\mathrm{km\,s^{-1}}$). NALs are observed in as many as $\sim 50\%$ of quasars at high red-shift (Misawa et al. 2007), while the frequency of Mini-BALs is significantly more uncertain with estimates ranging between $\sim 10 - 30\%$ (Ganguly & Brotherton 2008). Despite being observed in only a relatively small fraction of sources it is generally accepted that all high red-shift quasars host BAL winds and that the reason we view them in only a fraction of the population is due to their orientation to the line-of-sight (e.g., Junkkarinen 1983; Turnshek 1984). In this way the presence of winds in an AGN spectrum can simply be considered an extrapolation of the commonly held unified model. An alternative explanation for their relatively low frequency is that the observed fraction traces an evolutionary phase of AGN activity, such that all quasars launch massive spherical winds but only for $\sim 10 - 50\%$ of their life (e.g., Surdej & Hutsemekers 1987). In reality, a combination of these two explanations is likely (Morris 1988).

In the more local universe, low-velocity ($v_{\mathrm{out}} \sim 0 - 2,000\,\mathrm{km\,s^{-1}}$) UV NALs are routinely observed in $\sim 50 - 60\%$ of Seyfert 1 galaxies (Crenshaw et al. 1999). Moreover, there is a striking one-to-one correspondence between those sources which have low-velocity UV NALs and those which show evidence for soft X-ray absorption (Crenshaw et al. 1999; Kriss 2002, 2006) and, as such, the presence of absorption in the X-rays — the so-called 'warm absorber', an example of which is shown in Fig. 1.7 — is also strongly established. X-ray surveys independently show that at least 50% of

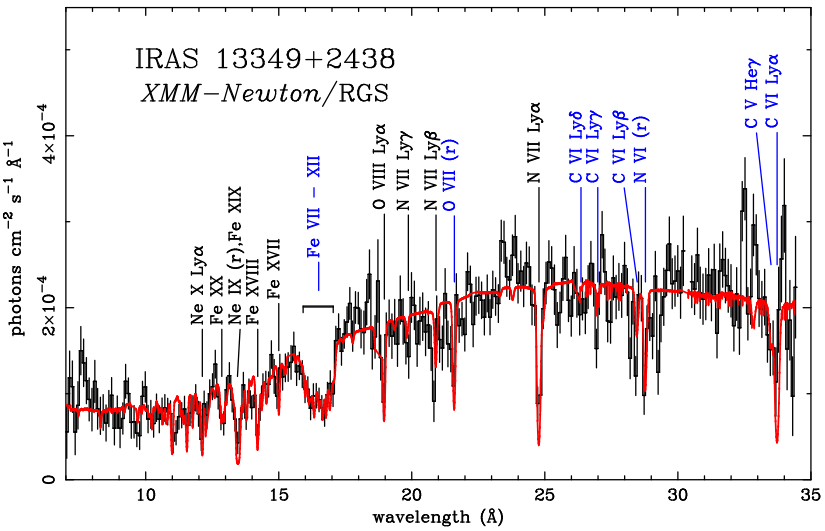


Figure 1.7: Spectrum showing a detailed view of the 'warm absorber' detected in the *XMM-Newton* RGS observation of IRAS 13349+2438 by Sako et al. (2001). The absorber is clearly complex, with a multitude of absorption lines present from ions ranging from He-like carbon through to H-like neon. As is shown by the different colour labels, two different ionisation state absorbers are required to adequately describe the data. Image taken directly from Sako et al. (2001).

local Seyfert 1 galaxies exhibit direct spectroscopic evidence for discrete absorption lines and photoelectric edges in their soft-band X-ray spectra (e.g., Reynolds 1997; Crenshaw, Kraemer & George 2003a; Blustin et al. 2005; McKernan, Yaqoob & Reynolds 2007). These absorption lines, which can be considered the X-ray analogue to UV NALs, typically have line-of-sight velocities ranging from a few hundred to around a thousand $\mathrm{km\,s^{-1}}$ (Blustin et al. 2005; McKernan, Yaqoob & Reynolds 2007), which is reminiscent of those found for the Seyfert UV NALs. In general, however, the soft-band absorber is in a higher average ionisation state than the UV gas and the two regimes are unlikely to be due to the same flow of mass (see below), although there can be limited overlap at the very lowest ionisation end of the X-ray spectrum (e.g., Kraemer et al. 2012).

The measured column density and ionisation parameter of the X-ray gas is usually

in the $\log(N_{\rm H}/{\rm cm}^{-2}) \sim 20-23$ and $\log(\xi/{\rm erg\,cm\,s}^{-1}) \sim 0-3$ range, which gives rise to K-shell absorption lines from ionised metals such as O VII-VIII, Ne IX-X, Mg XI-XII, and Si XIII-XIV, as well as the L-shell transitions of Fe XVII-XXIV. As such, the warm absorber is typically located on fairly large distances from the central black hole and may be associated with a wind originating from the putative parsec scale torus (Blustin et al. 2005), or perhaps with the later stages of an accretion disc wind which has propagated out to larger radii (Proga & Kallman 2004). Recent evidence points to the latter of these scenarios being more likely (e.g., Tombesi et al. 2013), although a contribution from more distant phenomena, e.g., the NLR, cannot be ruled out.

More recently, the higher throughput and larger effective area offered in the Fe K band ($E \sim 5-10\,{\rm keV}$) by the X-ray CCDs aboard *XMM-Newton* and *Suzaku* has been exploited to show that absorption, specifically in the form of very highly-ionised resonant absorption lines associated with the K$\alpha$ (1s$\rightarrow$2p) transitions of Fe XXV and Fe XXVI (hereafter 'Fe XXV He$\alpha$' and 'Fe XXVI Ly$\alpha$', respectively), is also manifested in the hard X-ray spectrum of a significant fraction of local AGN. These hard-band absorbers generally have much more extreme parameters than those found in either the UV or the soft X-rays, with $\log(N_{\rm H}/{\rm cm}^{-2}) \approx 23-24$ and $\log(\xi/{\rm erg\,cm\,s}^{-1}) \approx 3-6$ being fairly representative, and their outflow velocities relative to the host galaxy can reach mildly relativistic values (similar, and often in excess of, those seen in BALQSOs at higher red-shift). While evidence for such absorption lines was initially confined to detailed spectral studies of individual sources (e.g., Reeves, O'Brien & Ward 2003; Pounds et al. 2003a; Risaliti et al. 2005; Turner et al. 2008; Cappi et al. 2009; Giustini et al. 2011) the recent systematic archival *XMM-Newton* study conducted by Tombesi et al. (2010a, 2011a, 2012b) has shown that Fe XXV He$\alpha$ and / or Fe XXVI Ly$\alpha$ absorption lines are present in the X-ray spectra of $\gtrsim 40\%$ of radio-quiet AGN in the local universe ($z < 0.1$). Moreover, such outflows have also been detected in a small sample of local Broad Line Radio Galaxies (BLRGs; Tombesi et al. 2010b), and a few BALQSOs also show evidence for highly-ionised, very high-velocity X-ray BALs (e.g., Chartas et al. 2002, 2007). The prevalence of UV and X-ray winds in both the local and distant AGN population suggests that winds may represent an important addition to the commonly held AGN model.

In summary, then, the observational evidence for nuclear winds in AGN is overwhelming and they are frequently observed in both local and distant AGN populations. However, there is one pertinent question which needs to be addressed: how are the UV and X-ray absorbers related? Or, more specifically, what is the spatial and / or dynamic relationship between the two absorbers? Naïvely, the one-to-one correspondence between UV and X-ray absorption in local Seyferts, combined with their similar statistical frequency, may suggest that they share an origin in the same layer of ionised gas, and, indeed, claims along these lines were initially posed in the literature (e.g., Mathur 1994; Mathur et al. 1994; Mathur, Elvis & Wilkes 1995). However, as more detailed observations were made available it became apparent that the notion of the UV and X-ray absorption originating in the same gas, and thus being characterised by the same ionisation parameter, was demonstrably incorrect (e.g., Kriss 2004). While individual kinematic gas components in the UV can have a wide range of ionisation states they typically contribute negligible absorption in the soft X-rays (Crenshaw, Kraemer & George 2003a). The soft X-ray absorber itself is also complex, often comprising multiple kinematically distinct layers of gas with different ionisation parameters, which makes it difficult to reconcile the idea of the X-ray and UV absorbers arising in the same gas component. Variability arguments also weigh against the notion of a common origin. In a shared origin scenario one would expect spectral variability in the UV to trace that seen in the X-ray, or vice versa. However, this is contrary to what is found in observations. For example, Gallagher et al. (2004) found that despite large amplitude X-ray variability the UV spectrum BALQSO PG 2112+059 remained relatively constant. This strongly suggests that the UV material is distinct from the X-ray absorber, and even implies that the X-ray material is located closer to the central source. It is important to remember, however, that even though most UV and X-ray absorbers do not arise from the same gas, there is still a statistical connection which indicates a physical and / or geometric relationship between the two.

## 1.6 Aims of this thesis

In the previous few sections of this chapter I have outlined what is currently known about outflows / winds in AGN and described how they are believed to relate to the observed SMBH–host-galaxy scaling relations. As it stands, the most powerful AGN winds in terms of raw energetic output are those manifest in the Fe K band through Fe XXV He$\alpha$ and Fe XXVI Ly$\alpha$, largely due to their large apparent velocities. Recent work with *XMM-Newton* has helped established that such outflows may be a common feature of AGN X-ray spectra (e.g., Tombesi et al. 2010a) and that they may be energetically significant in terms of feedback (Tombesi et al. 2012a). However, despite these important recent advances there are still some pertinent questions about their nature. For instance, it is unclear how the flows are accelerated to their large velocities, or whether the wind properties are correlated with those of their host AGN. This thesis aims to both corroborate and complement the recent results which suggest that Fe K winds are relatively common in AGN, whilst simultaneously shedding light on some of the remaining unanswered questions. The subsequent chapters are organised as follows:

**Chapter 2** details the instruments, fitting techniques and statistical methods that I have used to carry out my research. Particular attention is paid to the *Suzaku* observatory, which has provided almost all of the spectra that I analyse in the remaining chapters.

**Chapter 3** describes a deep spectroscopic analysis of the complex warm absorber in radio-quiet quasar MR 2251-178; one of the brightest AGN in the local universe and the first AGN in which warm absorption was detected. This analysis is mostly based on *Suzaku* data but I also draw upon more recent *XMM-Newton* and *Chandra* observations as well to present a more rounded picture. This chapter is intended to highlight the important role that absorption can play in shaping the observed X-ray spectrum.

**Chapter 4** introduces the *Suzaku* outflow sample. This sample, which comprises 99

*Suzaku* observations of 51 Type $1 - 1.9$ AGN, forms the bulk of my doctoral research. In this chapter I outline the creation of the sample, perform a detailed statistically-driven search for highly-ionised Fe XXV He$\alpha$ and / or Fe XXVI Ly$\alpha$ absorption lines, and investigate the properties of any detected absorption systems using the XSTAR photo-ionisation code.

**Chapter 5** follows on from Chapter 4 by quantifying the parameters of the detected winds using simple geometric relations. Supplementing this, I also perform a correlation analysis amongst the absorber and wind parameters to determine whether there are any informative trends in the data, e.g., with the source Eddington ratio.

**Chapter 6** discusses the results obtained from Chapters 4 & 5 in a broader context. I investigate the likely acceleration mechanism for the winds (i.e., thermal, radiative or magnetic) by comparing the data to models available in the literature, and use recent theoretical constraints in an effort to quantify their likely energetic significance in terms of feedback.

**Chapter 7** summarises the major conclusions that I draw from my work and discusses future prospects in terms of both future observatories (i.e., *Astro-H* and *ATHENA+*) and more advanced disc-wind models.

# 2 Instrumentation, data analysis and statistical methods

## 2.1 The current generation of X-ray telescopes

### 2.1.1 *Suzaku*

*Suzaku* (Mitsuda et al. 2007) is the fifth Japanese X-ray satellite, following on from *Hakucho* (1979), *Tenma* (1983), *Ginga* (1987), and *ASCA* (Advanced Satellite for Cosmology and Astrophysics; 1993). The project is led by the Japanese Aerospace Exploration Agency (JAXA) in close collaboration with the National Aeronautics and Space Administration (NASA), and was jointly developed at JAXAs' Institute of Space and Astronautical Science (ISAS) and NASA's Goddard Space Flight Center (GSFC). *Suzaku* was launched from Uchinoura, Japan, on 2005 July 10 and now resides in a near-circular low-earth orbit with an apogee of 568 km, an inclination angle of 31.9° to the equator and an orbital period of $\sim 96$ minutes.

Schematics of the *Suzaku* observatory are shown in Fig. 2.1. The satellite weighs around 1680 kg, has an octagonal-shaped body with a diameter of 2.1 m and, with its extendible optical bench (EOB) deployed, has an operating length of $\sim 6.5$ m. Atop the EOB are five X-ray Telescopes (XRT; Serlemitsos et al. 2007) which correspond to five focal plane detectors on the base panel of the spacecraft. One of these is an X-ray micro-calorimeter (the X-ray spectrometer, XRS; Kelley et al. 2007), and the remaining four make up the X-ray Imaging Spectrometer (XIS; Koyama et al. 2007). Supplementing these is a third instrument — the Hard X-ray Detector (HXD; Takahashi et al. 2007) — which in principle allows *Suzaku* to detect X-rays with energies up to $\sim 600$ keV. Whilst the XRS was unfortunately rendered incapable of science on 2005 August 8 by a series of in-orbit coolant malfunctions[1], the HXD and most of the XIS units have operated to specification since launch.

[1]NASA press release: http://heasarc.gsfc.nasa.gov/docs/astroe/news/xrsend.html

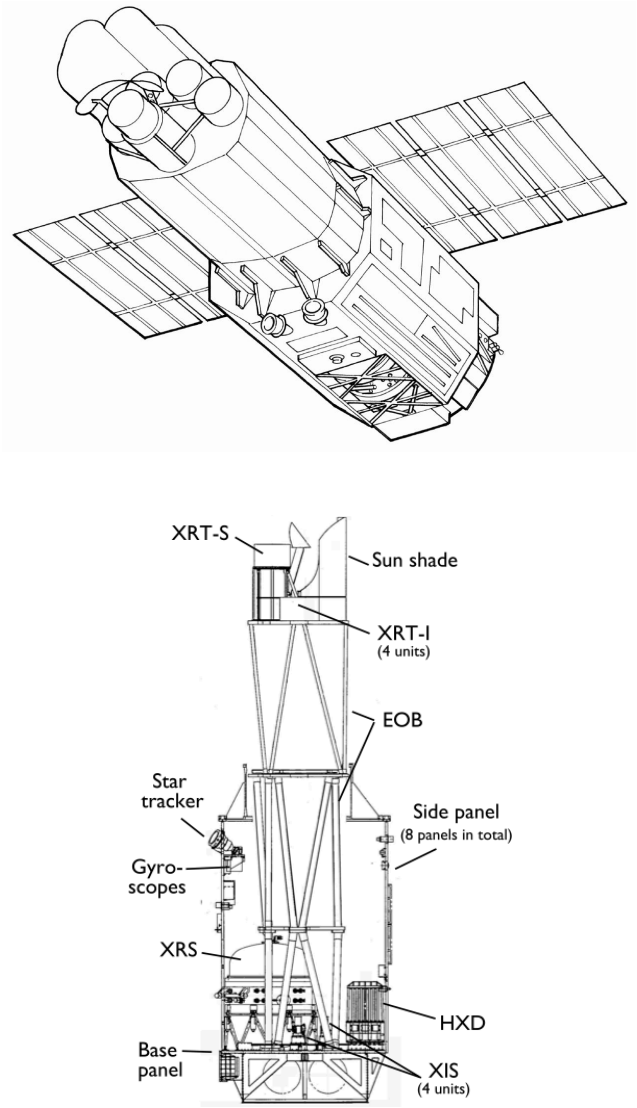


Figure 2.1: Diagrams of the *Suzaku* X-ray satellite. The top image shows the in-orbit appearance of the satellite with its solar panels and extensible optical bench (EOB) deployed. The bottom panel shows a cut-away schematic of the satellite and highlights the location of the various detectors and instruments. Both images taken from: Mitsuda et al. (2007).

### The X-ray Imaging Spectrometer (XIS)

The XIS instrument is made up of four discrete cameras, each of which has a silicon-based charge coupled device (CCD) operating in a photon-counting mode. The X-ray CCD converts an incident X-ray photon into a cloud of electrons, the magnitude of which is proportional to the energy of the absorbed X-ray photon. The four XIS cameras (named XIS $0, 1, 2, 3$) are each located in the focal plane of their corresponding XRT, which has a focal length of $\sim 4.5$ m and provides an angular resolution of $\sim 2'$. The XIS has a field of view 17.8 arcmin$^2$ and an energy resolution of $\sim 130$ eV (FWHM) at $\sim 6$ keV.

The XIS $0, 2, 3$ detectors are front-side illuminated (FI) while the XIS 1 is back-side illuminated (BI), and this affects their performance at different X-ray energies. In a FI CCD the X-ray sensitive electrodes are located on the 'top' of the CCD structure, while in a BI one the diodes are on the 'bottom' and the silicate base layers are thinned (see Fig. 2.2). The differences in structure influences the effective area and quantum detection efficiency (QDE) of FI and BI CCDs. Specifically, the difference in chip thickness means that the effective area of the BI XIS 1 exceeds the FI chips by nearly an order of magnitude at $\sim 0.4$ keV (c.f., Fig. 2.3), with the FI chips only becoming larger at $\gtrsim 4$ keV. Similar is also true for the QDE, leading to the FI chips having greater / lower sensitivity to harder/softer photons when compared to the BI chips.

A single FI chip has an effective area of 147 cm$^2$ at $\sim 8$ keV, leading to a theoretical total effective area of $\sim 440$ cm$^2$ at $\sim 8$ keV for the sum of the FI chips. However, on 2006 November 9 the XIS 2 suffered a suspected micro-meteoroid impact and was deemed incapable of producing useful scientific data[2]. Thus, the current effective area for the two remaining FI chips is $\sim 294$ cm$^2$ at $\sim 8$ keV, which is comparable to that offered by the *XMM-Newton* EPIC-pn detector. The XIS 0 was also struck by another suspected micro-meteoroid impact on 2009 June 23 but in this case the damage was insufficient to impact scientific data and *Suzaku* continues to operate with just the XIS 0 , 1 and 3 detectors[3].

[2] ftp://legacy.gsfc.nasa.gov/suzaku/doc/xis/suzakumemo-2007-08.pdf
[3] ftp://legacy.gsfc.nasa.gov/suzaku/doc/xis/suzakumemo-2010-01.pdf

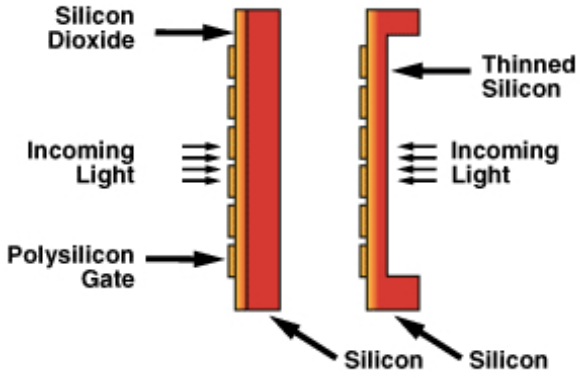


Figure 2.2: Cartoon comparing front- (left) and back-illuminated (right) CCDs. Back-side illuminated CCDs have a thinned silicon substrate which yields greater effective area and quantum efficiency at lower X-ray energies. This is discussed in greater detail in sect. 2.1.1. Image credit: http://www.photometrics.com/resources/learningzone/quantumefficiency.php

### The Hard X-ray Detector (HXD)

The HXD is a non-imaging instrument which extends the bandpass of *Suzaku* up to $\sim 600\,\mathrm{keV}$. The main part of the HXD consists of 16 individual 'well-counter units', arranged in a $4 \times 4$ formation, and these are surrounded by 20 bismuth germanate (BGO) scintillator 'anti-units' which act as both a background shield for the main detectors and a Wide-band All-sky Monitor (WAM; Yamaoka et al. 2006). Each well-counter unit houses two types of detector elements; four gadolinium silicate (GSO) crystal scintillators and four 2 mm-thick positive intrinsic negative (PIN) silicon diodes, and these are surrounded by an additional BGO scintillation unit which acts as both an active-collimator and background-detection unit. Each silicon PIN diode is placed in front of a GSO crystal. Each PIN-GSO pair is therefore able to detect X-rays continuously over the $10 - 600\,\mathrm{keV}$ energy range; the PIN diodes can detect X-rays with energies up to $\sim 70\,\mathrm{keV}$, but they gradually become transparent to photons harder than $\sim 30\,\mathrm{keV}$ which allows higher energy photons to pass through the PIN and be detected by the GSO.

In the HXD-PIN energy range the dominant contributor to background counts is the cosmic X-ray background (CXB; Boldt 1987), while for the GSO the background is likely to come from high energy particles such as cosmic rays. In both cases, the influence of background counts can be reduced by collimating the incoming photons before they strike the detector. Above each set of PIN diodes — and within the larger BGO well-type collimator — an additional set of passive phosphor bronze foil collimators are placed. These 'fine-collimators' passively define an energy dependent FOV for each PIN-GSO detector. At $E \lesssim 100\,\mathrm{keV}$ the fine-collimator is opaque to X-rays and defines a $34' \times 34'$ square FOV, but this widens to $4.5^\circ \times 4.5^\circ$ as the fine-collimator becomes transparent to X-rays at $E \gtrsim 100\,\mathrm{keV}$. X-ray counts from the CXB in PIN spectra are reduced by narrowing the PIN FOV, while the background counts for the GSO are reduced by nearly an order of magnitude by virtue of the surrounding BGO 'anti-units' and the BGO well-type collimator. In the former case, an empirically determined model of the CXB can then be subtracted from a PIN spectrum yielding an intrinsic hard X-ray spectrum of the source which is appropriate for scientific studies. For the GSO, extraneous background counts are excluded by comparing the read-out from the GSO and surrounding BSO crystals, which have different scintillation times. For a given on-axis pointing, interactions detected in the BGO crystal correspond to photons arriving off-axis from the intended source, and thus must be background, while counts detected in the GSO are caused by photons entering the front of the detector and so should be due to the observed X-ray source. Since the scintillation in the two different crystals will have different decay times, the source events can be filtered from the background events, yielding an intrinsic spectrum.

It should be noted that the line-of-sight axes with the highest effective area differ by $\sim 3.5'$ between the XIS and HXD, and as a result either pointing axis may be chosen depending upon the observation. This results in a $\sim 10\%$ increase in effective area for the nominal detector, and a marginal $\sim 2\%$ difference in the XIS/PIN cross-normalisation. *Suzaku*'s capabilities mean that it excels for observing low-luminosity soft X-ray sources, observations requiring data both above and below $\sim 10\,\mathrm{keV}$ simultaneously (e.g., for the study of X-ray reflection components; see §1.4.2), and rapid variability studies (down to

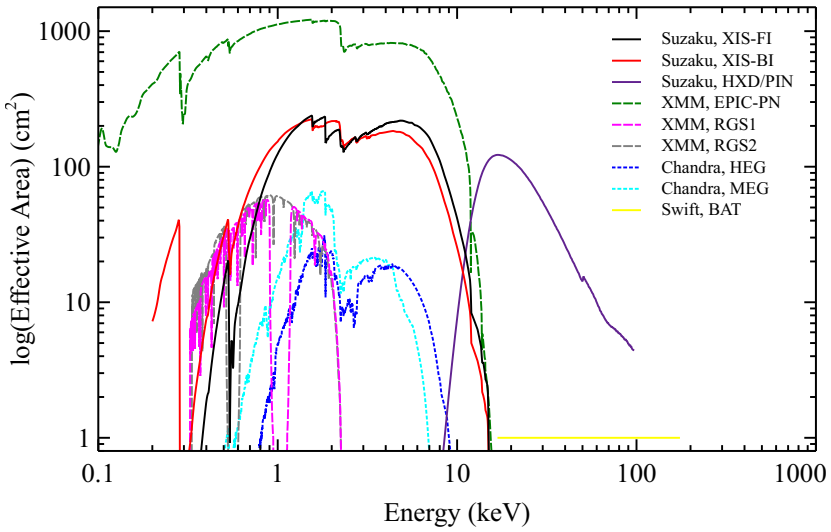


Figure 2.3: A plot showing the relative instrumental efficiency as a function of energy for the primary detectors aboard *Suzaku*, *Chandra*, *XMM-Newton* and *Swift*. The individual FI and BI XIS detectors are shown in black and red, respectively, with the HXD-PIN shown in purple. The *Chandra* HETG, which is made up of the MEG and HEG, are shown by the blue and cyan dotted lines, while pink, grey and green dashed lines correspond to the two RGS gratings and EPIC-pn aboard *XMM-Newton*, respectively. The yellow line shows the *Swift* BAT. Note that the effective area of only a single XIS-FI detector is depicted here, and so will be a factor of 2 higher for most observations (or a factor of 3 higher in observations prior to 2006 November when the XIS2 will also be available).

$\sim 10$ ms) due to decent timing resolution. However, for studies which require either high spatial- or spectral resolution, studies with the *Chandra* or *XMM-Newton* observatories would be more appropriate.

### 2.1.2 *XMM-Newton*

The *XMM-Newton* observatory (X-ray Multi-mirror Mission–Newton; Jansen et al. 2001) is a European Space Agency (ESA) led mission which was launched in 1999 December with the goal of performing X-ray spectroscopy at a high spectral resolution. The satellite

has a payload of three X-ray telescopes, each comprising 58 concentric mirror shells and having a focal length of 7.5 m. It occupies an elliptical orbit at an angle of $\sim 40^{\circ}$ to the equator, and has a long orbital period of $\sim 48$ hours which enables continuous observing for $\sim 145$ ks. There are two X-ray detectors at the foci of the three telescopes: the European Photon Imaging Camera (EPIC), for imaging and spectroscopy, and the Reflection Grating Spectrometer (RGS) for high resolution spectroscopy. The combined effective area of the mirrors is $4650\,\mathrm{cm}^2$ at 1.5 keV, and $\sim 3000\,\mathrm{cm}^2$ at 6 keV.

There are three EPIC cameras. Two of these make up the EPIC-MOS (Turner et al. 2001), which are front-illuminated CCD detectors situated at the prime focus of two of the concentric mirror shells. Each MOS camera has a $\sim 30'$ FOV, and is sensitive to X-rays over the $0.15 - 15$ keV energy range offering a FWHM energy resolution of $\sim 140$ eV at 6 keV. The third EPIC camera is the EPIC-pn (Strüder et al. 2001), which is a back-side illuminated CCD camera located at the primary focus of the third X-ray telescope. It has similar capabilities to the EPIC-MOS, i.e., has a $30'$ FOV, sensitivity throughout the $0.15 - 15$ keV energy range, and offers similar energy resolution. However, the EPIC-MOS differs from the EPIC-pn in that only $\sim 44\%$ of the incident X-ray photons focused by the mirrors actually reach the EPIC-MOS CCDs. This is because there are two Reflection Grating Arrays (RGAs) situated behind the X-ray telescopes in the EPIC-MOS focal plane which disperse $\sim 40\%$ of the incident X-rays from each telescope towards dedicated CCD arrays which are each located at the secondary focus of each mirror. As a result, the combined effective area of the two EPIC-MOS cameras is still below the single EPIC-pn CCD, which offers a maximum effective area of $\sim 1300\,\mathrm{cm}^2$ at $E \sim 1.5$ keV and $\sim 700 - 800\,\mathrm{cm}^2$ at the energies of the Fe K$\alpha$ line (i.e., $E \simeq 6 - 7$ keV; see Fig. 2.3).

The RGAs and associated dedicated CCD units comprise the Reflection Grating Spectrometer (RGS; den Herder et al. 2001), which provides the high-resolution spectroscopic capability of *XMM-Newton*. It is a dispersive instrument which uses a grooved mirror to split incoming X-ray photons into beams according to their wavelength; there are around $645\,\mathrm{grooves\,mm}^{-1}$ on the RGS mirrors, and interactions between the X-rays reflected from the apex and valley of these grooves create an interference pattern

whereby X-rays of different wavelength (or energy) are reflected under slightly different angles. The reflected X-rays are then detected on the dedicated RGS CCDs, with their energy (wavelength) determined by their relative position on the CCD read-out. The RGS detectors are sensitive to soft X-rays between $\sim 0.33$ and $\sim 2.5\,\mathrm{keV}$, have a peak effective area of $\sim 150\,\mathrm{cm}^2$ at $\sim 0.8\,\mathrm{keV}$, a high resolving power (i.e., $E/\Delta E = 150 - 800$) and, in the context of AGN, excel at studies of the soft X-ray warm absorber.

Supplementing these instruments, *XMM-Newton* also houses a co-aligned UV-optical imaging telescope (Mason et al. 2001) but as this is a non-X-ray instrument I do not discuss it further here.

### 2.1.3 *Chandra*

The *Chandra* X-ray observatory (Weisskopf et al. 2000) was launched in 1999 July and is one of NASA's great observatories. It has an X-ray telescope capable of spatial resolution of $\leq 0.5''$ and includes instruments for both high-resolution X-ray spectroscopy and imaging. Like *XMM-Newton*, *Chandra* occupies a highly elliptical orbit in order to minimise the amount of time it spends in the Earth's Van Allen radiation belts; the orbit has an apogee of $\sim 140,000\,\mathrm{km}$, a perigee of $\sim 10,000\,\mathrm{km}$, and the satellite has an orbital period of $\sim 48\,\mathrm{hours}$ which allows up to $\sim 173\,\mathrm{ks}$ of continuous uninterrupted observing time. *Chandra*'s scientific capability is provided by two separate units: the High Resolution Mirror Array (HRMA) and the Integrated Science Instrument Module (ISIM), which itself contains two X-ray detectors. The HRMA has a focal length of $10\,\mathrm{m}$ and a point spread function (PSF) capable of focusing around $\sim 80 - 95\%$ of an incident photon's energy into a circle of $1''$. This, in combination with its spatial resolution of $\leq 0.5''$, makes *Chandra* the only X-ray observatory currently capable of performing spatially-resolved spectroscopy in the X-ray regime.

As mentioned, the ISIM aboard *Chandra* consists of two instruments. These are the Advanced CCD Imaging Spectrometer (ACIS; Garmire et al. 2003) and the High Resolution Camera (HRC; Murray et al. 2000). These are both focal-plane detectors, but only one can be used at any given time. The ACIS consists of two separate arrays of

CCD detectors, both of which have an operating bandpass of $0.2 - 10\,\mathrm{keV}$: there is a $2 \times 2$ array for imaging (known as the ACIS-I), and a linear array of 6 chips (known as the ACIS-S) which can be used for either imaging or for the projection of spectra from the *Chandra* gratings, if they are deployed. The HRC, on the other hand, comprises two micro-channel plate components and is sensitive over the $0.1 - 10\,\mathrm{keV}$ range.

While both of these cameras can be operated independently, high resolution spectroscopy can also be obtained if one of two transmission gratings are swung into the optical path between the HRMA and the ACIS-S. These are the High Energy Transmission Grating (HETG; Canizares et al. 2005) and the Low Energy Transmission Grating (LETG; Brinkman et al. 2000). The HETG consists of both the Medium Energy Grating (MEG, sensitive between $0.4 - 5\,\mathrm{keV}$) and the High Energy Grating (HEG; $3 - 10\,\mathrm{keV}$), yielding a total bandpass of $0.4 - 10\,\mathrm{keV}$. Note that the *Chandra* gratings are *transmission* gratings which means that they function differently to the *reflection* gratings aboard *XMM-Newton*; with a reflection grating the diffracted and incident photon beams detected are on the same side of the grating, while in transmission gratings they are on different sides. The MEG and HEG have a FWHM resolution[4] of $\Delta\lambda \sim 0.023$Å and $\Delta\lambda \sim 0.012$Å, respectively, providing a resolving power of $E/\Delta E \simeq 100 - 1300$ (i.e., the HEG provides $\lambda/\Delta\lambda \sim 1000$ at $\sim 1\,\mathrm{keV}$).

### 2.1.4 *Swift*

*Swift* is a NASA led Gamma-Ray Burst mission which was launched in November 2004. It is a multi-wavelength observatory, with detectors operating in the $\gamma$-ray, X-ray, UV and optical wavebands, and is primarily geared to the study of $\gamma$-ray bursts and their afterglows. It operates in a low-earth orbital altitude of $\sim 600\,\mathrm{km}$ and performs a complete orbit of the earth once every $\sim 90$ minutes. In the X-rays, *Swift* is equipped with two detectors: the X-ray Telescope (XRT; Burrows et al. 2000), which provides sensitivity between $0.2 - 10\,\mathrm{keV}$, and the Burst Alert Telescope (BAT; Barthelmy et al.

[4]http://asc.harvard.edu/proposer/POG/html/HETG.html

2005), which is sensitive at much harder X-ray energies of $\sim 14 - 195\,\mathrm{keV}$. The BAT is a wide-angle detector with a two-steradian FOV which continuously monitors the sky for $\gamma$-ray bursts. The extensive FOV means that the *Swift* BAT provides the most sensitive X-ray survey of the sky to date, with a sensitivity down to $1.48 \times 10^{-11}\,\mathrm{erg\,cm^{-2}\,s^{-1}}$ in the $14 - 195\,\mathrm{keV}$ energy range over 90% of the sky (Baumgartner et al. 2010). During the first 58 months of the mission over 1092 hard X-ray bright sources have been detected, with lightcurves and hard X-ray spectra for each being made available on-line via the *Swift* BAT 58-Month Hard X-ray Survey catalog[5]. Spectra from the *Swift* BAT are often used together with those from other X-ray observatories to enable the broad-band spectral study of sources throughout the X-ray regime. In Chapter 3 I use both the *Suzaku* and *Swift* BAT spectra of radio-quiet quasar MR 2251-178 to perform a detailed broad-band analysis over the $\sim 0.6 - 180\,\mathrm{keV}$ range.

## 2.2 Outline of X-ray spectral analysis

### 2.2.1 Initial data processing

Modern X-ray observatories function by measuring the properties of individual photons as they strike a detector. This differs from observatories which operate at lower-energies (longer-wavelengths) which measure integrated photon fluxes, and is predominantly due to the fact that most X-rays are comparatively high energy and low in flux which allows them to be counted individually with relative ease. Each X-ray detection event is characterised by a 'pulse height amplitude' (PHA), which is the charge per pixel integrated over a given read-out time, a detection time, a grade and typically a 2 position co-ordinate which corresponds to a location on the CCD. A list of all PHA events along with their specific attributes is stored in an *event file* which, after processing, is made available to observers once the observation has been concluded. This file is stored in a multi-layered FITS (Flexible Image Transport System) format according to

[5]Available at: http://heasarc.gsfc.nasa.gov/docs/swift/results/bs58mon/

the Office of Guest Investigator Program (OGIP) standards outlined by the NASA's High Energy Astrophysics Science Archive Research Center (HEASARC) FITS Working Group. However, the raw data are unsuitable for analysis and detection events must be screened according to various criteria before any meaningful results can be obtained. In the case of *Suzaku*, the main considerations are:

- **Event Grade**

  In a CCD-based detector an 'event' is recorded whenever the magnitude a charge induced in a pixel exceeds a particular threshold. When this occurs, the charge states of the surrounding $3 \times 3$ and / or $5 \times 5$ pixel regions are also recorded and, according to the specific morphology of the charge distribution, is assigned a 'grade' (or 'pattern'). The assigned grade is determined by which of the surrounding pixels have an induced change above a given value and this varies according to the type of event. The different observatories define the 'grades' using different criteria, although they are essentially all referring to the same thing. For example, the ACIS CCD aboard *Chandra* has 256 different event grades depending upon the specific pixels which exceed the charge threshold[6]. In this convention, a grade 0 event is a single-pixel event, whilst a grade 255 event occurs when the charges in all 9 pixels of a $3 \times 3$ grid exceed the threshold. The former of these is a 'perfect' event, while the latter almost certainly indicates a particle impact as opposed to an X-ray photon detection. *Suzaku* uses a slightly different event grading system and awards event grades based on the shape of the charge distribution[7], although a grade 0 event still corresponds to a single-pixel event.

- **Pile-up**

  When counting individual photons pile-up can occur when two (or more) photons hit the same or adjacent CCD pixels within a single CCD read-out time. To

[6] http://space.mit.edu/ACIS/cal_report/node168.html
[7] http://www2.astro.psu.edu/xray/docs/TARA/TARA_users_guide/node12.html

zeroth order, the two photons cannot be distinguished and, as a result, they will be recorded as a single event with an energy equal to the sum of the incident photons and have a more complex pixel pattern (hence event grade). Pile-up can become an issue when observing bright (high-flux) sources and the resultant spectrum can appear skewed towards higher energies as the softer photons are either rejected or have their energies combined. If pile-up is anticipated in advance, its effects can be minimised by, for example, requesting a smaller CCD window or adopting a faster CCD read-out time. However, in the cases where it is unexpected it can be accounted for by modelling its effects during spectral analysis (e.g., Davis 2001), or by altering the acceptable event grades.

- **'Hot' and flickering pixels**

  In addition to the expected background of cosmic X-rays, CCD detectors in particular may suffer from electronic hotspots or flickering pixels which produce apparent signal events when there is no incident photon. For example, the electrons in the chip can be induced into an excited state by the latent heat produced by the system (i.e., thermal noise), or the CCD pixels may have different sensitivities to incoming light. Events from these regions are sometimes excluded on-board the spacecraft, or they can be accounted for during the data reduction process, e.g., by subtracting flat-field or dark-frame images from the source spectrum. In general, the effects of both hot and flickering pixels can be minimised by using CCDs where the pixel size is smaller than the detectors point response function, which enables hot and / or flickering pixels to be identified by comparing their brightness to that of the surrounding pixels. Alternatively, and as is the case with *Chandra*, the instruments can be cooled such that the ambient temperature of the spacecraft is below the excitation threshold of electrons in the CCD.

- **Cut-off rigidity**

  The cut-off rigidity (COR) is a measure of how the Earth's magnetosphere shields the space-craft from high energy particles. Charged cosmic particles which enter

the magnetosphere tend to be deflected away via the Lorentz force, i.e., the force $F$ on a moving charge with a velocity $v$ in a magnetic field of strength $B$ is given by $F = qvB$, with a direction orthogonal to both $v$ and $B$. However, the tendency for a particle to be deflected can be offset by the particle's momentum and, more specifically, its magnetic rigidity:

$$P = \frac{pc}{Ze}, \tag{2.1}$$

where $p$ is the particle;s relativistic momentum (in units of eV/c), $c$ is the speed of light, $e$ is the electron charge and $Z$ is the atomic number. Particles with a given rigidity will follow identical trajectories, whereas particles with the same momentum or energy, but different charges, will not. For each point in the magnetosphere there is a corresponding minimum rigidity, called the cut-off or threshold rigidity, and particles with a rigidity lower than the cut-off will be deflected before they reach that point. As such, an observational COR can be applied during data reduction such that events recorded when the satellite might be susceptible to cosmic particles are excluded.

- **South-Atlantic anomaly**

  The Van Allen radiation belts are regions of energetic charged particles which encompass the Earth, held in place by its magnetic field. These belts, which typically extend from an altitude of around 1,000 up to 60,000 km , protect the Earth's surface from stellar and cosmic radiation by 'trapping' charged particles. However, in one such region — known as the South Atlantic Anomaly (SAA) — the inner-most boundary for the Van Allen belt reaches 200 km, which results in an intense flux of energetic protons and electrons which are capable of damaging low-earth orbit satellites and space stations. As a result space-based detectors are often deactivated during their passage through the SAA to prevent damage. Even if the detector is deactivated the bombardment of particles may generate short-lived radiative particles which may also be detected as they decay. Therefore, it can also be important to exclude events recorded within a given time-frame since the spacecraft last passed through the SAA.

- **Satellite pointing angle**

  There are various considerations to be made when evaluating data acquired when the spacecraft was facing particular directions. For example, the angle between the satellite's pointing angle and the Earth's limb should be considered because particles in the Earth's outer atmosphere are capable of absorbing softer X-rays. Similarly, the angle between the pointing direction and the Earth's day–night terminator should also be considered because the scattering of cosmic rays in the Earth's atmosphere could also give rise to spurious X-ray detections. Furthermore, the angle between the pointing direction and the Sun is also important as Solar X-rays could scatter into the detector, causing further spurious detections. Each of these factors should be considered individually during the data reduction process to ensure a clean source spectrum.

Screening according to the above criteria allows an observer to exclude non-useful, hot, or otherwise spurious events. A large amount of data is retained for each individual 'good' event which allows for sophisticated multi-dimensional analysis. For example, if the instrument offers temporal resolution (low read-out time) the events can be selected from different time intervals or with different intensities, which allows time- and / or flux-resolved spectroscopy. Once the requirements of the observation have been decided, secondary spectral files which contain only 'useful' events can be selected from the raw event files using a program such as XSELECT (c.f., §2.3).

However, in their raw form the PHA events correspond to the sum of total charge (i.e., both source and background) per pixel per detector read-out time, and these need to be converted to counts per unit energy before spectroscopic analysis can be performed. There are a few steps to this process. For non-dispersive spectrometers such as the XIS aboard *Suzaku*, the PHA events are corrected for spatial and temporal variations in the detector as a spacecraft orbits the earth. This is generally carried out automatically during data-reduction using calibration files made available by the instrument calibration teams for each satellite; the corrected values are stored as PI (PHA invariant) events, which contains the total pulse height per discrete detector channel. The channel corresponds

to the voltage induced by the electron charge cloud. For the *Suzaku* XIS each discrete detector channel corresponds to a voltage of $\sim 3.6\,\mathrm{eV}$, such that the $1000^{\mathrm{th}}$ channel corresponds to events with a voltage of $\sim 3.6\,\mathrm{keV}$.

The corrected PI events are then convolved with the detector response functions which convert the channel voltage to input photon energies. The observed counts in detector channel PI, $C(i)$, is related to the incident spectrum $S(E)$ in energy space, as

$$C(i) = T \int R_{\mathrm{RMF}}(i, E) R_{\mathrm{ARF}}(E) S(E) dE, \tag{2.2}$$

where $R_{\mathrm{RMF}}(i, E)$ and $R_{\mathrm{ARF}}(E)$ are the unit-less detector responds matrix file (RMF) and the ancillary response file (ARF), respectively, and $T$ is the observation time in seconds. For a theoretically perfect detector the RMF would be a diagonal matrix, as each energy would be mapped to a single detector channel. However, real detectors always have a finite spread in their response function with some X-rays of energy $E$ ending up in channel $i$ while others appear in, for example, channel $i \pm 1$. The RMF maps from detector channel space into photon energy space by accounting for the finite probability that a photon of a given energy will be detected in a given spectral channel. The ARF combines the effective area of the detector with its quantum efficiency to create a time-averaged energy-dependent quantum efficiency curve, in units of [$\mathrm{cm}^2$ counts/photon]. Therefore, the observed counts per detector channel arises from the convolution of the physical input spectrum (source + background) with the overall response of the detector (ARF+RMF).

### 2.2.2 The 'forward-fitting' technique

The goal of X-ray spectoscopy is to gain physical insight into the properties of the intrinsic source spectrum by 'solving' eq. (2.2) for $S(E)$. The easiest way to accomplish this is to employ a so-called 'forward-fitting' technique, where one seeks to identify the model source spectrum which is most likely to have generated the observed distribution of counts.

To first order, the forward-fitting process is carried out as follows: (1) a physically motivated model is constructed according to which components are expected to be

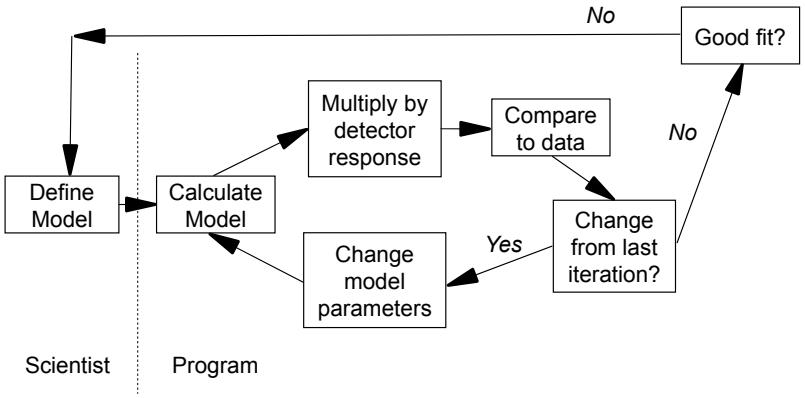


Figure 2.4: Flowchart outlining the steps involved with forward-fitting. Image taken from: Arnaud, Smith & Siemiginowska (2011).

present in the source; (2) the hypothesised spectrum is folded through the full detector response (i.e., RMF×ARF) and fitted to the observed counts spectrum; (3) The fit is assessed according to a chosen *merit function* (hereafter, 'fit statistic'), which measures the agreement between the data and a particular set of model parameters. A low fit statistic typically represents a close agreement between data and model; (4) if the agreement is poor, the model parameters are iteratively adjusted to find the minimum statistic, yielding 'best-fit parameters' for that particular model; (5) as real data are always subject to measurement error (noise) they will never exactly follow a given model, even if it is the correct one. Therefore a *goodness-of-fit* test is also performed, which assesses whether or not the minimised model parameters are an appropriate description of the data using a set statistical standard; (6) if the best-fit parameters are found to be unacceptable by the goodness-of-fit test the model can either be rejected or modified in an effort to better describe the observed data, and the process is carried out again until an acceptable fit has been achieved[8]. A flowchart depicting this process is shown in

[8]Note that even if the goodness-of-fit statistic is formally acceptable, the model parameters should still be considered on a physical basis to determine whether the model is physically appropriate given what we know about the AGN environment.

Fig. 2.4.

### 2.2.3 Merit functions and fit statistics

In X-ray astronomy the two most widely used merit functions are the $C$ and $S^2$ (colloquially called $\chi^2$, or chi-squared) statistics, and in both cases minimising these statistics is simultaneously maximising their *likelihood* function. Or, in other words, finding the best-fit model parameters by minimising the statistic is the same as finding the maximum probability that a particular set of model parameters gives rise to the observed data. Whether one uses the $C$ or $\chi^2$ statistics when fitting the data is determined by the number of counts per channel.

#### Poisson distribution and the Cash statistic

X-ray detectors natively operate in photon-counting mode. This means that detected events are characterised by small-number statistics in a given read-out time and thus follow the Poisson distribution. In this regime, the probability of observing $D_i$ events in bin $i$ of dataset $D$, assuming events occur independently at a predicted rate $M_i$, is given by

$$\mathrm{Prob}(D_i) = \mathcal{P}(D_i|M_i) = \frac{M_i^{D_i}}{D_i!}e^{-M_i}. \tag{2.3}$$

The most frequently used maximum likelihood function in the Poisson data limit is the $C$-statistic (Cash 1979), which follows

$$C = 2\sum_{i=1}^{N}(M_i - D_i \ln M_i), \tag{2.4}$$

and is appropriate when fitting data which has few counts per bin (low $D_i$), or when dealing with high resolution (grating) data which has many resolution elements. The factor of 2 arises to ensure that inferences made from the $C$-statistic agree with the widely used $\chi^2$ statistic at high $D_i$. Generally, the linear nature of the $C$-statistic means that it can be used regardless of the number of counts per bin in an X-ray spectrum,

however it does not have an easily computed goodness-of-fit test associated with it (see below).

### Gaussian distribution and the Chi-squared statistic

For large $D_i$ the Poisson probability distribution converges to the Gaussian (or normal) distribution which allows the $\chi^2$ statistic to be used effectively. Generally, the $C$ and $\chi^2$ statistics yield equivalent results when there are $D_i \gtrsim 20 - 25$ counts in each spectral channel. In the Gaussian limit the probability of observing $D_i$ events in bin $i$ of dataset $D$, given a predicted count rate $M_i$ is

$$\mathrm{Prob}(D_i) = P(D_i|M_i, \sigma_i) = \frac{1}{\sigma_i\sqrt{2\pi}} \exp\left[-\frac{(D_i - M_i)^2}{2\sigma_i^2}\right], \tag{2.5}$$

which follows a $\chi^2$ merit function described by

$$\chi^2 \equiv S^2 = \sum_{n=i}^{N} \frac{(D_i - M_i)^2}{\sigma_i^2}. \tag{2.6}$$

In both of these equations $\sigma_i$ is the standard deviation (error) in counts for channel $i$ (hence $\sigma_i^2$ is the variance) and is usually estimated as $\sqrt{D_i}$ by X-ray data reduction packages.

The presence of $\sigma_i$ in the denominator of eqs. (2.5) and (2.6) makes it immediately clear why the $\chi^2$ statistic is not suitable for data in the Poisson regime. Low count rate (or high resolution) data can contain spectral channels with have either very few or even zero counts. This causes downward fluctuations from a model ($D_i < M_i$) to be weighted more heavily than upward fluctuations ($D_i > M_i$) because, even though the numerator of chi-squared for the given bin will be the same, the denominator will be smaller for the downward fluctuation. As a result, the model becomes biased towards bins with lower counts which drives it below the model and yields an anomalously low fit statistic. Where possible, then, Poisson data are often 'binned-up' to uniformly contain in excess of $\sim 20 - 25$ counts in each bin. This both allows the $\chi^2$ statistic to be used, and also ensures that there is an easily interpretable goodness-of-fit statistic available which can be used to determine how well a given model fits the data.

### 2.2.4 Confidence bounds and local minima

Minimising the fit-statistic finds the parameters which best describe the observed counts spectrum for a given model. However, it is also important to determine how well each of those best-fit parameters is constrained. This is typically accomplished by appealing to confidence bounds, that is, by stating the probability that the true value of a parameter lies between values $x$ and $y$. As an example, one could claim that there is a 90% probability that the outflow velocity of an absorption line is between $1,000$ and $2,000\,\mathrm{km\,s^{-1}}$, which is another way of saying that given $N$ observations the best-fitting outflow velocity would lie between $1,000$ and $2,000\,\mathrm{km\,s^{-1}}$ 90% of the time. The confidence limits are generally found locally to the best-fitting parameter once the fit has been minimised, and are determined by varying the model parameter of interest until the fit statistic has changed by a critical amount. This approach is known as calculating the $\Delta$-statistic (e.g., the $\Delta\chi^2$). Formally, Avni (1976) showed that the confidence intervals for the $\chi^2$ statistic can be determined by solving

$$\chi^2(\beta) = \chi^2_{\mathrm{min}} \pm \Delta(\nu, \beta), \tag{2.7}$$

where $\beta$ is the required significance level, $\chi^2_{\mathrm{min}}$ is the minimised statistic value (i.e., the 'best-fit') and $\nu$ is the number of degrees of freedom in the fit (i.e., the number of channels minus the number of parameters). For a given $\nu$ there is a value of the $\Delta$-statistic which corresponds to a deviation with a set significance level. In X-ray astronomy it is customary to report parameter errors at the 90% confidence level (i.e., $\beta = 0.9$); for a single parameter this corresponds to $\Delta\chi^2 = 2.71$, for two parameters it is $\Delta\chi^2 = 4.61$, and so on[9]. Cash (1979) later showed that this approximation asymptotically holds for the $C$-statistic, making confidence bounds determined with this method prevalent throughout X-ray astronomy.

Even so, there is one important caveat which must be watched out for when forward-fitting data: the possibility of 'local minima' in the fit statistic. To maximise

[9]The $\Delta\chi^2$ values corresponding to different values of $\nu$ are widely available in textbooks (e.g., Spiegel, Lipschutz & Liu 2008).

the likelihood function for a specified model and a given dataset most fitting methods calculate the second derivative of the fit statistic at a given iterative step and move 'downhill' in statistic space, i.e., the parameters are adjusted such that the next iterative step has a smaller fit statistic. However, with this method it is possible for the fit to become 'stuck' in a local minimum (i.e., find a set of parameters where the second derivative of the fit statistic is only $> 0$ locally) instead of finding the global minimum which corresponds to the actual best-fit model. This problem can become particularly troublesome for complex multi-parameter models, or those which have correlated or degenerate model parameters. It is therefore important to both undertake the fitting process from different starting parameters, and to thoroughly evaluate the underlying statistics when deciding upon a best-fit model.

### 2.2.5 Hypothesis testing and the goodness-of-fit

Determining how well a given spectral model describes the observed counts spectrum is a crucial aspect of forward-fitting. For X-ray astronomy there are typically two hypotheses which one attempts to evaluate the probability of: firstly, there is the null-hypothesis ($H_0$) which asserts that the observed data are drawn from the underlying model (a positive claim), while the second is the alternative-hypothesis ($H_1$) which states that the data are *not* drawn from the model, or that they are described by some other model (a negative claim). There are two types of error which can arise from a hypothesis test: either the null-hypothesis is rejected when it is really true (a false positive or type-I error), or the null model is accepted when it is really false (a false negative or type-II error). Since it is not possible to minimise both types of error simultaneously, the approach typically taken is to report the probability of a type-I error occurring for a given model. For a given $\nu$ (degrees of freedom) a critical fit statistic can be found which corresponds to the probability of a type-I error occurring at a given $p$-value. In general, the $p$-value of a given fit, i.e., the probability of the observed data being drawn from a model given a measured fit statistic and the number of degrees of freedom assuming that the model is true, are calculated on-the-fly by spectral fitting packages (see §2.3) via a 'goodness-of-fit'

test. Generally, $H_1$ is initially assumed as true and the goal of spectral fitting is to prescribe a model which yields a $p$-value sufficiently large that $H_0$ can no longer be confidently rejected.

One of the reasons the $\chi^2$ fit statistic is used so widely throughout X-ray astronomy is that it also doubles as a 'goodness-of-fit' test. For a given fit it is straightforward to find the $\chi^2$ statistic and hence calculate the appropriate $p$-value from the underlying $\chi^2$ distribution. Another popular method — which is also even easier to interpret — is to calculate the so-called 'reduced-$\chi^2$', defined as the ratio of chi-squared test statistic to the number of degrees of freedom, i.e., $\chi^2_{\rm red} = \chi^2/\nu$. As a general rule, the $\chi^2$ value should be approximately equal to $\nu$ such that $\chi^2_{\rm red} \approx 1$ (corresponding to $p_{\rm null} = 0.5$). This is because the $\chi^2$ statistic is determined through the degree by which the data and model disagree given the measurement errors (see eq. 2.6); 'good' points will have a small ($< 1$) ratio of deviation from the measurement error, while 'bad' points have a ratio of deviation $> 1$ which means the model fails to go through the error bar. On average, a good fit will have as many large deviations as it does small ones, that is, on average the ratio of deviation to error will be $\sim 1$, and therefore $\chi^2 \approx \nu$; if the $\chi^2_{\rm red}$ value is much greater or much less than unity then the model is a poor fit because it is either missing too many points, is 'over-fitting' the data, or the errors have been over-estimated. Note that there is no analogous goodness-of-fit test that can be applied to Poisson data, although Monte Carlo methods can be used to infer a goodness of fit.

As a general rule of thumb a $\chi^2_{\rm red} \lesssim 1.1$ value (corresponding to $p_{\rm null} \gtrsim 0.001$) can largely be regarded as an acceptable fit to the data, although this can vary widely depending upon several factors, e.g., the complexity of the model, the $S/N$ in the spectrum, and the number of degrees of freedom (resolution elements) in the data. By comparison, a model which provides a poor description of the data (e.g., where $\chi^2_{\rm red} \gtrsim 1.3 - 1.5$) can yield $p_{\rm null} \lesssim 10^{-10}$. Therefore, aiming for a fit which describes the data within the regime of $\chi^2_{\rm red} \lesssim 1.1$ ensures that the underlying model is statistically plausible.

### 2.2.6 The F-test and Monte Carlo simulations

Often, one wishes to compare different models to see if the addition of a model component is statistically significant. An example which is encountered routinely in this thesis is determining the detection significance of an absorption or emission line in an X-ray spectrum. In principle, one way that this could be done is to simply use a likelihood ratio test, such as the F-test, to compare the fit statistic of two models; one with an absorption line ($H_1$), and one without ($H_0$). However, Protassov et al. (2002) showed that the F-test should not be used to determine the detection significance of atomic lines in complex spectral models as it neither takes into account the number of energy resolution bins over a given energy range nor the expected energy of a given atomic line. In cases where there is no *a priori* justification for expecting a spectral line at a particular energy and the line search is done over what is essentially an arbitrary energy range — as is often the case when dealing with strongly blue-shifted absorption lines — the F-test can over-predict the detection probability and, therefore, the derived significance for a line may not represent the 'true' statistical significance of a suspected absorption or emission line (see Protassov et al. 2002 for a detailed discussion regarding the caveats of using the F-test when dealing with atomic lines). A more appropriate and statistically robust approach in these cases is to sample the probability distribution under the null-hypothesis model by performing detailed Monte Carlo (MC) simulations.

MC simulations have been used a number of times in the literature to overcome the limitations of the F-test (e.g., Porquet et al. 2004c; Markowitz, Reeves & Braito 2006; Miniutti & Fabian 2006; Tombesi et al. 2010a,b) and they enable the statistical significance of a spectral line to be robustly determined independently of spectral noise and detector effects. The method of Monte Carlo that I use in this work follows the same process which was first outlined by Porquet et al. (2004c), and is carried out through the following steps:

(i) I simulate both XIS-FI and XIS-BI spectra from the null hypothesis model (i.e., the broadband continuum model with all narrow absorption lines in the Fe K band removed) using the *fakeit* command in XSPEC and subtract the appropriate

background files. These spectra are simulated such that they have the same exposure as the original data and use the same spectral response files;

(ii) I then fit the simulated XIS-FI(XIS-BI) spectra between $0.6 - 10.0(0.6 - 5.0)\,\mathrm{keV}$) with the null hypothesis model to produce a new and refined null hypothesis which takes into account the uncertainty in the null hypothesis model itself. During this process all of the continuum parameters bar the photon-index of the primary power-law and its normalization, and the normalization of any black-body component, are frozen to their best-fit parameters taken from the real data to prevent degeneracies between model components during re-fitting. The width of any broad Fe K emission profiles are fixed to their best-fit width but both the centroid energy and its normalization are allowed to vary;

(iii) from the refined null hypothesis model I then simulate a second set of simulated XIS-FI and XIS-BI spectra and again subtract the appropriate background files. These second simulated spectra are then fitted with the null hypothesis model and the resultant $\chi^2_{\mathrm{null}}$ value is recorded;

(iv) an unresolved ($\sigma = 10\,\mathrm{eV}$) Gaussian is then added to the model at $5\,\mathrm{keV}$ in the source rest-frame with its intensity initially set to zero but left free to vary between both positive and negative values to probe for both emission and absorption lines. This Gaussian line is then sequentially stepped between $5 - 9.5\,\mathrm{keV}$ (rest-frame) in $25\,\mathrm{eV}$ increments. After each step the $|\Delta\chi^2_{\mathrm{noise}}|$ was recorded relative to $\chi^2_{\mathrm{null}}$;

(v) this process is carried out for $T = 1000$ simulated spectra per observation yielding a distribution of $|\Delta\chi^2_{\mathrm{noise}}|$ under the null hypothesis which essentially maps the statistical significance of any deviations from the null hypothesis model which are solely due to random photon noise in the spectrum;

(vi) the measured significance of the line in the real spectrum $|\Delta\chi^2_{\mathrm{line}}|$ can then compared to the values in the $|\Delta\chi^2_{\mathrm{noise}}|$ distribution to assess how many simulated spectra have a random fluctuation with a detection significance over this threshold value.

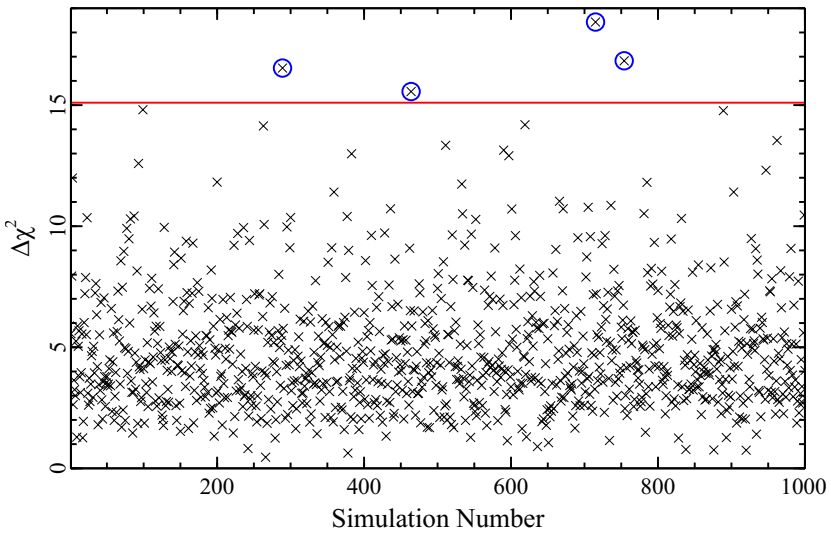


Figure 2.5: Plot showing an example probability distribution for spurious lines in Mrk 279, as estimated from Monte Carlo simulations. Each plotted point corresponds to the maximum statistical deviation measured for spurious lines in $T = 1000$ spectra simulated from a null hypothesis model which contains no atomic lines. The horizontal red line at $\Delta\chi^2 = 15.1$ corresponds to the statistical significance of a Fe XXVI Ly$\alpha$ absorption line detected in the real spectrum of Mrk 279. Only four simulated spectra generate lines with significances above this threshold (indicated by the blue circles), which means that the Fe XXVI Ly$\alpha$ line detected in the real spectrum is significant at the $P_{\rm MC} = 99.6\%$ confidence level.

If $N$ simulated spectra have $|\Delta\chi^2_{\rm noise}| \geq |\Delta\chi^2_{\rm line}|$ then the estimated confidence interval from Monte Carlo simulations is $P^{\rm Line}_{\rm MC} = 1 - \left(\frac{N_{\rm Line}}{T}\right)$. Moreover, if there are two absorption profiles consistent with a Fe XXV–XXVI pair the null probability of both lines simultaneously being a false detection can be inferred by multiplying the probabilities of each individual line.

MC simulations in this vein are used extensively throughout this thesis, particularly in Chapter 4 where I use Fe K absorption lines to assess for the presence of accretion-disc winds in a sample of *Suzaku* observed AGN. As an example, the MC-inferred distribution

of $|\Delta\chi^2_{\rm noise}|$ for the radio-quiet AGN Mrk 279 is shown in Fig. 2.5. Mrk 279 is included in the outflow sample and, as I will show later, is one of the many AGN which exhibit signatures of highly ionised absorption in their Fe K band. In this specific case, a Fe XXVI Ly$\alpha$ absorption line is detected in Mrk 279 for a $\Delta\chi^2_{\rm Ly\alpha} = 15.1$ improvement with respect to a null-hypothesis model which does not include the line.

Each point plotted in Fig. 2.5 corresponds to the statistical significance of the strongest spurious lines detected in $T = 1000$ spectra simulated using the process outlined previously. Only 4 simulated points are found to have $|\Delta\chi^2_{\rm noise}| \geq |\Delta\chi^2_{\rm Ly\alpha}|$, which means that the probability of observing a spurious line with a significance greater than the real line is only 0.4%. This indicates that the real line is detected at the $1 - (4/1000) = 0.996 \rightarrow 99.6\%$ confidence level. Another way to visualise this is to inspect the cumulative MC probability curve (red line in Fig. 2.6a), where it is even more clear that the real line is more significant than 99.6% of the simulated spurious ones. As a comparison, Fig. 2.6a also shows the cumulative F-test probability curve which was measured simultaneously from the same $T = 1000$ Monte Carlo simulations. From this, it is readily apparent that the F-test universally estimates the line to be less significant than the MC simulations; this is most apparent at detection probabilities of $\lesssim 0.01$, where the F-test reports spurious lines to be nearly an order of magnitude more significant than the more robust MC simulations (see Fig. 2.6b). For the Mrk 279 example considered above, the F-test indicates that the probability of observing a random fluctuation in the spectrum with a $\Delta\chi^2$ significance greater than the observed absorption line (which has $|\Delta\chi^2_{\rm Ly\alpha}| = 15.1$) is $3 \times 10^{-4}$, corresponding to a confidence level of 99.97% that the observed profile is a real spectral feature. Alternatively, the MC simulations estimate this same probability as $4 \times 10^{-3}$, yielding a significance of 99.6% for the real absorption profile. This simple demonstration highlights how the F-test can overestimate the confidence level for a blind search of narrow absorption lines, and also illustrates that these limitations can be overcome by performing robust MC simulations.

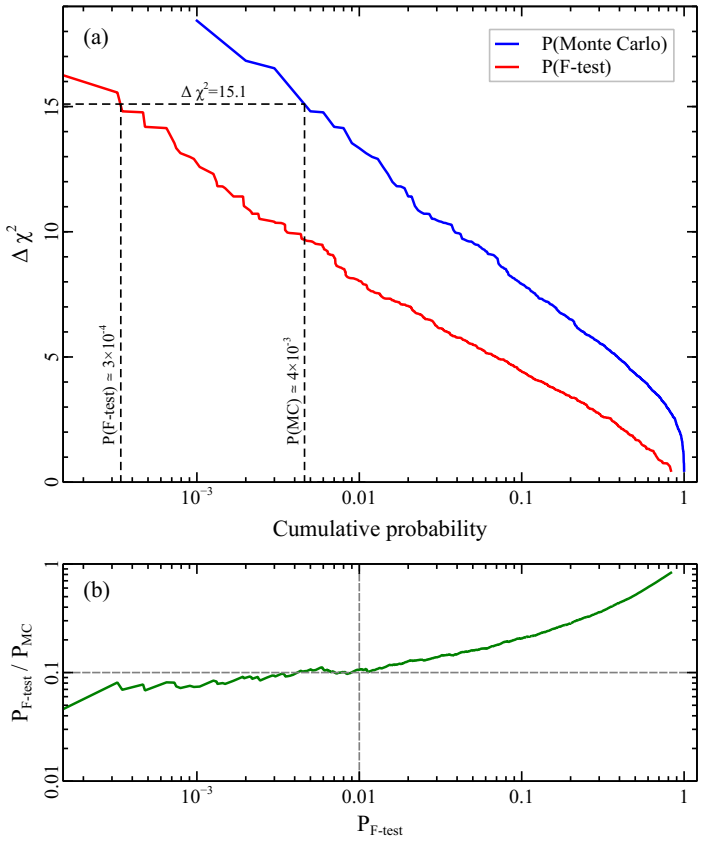


Figure 2.6: Comparison of the Monte Carlo and F-test cumulative probability distributions as measured from the 1000 simulated Mrk 279 spectra. Panel (a) clearly shows that the F-test systematically yields a higher significance for spuriously simulated lines than the more robust Monte Carlo simulations. Panel (b) shows the ratio of F-test to Monte Carlo significance as a function of F-test probability, and highlights that the significances measured via the F-test and MC simulations differ by around an order of magnitude.

## 2.3 Software

Data obtained with the major X-ray observatories are predominantly reduced using suites of computational programs and scripts which are made available by the various mission teams. The most prevalent amongst these is the HEASoft package[10] (also known

as FTOOLS), which is provided by the HEASARC and contains a collection of utilities for data reduction and analysis. Amongst these, HEASoft contains the complete set of mission-specific tools for the *Suzaku* and *Swift* satellites, plus a generic set of tools which can in principle be used with all other X-ray observatories, both past and present. Even so, and while the FTOOLs can be used with *XMM-Newton* and *Chandra* data, there are two independent and specialist software packages for these latter two satellites. These are known as the Chandra Interactive Analysis of Observations[11] (CIAO; Fruscione et al. 2006) and the *XMM-Newton* Scientific Analysis System [12] (SAS), respectively, and both are supported by extensive online documentation. For *Suzaku*, most data screening is performed using XSELECT. This is an FTOOL program which allows images, spectra and lightcurves to be generated from raw events files, and also allows goal-specific filters to be applied to the data which facilitates, for example, temporal- or flux-resolved spectroscopy.

Once data has been reduced it must be analysed, and this can be performed using a variety of programs, e.g., ISIS[13] (Houck & Denicola 2000), SHERPA[14] (Freeman, Doe & Siemiginowska 2001), SPEX[15] (Kaastra, Mewe & Nieuwenhuijzen 1996)and XSPEC[16] (Arnaud 1996). These programs are all capable of applying theoretical models to X-ray spectra, performing complex fitting algorithms and calculating the statistical tests which are both appropriate and necessary for effective spectral fitting. The most widely used of these (and the one which I have used to conduct the work presented in this thesis) is XSPEC, which is continuously developed and maintained by the HEASARC. In brief, XSPEC is a flexible and relatively simple-to-use command-line-driven X-ray spectral fitting package which is designed to be used with any spectrometer. It contains an extensive library of theoretical models which can be applied to X-ray data, and has the important capability of allowing users to define their own proprietary local models.

[10]http://heasarc.gsfc.nasa.gov/lheasoft/
[11]http://cxc.harvard.edu/ciao/index.html
[12]http://xmm.esac.esa.int/sas/
[13]http://space.mit.edu/cxc/isis/
[14]http://cxc.harvard.edu/sherpa4.4/index.html
[15]http://www.sron.nl/spex
[16]http://heasarc.gsfc.nasa.gov/docs/xanadu/xspec/index.html

## 2.4 Suzaku data reduction

The data that I use in the subsequent chapters of this thesis are predominantly obtained with the *Suzaku* space observatory. When *Suzaku* data are either made available by the instrumentation teams or obtained via one of the on-line catalogues they must be reduced, screened and processed to convert the raw data products into spectral files which are suitable for spectroscopic analysis. In this section I outline the generic reduction process for the XIS and HXD detectors aboard *Suzaku*; specifics on individual sources (e.g., source extraction region sizes, background count rates etc.) are detailed in the respective chapters.

### 2.4.1 XIS

Raw data for the three (four) XIS CCDs are generally screened into useful secondary spectral files using the XSELECT FTOOL. All data used in this thesis are screened within XSELECT to match the standard *Suzaku* screening criteria as recommended by the instrumentation team (c.f., §2.2.1), i.e., data are excluded if they were taken: (1) within 436 s of passage through the South Atlantic Anomaly (SAA), (2) within an Earth elevation angle (ELV) $< 5°$, and / or (3) within Earth day-time elevation angles $< 20°$. A cut-off rigidity (COR) criterion of $> 6$ GeV was also employed such that time intervals where the COR was below 6 GeV are also excluded. Finally, hot and flickering pixels are removed from the XIS images using the CLEANSIS script.

From the screened XIS images X-ray spectra for both the source and the background can be selected using a combination of the XSELECT FTOOL and the `ds9` SAOImage program. Generally, the source spectra for pointed observations are taken from a circular extraction region which is centred on the middle of the CCD frame, while background spectra are extracted from offset circles of the same radius with care taken to avoid the calibration sources at the corner of the CCD chips. The radius of the extraction region is determined by a combination of data quality and user discretion; faint sources will need a smaller extraction region than brighter ones to minimise the background contribution to

the source frame. Complementing the spectral files each detector in a given observation needs to have its underlying response function mapped: the redistribution matrix (RMF) and ancillary response (ARF) are generated using the XISRMFGEN and XISSIMARFGEN tasks, respectively.

The source and background spectra in conjunction with the ARF and RMF constitute a functional XIS spectrum which is suitable for analysis. However, it is often useful to co-add the front-illuminated XIS 0, (XIS 2) and XIS 3 spectra into a single source spectrum (hereafter referred to as XIS-FI) using the MATHPHA FTOOL. This has the effect of maximising the signal-to-noise ratio ($SNR$) available in the Fe K band, which is crucial when it comes to studying highly-ionised absorption lines in detail. Owing to higher background and lower effective area at higher X-ray energies the spectrum obtained from the back-illuminated XIS 1 (hereafter XIS-BI) cannot be co-added and are always analysed simultaneously with the XIS-FI in XSPEC as a separate input spectral file. During spectral fitting the XIS data need to be ignored between $1.6 - 2.1$ keV due to uncertainties associated with the Si K edges which are intrinsic to the detector assembly of the XIS instrument, with the remaining data being considered through the entire $0.6 - 10.0$ keV energy bandpass.

### 2.4.2 HXD

Source spectra for the HXD PIN are extracted from the 'cleaned' event files and, due to the total PIN background being time dependent across the orbit of the spacecraft, are screened according to the criteria which were outlined previously for the XIS (see above). The PIN is a collimating rather than an imaging instrument which means that the contribution of both the instrumental Non X-ray Background (NXB) and the Cosmic X-ray Background (CXB) need to be independently accounted for when estimating the total background. The total NXB can be generated using the response and tuned event files appropriate for each observation; the time-filter which was deduced as the result of the screening process of the source events was applied to the NXB background file to deduce the model-background which applies during the same time intervals covered by

the on-source data (i.e., only the 'good time intervals', GTIs, are considered). The effects of detector dead-time ($\approx 6.7\%$; see Kokubun et al. 2007) for a detailed description of PIN dead-time) must then be corrected for using the HXDDTCOR script, whilst the exposure of the NXB was then increased by $\times 10$ to reduce the effects of photons noise.

To account for the cosmic X-ray background (CXB) a background spectrum must be simulated. In this thesis I adopt the form of Boldt (1987), as recommended by the *Suzaku* instrumentation team, i.e.,

$$\mathrm{CXB}(E) = 9.0 \times 10^{-9} \left(\frac{E}{3\,\mathrm{keV}}\right)^{-0.29} \exp\left(\frac{-E}{40\,\mathrm{keV}}\right) \mathrm{erg\,cm^{-2}\,s^{-1}\,str^{-1}\,keV^{-1}}. \quad (2.8)$$

In order to calculate the total X-ray background the above product needs to be normalised to the FOV of the PIN detector using the appropriate flat-field detector response and then combined with the NXB to produce a total background count-rate summed over the PIN FOV. The resultant total background can then subsequently be subtracted from the source spectrum within XSPEC, yielding a background-subtracted PIN spectrum that provides energy sensitivity between $15 - 50\,\mathrm{keV}$. This broadens the total *Suzaku* bandpass to $0.6 - 50\,\mathrm{keV}$ when fitted in conjunction with spectra from the XIS. The HXD GSO is not used in the majority of this work due to its low sensitivity and high background for extragalactic sources.

# 3 The *Suzaku* observation of MR 2251−178[1]

## 3.1 Introduction

MR 2251−178 ($z = 0.064$; Bergeron et al. 1983; Canizares, McClintock & Ricker 1978) is one of the X-ray brightest AGN in the local universe ($L_{2-10\,\mathrm{keV}} \sim 2 - 9 \times 10^{44}\,\mathrm{erg\,s^{-1}}$). It was the first quasar detected solely through X-ray observations (Cooke et al. 1978; Ricker et al. 1978) and the first AGN known to host a warm absorber (Halpern 1984). The quasar is located on the outskirts of a cluster of $\sim 50$ galaxies (Phillips 1980) and is surrounded by an extended nebula of diffuse gas which gives rise to [O II], [O III] and H$\alpha$ emission at optical wavelengths (Macchetto et al. 1990; Phillips 1980) and O III-V absorption in the X-rays (Kaspi et al. 2004). The source has a central black hole mass of $\sim 2.4 \times 10^8 M_\odot$ (Dunn et al. 2008)and has a Fanaroff-Riley type I (FR I) radio morphology (Macchetto et al. 1990).

The first detailed study of MR 2251−178 in the X-ray regime was conducted by Halpern (1984) who, using a spectrum from the *Einstein* space observatory, noticed soft X-ray variability on time-scales of $\sim 1\,\mathrm{yr}$ caused by changes in both the column density of photo-ionised material along the line of sight and an associated change in the material's ionisation state (Halpern 1984). The ionisation state of the absorbing material was also later found to be strongly correlated with the source luminosity, with the absorber appearing to become more ionised when the source was at a larger luminosity, which thus strongly suggested the presence of partially-ionised 'warm' material along the line of sight (Mineo & Stewart 1993). Subsequent observations with *EXOSAT*, *Ginga* and *BeppoSAX* revealed the broad-band X-ray spectrum could be well described by a power-law of photon-index $\Gamma \sim 1.6 - 1.7$ which is absorbed by a column density of

[1]This chapter is partly based on published work entitled '*Broad-band X-ray spectroscopy of the Warm Absorber in radio-quiet quasar MR 2251−178*'; Gofford, J.; Reeves, J. N.; Turner, T. J.; Tombesi, F.; Braito, V.; Porquet, D.; Miller, L.; Kraemer, S. B.; Fukazawa, Y., MNRAS, **414**, 3307-3321.

All work was conducted by myself.

around a few $\times 10^{22}\,\mathrm{cm}^{-2}$ (Pan, Stewart & Pounds 1990; Mineo & Stewart 1993), and a high-energy roll-over at around 100 keV (Orr et al. 2001). In the UV, Mineo & Stewart (1993) found absorption lines due to Ly$\alpha$, N V and C IV with a systematic blue-shift of $\sim 300\,\mathrm{km\,s}^{-1}$; the C IV absorption in particular showed variability over a period of roughly 4 years which constrained the absorption clouds to within $r \lesssim 2.4$ kpc of the continuum source (Ganguly, Charlton & Eracleous 2001).

In 2004 Kaspi et al. (2004) performed a detailed spectral and temporal study of MR 2251−178 using a series of *ASCA*, *FUSE*, *BeppoSAX* and *XMM-Newton* observations which spanned over a period of $\sim 8.5$ yrs. In confirmation of previous studies Kaspi et al. (2004) also found the continuum to be described by an absorbed power-law of photon index $\Gamma \sim 1.6$, but also found that the continuum required a supplementary soft-excess at $E < 2$ keV to achieve an acceptable fit to the soft X-ray data. The grating spectrum from the *XMM-Newton* RGS revealed the warm absorber in MR 2251−178 to be multi-phase, consisting of at least two or three ionised absorption components with column densities in the range $10^{20-22}\,\mathrm{cm}^{-2}$, all of which had physical properties which appeared to vary between observations in accord to what was reported by Halpern (1984). This led Kaspi et al. (2004) to propose a scenario where absorption clouds were moving across the line of sight over a time-scale of 'several months'. In the *FUSE* spectrum further UV absorption lines from C III, H I and O VI were detected with velocity shifts similar to those found by Monier et al. (2001).

Prior to the *Suzaku* spectrum which is predominantly discussed in this chapter, the most recent observation of MR 2251−178 in the X-rays was published by Gibson et al. (2005) using the *Chandra* HETG. There, the authors found evidence for a highly-ionised Fe XXVI Ly$\alpha$ absorption line with a substantial blue-shifted velocity, $v_{\mathrm{out}} = 12,700 \pm 2,400\,\mathrm{km\,s}^{-1}$. By considering the kinematics of the absorber Gibson et al. (2005) inferred that unless the absorber is of a low covering fraction the mass-loss rate in MR 2251−178 is at least an order of magnitude larger than the source accretion rate.

In this chapter I present the analysis of a new broad-band *Suzaku* X-ray spectrum of MR 2251−178, along with the preliminary results of an extensive follow-up campaign with *XMM-Newton* and *Chandra*. The overall goal of this campaign was to derive a

detailed and high signal-to-noise ($S/N$) description of the AGN in MR 2251−178 in order to measure the properties of the primary continuum emission and any ionised absorption along the line of sight. Specifically, the interim objectives with *Suzaku* were to: (1) utilise broad-band X-ray data to constrain the properties of both the primary continuum and any discrete absorption lines; (2) utilise the good energy resolution made available through the *Suzaku* XIS to test for the presence (or absence) of any highly-ionised blue-shifted absorption lines in the Fe K band; (3) construct a self-consistent model of all necessary warm absorber components using the XSTAR photo-ionisation code. At the end of this chapter I describe the more recent *XMM-Newton* and *Chandra* observations of MR 2251−178, along with some preliminary results from their analysis. I also discuss the wider implications of these higher-quality datasets with regards to the *Suzaku* results as well.

## 3.2 Data Analysis

The *Suzaku* space observatory (Mitsuda et al. 2007) observed the radio-quiet quasar MR 2251−178 in the XIS nominal pointing position for a total elapsed duration of $\sim 287$ ks between the $7 - 10^{\rm th}$ of May 2009. Data from the three functioning X-ray Imaging Spectrometers (XIS; Koyama et al. 2007) and the Positive Intrinsic Negative (PIN) silicone diodes aboard the Hard X-ray Detector (HXD; Takahashi et al. 2007) were included in all analyses. The PIN data were further complemented in the hard X-ray band by the inclusion of data obtained by the Burst Alert Telescope (BAT) aboard *Swift* which observed the AGN during the 58 month all sky survey (Baumgartner et al. 2010). All of the *Suzaku* data were processed using version 2.3.12.25 of the *Suzaku* data reduction pipeline, and reduced following the process outlined in §2.4.1. A detailed summary of the observation is given in Table 3.1.

The background subtracted count rates for the XIS were $2.037 \pm 0.003$ counts s$^{-1}$ per CCD for the XIS-FI and $2.534 \pm 0.004$ counts s$^{-1}$ in the case of the XIS-BI, which, for a net source exposure of 136.9 ks, correspond to a net source flux of $F_{2-10\,\rm keV} =$

Table 3.1: Summary of *Suzaku* and *Swift* MR 2251−178 observations. *Columns*: (1) *Suzaku* observation ID; (2) Instrument; (3) Date of observation; (4) Net source exposure, in kiloseconds; (5) Measured source count rate, in units of $s^{-1}$; (6) measured source flux, in units of $\times 10^{-11}\,erg\,cm^{-2}\,s^{-1}$.

| | OBSID (1) | Inst. (2) | Date (3) | Exp. (4) | Count rate (5) | Flux (6) |
|---|---|---|---|---|---|---|
| *Suzaku* | 704055010 | XIS-FI | 2009-05-07 | 137 | $2.037 \pm 0.003$ | 4.29[a] |
| | | XIS-BI | | 137 | $2.534 \pm 0.004$ | 4.35[a] |
| | | PIN | | 104 | $0.135 \pm 0.003$ | 5.48[b] |
| | | GSO | | 89 | $< 0.3$ | $< 4.80$[c] |
| *Swift* | | BAT | | | $(14.5 \pm 0.3) \times 10^{-4}$ | 6.63[d] |

NOTES: [a] $2-10\,keV$; [b] $15-50\,keV$; [c] $50-100\,keV$ 90% upper limit; [d] $20-100\,keV$

$4.3 \times 10^{-11}\,erg\,cm^{-2}\,s^{-1}$ and $F_{2-10\,keV} = 4.4 \times 10^{-11}\,erg\,cm^{-2}\,s^{-1}$ in the $2-10\,keV$ band, respectively. As is shown in the lightcurves for the 3 individual XIS detectors (see Fig. 3.1) the source flux was relatively constant, i.e., $< 10\%$ fluctuations, over the course of the observation and there was no evidence for strong variability. All of the XIS spectra and their corresponding detector response files were binned to sample the half-width at half-maximum (HWHM) XIS energy resolution (i.e., $\sim 60\,eV$ resolution at $6\,keV$). Counts were additionally grouped with GRPPHA to achieve a minimum of 50 X-ray counts per energy resolution element to enable the use of $\chi^2$ minimisation technique, which was used for all subsequent spectral fitting.

For the PIN the background subtracted count rate was $0.135 \pm 0.003\,counts\,s^{-1}$, corresponding to a flux of $F_{15-50\,keV} = 5.48 \times 10^{-11}\,erg\,cm^{-2}\,s^{-1}$. The high flux exhibited by MR 2251−178 in the hard X-ray band was sufficient to trigger a positive detection with the HXD/GSO detector, which was also reduced to check the consistency of the supplementary *Swift* BAT data relative to the HXD/PIN at $E > 100\,keV$. The total (background subtracted) GSO exposure was 89.2 ks for a net count rate of $< 0.3\,counts\,s^{-1}$. This corresponds to a 90% upper limit on the $50-100\,keV$ flux of $F_{50-100\,keV} < 4.8 \times 10^{-11}\,erg\,cm^{-2}\,s^{-1}$. Note that the GSO data were not included during

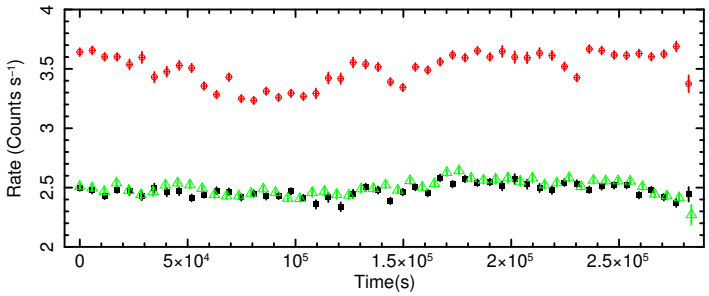


Figure 3.1: Lightcurves for the XIS0 (green triangles), XIS1 (red circles) and the XIS3 (black closed squares). Only small variations in the lightcurve were observed during the observations. $1\sigma$ error bars are roughly the size of the plot points.

spectral fitting, instead being used solely to determine the consistency of the time-average *Swift* BAT dataset. To enable the use of $\chi^2$ minimisation the PIN data were binned to a $5\sigma$ level above the background per energy bin between $15-50\,\mathrm{keV}$.

## 3.3 Broad-band Modelling

A detailed broad-band analysis of MR 2251−178 was conducted between $0.6-180\,\mathrm{keV}$ using version 12.6.0*q* of the XSPEC spectral fitting package (Arnaud 1996) and version 6.10 of the HEASoft suite. All of the spectral fits discussed in the following sections were modified by a constant Galactic column density of $N_H^{\mathrm{Gal}} = 2.42\times10^{20}\,\mathrm{cm}^{-2}$ using the `wabs` model (Morrison & McCammon 1983) in XSPEC to model the effects of photoelectric absorption by neutral material in the direction of the source which is intrinsic to the Milky Way Galaxy. To account for systematic uncertainties in the normalisation of the XIS-FI data relative to that of the XIS-BI a variable cross-normalisation factor was included in all models; generally the XIS-FI and XIS-BI were found to be consistent to within $\pm(2-3)\%$. The PIN normalisation was set to +16% of the XIS-FI, which is applicable for the XIS nominal pointing position and the version of the *Suzaku* pipeline with which the data were processed. The *Swift* BAT spectrum was time-averaged over a 58-month period between November 2004 and September 2009. Therefore a constant

multiplicative factor was included to allow for any re-normalisation of the spectrum which may have occurred between the pointed *Suzaku* observation and the time-averaged spectrum from the *Swift* BAT all-sky survey; a factor of $+(4-5)\%$ greater than that of the XIS instruments was sufficient in all fits.

### 3.3.1 Initial parametrisation

As a starting point I initially considered the X-ray spectrum of MR 2251−178 between $3-5\,\mathrm{keV}$. The $3-5\,\mathrm{keV}$ is typically devoid of strong atomic edges and/or lines which makes it a relatively 'clean' part of the X-ray spectrum. A fit of the continuum in this narrow energy band with a simple power-law of photon index $\Gamma = 1.56 \pm 0.01$ modified solely by Galactic absorption yields a reasonable fit to the data, with $\chi^2/\nu = 212.5/178$. Individually, the photon indices for the three XIS spectra were all in good agreement with the simultaneous fitted value; with the XIS 0, XIS 1 and XIS 3 datasets being described by spectral indices of $\Gamma = 1.55 \pm 0.01$, $\Gamma = 1.55 \pm 0.02$ and $\Gamma = 1.57 \pm 0.02$ between $3-5\,\mathrm{keV}$, respectively. However, extending the data coverage to include the full $0.6-180.0\,\mathrm{keV}$ bandpass reveals significant deviations from the simple power-law fit. In particular, there is a strong soft excess present below $0.7-0.8\,\mathrm{keV}$, and a trough between $0.8-1.6\,\mathrm{keV}$ which is presumably due to the warm absorber for which the source is well known. The positive residuals at $\sim 6.4\,\mathrm{keV}$ correspond to an Fe K$\alpha$ fluorescence line in the spectrum, which is relatively weak. At harder X-ray energies the PIN and BAT spectra appear to roll-over at $E \gtrsim 10\,\mathrm{keV}$, which is consistent with the high-energy cut-off reported by Orr et al. (2001) in the *BeppoSAX* spectrum. For completeness, and because the BAT spectrum was not contemporaneous with the *Suzaku* observation, the BAT data were compared with those obtained by the HXD/GSO to determine the validity of the high-energy cut-off. The GSO flux of $F_{50-100\,\mathrm{keV}} < 4.8 \times 10^{-11}\,\mathrm{erg\,cm^{-2}\,s^{-1}}$ was consistent with the $F_{50-100\,\mathrm{keV}} \sim 2.7 \times 10^{-11}\,\mathrm{erg\,cm^{-2}\,s^{-1}}$ measured by the BAT instrument, which implies that prominent roll-over in the BAT spectrum is indeed valid for the *Suzaku* observation despite the lack of a simultaneity between observations.

In light of the residuals due to missing spectral components the simple power-law

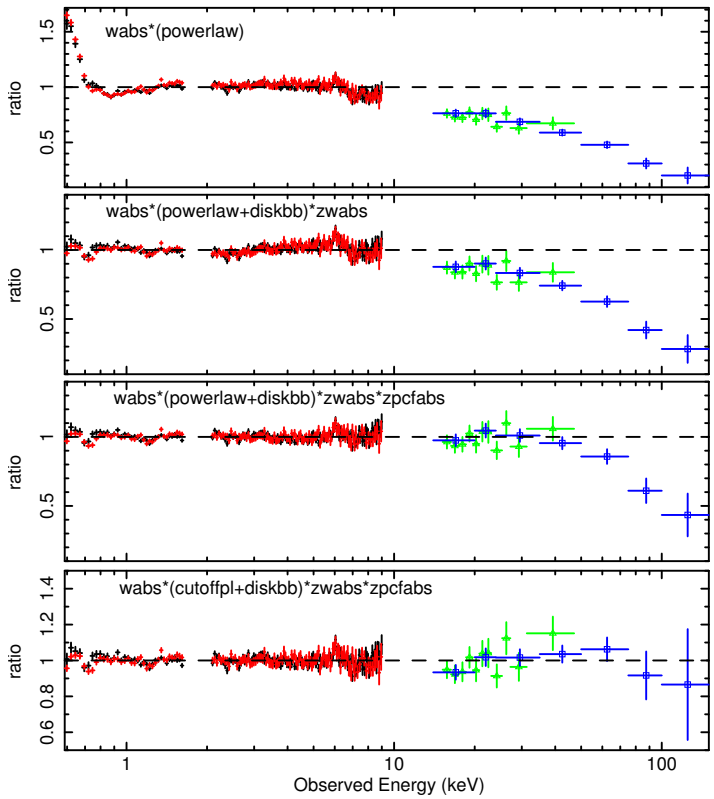


Figure 3.2: The broad-band data/model residuals of the *Suzaku* (XIS-FI: black, XIS-BI: red, PIN: green open triangles) and *Swift* (BAT: blue open squares) data when fit with a variety of parametrising models (see §3.3.1). From top to bottom: (1) Residuals when fit solely by the 3–5 keV best-fit power–law (2) Residuals of the same data when fit an accretion disc black body and power-law absorbed by a fully-covering neutral absorber. (3) As above, except with an additional partial-covering absorber included in the model. (4) As above, but with a cut-off power-law. Note that the Fe K$\alpha$ has not been fit for illustrative purposes.

model yields an extremely poor fit to the data ($\chi^2/\nu = 4733.3/348$; see Fig. 3.2, upper panel). In order to better parametrise the broad-band $0.6 - 180$ keV continuum the power-law was replaced with a more complicated model of the form $N_H^{\rm Gal} \times$ (`powerlaw` + `diskbb` + `zgauss`) $\times$ `zwabs`, where the `diskbb` component is a simple parametrisation of the soft excess as an accretion disc blackbody (Mitsuda et al. 1984), `zgauss` is a Gaussian profile to fit the Fe K$\alpha$ fluorescence emission line at 6.4 keV and `zwabs` is a

neutral photoelectric absorber modelled in the source rest-frame (i.e., at $z = 0.064$). With this model the fit is drastically improved from what was had previously, but is still quite poor statistically ($\chi^2/\nu = 1111.1/340$) and formally unacceptable. Even so, in this model the photon-index of the power-law component has softened slightly to $\Gamma = 1.67 \pm 0.01$ and is absorbed by a neutral column of $N_{\rm H} \sim 1.1 \times 10^{21}\,{\rm cm}^{-2}$, which is similar to that found by Ramírez et al. (2008) in previous *Chandra* LETG observation of the AGN. The soft excess is modelled by an accretion disc blackbody with a temperature of $kT \sim 60\,{\rm eV}$, while the unresolved ($\sigma < 391\,{\rm eV}$) Fe K$\alpha$ fluorescent line at $E = \left(6.43^{+0.04}_{-0.03}\right)\,{\rm keV}$ suggests the presence of a neutral or mildly ionised reflection component. As shown in Figure 3.2 (second panel), the poor fit is largely due to the simple parametrising models inability to adequately reproduce the spectral curvature present in the spectrum which suggests that additional absorption is required. The addition of an absorber with $N_{\rm H} \sim 9 \times 10^{22}\,{\rm cm}^{-2}$ which covers $\sim 25\%$ of the source adequately accounts for the residual spectral curvature present in the XIS data, and improves the fit statistic to $\chi^2/\nu = 565.5/338$ for two additional free parameters. Moreover, with a photon index of $\Gamma = 1.83 \pm 0.01$, this new model is able to replicate the observed flux in the HXD/PIN data. Even so, the model is still unable to reproduce the roll-over present in the BAT data (Fig. 3.2, third panel). The traditional flat power-law was therefore replaced with a `cutoffpl` component which models a power-law with an exponential high-energy cut-off ($E_{\rm cut}$), which improves the fit by $\Delta\chi^2/\Delta\nu = 63.2/1$ by virtue of fitting the BAT roll-over. The resultant best-fit parameters for the parametrisation of the continuum are listed in Table 3.2.

### 3.3.2 Absorption Lines

There are several discrete absorption features evident in the spectrum below 3 keV and in the Fe K band (see Table 3.3). To constrain their parameters these absorption lines were initially modelled with Gaussian profiles fitted in the rest-frame of the AGN, with the spectral parameters and statistical significances of each line being determined against the best-fit continuum model discussed above. Monte Carlo (MC) simulations were performed in the vicinity of each absorption line using the method outlined in §2.2.6 to

Table 3.2: Parameters for best-fitting continuum parametrisation. *Columns:* (1) model component name; (2) model parameter; (3) best-fitting parameter value, with 90% errors.

| Component (1) | Parameter (2) | Value (3) |
|---|---|---|
| `cutoffpl` | $\Gamma$ | $1.72 \pm 0.03$ |
| | $E_{\rm cut}$ | $\left(121^{+34}_{-23}\right)$ keV |
| `diskbb` | $kT$ | $(57 \pm 1)$ eV |
| `zwabs` | $N_{\rm H}$ | $(1.03 \pm 0.02) \times 10^{21}\,{\rm cm}^{-2}$ |
| `zpcfabs` | $N_{\rm H}$ | $\left(8.90^{+0.61}_{-0.54}\right) \times 10^{22}\,{\rm cm}^{-2}$ |
| | $f_{\rm cov}$ | $(16 \pm 1)\,\%$ |

robustly assess the statistical significances versus random spectral fluctuations.

### The Soft X-ray band

There are two strong absorption lines below 2 keV (Fig. 3.3; top panel), both of which are unresolved. The first, which is detected at a rest-frame energy of $E = (0.77 \pm 0.01)$ keV, is consistent with the Fe I-XVI M-shell unresolved transition array (UTA) which is expected between $0.729 - 0.775$ keV (Behar, Sako & Kahn 2001; Netzer 2004). The line equivalent width ($EW$) is $-(7 \pm 2)$ eV and its addition improves the global fit by $\Delta\chi^2/\Delta\nu = 65.6/2$, for a Monte Carlo significance, $P_{\rm MC}$, of $> 99.9\%$. The second residual profile has a rest-frame energy of $1.29 \pm 0.01$ keV, and, like the Fe UTA, is highly significant to the model ($\Delta\chi^2/\Delta\nu = 66.1/2$; $P_{\rm MC} > 99.9\%$). However, this second profile, which has an $EW = -\left(4^{+2}_{-1}\right)$ eV, has a more ambiguous identification as its rest-frame energy does not directly correspond to any of the $1s \rightarrow 2p$ transitions which are typically found to be strong in the X-rays. The observed energy range for this line, i.e., $1.28 - 1.30$ keV, is populated by an array of high-order transitions from low-abundance elements. For example, the $2s \rightarrow nd$ transitions of Co XVIII-XX are found in this energy range but can be ruled out as a possible identification based on its negligible astrophysical

abundance (i.e., $Z_{\rm Co}/Z_{\rm H} \sim 10^{-8}$). The line is also unlikely to be identified with any blue-shifted transitions for the expected $1s \rightarrow 2p$ X-ray lines (e.g., from O or Ne) without an extreme outflow velocity (i.e., $v_{\rm out} \gtrsim 0.3 - 0.4\,{\rm c}$) which is much faster than that typically found in AGN warm absorbers (e.g., Blustin et al. 2005; McKernan, Yaqoob & Reynolds 2007; Crenshaw, Kraemer & George 2003a). On the basis of the *Suzaku* data alone there are two plausible identifications for this line, of which one is confirmed through subsequent *Chandra* and *XMM-Newton* observations. The first possibility is that provided the absorbing gas be of sufficiently low ionisation the line could be associated with a blend of the inner-shell Mg lines which are present throughout the observed energy range (Behar & Netzer 2002). The $1s \rightarrow 2p$ lines of Mg in its Li-like (Mg X), Be-like (Mg IX), B-like (Mg VIII), C-like (Mg VII) and N-like (Mg VI) charge states in particular, which occur at mean energies of $E \sim 1.34\,{\rm keV}$, $E \sim 1.32\,{\rm keV}$, $E \sim 1.31\,{\rm keV}$, $E \sim 1.29\,{\rm keV}$ and $E \sim 1.28\,{\rm keV}$, respectively, could provide a plausible identification should the lines be blended together at the energy resolution of the XIS CCDs. An alternative interpretation which I also considered was that the line may be due to velocity shifted $2s \rightarrow 3p$ transitions of Fe XXIII-XXV, which occur between $E \sim 1.17 - 1.24\,{\rm keV}$. This would require a blue-shift of $v_{\rm out} \sim 12,000 - 30,000\,{\rm km\,s^{-1}}$ relative to MR 2251−178, which is more reminiscent of outflows found in the Fe K band than those at lower energies. However, in the presence of an outflow at Fe K (see §3.3.2), and because it Fe XXIV and Fe XXV can co-exists at ionisation states between $\log(\xi/{\rm erg\,cm\,s^{-1}}) \sim 2.5 - 4$, such an identification is plausible for a narrow range of absorber parameter space and therefore could not be ruled out based solely on the *Suzaku* data. Due to the ambiguities regarding the identification of the $E \sim 1.29\,{\rm keV}$ line I assert a positive identification based on solely the *Suzaku* data, and instead leave the profile modelled as a narrow Gaussian in all subsequent analyses. The true identification for this line, as revealed through *XMM-Newton* and *Chandra* observations, is discussed in §3.6.1.

There are two further absorption lines at $E = (2.52 \pm 0.02)\,{\rm keV}$ and $E = (2.79 \pm 0.03)\,{\rm keV}$ in the source rest-frame, with $EW$s of $-(6 \pm 2)\,{\rm eV}$ and $-(5 \pm 2)\,{\rm eV}$, respectively (Fig. 3.3; middle panel). Both of these lines are significant at the $P_{\rm MC} > 99.9\%$ level and, individually, their addition improves the model by a further $\Delta\chi^2/\Delta\nu = 15.9/2$

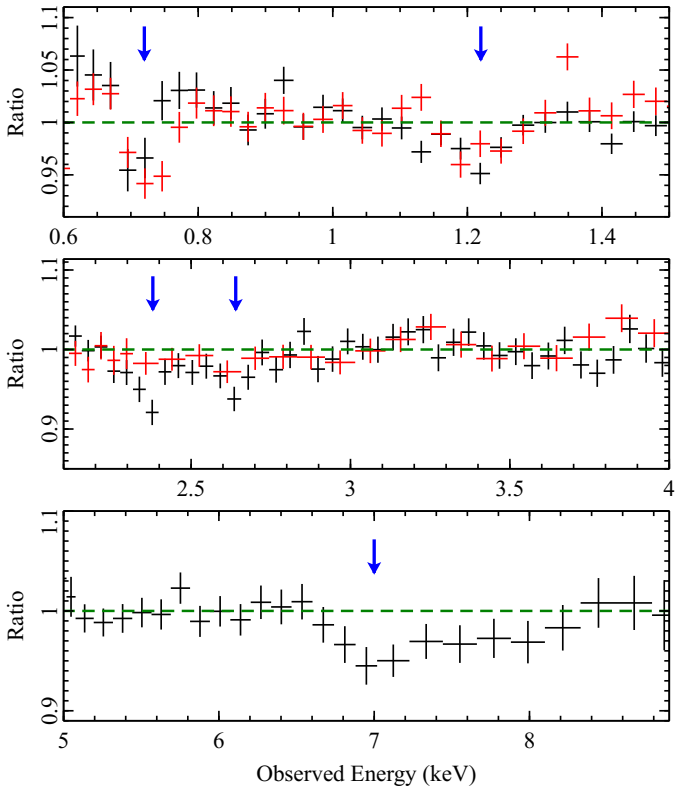


Figure 3.3: XIS-FI (black points) and XIS-BI (red points) residuals when fit with the best-fit continuum parametrisation, as discussed in §3.3.1. The positions of the absorption lines are clearly labelled The XIS-BI data have been omitted in the bottom panel due to reduced $S/N$ at Fe K and the remaining XIS-FI data have been additionally binned by a factor of 3 above the HWHM energy resolution of the detectors for clarity. The Fe K$\alpha$ fluorescence line has been included in these fits.

and $\Delta\chi^2/\Delta\nu = 10.9/2$. The strongest atomic features expected between $2-3$ keV are those associated with the $1s \rightarrow 2p$ transitions of S XV ($E \sim 2.461$ keV) and S XVI ($E \sim 2.623$ keV) but the measured rest-frame energies of the absorption lines do not correspond to either of these. Moreover, the only atomic lines which have rest-frame energies consistent with the observed profiles are those associated with extremely low abundance elements (e.g., Kr, Rb and Mo) which are unlikely to contribute strongly in the X-ray regime. The higher energy profile is marginally consistent with the nearby He$\beta$

transition of S XV at $E \sim 2.88\,\mathrm{keV}$, but such an identification is again unlikely given that the corresponding He$\alpha$ transition — which is expected to be much stronger — is not observed. Therefore a $v_{\mathrm{out}} \sim 0\,\mathrm{km\,s^{-1}}$ solution for both lines is very unlikely and they are probably associated with velocity shifted material. The most conservative identification is with the previously mentioned S XV He$\alpha$ and S XVI Ly$\alpha$ lines, which would require outflow velocities of $v_{\mathrm{out}} = (6,000 \pm 3,000)\,\mathrm{km\,s^{-1}}$ and $v_{\mathrm{out}} = (21,000 \pm 3,000)\,\mathrm{km\,s^{-1}}$, respectively. Assuming this conservative identification is correct this interestingly suggests that there may be kinematic structure to the outflowing absorber, which is a point that I return to later.

### The Fe K region

There are further residuals present in the Fe K region. In addition to the Fe K$\alpha$ fluorescence line there is a clear broad absorption trough between $\sim 6.5-8\,\mathrm{keV}$ (Fig. 3.3, bottom panel). I initially modelled it with a $\sigma = \left(209^{+244}_{-108}\right)\,\mathrm{eV}$ broadened Gaussian at $E = \left(7.57^{+0.19}_{-0.12}\right)\,\mathrm{keV}$ with an $EW$ of $-\left(26^{+18}_{-12}\right)\,\mathrm{eV}$. This resulted in a $\Delta\chi^2/\Delta\nu = 16.6/3$ improvement to the fit, corresponding to a $P_{\mathrm{MC}} > 99.3\%$ significance from Monte Carlo simulations. With the broad absorption component present in the model the width of the Fe K$\alpha$ emission is more tightly constrained than before, with $\sigma < 117\,\mathrm{eV}$ and $EW = \left(25^{+12}_{-8}\right)\,\mathrm{eV}$.

Iron is expected to contribute the strongest lines in the observed energy range. In particular, the $1s \rightarrow 2p$ K$\alpha$ transitions are expected to be particularly strong, as are the many resonance transitions associated with the Fe K-shell edge at $\sim 7.1\,\mathrm{keV}$ (Kallman et al. 2004). If due to K$\alpha$ transitions this immediately places a constraint on the possible identifications for the absorption as being due to at least Fe XVIII ($E \sim 6.5\,\mathrm{keV}$), where the Fe ions become sufficiently ionised to have a vacancy in their L-shell for a $1s$ electron transition. Above this ionisation state, the K$\alpha$ transitions occur between $E \sim 6.5 - 6.6\,\mathrm{keV}$ for Fe XVIII-XXIV, and at $E \sim 6.7\,\mathrm{keV}$ and $E \sim 6.97\,\mathrm{keV}$ for Fe XXV and Fe XXVI, respectively. If the broad trough is identified with solely Fe XXV a velocity shift of $v_{\mathrm{out}} = \left(39,000^{+9,000}_{-6,000}\right)\,\mathrm{km\,s^{-1}}$ is required, while if identified with Fe XXVI the required velocity is slightly lower, at $v_{\mathrm{out}} = \left(30,000^{+9,000}_{-6,000}\right)\,\mathrm{km\,s^{-1}}$. Alternatively, at the

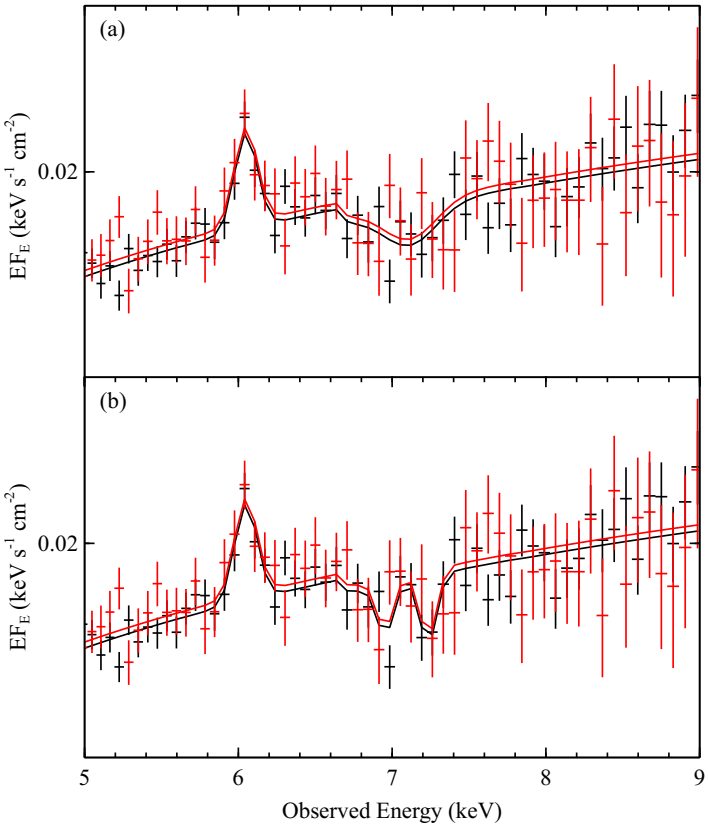


Figure 3.4: The Fe K band. *Top:* the absorption feature fit with a broad Gaussian. *Middle:* the same absorption feature when fit as two separate Gaussian lines using the method outlined in §3.3.2.

energy resolution of the XIS CCDs the broad absorption may represent a blend of the Fe XXV and Fe XXVI K$\alpha$ lines rather than it just being a single discrete profile. To assess for this possibility I replaced the single broad profile with two narrower absorption lines ($\sigma = 50\,\mathrm{eV}$) at fixed rest-frame energies of 6.7 keV and 6.97 keV, with their common velocity shift left as a free parameter. This approach yielded a slightly improved fit in comparison to that of a broad Gaussian obtained previously, for a $\Delta\chi^2/\Delta\nu = 18.1/3$. The common velocity shift was $v_{\mathrm{out}} = (30,000 \pm 3,000)\,\mathrm{km\,s^{-1}}$ and the the higher energy profile in particular, which would correspond to Fe XXVI, is well fitted in the new model. However, as Fig. 3.4 shows, the new model may slightly under-predict the intensity of the

Table 3.3: Summary of X-ray absorption and emission lines. *Columns:* (1) Line identification; (2) Line energy in the source rest-frame ($z = 0.064$), in units of keV; (3) Expected line energy in the observer frame, in units of keV; (4) Line flux in units of $\times 10^{-6}\,\mathrm{erg\,cm^{-2}\,s^{-1}}$; (5) Measured $\sigma$-width, in units of eV; (6) Line equivalent width, in units of eV; (7) Change in fit statistic when removing a Gaussian to the best-fit model; (8) Monte Carlo significance, in per cent.

| Line ID (1) | $E_{\rm rest}$ (2) | $E_{\rm lab}$ (3) | Flux (4) | $\sigma$ (5) | $EW$ (6) | $\Delta\chi^2$ (7) | $P_{\rm MC}$ (8) |
|---|---|---|---|---|---|---|---|
| Fe UTA | $0.77^{+0.01}_{-0.01}$ | $0.729 - 0.775$ | $-241.0^{+67.0}_{-60.0}$ | $10^*$ | $-7^{+2}_{-2}$ | 65.6 | $> 99.9$ |
| Mg/Fe L | $1.29^{+0.01}_{-0.01}$ | 1.165 | $-38.0^{+14.7}_{-11.3}$ | $< 44$ | $-4^{+2}_{-1}$ | 66.1 | $> 99.9$ |
| S XV | $2.52^{+0.02}_{-0.02}$ | 2.461 | $-17.2^{+5.7}_{-5.7}$ | $10^*$ | $-6^{+2}_{-2}$ | 15.9 | $> 99.9$ |
| S XVI | $2.79^{+0.03}_{-0.03}$ | 2.623 | $-11.5^{+4.7}_{-4.8}$ | $10^*$ | $-5^{+2}_{-2}$ | 10.9 | $> 99.9$ |
| Fe K$\alpha$ | $6.43^{+0.04}_{-0.03}$ | 6.4 | $14.0^{+6.7}_{-4.2}$ | $< 117$ | $25^{+12}_{-8}$ | 52.9 | — |
| Fe XXV-XXVI | $7.57^{+0.19}_{-0.12}$ | $6.7 - 6.97$ | $-8.9^{+6.0}_{-4.7}$ | $209^{+244}_{-108}$ | $-26^{+18}_{-12}$ | 16.6 | 99.3 |

$^*$ Denotes parameter was fixed at listed value

lower energy profile at $E = \left(7.36^{+0.09}_{-0.11}\right)$ keV (rest-frame; $E = 6.92$ keV observed) which may be indicative of some finer velocity structure in the outflow.

## 3.4 Photo-ionisation modelling

With both the general continuum and absorption lines parametrised, I replaced the simple parametrising absorbers (i.e., `zpcfabs` and `zwabs`) with a series of self-consistent grid models generated using the XSTAR photo-ionisation code. Each XSTAR grid contained a series of models, each pertaining to a particular photo-ionised spectrum with a characteristic ionisation parameter ($\xi$), a column density ($N_{\rm H}$), and a red-shift ($z$). In addition, each grid is attributed an intrinsic turbulent velocity ($v_{\rm turb}$) upon generation which modifies the intrinsic width of the atomic lines with the effects of Doppler broadening. Once generated, the XSTAR grid is used as a simple multiplicative model in XSPEC to simultaneously and self-consistently model the broad-band continuum

and any spectral lines which may be present in the X-ray spectrum.

### 3.4.1 Fully-covering absorption models

I initially modelled the spectrum under the assumptions that the photo-ionised absorbers fully cover the view to the ionising source, and that the soft-excess at $E < 1\,\mathrm{keV}$ was attributable to an intrinsic continuum component. I sequentially added XSTAR grids to a baseline continuum model of the form

$$N_H^{\mathrm{Gal}} \times (\texttt{cutoffpl} + \texttt{diskbb} + \texttt{zgauss}) \times \mathrm{XSTAR} \tag{3.1}$$

until an acceptable fit had been achieved. Solar abundances (Grevesse & Sauval 1998) were assumed throughout unless otherwise is explicitly stated.

#### Soft X-rays

In the soft X-ray band two low turbulence ($v_{\mathrm{turb}} = 200\,\mathrm{km\,s^{-1}}$) absorbers are required to get a good fit to both the Fe UTA absorption line and the general spectral curvature below 10 keV (see Fig. 3.5). The first absorber (Zone 1A; $\Delta\chi^2/\Delta\nu = 93.7/3$) is lowly ionised and mainly responsible for the Fe UTA, while the second absorber (Zone 2A; $\Delta\chi^2/\Delta\nu = 36.9/2$) fits the curvature. These absorbers also imprint a shallow Fe K-shell edge at $E \sim 7.1\,\mathrm{keV}$, however its depth is insufficient to adequately replicate the entirety of the higher-energy absorption trough (see §3.4.1). For fitting purposes Zones 1A and 2A were assumed to be co-spatial and their common outflow velocity was fixed to $v_{\mathrm{out}} = 300\,\mathrm{km\,s^{-1}}$ to be consistent with the UV outflows reported in this source by Monier et al. (2001). Allowing their outflow velocities to vary independently did not yield any appreciable change in the fit statistic and they were thus left fixed throughout.

While they provide a good fit to the Fe UTA and the broad-band spectral curvature, absorption Zones 1A and 2A do not account for the absorption line present at $\sim 1.3\,\mathrm{keV}$ (see Fig. 3.5) which suggests that there may be additional zones of gas comprising the warm absorber. Even so, the addition of more absorbers only yielded a negligible

improvement to the fit and subsequent XSTAR tables were still unable to account for the observed residual profile. There are a number of reasons that the line at $\sim 1.3\,\mathrm{keV}$ could be difficult to account for with XSTAR. Should the line represent a blend of inner-shell Mg transitions the lines are likely very sensitive to the distribution of photons in the continuum. In this scenario an input continuum for the XSTAR grid which is too hard (i.e., a continuum with too many high energy photons) could over-ionise the inner-shell lines and therefore reduce their contribution in the model when using XSTAR. This possibility is investigated further in §3.4.2, where more complex absorption geometries are considered.

Alternatively, if the line is associated with Fe XXIII-XXV the observed profile could be due to a zone of absorption which is spatially distinct from the traditional soft X-ray warm absorber. In this case the absorber may be located at smaller radii than the more distant gas and thereby be characterised by higher ionisation. Indeed, due to the breadth of the profile a phenomenologically valid solution for the $\sim 1.3\,\mathrm{keV}$ line can be obtained using a high turbulence (i.e., $v_{\mathrm{turb}} = 5,000\,\mathrm{km\,s^{-1}}$) XSTAR table with $N_{\mathrm{H}} \sim (5-6)\times10^{21}\,\mathrm{cm^{-2}}$, $\log(\xi/\mathrm{erg\,cm\,s^{-1}}) \sim 3$ and an outflow velocity of $v_{\mathrm{out}} \sim 40,000\,\mathrm{km\,s^{-1}}$. This is consistent with the line being identified with Fe XXIII-XXV which suggests that such a solution may be plausible. Interestingly, the solution also contributes shallow absorption at Fe K — likely due to Fe XXV — but, again, it is too shallow to model the entire broad trough. Even so, it is important to note that this solution is being driven by the requirement of fitting the broad line at $\sim 1.3\,\mathrm{keV}$ rather than the Fe K profile itself, and that the validity of the solution is strongly dependent on the order in which the absorbers are added to the model. For example, should the absorption trough at Fe K be fitted first then the line at $E \sim 1.3\,\mathrm{keV}$ can no longer be accounted for with the above XSTAR table. Due to these caveats, in addition to the inherent ambiguity with regards to whether the line is actually inner-shell Mg or moderately-ionised Fe, the $\sim 1.3\,\mathrm{keV}$ line profile was left modelled with a Gaussian.

Table 3.4: MR 2251−178: Fully covering model parameters

| **Best-fit model components** | | | |
|---|---|---|---|
| Component | Parameter | Value | $\Delta\chi^{2\,h}$ |
| Galactic absorption | $N_H^{\mathrm{Gal}\,\dagger}$ | $2.42 \times 10^{20}$ | — |
| `cutoffpl` | $\Gamma$ | $1.63 \pm 0.01$ | — |
| | $E_{\mathrm{cut}}^{f}$ | $65^{+8}_{-6}$ | |
| `reflionx` | Abund | $1^{*}$ | $77.2^{\,i}$ |
| | $\xi^{\,f}$ | $< 27$ | |
| | $R^{\ddagger}$ | $< 0.2$ | |
| `diskbb` | $T_{\mathrm{in}}^{c}$ | $68^{+4}_{-4}$ | 114.6 |
| | norm | $\left(7.69^{+6.79}_{-3.45}\right) \times 10^5$ | |
| `Gaussian` | $E^{d}$ | $1.29^{+0.01}_{-0.01}$ | 60.7 |
| | $EW^{e}$ | $-5^{+1}_{-1}$ | |
| | intensity | $-38.5^{+7.1}_{-7.1}$ | |
| Soft X-ray 1 | $N_{\mathrm{H}}^{\dagger}$ | $(5.4 \pm 0.4) \times 10^{20}$ | 93.7 |
| (Zone 1A) | $\log(\xi)^{\,f}$ | $-0.23^{+0.10}_{-0.12}$ | |
| | $v_{\mathrm{out}}^{g}$ | $300^{\,*}$ | |
| Soft X-ray 2 | $N_{\mathrm{H}}^{\dagger}$ | $\left(5.6^{+1.3}_{-2.1}\right) \times 10^{21}$ | 36.9 |
| (Zone 2A) | $\log(\xi)^{\,f}$ | $2.21^{+0.08}_{-0.07}$ | |
| | $v_{\mathrm{out}}^{g}$ | $300^{\,*}$ | |
| S XV | $N_{\mathrm{H}}^{\dagger}$ | $\left(8.9^{+1.4}_{-3.7}\right) \times 10^{21}$ | 76.4 |
| (Zone 3A) | $\log(\xi)^{\,f}$ | $2.44^{+0.24}_{-0.22}$ | |
| | $v_{\mathrm{out}}^{g}$ | $6,300^{+5,100}_{-4,200}$ | |
| S XVI | $N_{\mathrm{H}}^{\dagger}$ | $> 1.0 \times 10^{22}$ | 32.9 |
| (Zone 4A) | $\log(\xi)^{\,f}$ | $3.37^{+0.12}_{-0.41}$ | |
| | $v_{\mathrm{out}}^{g}$ | $21,000^{+3,000}_{-3,000}$ | |
| Fe XXV-XXVI | $N_{\mathrm{H}}^{\dagger}$ | $\left(1.03^{+1.43}_{-0.54}\right) \times 10^{22}$ | 15.1 |
| (Zone 5A) | $\log(\xi)^{\,f}$ | $3.84^{+0.37}_{-0.17}$ | |
| | $v_{\mathrm{out}}^{g}$ | $30,300^{+2,700}_{-3,000}$ | |

[*] Indicates parameter was frozen at this value;
[†] Absorber column density in units of $\mathrm{cm}^{-2}$;
[‡] Fraction of reflected flux, see text for details;
[b] Power-law cut-off energy in units of keV;
[c] Accretion disc black body temperature, in units of eV;
[d] Absorption line centroid energy, in units of keV;
[e] Absorption line equivalent width, in units of eV;
[f] Ionisation parameter in units of $\mathrm{erg\,cm\,s^{-1}}$;
[g] Outflow velocity of absorber given in units of $\mathrm{km\,s^{-1}}$;
[h] Significance of component with respect to the final best-fitting model;
[i] Statistical significance of `reflionx` component is given in comparison to a fit where Fe K$\alpha$ is left unmodelled;
[j] Line intensity, in units of $\mathrm{photons\,cm^{-2}\,s^{-1}}$.

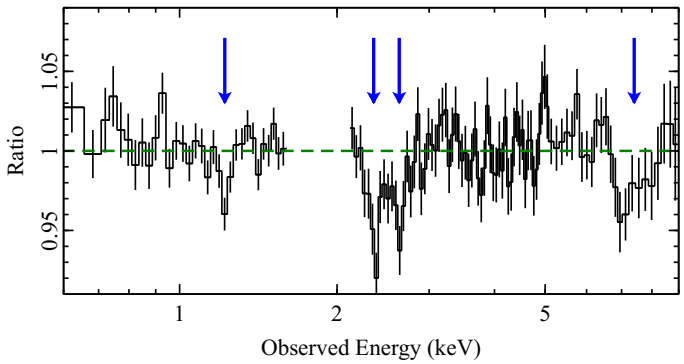


Figure 3.5: Residuals of the XIS-FI data when fitted with two lowly ionised soft X-ray absorbers. The position of the suspected Fe L/Inner-Mg, S XV, S XVI and Fe XXV-XXVI absorption lines are identified. For clarity, the XIS-BI data have again been omitted. Data between 1.6-2.1 keV have been removed due to the instrumental Si K edge. See text for further details.

### sulphur

The physical interpretation of the lines at 2.52 keV and 2.79 keV was also quite uncertain. In particular, a satisfactory fit to the lines could not be obtained assuming solar abundances, and the lack of other discrete absorption features meant that the necessary over-abundance of sulphur was entirely unconstrained due to the degeneracy between column density and ionic abundance. To probe the likely physical conditions of the absorbing gas I thus parametrised the lines using a column density comprising solely of sulphur ($N_{\rm S}$) at solar abundances. As discussed previously in §3.3.2, the most conservative interpretation is that the two profiles are identified with the K$\alpha$ transitions of He- and H-like sulphur, respectively. For this interpretation the lines are well modelled by the addition of two further ionised absorbers. The first (Zone 3A), which models S XV at $\sim 2.5$ keV, is described by $\log(\xi/{\rm erg\,cm\,s^{-1}}) = 2.44^{+0.24}_{-0.22}$ and a sulphur column density of $N_{\rm S} = \left(1.9^{+0.3}_{-0.8}\right) \times 10^{17}\,{\rm cm^{-2}}$. For a solar sulphur/hydrogen abundance ratio of $2.14 \times 10^{-5}$ (Grevesse & Sauval 1998) this corresponds to a hydrogen column of $N_{\rm H} = \left(8.9^{+1.4}_{-3.7}\right) \times 10^{21}\,{\rm cm^{-2}}$, which is similar to the column densities reported previously for this source (i.e., Orr et al. 2001; Kaspi et al. 2004; Gibson et al. 2005; Ramírez et al. 2008). The net outflow velocity of this absorber

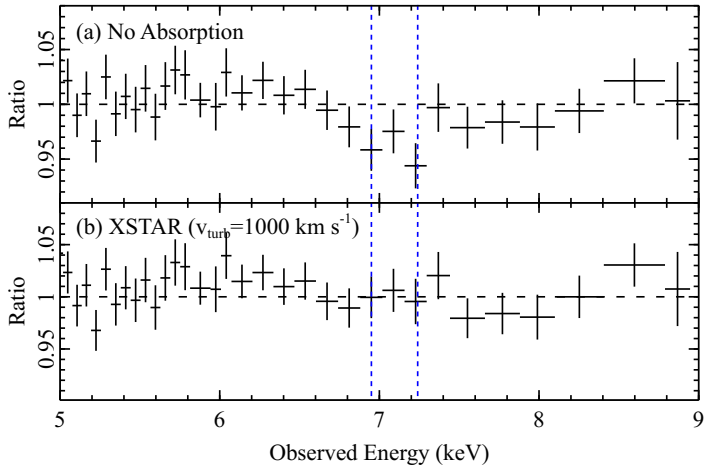


Figure 3.6: Ratio plots showing the residuals which remain in the Fe K band when fitting the continuum with a fully-covering absorption interpretation. The vertical dashed lines (blue) indicate the positions of the suspected Fe XXV He$\alpha$ and Fe XXVI Ly$\alpha$ absorption profiles. In panel (a) no additional absorption is included and there are two residual profiles present. As shown in panel (b) a highly-ionised absorption table accounts for profiles simultaneously. See text for further details.

is $v_{\rm out} = \left(6,300^{+5,100}_{-4,200}\right)\,{\rm km\,s^{-1}}$, which was consistent with that found when fitting simple Gaussians. At this column density and ionisation parameter the grid also contributes He$\beta$ ($1s \rightarrow 3p$) and weak He$\gamma$ ($1s \rightarrow 4p$) lines in addition to the strong K$\alpha$, however the energy separation of the additional lines was insufficient to simultaneously fit the residuals which remained at $\sim 2.8\,{\rm keV}$ and a second grid is required. This second absorber (Zone 4A; $\Delta\chi^2 = 32.9$) is described by $N_{\rm S} > 2.2 \times 10^{17}\,{\rm cm^{-2}}$ (equivalent to $N_{\rm H} > 1 \times 10^{22}\,{\rm cm^{-2}}$) and $\log(\xi/{\rm erg\,cm\,s^{-1}}) = 3.37^{+0.12}_{-0.41}$. The outflow velocity is $v_{\rm out} = (21,000 \pm 3,000)\,{\rm km\,s^{-1}}$, which is again consistent with that found from simple Gaussian fitting.

### The Fe K band

While the soft X-ray absorbers (i.e., Zones 1A and 2A) contribute a shallow Fe K-shell edge at $\sim 7.1\,{\rm keV}$ there are still significant absorption residuals present in the Fe K band. Consistent with what was found from Gaussian fitting previously the Fe K

absorption appears to comprise two discrete profiles at rest-frame energies of $E \sim 7.43$ and $\sim 7.69\,\mathrm{keV}$, respectively. While there remains some uncertainty regarding the identification of the individual profiles by virtue of the $\sim 1.3\,\mathrm{keV}$ line — which may also be due to Fe — the presence of two profiles at Fe K with an energy separation equal to that expected for Fe XXV He$\alpha$ and Fe XXVI Ly$\alpha$ implies an association with these ions from the same layer of absorbing gas (see Fig. 3.6, top panel). Indeed, both profiles can be accounted for simultaneously using a single XSTAR absorber (Fig. 3.6, bottom panel) for $\Delta\chi^2/\Delta\nu = 15.1/3$, which lends weight to the conservative identification. From XSTAR the absorbing gas is characterised by $N_\mathrm{H} = \left(1.03^{+1.43}_{-0.54}\right) \times 10^{22}\,\mathrm{cm}^{-2}$ and $\log(\xi/\mathrm{erg\,cm\,s}^{-1}) = 3.84^{+0.37}_{-0.17}$, with an outflow velocity of $v_\mathrm{out} = \left(30, 300^{+2,700}_{-3,000}\right)\,\mathrm{km\,s}^{-1}$.

#### Reflection component

For additional self-consistency I replaced the Gaussian line which had thus far been modelling the Fe K$\alpha$ fluorescent emission with the `reflionx` ionised reflection model (Ross & Fabian 2005a) which self-consistently takes into account any reprocessing due to reflection in a face-on system. Fixed Solar abundances were assumed and the photon-index of the reflected power-law was tied to that of the intrinsic power-law. The addition of a lowly ionised ($\xi < 27\,\mathrm{erg\,cm\,s}^{-1}$) reflection component with a low reflection fraction ($R < 0.2$, where $R = \Omega/2\pi$ and $\Omega$ is the solid angle subtended by the reflector) reproduces the observed Fe K$\alpha$ profile and improves the fit in the hard X-ray band, yielding a final fit statistic for the fully-covering absorption model of $\chi^2/\nu = 295.5/253$ ($\chi^2_\mathrm{reduced} = 1.17$). The overall best-fit model parameters for the fully-covering model are listed in Table 3.4. The parameters of the continuum are noted in Table 3.5.

### 3.4.2 Partially-covering absorption models

Partially-covering absorption scenarios have typically been used in the literature as means of fitting prominent hard X-ray excesses (e.g., NGC 1365, Risaliti et al. 2009; 1H 0419-577, Turner et al. 2009; PDS 456, Reeves et al. 2009), with such models typically

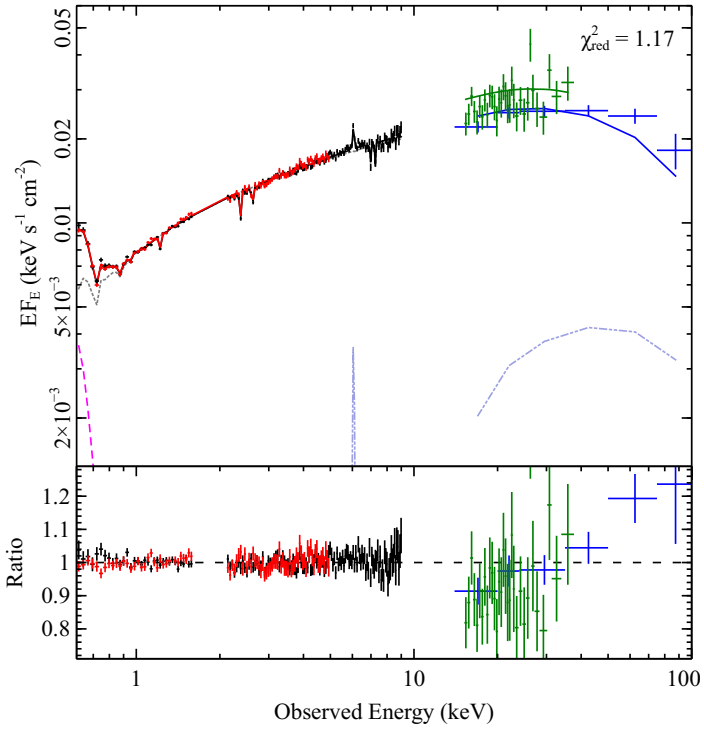


Figure 3.7: Unfolded spectrum showing the best-fit fully-covering model for MR 2251−178. Data for the XIS-FI (black), XIS-BI (red), HXD/PIN (green) and *Swift* BAT (blue) are shown. *Top*: Unfolded broad-band spectrum between 0.6 − 150 keV along with the contribution of various spectral components. The primary power-law, `diskbb` and reflection component are denoted by the dotted (grey), dashed (magenta) and dash-double-dotted (pale blue) lines, respectively. The solid lines correspond to the best-fitting model for each respective dataset. *Bottom*: Corresponding data/model residuals. The fully-covering model provides a reasonable fit to the spectrum below 10 keV but does not correctly account for the hard X-ray data. See text for further discussion.

requiring the intrinsic source flux below 10 keV to be strongly absorbed by clumps of Compton-thick material (i.e., $N_{\rm H} > 10^{24}\,{\rm cm}^{-2}$). However, should the partially covering clouds be Compton-thin then the absorption-dominated models can also replicate the appearance of the soft excess, and, in the context of the MR 2251−178 spectrum, may also provide a means of self-consistently fitting the roll-over present in the hard X-ray data without needing an ad-hoc cut-off. Moreover, should a partially-covering interpretation

Table 3.5: MR 2251−178 intrinsic continuum parameters.

| Model | Flux[a] | | Luminosity[b] | |
|---|---|---|---|---|
| | $F_{0.6-2.0}$ | $F_{2.0-10.0}$ | $L_{0.6-2.0}$ | $L_{2.0-10.0}$ |
| Fully-covering | $3.0 \times 10^{-11}$ | $4.5 \times 10^{-11}$ | $2.83 \times 10^{44}$ | $4.41 \times 10^{44}$ |
| Partial-covering | $5.1 \times 10^{-11}$ | $6.4 \times 10^{-11}$ | $5.97 \times 10^{44}$ | $7.42 \times 10^{44}$ |

[a] observed source flux in the $0.6 - 2.0$ keV and $2.0 - 10.0$ keV energy bands, given in units of erg cm$^{-2}$ s$^{-1}$;
[b] unabsorbed source luminosity between $0.6 - 2.0$ keV and $2.0 - 10.0$ keV, given in units of erg s$^{-1}$

prove viable it may allude to a more appropriate power-law slope for the XSTAR tables, which could yield a more suitable fit to the soft X-ray warm absorber and the line at $\sim 1.3$ keV.

In such an absorption geometry the partially covering clouds would need to be very compact in size and located close to the ionising source so as to only obscure a fraction of the emergent continuum. One possibility is that the partial coverer may be associated with a clumpy disc-wind, where the covering fraction relates to the filling factor of the denser clouds, while the more ionised absorbers appear to fully cover the source along the line-of-sight by virtue of being located further from the ionising source. Absorption dominated models have been effective in explaining the broad-band spectral properties of objects such as MCG -6-30-15 (Miller, Turner & Reeves 2008) and 3C 445 (Reeves et al. 2010), and are consistent with the theoretical expectations that disc-winds are inhomogeneous outflows which contain clumps of dense high column-density material (e.g., Proga & Kallman 2004; Sim et al. 2010). For these reasons, I also considered the possibility that there may be one or more partially-covering absorption components present in MR 2251−178.

Initially, I constructed the partially-covering model assuming two co-spatial partially-covering absorbers and two co-spatial distant absorbers:

$$N_H^{\rm Gal} \times (\texttt{powerlaw}_1 + \texttt{reflionx} + \texttt{powerlaw}_2 \times \mathrm{XSTAR}_{\rm pcov1} + \texttt{powerlaw}_3 \times \mathrm{XSTAR}_{\rm pcov2}) \times \mathrm{XSTAR}_{\rm 1B} \times \mathrm{XSTAR}_{\rm 2B} \quad (3.2)$$

where $\texttt{powerlaw}_2$ and $\texttt{powerlaw}_3$ are the partially-covered components of the intrinsic emission and $\texttt{powerlaw}_1$ represents the continuum which leaks through the absorption layers. The distant absorbers, $\mathrm{XSTAR}_{\rm 1B}$ and $\mathrm{XSTAR}_{\rm 2B}$, provide good fits to the Fe UTA and the spectral curvature below 10 keV, while the `reflionx` component was retained to account for the Fe K$\alpha$ emission line. The three strong absorption lines at $E \sim 1.3$ keV, $\sim 2.5$ keV and $\sim 2.8$ keV are still present in the data but, as was the case in the fully-covering model, an unambiguous fit could not be found with XSTAR. For simplicity, these lines were therefore modelled using Gaussians yielding parameters consistent with those obtained previously (see Table 3.3). The best-fit partially-covering model, including the relative contributions of the various spectral components and the associated data/model residuals, are shown in Fig. 3.8.

In this model the intrinsic continuum is described by a $\Gamma = 2.09 \pm 0.01$ power-law, with the softer $\Gamma$ providing a much better fit to the hard X-ray data. The PIN data in particular are especially well fitted, with the model providing a better representation of the source flux between $15 - 50$ keV. Both of the partially-covering absorbers cover in the range of $\sim 30 - 40\%$ of the continuum with a moderate-to-high column of gas, while the two fully-covering distant absorbers have parameters which are similar to those obtained in the fully-covering interpretation (see Table 3.6). Furthermore, the increased absorption also provides a good fit to the soft X-ray data which demonstrates another case in which the soft-excess may be a manifestation of absorption rather than an intrinsic continuum component (c.f., Miller, Turner & Reeves 2009). Overall, the model provides an excellent fit to the broad-band *Suzaku* spectrum yielding a final fit statistic of $\chi^2/\nu = 260.1/253$ ($\chi^2_{\rm reduced} = 1.03$; see Fig. 3.8).

### The Fe K region

The partially-covering model yields a significantly different interpretation to the Fe K region than the fully-covering one. The residual absorption profiles which were present at

Table 3.6: Best-fit parameters for the partially-covering model of MR 2251−178.

| **Partial-covering model** | | | |
|---|---|---|---|
| Component | Parameter | Value | $\Delta\chi^{2\,e}$ |
| Galactic absorption | $N_{\rm H}^{Gal\,\dagger}$ | $2.42 \times 10^{20}$ | ··· |
| `powerlaw` | $\Gamma$ | $2.09 \pm 0.01$ | ··· |
| `reflionx` | Abund | $1^{\,*}$ | $45.0^{\,f}$ |
| | $\xi^{\,c}$ | $< 6.45$ | |
| | $R$ | $< 0.2$ | |
| Partial-coverer 1 | $N_{\rm H}^{\dagger}$ | $\left(6.60^{+0.29}_{-0.28}\right) \times 10^{23}$ | 234.4 |
| (Zone pcov1) | $\log(\xi)^{\,c}$ | $1.37^{+0.16}_{-0.16}$ | |
| | $v_{\rm out}^{d}$ | $0^{*}$ | |
| | $f_{\rm cov}$ | $\left(36^{+3}_{-2}\right)\,\%$ | |
| Partial-coverer 2 | $N_{\rm H}^{\dagger}$ | $\left(6.33^{+0.26}_{-0.28}\right) \times 10^{22}$ | 146.3 |
| (Zone pcov2) | $\log(\xi)^{\,c}$ | $1.96^{+0.04}_{-0.05}$ | |
| | $f_{\rm cov}$ | $\left(32^{+1}_{-3}\right)\,\%$ | |
| | $v_{\rm out}^{d}$ | $0^{*}$ | |
| Soft X-ray 1 | $N_{\rm H}^{\dagger}$ | $\left(1.64^{+0.04}_{-0.05}\right) \times 10^{21}$ | 104.8 |
| (Zone 1B) | $\log(\xi)^{\,c}$ | $0.98^{+0.02}_{-0.02}$ | |
| | $v_{\rm out}^{d}$ | $< 1200$ | |
| Soft X-ray 2 | $N_{\rm H}^{\dagger}$ | $\left(5.40^{+0.91}_{-1.12}\right) \times 10^{21}$ | 33.4 |
| (Zone 2B) | $\log(\xi)^{\,c}$ | $2.84^{+0.06}_{-0.07}$ | |
| | $v_{\rm out}^{d}$ | $< 1200^{*}$ | |

[*] Indicates parameter was frozen at this value;
[†] Absorber column density, in units of $\rm cm^{-2}$;
[c] Ionisation parameter, in units of $\rm erg\,cm\,s^{-1}$;
[d] Outflow velocity of absorber given in units of $\rm km\,s^{-1}$;
[e] Significance of component when removed from the best-fitting model;
[f] Statistical significance of `reflionx` component is given in comparison to a fit where Fe K$\alpha$ is left unmodelled.

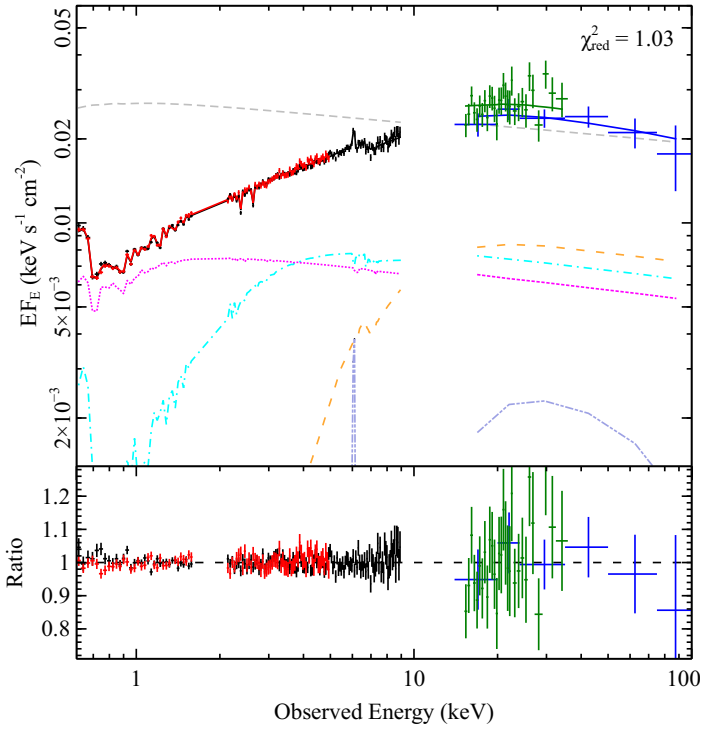


Figure 3.8: Unfolded spectrum showing the best-fit partial covering model for MR 2251−178. *Top*: As in Fig. 3.7 the top panel shows the unfolded broad-band spectrum. The dash-dotted (cyan) and dashed (orange) lines show the contribution of partial covering components 3B and 4B, respectively, while the dotted (magenta) line shows the continuum which leaks through both absorption layers. The reflection component is denoted by the dash-double-dotted (pale blue) line. *Bottom*: Corresponding data/model residuals. Overall, the partial covering model provides a very good description to the *Suzaku* observation. The dashed grey line shows the intrinsic continuum in MR 2251−178 when all absorbers and the reflection component have been removed.

$E \sim 7.39$ keV and $E \sim 7.69$ keV in the fully-covering model are no longer necessary, with all of the residuals at Fe K being accounted for by an ionised Fe K-shell edge imparted by the larger columns of absorbing gas (see Fig. 3.9c,d). Visually, both the fully- and partial-covering models provide good fits to the Fe K band, with neither model showing any additional residuals. If both models are considered between just $5-9$ keV to isolate the Fe K band the fits are also similar statistically, with $\chi^2_{\rm pcov} = 54.3/37$ and $\chi^2_{\rm fcov} = 47.8/36$,

which is insufficient to conclusively decide towards a more 'correct' model. Therefore, the presence and intensity of the Fe K band absorption lines in MR 2251−178 is dependent on the interpretation of the broad-band spectrum.

## 3.5 *Suzaku* discussion

### 3.5.1 The soft excess

The *Suzaku* spectrum has demonstrated that the soft-excess in MR 2251−178 can be adequately modelled as either an intrinsic component of the emergent X-ray continuum or as the side effect of an absorption dominated spectrum. While the fully-covering absorption model provides a statistically acceptable fit to the data, it comes with the caveat that it parametrised the soft-excess as the thermal emissions from a geometrically thin accretion disc using the `diskbb` model. This approach is simple and generally provides good fits to soft-excesses in a wide range of objects, however such an interpretation typically requires a seed thermal continuum with a temperature higher than that which is expected for geometrically thin accretion discs (e.g., Shakura & Sunyaev 1973; Porquet et al. 2004b; Gierliński & Done 2004). As previously shown in eq. (1.14) the expected temperature at radius $r$ for a geometrically thin accretion disc can be approximated by

$$T(r) \approx 3.5 \times 10^7 \eta^{-\frac{1}{4}} \left(\frac{\dot{M}}{\dot{M}_{\rm edd}}\right)^{\frac{1}{4}} \left(\frac{M_{\rm BH}}{M_\odot}\right)^{-\frac{1}{4}} \left(\frac{r}{r_{\rm s}}\right)^{-\frac{3}{4}} K. \tag{3.3}$$

For $(\dot{M}_{\rm acc}/\dot{M}_{\rm edd}) \sim 0.15$ (see later) and $M_{\rm BH} \simeq 2.4 \times 10^8 M_\odot$ (Dunn et al. 2008) appropriate for MR 2251−178, and assuming that most of the emission originates at the ISCO of a non-spinning Schwarzschild black hole (i.e., $r = r_{\rm isco} = 3r_{\rm s}$ and $\eta = 0.06$), yields $kT \approx 20\,{\rm eV}$. This is roughly 3 times cooler than the best-fitting `diskbb` temperature ($kT \sim 62\,{\rm eV}$). Another scenario is that the black hole in MR 2251−178 could be spinning. However, even a maximally spinning Kerr black hole (i.e., one with $r_{\rm isco} = 0.62\,r_s$ and $\eta \simeq 0.32$) yields a temperature similar to the standard slim disc to within a factor of 2, which is still below the temperature measured with the `diskbb` at the 90% level. A

spinning but inefficiently accreting black hole could remain plausible but it is important to note that the main observational characteristic of a spinning black hole, e.g., the reflection component and the (broad) Fe K emission component, are either relatively weak or un-observed in MR 2251−178 which makes such a scenario unlikely. Therefore, it appears as though the soft excess in MR 2251−178 cannot easily be attributed to the thermal emission of the disc without additional modification.

The soft excess could also be the Wien tail of lower energy photons from the accretion disc which have been Comptonised by a hot corona located above the plane of the disc (e.g., Czerny & Elvis 1987; Haardt & Maraschi 1991, 1993; Nayakshin, Kazanas & Kallman 2000; Nayakshin 2001). If the distribution of electrons in such a Comptonising corona is quasi-Maxwellian (i.e., has both a thermal and non-thermal component; see Coppi 1999), it may be able to produce both the hard X-ray power-law continuum for which it is typically invoked, as well as the soft excess. To see whether this interpretation was feasible I replaced the `diskbb` component in the best-fitting fully-covering model with `comptt` (Titarchuk 1994). The thermal temperature of the input accretion disc photons were fixed to the theoretically expected $kT \approx 20\,\mathrm{eV}$, while the red-shift was fixed to that of the source. The resulting fit was statistically comparable to that obtained when using `diskbb` ($\chi^2/\nu = 335.1/308$), and the other model parameters were all also consistent with the previous model. The Comptonising electron temperature is found to be $kT < 5.3\,\mathrm{keV}$ and the optical depth of the corona is $\tau \sim 0.40^{+0.14}_{-0.36}$.

Another explanation which has been proposed for soft-excesses in general is that they may be the result of ionised reflection from optically thick matter in the nuclear regions of the AGN, e.g., the accretion disc, the broad line region (BLR) or the molecular torus. However, due to the lack of a strong ionised reflection component, the weak Fe K$\alpha$ line, and the absence of a broadened iron line, this seems unlikely in the case of MR 2251−178.

Therefore, the soft-excess in MR 2251−178 is phenomenologically well modelled by either a thermal accretion disc blackbody or as the result of the Comptonisation of soft thermal photons from the accretion disc. However, the partial-covering interpretation is also capable of replicating the soft-excess as the by-product of complex absorption, albeit

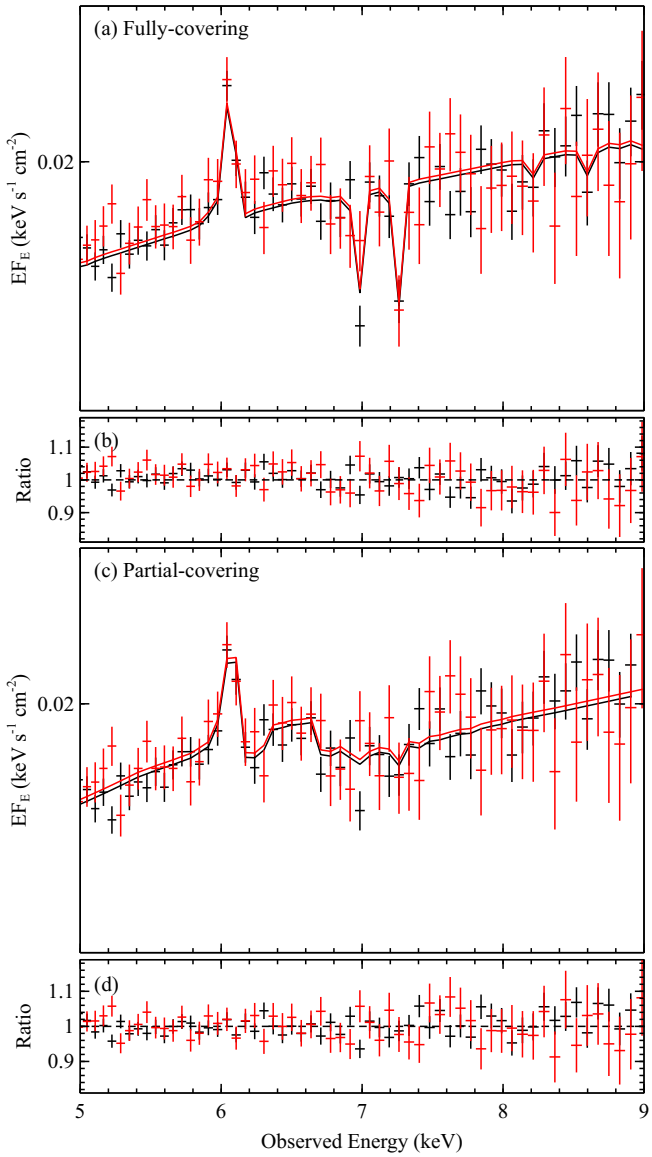


Figure 3.9: Plots showing a comparison of the fit to the Fe K band in both the fully- and partially-covering models, highlighting the radically different spectral interpretations of the hard-band data. Panels correspond to: (a) unfolded and enlarged view of the X-ray spectrum in the Fe K band of the fully-covering absorption model; (b) data/model residuals for the fully-covering model; (c) unfolded and enlarged view of the Fe K band when spectrum fitted with a partially-covering absorption model; (d) data/model residuals for the partially-covering model. See text for further details.

with a steeper power-law photon index, i.e., $\Gamma \sim 2.1$, which is similar to the value found commonly for other radio-quiet quasars (e.g., Porquet et al. 2004b). The lack of a strong ionised reflection component above 10 keV and the absence of a broadened Fe K$\alpha$ line suggests than an origin through blurred reflection is unlikely.

### 3.5.2 The Fe K$\alpha$ line

From past observations there has been significant uncertainty in the reported *EW* of the Fe K$\alpha$ emission in MR 2251−178: i.e., $125^{+100}_{-105}$ eV (*Ginga*; Mineo & Stewart 1993), $190^{+140}_{-95}$ eV (*ASCA*; Reynolds 1997), $62^{+12}_{-25}$ eV, (*BeppoSAX*; Orr et al. 2001) $53 \pm 20$ eV (*XMM-Newton*; Kaspi et al. 2004) and $23^{+14}_{-13}$ eV (*Chandra*; Gibson et al. 2005). This uncertainty may be due to the previous observations lacking the spectral resolution and $S/N$ in the Fe K band in order to resolve the absorption feature blue-ward of the Fe K$\alpha$ – be it due to discrete resonant Fe XXV He$\alpha$ and Fe XXV Ly$\alpha$ absorption or an ionised Fe K-shell edge – which may have artificially broadened the measured *EW* of the Fe K emission line. Incidentally, it is interesting to note that the two observations thus far which have reported the possible presence of highly-ionised Fe K absorption (i.e., this work and Gibson et al. 2005) have also reported the tightest constraint on the Fe K$\alpha$ *EW*.

Even so, the Fe K$\alpha$ *EW* found in the *Suzaku* spectrum is still below average. Based on an archival study of 36 sources in the *Chandra* HETG archive (which includes MR 2251−178) Shu, Yaqoob & Wang (2010) have reported the narrow core of the Fe K$\alpha$ emission line has a weighted mean *EW* of $(70 \pm 4)$ eV, which is substantially broader than that which is found in this work. Furthermore, from their large *Suzaku* study of nearby Seyfert galaxies Fukazawa et al. (2011) have found a mean Fe K$\alpha$ *EW* of around 55 eV for sources which are absorbed by column densities similar to MR 2251−178 (i.e., $N_{\rm H} \lesssim 10^{22-23}\,{\rm cm}^{-2}$). Given that MR 2251−178 is a highly X-ray luminous AGN, the apparent weakness of the Fe K$\alpha$ line could be a result of the 'X-ray Baldwin Effect' — an apparent anti-correlation between source X-ray luminosity and the *EW* of the Fe K$\alpha$ line — which has been well documented in the literature (e.g., Iwasawa & Taniguchi

1993; Page et al. 2004; Jiang, Wang & Wang 2006; see also Shu, Yaqoob & Wang 2010 and Fukazawa et al. 2011). Given that MR 2251−178 has a FR I radio morphology it could also be due to a dilution of the observed X-ray spectrum by an X-ray component emitted in a radio-jet. The radio-loudness of an object is typically given in terms of the radio-loudness parameter, $R_{\rm L} = \log(F_{5\,\rm GHz}/F_{4400\rm \AA})$, where $F_{5\,\rm GHz}$ is the monochromatic radio flux at 5 GHz and $F_{4400\rm \AA}$ is the optical flux at $\lambda = 4400$Å. In this regime, objects where $R_{\rm L} > 1$ are regarded as radio-loud, while those where $R_{\rm L} < 1$ are radio-quiet. For MR 2251−178 $R_{\rm L} = -0.43$ (Reeves & Turner 2000) which suggests that any radio-jet in the source is very weak and therefore is unlikely to contribute in the X-ray band.

Alternatively, the weakness of the Fe K$\alpha$ emission may be due to the inner accretion disc being shielded by circumnuclear material. Such a scenario could also explain the lack of a strong ionised reflection component because the observed reflection would have to originate at larger distances from the central engine, i.e., the BLR or the torus, in order to be observed. Sim et al. (2010) have also recently shown that Fe K$\alpha$ emission can originate via reflection from dense material in an outflowing wind (with $EW \sim 10$s of eV), which may also be applicable here if the source is partially-covered by a stratified complex absorber, while Miller et al. (2010) and Yaqoob et al. (2010) have both shown that the $EW$ of Fe K$\alpha$ can become suppressed in the presence of absorbers with column densities similar to those found here.

## 3.6 Follow-up observations

Prompted by the ambiguities which remained following the *Suzaku* observation an extensive semi-contemporaneous observing campaign of MR 2251−178 was conducted using *XMM-Newton* and *Chandra* (with PI: J. N. Reeves, Co-I: J. Gofford and others). The primary goals of this campaign were to address the following:

1. **Establish the origin of the line at $\sim 1.3$ keV**. At the energy resolution of the *Suzaku* CCDs the line is unresolved and can conceptually be due to either a blend of $2s \rightarrow 3p$ Fe L-shell transitions outflowing with $v_{\rm out} \sim 0.1\,$c, or due to a

blend of inner-shell Mg lines with a more modest $v_{\rm out}$ of a few hundred $\rm km\,s^{-1}$. Because of the difference in outflow velocity the correct identification of the line will have strong effects on the inferred source energetics (which are $\propto v_{\rm out}^3$). Using the much higher spectral-resolution offered by the *XMM-Newton* RGS and the *Chandra* HETG grating spectrometers the line would be resolved into its individual constituent profiles, and therefore resolve the ambiguity.

2. **Further probe the origin of the lines at $\sim 2.5$ keV and $\sim 2.8$ keV**. From the *Suzaku* data these lines have been conservatively identified with He- and H-like sulphur at different outflow velocities, but a self-consistent fit to the lines using XSTAR was not found for either the fully- or partially-covering models. Obtaining such a fit would enable the properties and energetics of an additional absorption layer to be constrained, which would further elude to the inner structure of the AGN in MR 2251−178. The grating instruments aboard *XMM-Newton* and *Chandra* will offer a higher resolution view of these lines, which should enable them to be probed in greater detail.

3. **Investigate the validity and robustness of the partially-covering interpretation**. The *Suzaku* data showed that a complex absorption geometry in which a soft $\Gamma \sim 2.1$ continuum is partially-covered by multiple layers of clumpy gas could, in principle, be responsible for the properties of the broad-band spectrum in MR 2251−178 (i.e., both the soft-excess and the hard X-ray data). However, on the basis of the *Suzaku* data alone the viability of such a model remains an open question. The data obtained from the *XMM-Newton* and *Chandra* observations, in conjunction with archival data, would allow the partial-covering model to be tested over multiple epochs as a means of fitting long-term spectral variability. The high-resolution view of the warm absorber would also provide another test for the validity of the partially-covering model. Furthermore, given that the presence of Fe K absorption lines is contingent on the model being employed for the broad-band continuum, confirming (or ruling out) the partial-covering model would also have a strong influence on the inferred

source energetics.

At the time of writing the analysis of these extensive datasets is on-going. However, in the remainder of this chapter the initial results obtained from these observations are presented.

### 3.6.1 *XMM-Newton*

In November 2011 *XMM-Newton* observed MR 2251−178 three times for a total co-added net exposure of 389 ks. One of the aims of the observing campaign was to test the partial-covering model. Both the RGS and the EPIC-pn spectra were initially fitted with the best-fitting partial-covering model obtained for the *Suzaku* dataset; because the *Swift* BAT lightcurve was relatively constant over its 58-month duration it was also included in the EPIC-pn fit to enable the hard X-ray data to be constrained at $E > 10$ keV. The model was sequentially iterated back and forth between the EPIC-pn and the RGS data to self-consistently constrain the soft X-ray warm absorption and the broader continuum. Due to the spectral complexity of the RGS data in particular the specific parameters and associated errors for individual line profiles (e.g., intensities, equivalent widths, etc.) are not available at the time of writing and the description of the soft-band spectrum is therefore mainly qualitative.

#### RGS

The *XMM-Newton* RGS provides an energy coverage of $0.4 - 2.0$ keV and therefore provides a high quality view of the soft X-ray warm absorber. Enlarged portions of the RGS spectrum of MR 225-178 are shown in Fig. 3.10. The warm absorber is clearly complex, comprising a wealth of atomic features. Notably, inner-shell (i.e., ionisation states of Li-like and below) and higher-order (i.e., the $1s \rightarrow np$ transitions, where $n \geq 3$) absorption lines are detected throughout the spectrum. Panel (a) of Fig. 3.10 shows that the higher-order line series of C VI is particularly prominent, with the C VI K-shell edge also being detected at $\sim 0.49$ keV (rest-frame). N VI, N VII, O VII and O VIII also have

higher-order line series (albeit without discretely detected K-shell edges), with each ion reaching at least the $1s \rightarrow 4p$ transition. Complementing the array of absorption lines there is also some interesting interplay between emission and absorption components (e.g., see O VII line in Fig. 3.10). The O VII ($1s2p \rightarrow 1s^2$) emission line at $E \sim 574\,\mathrm{eV}$ is superposed by three narrow absorption lines corresponding to velocity shifted O VII ($1s^2 \rightarrow 1s2p$) and the two lines which make up the O VI ($1s^22s \rightarrow 1s2s2p$) doublet. Again, similar structures are present at other energies, with N VII, O VIII and Ne IX all showing emission superposed by absorption.

From panels (a) and (b) of Fig. 3.10, both neon and magnesium also show evidence for inner-shell absorption from at least their Be-like ionisation states (c.f., Behar & Netzer 2002). Indeed, the inner-shell lines for Mg in particular occur throughout the $\sim 1.2 - 1.3\,\mathrm{keV}$ energy range which further suggests that the line present at $\sim 1.3\,\mathrm{keV}$ in the *Suzaku* spectrum may be due to a blend of the inner-shell profiles. The preliminary list of atomic lines present in the RGS data — including details such as the responsible ion, the electron transition and the velocity-corrected centroid energies in the source rest-frame — is given in Table 3.8.

In terms of photo-ionisation modelling, a self-consistent fit to both the inner-shell and higher-order absorption lines in the RGS data requires three zones of fully-covering XSTAR absorption in excess of the two which partially-cover the source (see Table 3.7). In addition to the Zones 1 and 2, which have similar parameters to those found previously for the *Suzaku* data, a further grid ($v_{\mathrm{turb}} = 100\,\mathrm{km\,s^{-1}}$) is needed to fit the plethora of low ionisation potential inner-shell and higher-order lines.

To correctly account for the intensity of the low ionisation lines the new grid requires a much softer input continuum than the other absorption tables (which have $\Gamma_{\mathrm{input}} = 2.0$) in order to not over-ionise the gas and reduce their intensity in the spectrum. The necessary XSTAR continuum has $\Gamma_{\mathrm{input}} = 2.5$. This is much softer than that which has typically been found for MR 2251−178 assuming a fully-covering absorption model, which is of the order of $\Gamma = 1.6 - 1.7$ (e.g., Pan, Stewart & Pounds 1990; Mineo & Stewart 1993; Kaspi et al. 2004; Gibson et al. 2005, also see §3.4.1), but is similar to that found if the source is partially-covered by two layers of gas. This lends weight to the

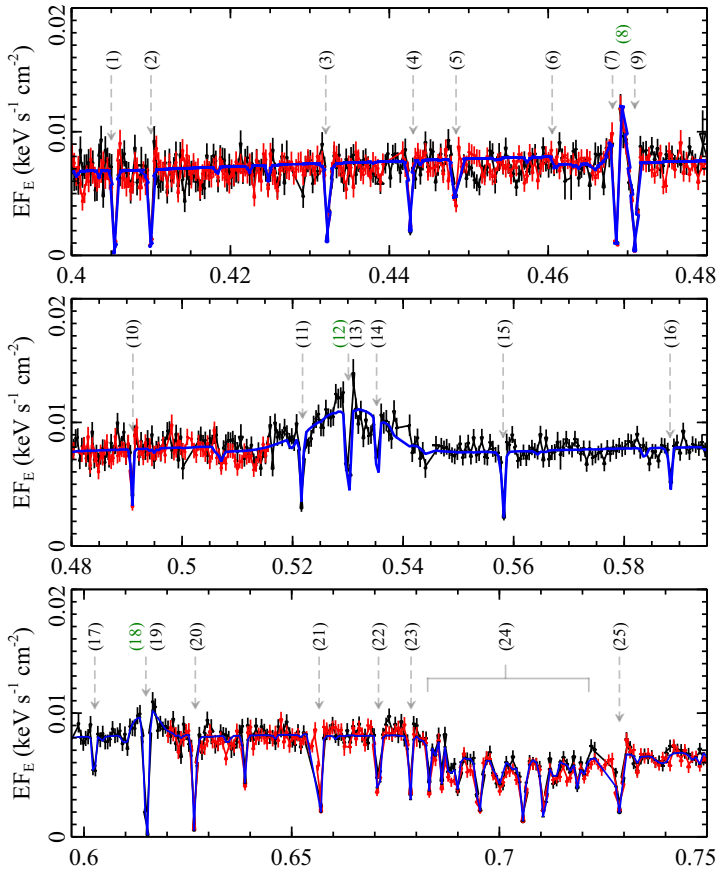


Figure 3.10: Enlarged view of the *XMM-Newton* RGS data (RGS1: black, RGS2: red). The best-fit model for the soft X-ray absorber, comprising three absorption zones, is shown by the blue line. There are a plethora of ionised lines present originating from C, N, O and the Fe M-shell; including the higher-order $1s \rightarrow np$ (where $n \geq 3-6$) line series of C, N and O. There is also some complex interplay between the absorption and underlying emission components, which are further discussed in the text. The likely identification of the numbered lines are presented in Table 3.8. Green numbers denote the position of emission components.

notion that MR 2251−178 may, indeed, have an intrinsically soft continuum which is partially-covered by a complex and stratified absorber.

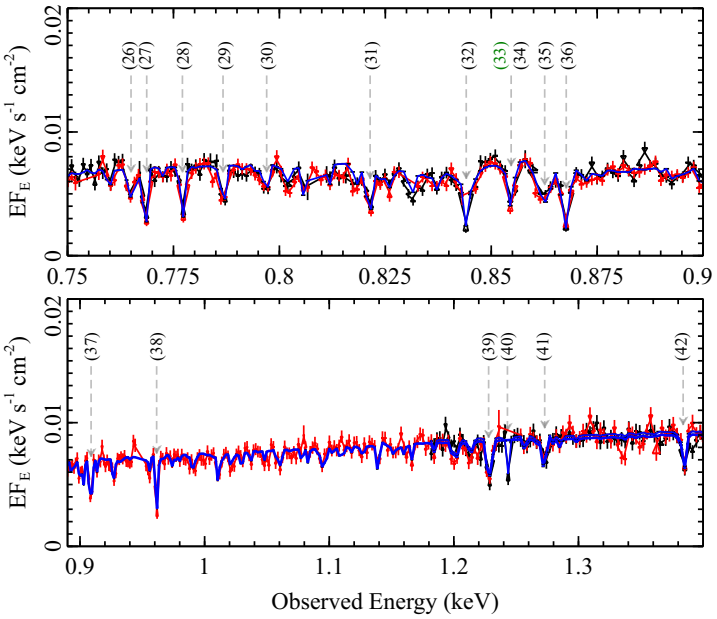


Figure 3.10: *continued* – Enlarged view of the *XMM-Newton* RGS data showing the Ne and Mg energy regimes. The blue line again shows the best-fit absorption model. Both Ne and Mg have a number of inner-shell lines (i.e., the B-, Be-, Li-like charge states) present in the spectrum. As in the previous panel, the likely identification of the numbered lines are presented in Table 3.8, and the green numbers denote the position of underlying emission components.

Table 3.7: *XMM-Newton* RGS absorber parameters. *Columns:* (1) Column density, in units of $10^{21}\,\mathrm{cm}^{-2}$; (2) Ionisation parameter, in units of $\mathrm{erg\,cm\,s}^{-1}$; (3) Outflow velocity, in units of $\mathrm{km\,s}^{-1}$.

| Zone | $N_{\mathrm{H}}$ (1) | $\log \xi$ (2) | $v_{\mathrm{out}}$ (3) |
|---|---|---|---|
| 1 | $3.57^{+1.75}_{-1.35}$ | $2.73^{+0.09}_{-0.15}$ | $< 100$ |
| 2 | $1.39^{+0.26}_{-0.19}$ | $2.00^{+0.09}_{-0.03}$ | $480^{+60}_{-60}$ |
| 3 | $2.11^{+0.09}_{-0.09}$ | $1.26^{+0.03}_{-0.03}$ | $490^{+30}_{-30}$ |

Table 3.8: List of atomic lines detected in the *XMM-Newton* RGS spectrum. *Columns:* $^{\diamond}$Denotes a line which is seen in emission; $^{\dagger}$The rest-frame energies correspond to the energy where an atomic line is seen to have the greatest intensity, and is measured directly from the spectrum using the `cursor` command in XSPEC; $^{\top}$Expected transition energies and electron transitions are taken from the NIST online database of atomic spectra. Energies for the inner-shell lines are taken from Behar & Netzer (2002). $^{\ddagger}$Fe lines are likely blends of many transitions so expected transition energies have been omitted from the table for brevity.

| | Identification | $E_{\rm Obs}$ (eV) | $E^{\dagger}_{\rm Rest}$ (eV) | $E^{\top}_{\rm Lab}$ (eV) | | Identification | $E_{\rm Obs}$ (eV) | $E^{\dagger}_{\rm Rest}$ (eV) | $E^{\top}_{\rm Lab}$ (eV) |
|---|---|---|---|---|---|---|---|---|---|
| 1. | N VI ($1s^2 \rightarrow 1s2p$) | 405.1 | 430.3 | 430.7 | 22. | O VII ($1s^2 \rightarrow 1s5p$) | 670.9 | 712.8 | 712.7 |
| 2. | C VI ($1s \rightarrow 3p$) | 409.8 | 435.6 | 435.5 | 23. | O VII ($1s^2 \rightarrow 1s6p$) | 678.8 | 721.2 | 720.7 |
| 3. | C VI ($1s \rightarrow 4p$) | 432.3 | 459.0 | 459.4 | 24. | Fe M-shell UTA$^{\ddagger}$ | - | - | - |
| 4. | C VI ($1s \rightarrow 5p$) | 443.2 | 470.7 | 470.4 | 25. | O VIII ($1s \rightarrow 3p$) | 728.9 | 774.4 | 774.6 |
| 5. | C VI ($1s \rightarrow 6p$) | 448.1 | 476.0 | 476.4 | 26. | Fe XVII$^{\ddagger}$ | 764.7 | 812.4 | - |
| 6. | C VI K-edge | 460.0 | 489.7 | 489.9 | 27. | O VIII ($1s \rightarrow 4p$) | 768.4 | 816.4 | 816.9 |
| 7. | N VI ($1s^2 \rightarrow 1s3p$) | 467.4 | 497.3 | 496.7 | 28. | Fe XVII-XIX$^{\ddagger}$ | 777.4 | 825.9 | - |
| 8. | N VII$^{\diamond}$ ($2p \rightarrow 1s$) | 470.2 | 500.3 | 500.4 | 29. | O VIII ($1s \rightarrow 5p$) | 787.1 | 836.2 | 836.6 |
| 9. | N VII ($1s \rightarrow 2p$) | 470.9 | 501.1 | 500.4 | 30. | O VIII ($1s \rightarrow 6p$) | 797.0 | 846.8 | 847.2 |
| 10. | N VI ($1s^2 \rightarrow 1s4p$) | 491.1 | 521.8 | 521.6 | 31. | Ne V (–) | 821.7 | 872.8 | 872.0 |
| 11. | O VI ($1s^2 2s \rightarrow 1s2s2p$) | 521.8 | 554.4 | 554.2 | 32. | Fe XVII-XIX$^{\ddagger}$ | 844.1 | 896.8 | - |
| 12. | O VII$^{\diamond}$ ($1s2p \rightarrow 1s^2$) | 534.2 | 568.4 | 568.6 | 33. | Ne IX$^{\diamond}$ ($1s2p \rightarrow 1s^2$) | 866.6 | 922.1 | 922.0 |
| 13. | O VI ($1s^2 2s \rightarrow 1s2s2p$) | 530.1 | 563.2 | 562.6 | 34. | Ne VIII ($1s^2 \rightarrow 1s2s2p$) | 854.7 | 908.1 | 908.7 |
| 14. | O VII ($1s^2 \rightarrow 1s2p$) | 535.2 | 568.6 | 568.6 | 35. | Fe XIX$^{\ddagger}$ | 862.9 | 916.8 | - |
| 15. | N VII ($1s \rightarrow 3p$) | 558.1 | 592.9 | 592.9 | 36. | Ne IX ($1s^2 \rightarrow 1s2p$) | 867.7 | 921.9 | 922.0 |
| 16. | N VII ($1s \rightarrow 4p$) | 588.3 | 625.0 | 625.4 | 37. | Fe XX | 908.9 | 965.5 | - |
| 17. | N VII ($1s \rightarrow 5p$) | 602.6 | 640.2 | 640.4 | 38. | Ne X ($1s \rightarrow 2p$) | 961.5 | 1021.5 | 1021.5 |
| 18. | O VIII ($1s \rightarrow 2p$) | 614.9 | 653.3 | 653.5 | 39. | Mg VIII (–) | 1227.9 | 1304.6 | 1305.5 |
| 19. | O VIII$^{\diamond}$ ($2p \rightarrow 1s$) | 615.1 | 654.5 | 653.5 | 40. | Mg IX (–) | 1243.0 | 1320.6 | 1321.4 |
| 20. | O VII ($1s^2 \rightarrow 1s3p$) | 626.8 | 665.9 | 665.6 | 41. | Mg XI ($1s^2 \rightarrow 1s2p$) | 1272.9 | 1352.4 | 1353.3 |
| 21. | O VII ($1s^2 \rightarrow 1s4p$) | 656.6 | 697.6 | 697.1 | 42. | Mg XII ($1s \rightarrow 2p$) | 1385.4 | 1471.9 | 1472.3 |

### EPIC-pn

Extending the soft-band RGS model to the full EPIC-pn bandpass shows that the partially-covering model provides a good description of the broad-band data. As shown in panels (a) and (b) of Fig. 3.11, which show the best-fit model to the combined *XMM-Newton* EPIC-pn and *Swift* BAT data along with the associated residuals, respectively, the partially-covering model is again able to simultaneously account for the soft- and hard-band X-ray data. In particular, in the presence of the three fully-covering distant absorbers, there are no significant residuals remaining between $0.6 - 10.0\,\mathrm{keV}$; the ambiguous absorption line which was prominent at $\sim 1.3\,\mathrm{keV}$ in the *Suzaku* data is not apparent in the *XMM-Newton* spectrum once the soft absorption grid has accounted for the inner-shell Mg lines. In further comparison with the *Suzaku* data the strong lines which were present at $\sim 2.5\,\mathrm{keV}$ and $\sim 2.8\,\mathrm{keV}$, and conservatively associated with blue-shifted S XV He$\alpha$ and S XVI Ly$\alpha$, respectively, are not significantly present in the *XMM-Newton* EPIC-pn data with lower limits on their *EW* of $> -4$ and $> -3\,\mathrm{eV}$, respectively. These are roughly a factor of 2 lower than those found in the *Suzaku* data which means that the absorption layer responsible for them may be transient or subject to intrinsic variability between the two observation epochs. The Fe K absorption is accounted for by the partially-covering absorber.

By virtue of the inclusion of a third soft X-ray absorber the parameters of the broad-band fit to the *XMM-Newton* data is subtly different to the one found for *Suzaku*. For example, the *XMM-Newton* data requires a slightly softer continuum than the *Suzaku* one, with $\Gamma_{\mathrm{xmm}} = 2.14 \pm 0.01$. Even so, the parameters of the principal partially-covering absorbers are relatively consistent between the two observations, with the main differences appearing to arise from changes in their ionisation state and the fraction of the source which is covered by the absorbing gas. The possibility that the long-term variability exhibited by MR 2251−178 could be changes in a complex absorber is investigated in §3.6.3, where a multi-epoch description of the source using all available X-ray observations from the last decade is constructed.

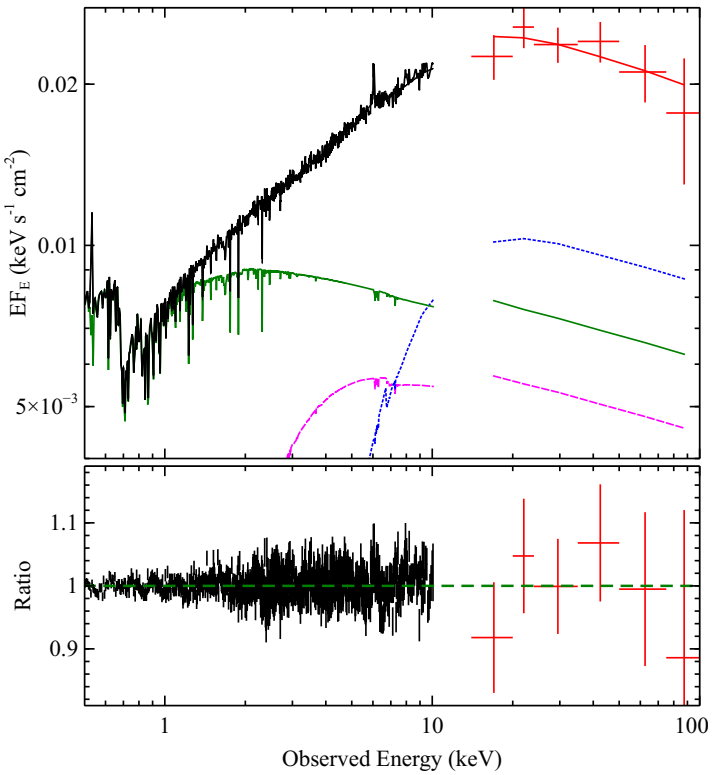


Figure 3.11: Time-averaged 2011 *XMM-Newton* EPIC-pn and *Swift* BAT spectra of MR 2251−178 when fitted with the best-fit *Suzaku* partial-covering model. The blue (dotted) and magenta (dashed) lines represent the two partially-covering absorption layers, while the solid (green) line shows the continuum which leaks through both absorbers. The partial-covering interpretation provides a good fit to both spectra with an intrinsic $\Gamma = 2.14 \pm 0.01$ power-law covered by two partially-covering absorbers, plus three zones of distant fully-covering absorption. There are no strong residuals remaining between $0.6 - 10.0$ keV and no significant Fe K absorption is detected. See text for further details.

### 3.6.2 *Chandra* HETG

The High Energy Transmission Grating (HETG) aboard *Chandra* observed MR 2251−178 for 392.9 ks in October 2011, making it semi-contemporaneous with the *XMM-Newton* observation. Directly applying the best-fitting partially-covering *XMM-Newton* model to the HETG data provides a good description to the data after some subtle refitting. As in the RGS data, both the higher-order line series of O VII and O VIII, as well as

the Fe UTA and the inner-shell Ne and Mg lines, are clearly apparent in the HETG spectrum. As shown in Fig. 3.12 the inner-shell Ne and Mg series are particularly well defined in the HETG data, with the B-, Be-, Li-, He- and H-like charge states of each element giving rise to discrete lines. There are no residual lines detected at $\sim 2.5$ keV or $\sim 2.8$ keV, which again suggests that the sulphur lines detected in the *Suzaku* spectrum are variable, possibly transient. Lower limits of $> -4$ and $> -2$ eV can be placed on the *EW* of these lines, respectively, which is again roughly a factor of 2 less than those found with *Suzaku*. The continuum parameters for the HETG spectrum are consistent with those obtained from both the *Suzaku* and *XMM-Newton* data.

The HETG has a wider bandpass than the RGS which enables some additional tests to be applied to the inner-shell lines in particular. Fig. 3.12 shows a comparison between the fit to the warm absorber when the third component of XSTAR absorption has a $\Gamma_{\rm input} = 2.5$ (red line) or $\Gamma_{\rm input} = 2.0$ (blue line). In the absence of a soft input continuum the model is clearly unable to account for the depth of the inner-shell B-, Be- and Li-line charge states of Ne or Mg which suggests that the softer continuum is strongly required by the data. The necessary power-law slope is more in line with MR 2251−178 being partially- rather than fully-covered by layers of gas as has traditionally been assumed (e.g., Pan, Stewart & Pounds 1990; Mineo & Stewart 1993; Kaspi et al. 2004), which lends further weight to a scenario where MR 2251−178 is dominated by complex absorption. A fully detailed spectral analysis of these datasets is currently on-going and is to be published in forthcoming works.

### 3.6.3 Multi-epoch variability

The *Suzaku* data, in conjunction with the follow-up *XMM-Newton* and *Chandra* observations, have demonstrated that a relatively soft power-law continuum attenuated by complex partially-covering absorption is able to self-consistently describe the broad-band properties of MR 2251−178. Moreover, in light of the inner-shell Ne and Mg absorption lines necessitating an ionising continuum which is much softer than that found through fully-covering absorption models, the partially-covered interpretation is somewhat

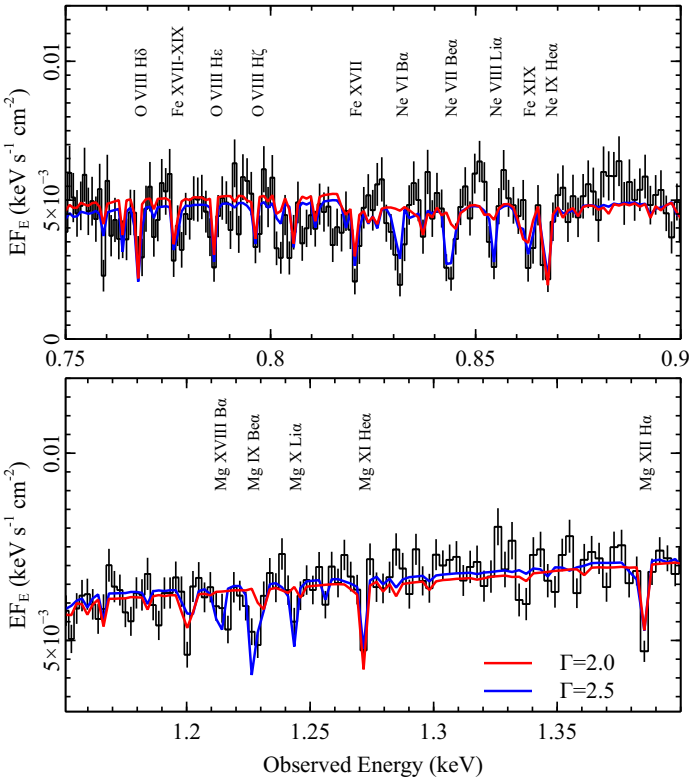


Figure 3.12: Enlarged portions of the 2011 *Chandra* HETG observation of MR 2251−178, focussing on the Ne and Mg energy bands. The HETG data give a much clearer view of the inner-shell Ne and Mg lines than was possible with the *XMM-Newton* RGS. Both elements have lines due to their B-, Be- and Li-like charge states. The solid lines correspond to the fit that is obtained when the third fully-covering XSTAR absorber has an input photon continuum of $\Gamma_{\rm input} = 2.0$ (red) and $\Gamma_{\rm input} = 2.5$ (blue). Importantly, the inner-shell lines cannot be accounted for without an intrinsically soft X-ray continuum, which in turn provides evidence for a partially-covered X-ray spectrum. See text for further details.

preferred by the new data. A powerful means to assess the long-term plausibility of partially-covering models such as this is to use time-resolved spectroscopy (often in conjunction with principal component analysis, PCA) to test whether a particular model can account for the variability in a source's X-ray spectrum over a given stretch of time. Such studies have been conducted in the literature using both short ($\Delta t \sim$ ks) and long

Table 3.9: Summary of observations included in multi-epoch variability analysis. *Columns:* (1) Observatory name; (2) Observation start date; (3); Instrument (4); Observation net exposure after processing, in units of ks; (5) Net source count rate; (6) Work in which dataset was initially published. An * indicates that the observation is reported in either this thesis or a forthcoming work.

| Mission (1) | Date (2) | Inst. (3) | Exp. (4) | Count Rate (5) | Reference (6) |
|---|---|---|---|---|---|
| *XMM-Newton* | 2002-05-18 | EPIC-pn | 39.4 | $5.780 \pm 0.001$ | Kaspi et al. (2004) |
| | 2011-11-11 | EPIC-pn | 270.5 | $15.330 \pm 0.007$ | * |
| *Chandra* | 2002-09-11 | MEG | 146.3 | $0.154 \pm 0.001$ | Gibson et al. (2005) |
| | | HEG | | $0.081 \pm 0.001$ | |
| | 2011-09-29 | MEG | 392.9 | $0.237 \pm 0.001$ | * |
| | | HEG | | $0.121 \pm 0.001$ | |
| *Suzaku* | 2009-05-07 | XIS-FI | 137.0 | $2.037 \pm 0.003$ | * |

($\Delta t \sim$ yrs) time-slices, and have been successful in asserting plausible partially-covering models for a number of AGN in recent years (e.g., NGC 4395, Nardini & Risaliti 2011; Mrk 766, Miller et al. 2007; Turner et al. 2007; Risaliti et al. 2011; NGC4051, Miller et al. 2010).

Over the last decade there have been five notable observations of MR 2251−178 in the X-rays: one with *Suzaku* (in 2009, presented here), two with *XMM-Newton* (in 2002, Kaspi et al. 2004; and 2011, discussed above) and two with the *Chandra* HETG (in 2002, Gibson et al. 2005; and 2011, also discussed above). A multi-epoch spectral fitting of these observations will therefore allow the long-term viability of the partial-covering absorption model to be probed over a relatively long temporal baseline ($\sim 10$ yrs). In the remainder of this section the preliminary results of such a fit are discussed. A summary of the five observations used is given in Table 3.9; in the case of *XMM-Newton* only the EPIC-pn spectra were used because the bandpass of the RGS is insufficient to constrain the broad-band components.

The initial partial-covering model was that which was found to fit both the 2011

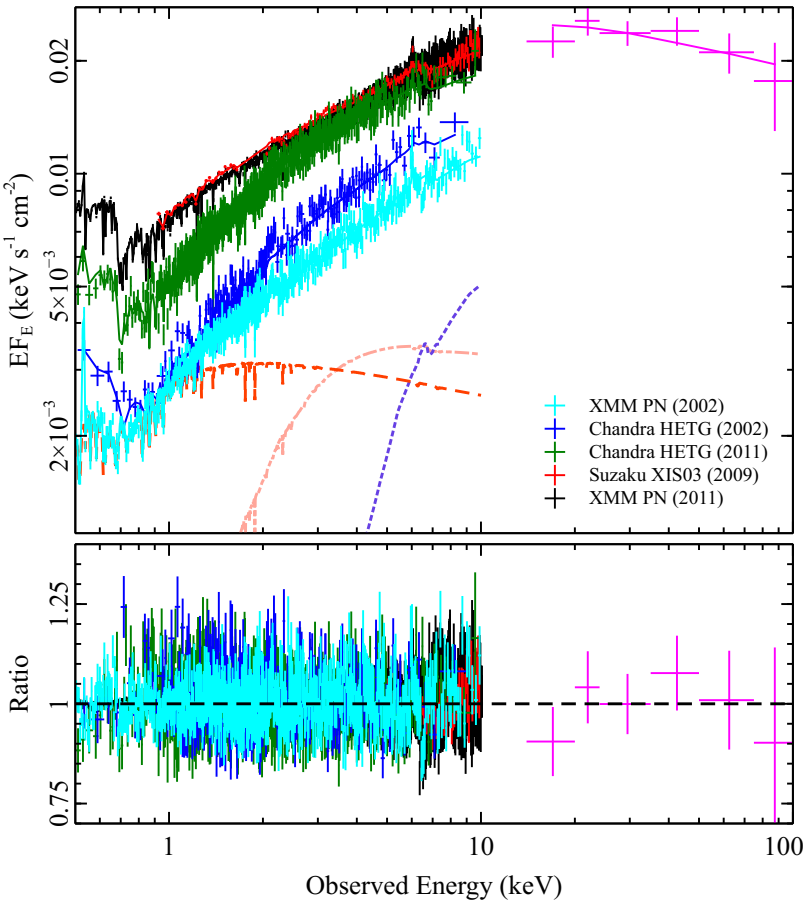


Figure 3.13: Plot showing the multi-epoch partially-covering fit for MR 2251−178 (top) and associated data/model residuals (bottom). Datasets for *XMM-Newton* (2002, cyan; 2011, black), the *Chandra* HETG (2002, blue; 2011, green), the *Suzaku*/XIS-FI (2009, red) and the 58-month time-averaged *Swift* BAT (pink). The primary continuum is described by a $\Gamma = 2.17 \pm 0.03$ power-law, which is covered by two partially-covering absorbers and three distant absorption components. In the top panel the blue (dotted), pink (dot-dashed) and orange (dashed) lines show the contributions of the $\sim 10^{23}\,\mathrm{cm}^{-2}$ partial-covering layer, the $\sim 10^{22}\,\mathrm{cm}^{-2}$ partial-covering layer, and the component which is transmitted through both layers, respectively. The bottom panel shows that the partially-covering model self-consistently provides a very good description of all datasets which suggests that the variability history of MR 2251−178 could be attributed to complex absorption. The best-fit parameters for this model are given in Table 3.10.

*XMM-Newton* observation and the *Swift* BAT hard X-ray spectrum simultaneously, and had the same form in XSPEC:

$$N_H^{\rm Gal} \times (\texttt{powerlaw}_1 + \texttt{reflionx} + \mathrm{XSTAR}_{\rm pcov1} \times \texttt{powerlaw}_2 + \mathrm{XSTAR}_{\rm pcov2} \times \texttt{powerlaw}_3) \times \mathrm{XSTAR}_{\rm 1C} \times \mathrm{XSTAR}_{\rm 2C} \times \mathrm{XSTAR}_{\rm soft} \tag{3.4}$$

The soft XSTAR grid was included in the model to account for the lower ionisation potential lines which are prevalent in the soft X-ray band. From this starting model, the additional observations were sequentially added to the fit and the normalisations of the `powerlaw` components for each spectrum were allowed to float such that an internally self-consistent fit could be found; allowing the `powerlaw` normalisations to float mimics the effects of changing absorber covering fraction which allows any intra-epoch variability to be accounted for solely through changes in the absorbing layers. For simplicity the outflow velocity of the soft X-ray absorbers were left fixed to the values found for the 2011 *XMM-Newton* observation. The partially-covering components were left fixed in the source rest-frame because they are difficult to constrain in the absence of discrete absorption features. Fig. 3.13 shows the resultant fit and associated residuals once all 5 datasets had been added to the model. The corresponding model parameters are reported in Table 3.10. Fig. 3.13 clearly shows that the partially-covering model is capable of providing a reasonable description to all five fitted observations ($\chi^2/\nu = 5937.8/5240$; $\chi^2_{\rm reduced} = 1.13$).

The spectral changes observed over the last decade can all be accounted for through changes in absorber covering fraction which varies between $\sim (30-60)\%$ and $\sim (20-40)\%$ over the 10 year period for the pcov1 and pcov2 components, respectively. The only exception is the 2002 *XMM-Newton* observation – in which MR 2251−178 was viewed in its lowest flux state – which also requires a drop in ionisation state of the soft X-ray absorber to achieve a good fit. In comparison with the single-epoch *Suzaku* and *XMM-Newton* fits the multi-epoch one again yields subtly different continuum parameters. The intrinsic $\Gamma$ appears to be slightly softer in the multi-epoch fit (i.e., $\Gamma = 2.17 \pm 0.03$) but is still consistent with that found before at the 90% level. The column densities of the partially-covering components are also similar to the single-

Table 3.10: Best-fit complex absorption parameters for the multi-epoch fit to MR 2251−178.

| Component | Parameter | *XMM-Newton* (2011) | *Chandra* (2011) | *Suzaku* (2009) | *Chandra* (2002) | *XMM-Newton* (2002) |
|---|---|---|---|---|---|---|
| `powerlaw` | $\Gamma$ | $2.17^{+0.03}_{-0.03}$ | – | – | – | – |
| | norm$^a$ | $37.06^{+0.52}_{-0.52}$ | $36.24^{+0.80}_{-0.80}$ | $31.06^{+1.32}_{-1.32}$ | $23.76^{+1.65}_{-1.65}$ | $19.57^{+0.59}_{-0.59}$ |
| `reflionx` | $\xi$ | $< 1.51$ | – | – | – | – |
| | $A_{\rm Fe}$ | 1.00 | – | – | – | – |
| | norm$^b$ | $2.12^{+0.36}_{-0.51}$ | – | – | – | – |
| XSTAR$_{\rm pcov1}$ | $N_{\rm H}^c$ | $685.31^{+24.23}_{-23.91}$ | – | – | – | – |
| | $\log \xi^d$ | $1.20^{+0.10}_{-0.11}$ | – | – | – | – |
| | $f_{\rm cov}^e$ | $\left(49^{+1}_{-2}\right)$ % | $\left(44^{+3}_{-2}\right)$ % | $\left(38^{+5}_{-5}\right)$ % | $\left(50^{+10}_{-9}\right)$ % | $\left(55^{+4}_{-4}\right)$ % |
| XSTAR$_{\rm pcov2}$ | $N_{\rm H}^c$ | $55.53^{+1.34}_{-1.36}$ | – | – | – | – |
| | $\log \xi^d$ | $1.00^{+0.01}_{-0.02}$ | – | – | – | – |
| | $f_{\rm cov}^e$ | $\left(23^{+1}_{-1}\right)$ % | $\left(26^{+1}_{-1}\right)$ % | $\left(40^{+2}_{-3}\right)$ % | $\left(34^{+4}_{-3}\right)$ % | $\left(26^{+3}_{-3}\right)$ % |
| XSTAR$_{\rm 1C}$ | $N_{\rm H}^c$ | $1.86^{+0.39}_{-0.27}$ | – | – | – | – |
| | $\log \xi^d$ | $2.10^{+0.08}_{-0.12}$ | – | – | – | – |
| | $v_{\rm out}^e$ | 330* | – | – | – | – |
| XSTAR$_{\rm 2C}$ | $N_{\rm H}^c$ | $2.44^{+0.64}_{-0.61}$ | – | – | – | – |
| | $\log \xi^d$ | $2.84^{+0.07}_{-0.06}$ | – | – | – | – |
| | $v_{\rm out}^e$ | 300* | – | – | – | – |
| XSTAR$_{\rm soft}$ | $N_{\rm H}^c$ | $2.24^{+0.03}_{-0.03}$ | – | – | – | – |
| | $\log \xi^d$ | $1.15^{+0.01}_{-0.01}$ | – | – | – | $0.12 \pm 0.03$ |
| | $v_{\rm out}^e$ | 100* | – | – | – | – |

[a] Power-law normalisation given as the *total* of the intrinsic continuum. i.e., the normalisation summed over all `powerlaw` components
[b] `reflionx` normalisation, in units of $10^{-5}$;
[c] Absorber column density, in units of $10^{21}\,{\rm cm}^{-2}$;
[d] Absorber ionisation parameter, in units of $\rm erg\,cm\,s^{-1}$;
[e] Covering fraction of partially-covering absorbers, in %;
[f] Absorber outflow velocity, in units of $\rm km\,s^{-1}$;
[*] Indicates that the parameter was fixed at this value throughout fitting.

epoch fits, with columns of $\sim 10^{22-23}\,{\rm cm}^{-2}$, but both grids are slightly less ionised which eludes to a level of model dependency for the partially-covering components. Even so, the effectiveness of the partially-covering absorption model when it comes to

describing the multi-epoch data demonstrates that such a model is more than capable of accounting for the variability exhibited by MR 2251−178 over the last decade. This suggests that the complex absorption interpretation for the broad-band spectrum may provide a robust description of the source, although more work is still required. As with the individual *XMM-Newton* and *Chandra* observations a variability analysis of MR 2251−178 is currently on-going and a fully detailed account is to be presented in forthcoming published work.

## 3.7 Chapter summary

Using data obtained from the *Suzaku* satellite in 2009, with *XMM-Newton* and *Chandra* in 2011, and with the 58-month time-averaged *Swift* BAT, I have presented both a broad-band and a preliminary high-resolution spectral analyses of the radio-quiet quasar MR 2251−178 in the X-rays. The main results for this analysis are summarised below:

1. The *Suzaku* and *Swift* BAT observations reveal that the continuum has considerable curvature at $E \gtrsim 10\,\mathrm{keV}$ and, although its requirement is contingent to the interpretation of the primary continuum, a soft-excess may also be present below 1 keV. A weak, $EW = \left(26^{+16}_{-6}\right)\,\mathrm{eV}$, unresolved ($\sigma < 117\,\mathrm{eV}$), Fe K$\alpha$ emission line from a neutral or mildly-ionised reflector is present at $\sim 6.4\,\mathrm{keV}$. Through consideration of both fully- and partially-covering absorption models this analysis has shown that the soft-excess and spectral curvature in MR 2251−178 can be equally well modelled as the by-product of a soft power-law continuum which is dominated by complex absorption, or as an intrinsic hard continuum component supplemented by additional soft emission and a high-energy roll-over.

2. In the soft X-ray band of the *Suzaku* spectrum two discrete absorption lines are detected at high significance (i.e., $P_{\mathrm{MC}} > 99\%$). The first, which is detected between $\sim 0.73 - 0.78\,\mathrm{keV}$ (rest-frame), is due to the Fe M-shell UTA. While the second line at $E \sim 1.3\,\mathrm{keV}$ has an ambiguous origin on the basis of the *Suzaku* data, follow-up

observations with *XMM-Newton* and *Chandra* show that the line is likely comprised of inner-shell Mg in its B-, Be-, Li- and He-like charge states which are blended together at the resolution of the *Suzaku* XIS. Two further absorption lines are detected at $\sim 2.5\,\mathrm{keV}$ and $\sim 2.8\,\mathrm{keV}$ in the *Suzaku* spectrum, and are conservatively identified with the K$\alpha$ lines of S XV and S XVI blue-shifted by $v_{\mathrm{out}} \sim 6,000\,\mathrm{km\,s^{-1}}$ and $v_{\mathrm{out}} \sim 21,000\,\mathrm{km\,s^{-1}}$, respectively. These lines are not significantly present in the subsequent *XMM-Newton* or *Chandra* observations, with upper limits on their *EW* being a factor of at least two lower in the newer observations. This suggests that they are variable, possibly transient.

3. Atomic complexity is present in the Fe K band, although its interpretation is radically different depending on the model employed for the broad-band continuum. In the event that the source has an intrinsically hard continuum ($\Gamma \sim 1.6 - 1.7$) then a residual trough is detected at $\sim 7.5\,\mathrm{keV}$ in the source rest-frame, which is consistent with a blend of Fe XXV–XXVI K$\alpha$ absorption lines at an outflow velocity of $\sim 0.1\,\mathrm{c}$. However, should the source continuum be intrinsically soft and partially-covered instead, then all of the residuals at Fe K are accounted for with an ionised Fe K-shell edge. The detection of a highly-ionised outflow in MR 2251−178 is therefore model dependent.

4. A preliminary analysis of follow-up *XMM-Newton* and *Chandra* observations from 2011 has been presented. In particular, the viability of the partially-covering interpretation has been presented through a multi-epoch analysis comprising all of the available *XMM-Newton*, *Chandra* and *Suzaku* observations from the last decade. Two layers of partially-covering gas over an intrinsically soft continuum are capable of accounting for the bulk of the broad-band spectral variability in all observations, with the primary mode of variability being changes in the absorber covering fraction coupled with changes in intrinsic source flux. Moreover, the high-resolution *XMM-Newton* RGS and *Chandra* HETG grating data reveal the presence of both inner-shell Ne and Mg absorption lines, and higher-order line series of C, N, and O. Modelling these lines with XSTAR requires an intrinsically soft input continuum which is significantly softer

than that which is found for a traditional non-partially-covered model (i.e., $\Gamma \sim 2.5$ rather than $\Gamma \sim 1.6 - 1.7$). While analysis of follow-up observations is on-going, these points suggest that the absorber in MR 2251−178 may consist of stratified clumps of material which partially-cover the sight-line.

# 4 Outflow sample I – line detection and absorber properties[1]

## 4.1 Introduction

In this chapter I use archival *Suzaku* observations of a large sample of AGN to characterise the properties of highly-ionised outflows in the Fe K band. To date, the most comprehensive study of these outflows has been conducted by Tombesi et al. (2010a) who performed a systematic narrow-band (i.e., $3.5-10.5$ keV) analysis of 42 sources (with 101 observations) obtained from the *XMM-Newton* archive, using a simple baseline model to describe the AGN continuum in the Fe K band. Their baseline model consisted of a power-law, narrow Gaussians and neutral absorption (where required) to approximate for any spectral curvature. This phenomenological approach yielded a fit to the $4-10$ keV energy band of most sources which was sufficient to enable the systematic search of Fe XXV He$\alpha$ and Fe XXVI Ly$\alpha$ absorption lines without needing to take additional spectral complexity into account. Moreover, Tombesi et al. (2010a) found that this approach resulted in continuum parameters which were largely consistent with those found by authors who conducted a more thorough fit using the entire *XMM-Newton* bandpass. However, while this approach is suitable for most sources it is important to note that in those which have more complex X-ray spectra, e.g., those which are very heavily absorbed or those with strong hard excesses, using a narrow-band fit can yield a model which is a poor representation of the data when extrapolated to consider the higher and lower energy regimes. The only way to overcome this limitation is by performing a detailed broad-band analysis. *Suzaku* is currently the only X-ray observatory which offers a sufficiently broad bandpass (i.e., $0.6-50$ keV) to allow for the effects of soft-band absorption, the soft-excess *and* the

[1]This chapter is partly based on published work entitled '*The Suzaku view of highly ionized outflows in AGN – I. Statistical detection and global absorber properties*'; Gofford, J.; Reeves, J. N.; Tombesi, F.; Braito, V.; Turner, T. J.; Miller, L.; Cappi, M.; MNRAS, **430**, 60-80.

All work was conducted by myself.

Compton reflection component to be constrained simultaneously. This makes it the ideal instrument to confidently constrain the underlying continuum and to robustly assess for the presence of highly-ionised outflows in AGN.

## 4.2 Sample Selection

The *Suzaku* sample was selected from the Data ARchive and Transmission System[2] (DARTS; Tamura et al. 2004) which contains all publicly available *Suzaku* observations categorised by the classification of the target source. I created a preliminary sample of AGN by positionally cross-correlating the targeted pointing coordinates of all publicly available *Suzaku* observations of extragalactic compact sources (as of the end of 2011 December) against the known positions of sources contained in the VERONCAT catalog of Quasars & AGN (Véron-Cetty & Véron 2010).

The VERONCAT contains an extensive list of local AGN, all of which have been quantitatively classified based upon their optical properties using the criteria introduced by Winkler (1992). Observations of non-AGN which were matched by virtue of their having a similar position to a known AGN on the sky, such as those of extragalactic Ultra-luminous X-ray Sources (ULXs; Feng & Soria 2011) or X-ray bright supernovae, were systematically excluded. Only those observations with exposures long enough to ensure that the net source counts between $2-10\,\mathrm{keV}$ in the source rest-frame exceeded $\sim 15,000$ were retained (typical exposures were $\gtrsim 50\,\mathrm{ks}$) such that a narrow (i.e., $EW = 30\,\mathrm{eV}$) absorption feature was detectable at 95% from Monte Carlo (MC) simulations at source rest-frame energies of up to $8-9\,\mathrm{keV}$ (see §2.2.6). In the case of the high red-shift quasar APM 08279+5255, which shows evidence for absorption lines at rest-frame energies of $E > 10\,\mathrm{keV}$ (e.g., Saez, Chartas & Brandt 2009; Chartas et al. 2009; Saez & Chartas 2011) I measured the total source counts from the entire XIS bandpass (i.e., $0.6-10\,\mathrm{keV}$ in the observer frame) because the Fe K features are shifted to much lower energies due to the high red-shift of the AGN.

[2] http://darts.jaxa.jp/astro/suzaku/

Table 4.1: Source classifications.

| Source Type | Number |
|---|---|
| Sy $1.0-1.2$ | 17 |
| Sy 1.5 | 11 |
| Sy $1.8-1.9$ | 6 |
| NLSy 1 | 6 |
| BLRG | 6 |
| QSO | 5 |
| **Total** | **51** |

As highly-ionised outflows are thought to originate at relatively small distances from the central nucleus (e.g., Tombesi et al. 2011a, 2012a) it is important that the primary continuum emission from the central nucleus, rather than that which is reprocessed/scattered by circumnuclear material out of the line of sight, is observed directly such that the outflows can be detected. To this end I also excluded all Type-2 sources to make sure that *all* sources were optically-thin to X-rays below 10 keV.

Therefore only those sources with a Type $1.0-1.9$ orientation to the line of sight as per the classifications listed on the *NASA/IPAC Extragalactic Database* (hereafter NED), via the VERONCAT catalogue itself or through literary sources, were included. The radio-quiet AGN ESO 103-G035 ($z = 0.01329$) which, despite being classified as Type-2.0 in the VERONCAT and on NED is often regarded as a Type-1.9 Seyfert in the literature (e.g., Warwick, Pounds & Turner 1988) by virtue of the presence of a moderately broad H$\alpha$ line in its optical spectrum (Phillips et al. 1979), is also conservatively included in the sample.

Observation details for all sources included in the heterogeneously selected sample are listed in Table 4.4. In total, there are 99 observations of 51 AGN spanning a wide range of spectral types and radio-properties. As shown in Table 4.1 the sample is dominated by low-moderate inclination Seyfert $1.0-1.5$ galaxies (28/51; 34/51 if Narrow Line Seyfert 1s are included), and contains comparatively few high-inclination (Type

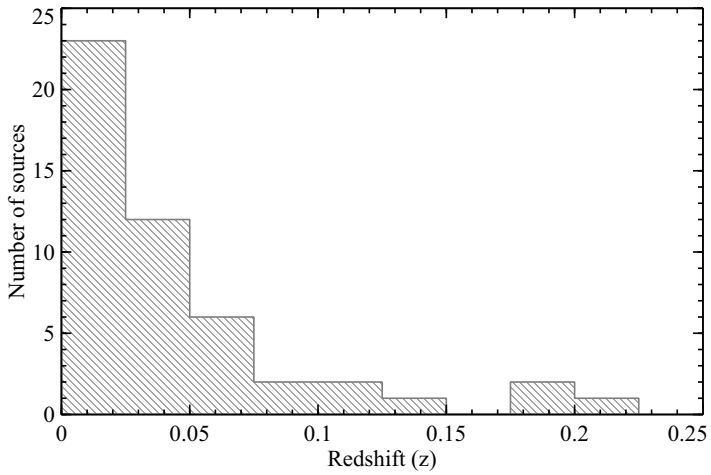


Figure 4.1: Histogram showing the distribution of sources included in this work. The high red-shift QSO APM 08279+5255 ($z = 3.91$) has been omitted for scaling purposes.

$1.8 - 1.9$) Seyferts (6/51). There are 6 radio-loud sources in the sample, including all 5 of the Broad Line Radio Galaxies (BLRGs) included in the Tombesi et al. (2010b) outflow case study, and 5 QSOs. The distributions of source red-shift and total $2 - 10$ keV counts (for the XIS-FI detector) are shown in Fig. 4.1 and Fig. 4.2, respectively. The AGN are predominantly local, with $\sim 90\%$ of the sample being located at a red-shift of $z \lesssim 0.1$, but also include more distant objects such as PDS 456 ($z = 0.1840$), 1H 0419−577 ($z = 0.1040$), PKS 0558−504 ($z = 0.1372$) and PBC J0839.7−1214 ($z = 0.198$). The gravitationally lensed quasar APM 08279+5545 is by far the most distant object in the sample with a red-shift of $z = 3.91$. As shown in Fig. 4.2 the total $2 - 10$ keV counts for the fitted spectra span two orders of magnitude but are approximately normally distributed about the peak and mean number of $10^5$ counts.

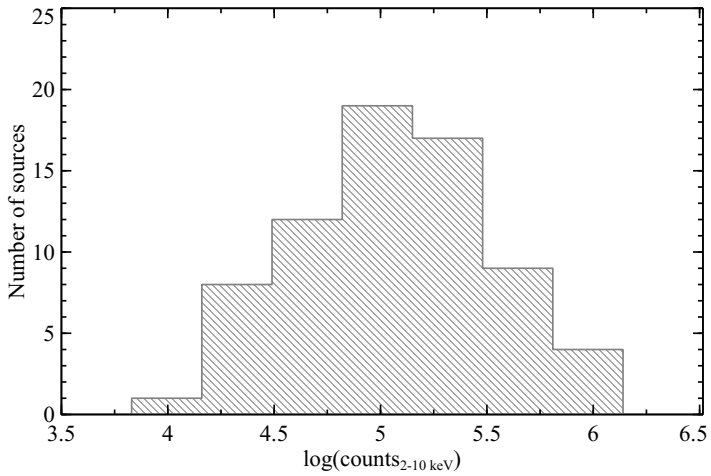


Figure 4.2: Histogram showing the logarithm of the total front-illuminated XIS $2-10$ keV counts in all fitted spectra. In stacked spectra (see table 4.4) the total co-added counts are considered here, rather than the counts in each individual sequence.

## 4.3 Data reduction

All of the observations included in the sample were reduced in accordance to the process outlined in §2.4. Source spectra were extracted from within circular regions of radius $1.5' \leq r < 3.0'$ to ensure good coverage of the source events, while background spectra were typically extracted from offset circles of the same radius with care taken to avoid the chip corners containing the Fe55 calibration sources. For intrinsically faint sources the background spectra were extracted from circles larger than those of the source and the ratio of source/background area was accounted for with an appropriate background scaling factor.

Where possible spectra obtained from the front-illuminated XIS detectors were combined into a single XIS-FI spectrum using MATHPHA in order to maximize signal-to-noise ($S/R$) in the Fe K band. Most of the observations in the sample have data available for at least the XIS 0 and XIS 3, with a further 22 also having data for the XIS 2 (see Table 4.4). For SWIFT J2127.4+5654 (OBSID 702122010) only data for the

front-illuminated XIS 3 camera are available because the XIS 0 was not operational during the observation. Spectra for the back-illuminated XIS 1 (hereafter XIS-BI) were also reduced using the same process and were analysed simultaneously as a separate input spectrum. All XIS spectra were grouped to have a minimum of 50 counts per energy bin to enable the use of the $\chi^2$ fit statistic. Net XIS exposures and the total background subtracted $2-10$ keV count rates (in the source rest-frame), for both the co-added XIS-FI and the XIS-BI detectors, are listed in Table 4.4.

For the PIN, all background subtracted spectra were binned to *at least* the $3\sigma$ level above background (typically $> 5\sigma$) to enable the use of the $\chi^2$ fit statistic. Hard X-ray faint and/or high background observations where source count rates were $< 4\%$ of the PIN total were not considered. Only APM 08279+5255 and PDS 456, amounting to a total of five observations, met this criterion (see Table 4.4). As with the XIS data, the final PIN exposures and the total background subtracted rest-frame $15-50$ keV counts are listed in Table 4.4.

## 4.4 Data analysis

I conducted a detailed broad-band spectral analysis of all sources using version 12.6.0q of the XSPEC spectral fitting package. I considered XIS-FI data between $0.6-10.0$ keV, whilst the XIS-BI were only included between $0.6-5.0$ keV due to decreasing S/N in the Fe K band which could hamper absorption line detection. All XIS spectra were excluded between $1.6-2.1$ keV due to uncertainties in calibration associated with the Si K detector edge. Where available, PIN data were included to cover at least the $15-40$ keV energy range. In all cases, the spectral models are modified by the appropriate column density of Galactic absorption using values taken from the Leiden/Argentine/Bonn Survey of Galactic H I (Kalberla et al. 2005) which were obtained from the on-line version of the $N_H$ FTOOL[3]. The values of Galactic absorption for each source are listed in Table 4.4.

[3]http://heasarc.gsfc.nasa.gov/cgi-bin/Tools/w3nh/w3nh.pl

Table 4.2: *Suzaku* observation details. *Columns:* (1) Source name; (2) Source type; (3) Cosmological red-shift according to the NED; (4) Galactic absorption column density, in units of $10^{21}\,\mathrm{cm}^{-2}$; (5) *Suzaku* observation ID; (6) Starting date of observation; (7) XIS(HXD) net exposures, in kilo-seconds; (8) Total number of (background subtracted) $2-10\,\mathrm{keV}$ counts for the (co-added) XIS-FI(BI) spectra, in units of $10^3$; (9) Total background subtracted PIN counts in the $15-50\,\mathrm{keV}$ band, in units of $10^3$.

| Source | Type | red-shift (z) | $N_{\mathrm{H}}^{\mathrm{Gal}}$ | OBSID | Date yyyy-mm-dd | Exposure XIS(PIN) | Source net counts XIS-FI(BI) | PIN |
|---|---|---|---|---|---|---|---|---|
| (1) | (2) | (3) | (4) | (5) | (6) | (7) | (8) | (9) |
| 1H 0419−577 | Sy 1.5 | 0.10400 | 0.126 | 702041010 | 2007-07-25 | 205.9(142.6) | 213.4(113.8) | 49.8 |
| | | | | 704064010 | 2010-01-16 | 246.2(122.8) | 89.6(46.5) | 36.6 |
| | | | | stacked[all] | ··· | ··· | 302.9(160.4) | 79.6 |
| 3C 111 | BLRG | 0.04850 | 2.910 | 703034010[a] | 2008-08-22 | 122.4(101.9) | 106.3(49.8) | 36.2 |
| | | | | 705040010[b] | 2010-09-02 | 80.7(67.9) | 199.7(95.4) | 26.6 |
| | | | | 705040020[c] | 2010-09-09 | 79.4(66.5) | 258.8(127.1) | 27.4 |
| | | | | 705040030[d] | 2010-09-16 | 80.4(65.6) | 251.0(127.2) | 28.1 |
| 3C 120 | BLRG | 0.03300 | 1.060 | 700001010[a]‡ | 2006-02-09 | 41.9(31.9) | 152.3(50.3) | 13.1 |
| | | | | 700001020[b]‡ | 2006-02-16 | 41.6(34.5) | 134.3(44.7) | 15.5 |
| | | | | 700001030[c]‡ | 2006-02-23 | 40.9(36.2) | 135.3(45.6) | 15.7 |
| | | | | 700001040[d]‡ | 2006-03-02 | 40.9(37.9) | 139.5(48.3) | 16.1 |
| | | | | stacked[bcd] | ··· | ··· | 409.1(138.5) | 44.6 |
| 3C 382 | BLRG | 0.05890 | 0.698 | 702125010 | 2007-04-27 | 130.6(114.3) | 274.5(136.1) | 45.5 |
| 3C 390.3 | BLRG | 0.05610 | 0.347 | 701060010 | 2006-12-14 | 99.4(92.1) | 151.6(71.8) | 38.3 |
| 3C 445 | BLRG | 0.05590 | 0.449 | 702056010 | 2007-05-25 | 139.8(109.5) | 41.9(20.2) | 40.8 |
| 4C +74.26 | BLRG | 0.10400 | 1.160 | 702057010 | 2007-10-28 | 91.6(87.3) | 107.0(36.5) | 33.8 |
| APM 08279+5255 [a] | QSO | 3.91000 | 0.411 | 701057010[a]‡ | 2006-10-12 | 102.3(···) | 4.6(1.6)[a] | ··· |
| | | | | 701057020[b]‡ | 2006-11-01 | 102.3(···) | 4.5(1.6)[a] | ··· |
| | | | | 701057030[c] | 2007-03-24 | 117.2(···) | 3.3(1.8)[a] | ··· |
| | | | | stacked[all] | ··· | ··· | 14.8(6.4)[a] | ··· |
| Ark 120 | Sy 1.0 | 0.03270 | 0.978 | 702014010 | 2007-04-01 | 100.9(89.5) | 152.1(78.7) | 32.3 |
| Ark 564 | NLSy1 | 0.02468 | 0.564 | 702117010 | 2007-06-26 | 100.0(81.3) | 102.7(54.4) | 23.5 |
| CBS 126 | Sy 1.2 | 0.07888 | 0.097 | 705042010 | 2010-10-18 | 101.5(84.2) | 21.6(10.7) | 24.8 |
| ESO 103−G035 | Sy 1.9 | 0.01329 | 0.764 | 703031010 | 2008-10-22 | 91.5(75.1) | 77.3(31.8) | 34.2 |

Continued on next page...

Table 4.2: Observation summary (continued)

| Source | Type | red-shift (z) | $N_{\rm H}^{\rm Gal}$ | OBSID | Date yyyy-mm-dd | Exposure XIS(PIN) | Source net counts XIS-FI(BI) | PIN |
|---|---|---|---|---|---|---|---|---|
| (1) | (2) | (3) | (4) | (5) | (6) | (7) | (8) | (9) |
| Fairall 9 | Sy 1.2 | 0.04700 | 0.316 | 702043010 | 2007-06-07 | 167.8(127.3) | 227.3(117.7) | 49.3 |
| | | | | 705063010 | 2010-05-19 | 229.3(162.2) | 226.9(103.9) | 56.8 |
| IC 4329A | Sy 1.2 | 0.01610 | 0.461 | 702113010[a] | 2007-08-01 | 25.5(20.1) | 131.0(64.8) | 11.4 |
| | | | | 702113020[b] | 2007-08-06 | 30.6(24.1) | 197.8(100.1) | 15.4 |
| | | | | 703113030[c] | 2007-08-11 | 24.2(22.1) | 160.6(67.1) | 14.5 |
| | | | | 703113040[d] | 2007-08-16 | 24.2(18.9) | 133.3(67.1) | 11.5 |
| | | | | 703113050[e] | 2007-08-20 | 24.0(17.5) | 83.2(40.9) | 9.4 |
| | | | | stacked[all] | ··· | ··· | 712.7(359.0) | 61.7 |
| IGR J16185−5928 | NLSy1 | 0.03500 | 2.070 | 702123010 | 2008-02-09 | 76.7(69.6) | 24.1(8.1) | 15.9 |
| IGR J21247+5058 | Sy 1.0 | 0.0200 | 10.000 | 702027010 | 2007-04-16 | 85.0(66.4) | 233.1(103.7) | 38.4 |
| MCG -02-14-009 | Sy 1.0 | 0.02845 | 0.948 | 703060010 | 2008-08-28 | 142.2(120.0) | 24.1(10.6) | 20.5 |
| MCG -2-58-22 | Sy 1.5 | 0.04686 | 0.291 | 704032010 | 2009-12-02 | 139.0(98.0) | 324.0(129.6) | 38.3 |
| MCG -5-23-16 | Sy 1.9 | 0.00849 | 0.800 | 700002010 | 2005-12-07 | 95.7(79.7) | 626.8(198.5) | 54.0 |
| MCG -6-30-15 | Sy 1.2 | 0.00775 | 0.392 | 700007010[a]‡ | 2006-01-09 | 143.3(118.9) | 504.2(167.0) | 51.3 |
| | | | | 700007020[b]‡ | 2006-01-23 | 98.5(76.8) | 304.6(105.0) | 35.1 |
| | | | | 700007030[c]‡ | 2006-01-27 | 96.7(89.8) | 327.5(109.1) | 38.7 |
| | | | | stacked[all] | ··· | ··· | 1136.3(381.1) | 120.3 |
| MCG +8-11-11 | Sy 1.5 | 0.02050 | 1.840 | 702112010 | 2007-09-17 | 98.8(82.9) | 295.8(141.2.2) | 42.1 |
| MR 2251−178 | RQQ | 0.06400 | 0.242 | 704055010 | 2009-05-07 | 136.9(103.8) | 330.9(171.6) | 38.7 |
| Mrk 79 | Sy 1.2 | 0.02220 | 0.527 | 702044010 | 2007-04-03 | 83.7(76.9) | 70.5(36.6) | 20.1 |
| Mrk 110 | Sy 1.0 | 0.03530 | 0.130 | 702124010 | 2007-11-02 | 90.9(80.4) | 93.7(46.4) | 29.4 |
| Mrk 205 | Sy 1.0 | 0.07085 | 0.240 | 705062010 | 2010-05-22 | 101.5(85.3) | 36.0(15.9) | 29.3 |
| Mrk 279 | Sy 1.0 | 0.03050 | 0.152 | 704031010 | 2009-05-14 | 160.4(139.8) | 43.8(23.5) | 40.3 |
| Mrk 335 | NLSy1 | 0.02580 | 0.366 | 701031010‡ | 2006-06-21 | 151.3(131.7) | 162.6(49.0) | 45.9 |
| Mrk 359 | Sy 1.5 | 0.01739 | 0.426 | 701082010 | 2007-02-06 | 107.5(96.1) | 27.2(13.6) | 8.8 |
| Mrk 509 | Sy 1.5 | 0.03440 | 0.425 | 701093010[a]‡ | 2006-04-25 | 24.6(14.5) | 93.8(30.8) | 6.6 |
| | | | | 701093020[b]‡ | 2006-10-14 | 25.9(21.2) | 122.9(43.8) | 10.5 |
| | | | | 701093030[c] | 2006-11-15 | 24.5(17.3) | 73.9(40.8) | 8.0 |
| | | | | 701093040[d] | 2006-11-27 | 33.1(27.6) | 92.4(49.3) | 12.5 |
| | | | | stacked[bcd] | ··· | ··· | 289.3(133.8) | 30.8 |

Continued on next page...

Table 4.2: Observation summary (continued)

| Source | Type | red-shift (z) | $N_{\rm H}^{\rm Gal}$ | OBSID | Date yyyy-mm-dd | Exposure XIS(PIN) | Source net counts XIS-FI(BI) | PIN |
|---|---|---|---|---|---|---|---|---|
| (1) | (2) | (3) | (4) | (5) | (6) | (7) | (8) | (9) |
| | | | | 705025010 | 2010-11-21 | 102.1(85.7) | 325.2(171.4) | 37.8 |
| Mrk 766 | Sy 1.0 | 0.01290 | 0.178 | 701035010 | 2006-11-16 | 97.9(90.5) | 175.5(108.5) | 31.6 |
| | | | | 701035020 | 2007-11-17 | 59.4(47.7) | 73.0(40.3) | 17.1 |
| Mrk 841 | Sy 1.5 | 0.03640 | 0.222 | 701084010[a] | 2007-01-22 | 51.8(43.7) | 36.3(18.0) | 14.5 |
| | | | | 701084020[b] | 2007-07-23 | 50.9(44.4) | 35.9(18.4) | 16.1 |
| | | | | stacked[all] | ··· | ··· | 72.2(37.4) | 31.3 |
| NGC 1365 | Sy 1.8 | 0.00546 | 0.134 | 702047010 | 2008-01-21 | 160.5(136.6) | 96.8(48.2) | 53.9 |
| | | | | 705031010 | 2010-06-27 | 151.6(114.3) | 35.5(15.9) | 42.2 |
| | | | | 705031020 | 2010-07-15 | 302.2(231.5) | 45.8(21.4) | 76.2 |
| NGC 2992 | Sy 1.9 | 0.00771 | 0.487 | 700005010[a]‡ | 2005-11-06 | 38.8(29.9) | 23.0(6.7) | 9.8 |
| | | | | 700005020[b]‡ | 2005-11-19 | 39.7(31.9) | 39.6(13.1) | 10.4 |
| | | | | 700005030[c]‡ | 2005-12-13 | 46.9(41.5) | 41.9(12.8) | 14.4 |
| | | | | stacked[all] | ··· | ··· | 84.7(25.0) | 36.1 |
| NGC 3227 | Sy 1.5 | 0.00386 | 0.199 | 703022010 | 2008-10-28 | 58.9(48.1) | 117.7/60.8 | 22.1 |
| | | | | 703022020 | 2008-11-04 | 53.7(46.7) | 38.5(17.3) | 19.6 |
| | | | | 703022030 | 2008-11-12 | 56.6(46.7) | 61.0(28.5) | 20.4 |
| | | | | 703022040 | 2008-11-20 | 64.6(43.4) | 24.1(11.8) | 15.1 |
| | | | | 703022050 | 2008-11-27 | 79.4(37.4) | 69.7(32.9) | 15.4 |
| | | | | 703022060 | 2008-12-02 | 51.4(36.9) | 32.1(14.7) | 15.4 |
| NGC 3516 | Sy 1.5 | 0.00884 | 0.345 | 100031010‡ | 2005-10-12 | 134.6(115.4) | 233.3(75.4) | 50.7 |
| | | | | 704062010 | 2009-10-28 | 251.4(178.2) | 149.0(73.4) | 55.6 |
| NGC 3783 | Sy 1.5 | 0.00973 | 0.991 | 701033010‡ | 2006-06-24 | 75.7(68.3) | 302.4(103.0) | 32.2 |
| | | | | 704063010 | 2009-07-10 | 172.8(174.0) | 472.1(234.0) | 84.0 |
| NGC 4051 | NLSy1 | 0.00234 | 0.115 | 700004010‡ | 2005-11-10 | 119.6(112.6) | 76.4(24.3) | 42.0 |
| | | | | 703023010 | 2008-11-06 | 274.5(204.5) | 349.6(132.5) | 72.0 |
| | | | | 703023020 | 2008-11-23 | 78.4(58.5) | 72.0(35.0) | 21.3 |
| NGC 4151 | Sy 1.5 | 0.03320 | 0.230 | 701034010 | 2006-12-18 | 125.0(123.5) | 218.2(97.5) | 75.8 |
| NGC 4395 | Sy 1.8 | 0.00106 | 0.135 | 702001010 | 2007-06-02 | 101.5(95.0) | 19.4(9.2) | 30.4 |
| NGC 4593 | Sy 1.0 | 0.00900 | 0.189 | 702040010 | 2007-12-15 | 118.8(101.6) | 66.3(25.1) | 34.7 |
| NGC 5506 | Sy 1.9 | 0.00618 | 0.408 | 701030010[a]‡ | 2006-08-08 | 47.8(38.6) | 372.5(119.7) | 25.4 |

Continued on next page...

Table 4.2: Observation summary (continued)

| Source | Type | red-shift (z) | $N_{\rm H}^{\rm Gal}$ | OBSID | Date yyyy-mm-dd | Exposure XIS(PIN) | Source net counts XIS-FI(BI) | PIN |
|---|---|---|---|---|---|---|---|---|
| (1) | (2) | (3) | (4) | (5) | (6) | (7) | (8) | (9) |
| | | | | 701030020[b]‡ | 2006-08-11 | 53.3(44.8) | 438.9(141.2) | 29.9 |
| | | | | 701030030[c] | 2007-01-31 | 57.4(44.7) | 281.1(133.5) | 29.1 |
| | | | | stacked[all] | ··· | ··· | 1067.5(392.4) | 82.2 |
| NGC 5548 | Sy 1.5 | 0.01718 | 0.155 | 702042010[a] | 2007-06-18 | 31.1(25.6) | 11.0(5.3) | 7.5 |
| | | | | 702042020[b] | 2007-06-24 | 35.9(31.2) | 21.7(10.8) | 9.3 |
| | | | | 702042040[c] | 2007-07-08 | 30.7(27.0) | 35.9(16.4) | 8.5 |
| | | | | 702042050[d] | 2007-07-15 | 30.0(24.5) | 23.3(10.7) | 7.7 |
| | | | | 702042060[e] | 2007-07-22 | 28.9(23.1) | 43.3(19.9) | 7.9 |
| | | | | 702042070[f] | 2007-07-29 | 31.8(27.6) | 31.6(14.5) | 8.5 |
| | | | | 702042080[g] | 2007-08-05 | 38.8(30.4) | 20.5(10.0) | 9.6 |
| | | | | stacked[all] | ··· | ··· | 187.4(107.8) | 66.3 |
| NGC 7213 | Sy 1.0 | 0.00584 | 0.106 | 701029010‡ | 2006-10-22 | 90.7(84.3) | 370.2(145.0) | 35.3 |
| NGC 7469 | Sy 1.0 | 0.01630 | 0.445 | 703028010 | 2008-06-24 | 112.1(85.3) | 116.2(58.2) | 32.3 |
| PBC J0839.7−1214 | QSO | 0.19787 | 0.568 | 705007010 | 2010-05-08 | 80.6(···) | 35.5(17.7) | ··· |
| PDS 456 | RQQ | 0.18400 | 1.960 | 701056010 | 2007-02-24 | 190.6(···) | 34.0(16.7) | ··· |
| | | | | 705041010 | 2011-03-16 | 125.5(···) | 17.0(7.9) | ··· |
| PG 1211+143 | RQQ | 0.08090 | 0.274 | 700009010‡ | 2005-11-24 | 97.6(78.8) | 19.4(5.9) | 8.9 |
| PKS 0558−504 | NLSy1 | 0.13720 | 0.337 | 701011010[a] | 2007-01-17 | 20.6(17.6) | 11.8(5.9) | 4.8 |
| | | | | 701011020[b] | 2007-01-18 | 18.9(16.7) | 16.0(8.1) | 6.5 |
| | | | | 701011030[c] | 2007-01-19 | 21.3(17.8) | 12.0(6.2) | 6.8 |
| | | | | 701011040[d] | 2007-01-20 | 19.7(16.0) | 18.3(8.2) | 6.3 |
| | | | | 701011050[e] | 2007-01-21 | 19.5(15.2) | 17.1(8.2) | 5.4 |
| | | | | stacked[all] | ··· | ··· | 76.2(44.6) | 21.0 |
| RBS 1124 | Sy 1.2 | 0.20800 | 0.152 | 702114010 | 2007-04-14 | 86.2(83.0) | 16.6(7.4) | 21.5 |
| SW J2127.4+5654 | Sy 1.0 | 0.01440 | 7.650 | 702122010† | 2007-12-09 | 91.7(83.3) | 69.5(81.4) | 31.2 |
| TON S180 | NLSy1 | 0.06198 | 0.136 | 701021010 | 2006-12-09 | 120.7(102.4) | 43.5(-) | 27.2 |

† Only the XIS 3 spectrum was available during the observation of SWIFT J2127.4+5654;
‡ Indicates that the XIS 2 was operational during the observation and is included as part of the co-added XIS-FI spectrum;
[a] The total net source counts listed in column (8) for APM 08279+5255 are taken from $0.6 - 10$ keV in the observer frame. See text for further details.

I included a constant multiplicative factor in all models to account for the XIS/PIN cross-normalisation whose value depends not only on the nominal pointing of the observation, but also the version of the *Suzaku* pipeline with which the data have been processed. The current XIS/PIN ratios suitable for version 2 processed data are 1.16(1.18) for the XIS(HXD) nominal pointing positions[4]. However, the cross-normalisation was up to $\sim 5-6\%$ lower for data processed with version 1 of the pipeline, corresponding to a XIS/PIN ratio of 1.09(1.13)[4] in the XIS(PIN) nominal pointing positions. While the difference is only small the additional uncertainty can have a considerable effect on the continuum parameters at $E > 10\,\mathrm{keV}$, particularly in hard X-ray bright sources with a high PIN count rate where the model can become driven by the hard X-ray band. To account for any systematic effects associated with the instrumental cross-calibration I therefore allow the cross-normalisation in each model to vary $\pm 5\%$ about the values suggested by the *Suzaku* team to take into account any systematic errors.

There are 20 AGN in the sample which have two or more *Suzaku* observations. For APM 08279+5255, IC 4329A, MCG -6-30-15, Mrk 841, NGC 5506, NGC 5548 and PKS 0558−504 the different observations are similar in spectral shape. This allows them to be co-added using the appropriate relative weighting factors to take into account differences in individual exposures, with the resultant time-averaged spectra for these sources being used in all subsequent analyses. 1H 0419−577 and NGC 2992 both had observations which were taken in different *Suzaku* nominal pointing positions which could influence co-adding. However, the detector effective area in these cases was always consistent to within $\pm 10\%$ and so the spectra were still co-added using the mean of the response files. Any additional systematic uncertainty introduced was adequately accounted for by the variable XIS/PIN cross-normalisation. For 3C 120 and Mrk 509, which both showed notable variability between observations, I fitted their available spectra jointly depending on the extent of their spectral variability between epochs. In 3C 120 I followed the analysis method of Kataoka et al. (2007) and Tombesi et al. (2010b) by co-adding OBSIDs 700001020, 70001030 and 70001040, which are all of a similar

[4]http://www.astro.isas.jaxa.jp/suzaku/doc/suzakumemo/suzakumemo-2007-11.pdf

spectral shape and flux level, and fitted them jointly with OBSID 700001010 which has a more prominent underlying soft-excess. For Mrk 509, which is well known for having a strong soft-excess (Mehdipour et al. 2011) I fitted OBSID 701093010, the stacked OBSIDs 701093020+701093030+701093040, and OBSID 705025010 simultaneously to account for the observed variability in the soft X-ray band.

The remaining nine sources with more than one observation (3C 111, Fairall 9, Mrk 766, NGC 1365, NGC 3227, NGC 3516, NGC 3783, NGC 4051 and PDS 456) show strong spectral variability in both the shape of the spectrum and/or drastic changes in flux state which made co-adding impractical. For these sources I fitted the available spectra simultaneously, and a model was constructed to describe the observed spectral variability with as few additional free parameters as possible. For NGC 1365, OBSIDs 702047010 and 705031010 are dominated by very deep Fe K absorption lines. These lines are not clearly apparent in OBSID 705031020, possibly due to the source dropping into a quasi-scattering-dominated state (see Maiolino et al. 2010 for details of the variability patterns in this source). For simplicity I therefore only fitted OBSID 702047010 and OBSID 705031010 simultaneously, and fitted OBSID 705031020 separately.

The $\chi^2$ minimization technique is used throughout this analysis, with all statistical errors quoted to the 90% confidence level ($\Delta\chi^2 = 2.71$ for one parameter of interest). Where I quote statistical significance of model components in terms of a $\Delta\chi^2$ value I have removed the component from the model and refitted the data to ensure that the order in which components are added to the model has no influence on the derived statistics. When I refer to statistical changes to a fit a positive $\Delta\chi^2$ denotes a worsening of the fit, while a negative $\Delta\chi^2$ indicates a statistical improvement. Finally, positive outflow velocities correspond to a net blue-shift relative to the systemic velocity of the host galaxy, while a negative velocity indicates a net red-shift.

### 4.4.1 Model Construction

All spectra were first fitted with a power-law modified solely by Galactic absorption. Additional components were added to the model and retained provided their significance

exceeded the 99% confidence level by the F-test. Any emission lines in the soft X-ray band were fitted with narrow Gaussians ($\sigma \sim 5\,\mathrm{eV}$). For multi-epoch sources I initially devised a broad-band fit to the observation with the highest flux. Later observations were then sequentially added to the model, and I allowed continuum/absorption parameters to vary independently until a simultaneous fit to all spectra had been achieved using as few free parameters as possible. Once I had found a statistically acceptable fit to the broad-band spectrum of each source, I fitted any necessary emission components and then performed a systematic and methodical search for Fe K absorption lines between $5 - 10\,\mathrm{keV}$ using contour-plots in the energy-intensity plane (§4.4.2) in conjunction with MC simulations (§2.2.6).

The specific approach that I took for modelling individual spectral components are outlined below, and the continuum parameters for each source are noted in Table B.1 and those for the warm absorber are listed in Tables B.2 and B.3 for single- and multi-epoch spectra, respectively. A description of the underlying modelling assumptions and associated caveats is presented in §4.7.1.

### Warm absorption I: Fully covering

Depending on the properties of the intervening material (such as its ionisation state and column density) absorption by circumnuclear material can add significant spectral curvature to the observed X-ray spectrum and can therefore have a direct effect on the continuum and line parameters measured in broad-band models. In this study I model warm absorption components using a suite of XSTAR (v. 2.2.1bc) tables which are all generated assuming input values which are 'typical' for local Seyfert galaxies[5] (e.g., Tombesi et al. 2011a). The XSTAR tables cover a wide range of parameter space in terms of column densities [$18 < \log(N_{\mathrm{H}}/\mathrm{cm}^{-2}) \leq 24$], and ionisation parameter

[5]Absorption grids are described by: an illuminating photon index of $\Gamma = 2.1$, a gas density of $n = 10^{10}\,\mathrm{cm}^{-3}$, a micro-turbulent velocity of $v_{\mathrm{turb}} = 100\,\mathrm{km\,s}^{-1}$, and an integrated model luminosity of $L = 10^{44}\,\mathrm{erg\,s}^{-1}$ between $1 - 1000\,\mathrm{Rydbergs}$.

$[-3 < \log(\xi/\mathrm{erg\,cm\,s^{-1}}) \leq 6]$ which makes them well suited for accounting for all manner of warm absorption.

I include zones of fully-covering warm absorption in models where they are necessary to achieve a good fit to the soft X-ray band; in some cases more than one absorption zone is needed. In these cases I allow the column density and ionisation parameter of each zone to vary independently, which corresponds to an absorption geometry comprising of multiple layers of gas. At the energy resolution of the XIS CCDs the bound-bound absorption lines required to constrain the outflow velocity of individual layers of soft X-ray absorption are unresolved, and all absorption zones are therefore fitted as stationary in the source rest-frame (i.e., fixed outflow velocities of $v_{\rm out} = 0\,\mathrm{km\,s^{-1}}$). Allowing the outflow velocity of the soft X-ray absorber to vary always has a negligible effect on the reported Fe K absorption line parameters which are reported in Table 4.3.

### Warm absorption II: Partial covering

In addition to fully-covering absorption, I also consider the possibility that the sight-line to a source is only partially covered. In this absorption geometry a fraction $f_{\rm cov} < 1$ of the source flux is absorbed with the remaining $1 - f_{\rm cov}$ leaking through the absorption layer. For simplicity I account for partially-covering absorption layers through a customized version of the `zxipcf` model[6] which enables the effects of partially-ionised partially-covering absorption to be accounted for without needing to use complicated nested power-laws and XSTAR tables (see Reeves et al. 2008a.). As in `zxipcf` the free parameters in my customized table model are column density ($N_{\rm H}$), ionisation parameter ($\log \xi$), covering fraction ($f_{\rm cov}$) and red-shift relative to the observer ($z_{\rm o}$). The model is based on the same tables as discussed previously in §4.4.1 and therefore has a slightly lower turbulent velocity than `zxipcf`, at $v_{\rm turb} = 100\,\mathrm{km\,s^{-1}}$, but covers the same parameter space in terms of column density and ionisation parameter.

[6]The standard `zxipcf` uses a specific grid with the following parameters: $\Gamma = 2.2$, $n = 10^{10}\,\mathrm{cm^{-3}}$, $v_{\rm turb} = 200\,\mathrm{km\,s^{-1}}$, $L = 10^{44}\,\mathrm{erg\,s^{-1}}$

Partially-covering absorption can have a strong effect on the observed continuum with moderate column densities of material ($N_{\rm H} \sim 10^{23}\,{\rm cm}^{-2}$) adding considerable spectral curvature at $E < 10\,{\rm keV}$ (Reeves et al. 2004; Risaliti et al. 2005; Braito et al. 2011; Turner et al. 2011). Bound-free transitions in similar column density material can also fit broad residual emission profiles in the Fe K band (Inoue & Matsumoto 2003; Miller, Turner & Reeves 2008, 2009; Tatum et al. 2012), and partial-covering by Compton-thick material ($N_{\rm H} \gtrsim 10^{24}\,{\rm cm}^{-2}$) can reduce the observed emission below 10 keV with the true intrinsic continuum only becoming apparent at higher energies as a 'hard excess' of emission relative to that expected from standard reflection models (Reeves et al. 2009; Turner et al. 2009; Risaliti et al. 2009; Tatum et al. 2013).

I only include partially-covering absorbers if and when they are required by the data at the $P_{\rm F} \geq 99\%$ confidence level, and a satisfactory fit to the data could not be achieved using solely fully-covering absorption. Several AGN appear to need multiple partially-covering absorption zones which suggests the presence of a clumpy stratified absorber along the line of sight. Again, all absorber parameters are listed in Tables B.2 and B.3 in Appendix B. In some circumstances the need of a high column density partially-covering component can be contingent on the means with which the underlying reflection component is modelled leading to some model degeneracies. However, as I go on to discuss in §4.7.1 partial-covering has little measurable effect on the parameters measured for any highly-ionised absorption line systems, regardless of whether the hard X-ray data are fitted with reflection or not.

### The soft-excess

Relative to the low energy extrapolation of the power-law continuum in the $2-10\,{\rm keV}$ band the X-ray spectra of AGN often show a smooth increase in emitted flux below $\sim 1\,{\rm keV}$ (Turner & Pounds 1988; Porquet et al. 2004a; see Chapter 1). thermal temperature of this 'soft-excess' suggests it is unlikely to be the direct emission from a standard accretion disc without additional reprocessing (Sobolewska & Done 2007; Done et al. 2012). Alternative explanations posit that the soft-excess may be due to an increase

in optical depth associated with circumnuclear O VII-VIII and Fe L-shell transitions at $E \lesssim 0.7\,\mathrm{keV}$ which can enhance either the transmitted or reflected flux along the sight-line through smeared absorption (e.g., Chevallier et al. 2006; Sobolewska & Done 2007; Done & Nayakshin 2007) or blurred reflection (e.g., Crummy et al. 2006; Nardini et al. 2011; Brenneman et al. 2011; Nardini, Fabian & Walton 2012) effects. Furthermore, in some sources (e.g., Mrk 766, Miller et al. 2007; MCG -6-30-15, Miller, Turner & Reeves 2008) the 'excess' could simply be a product of complex absorption and just be the manifestation of opacity around $\sim 1 - 2\,\mathrm{keV}$.

Regardless of its true physical origin I use the `bbody` model to take a purely phenomenological approach to fit the soft-excess. This model, which represents the emission from a constant temperature blackbody, is not necessarily physically motivated but modelling the soft-excess in this manner offers a simple parametrisation of any 'excess' soft X-ray emission which is sufficient to get a good handle on the underlying continuum parameters. For completeness I also investigate the effects that other means of modelling the soft-excess may have on any Fe K-band absorption lines, §4.7.1. Roughly half of the sources in the sample (24/51; $\sim 47\%$) show evidence for a soft-excess, of which 22/24 are fit with a `bbody` component. In 3C 120 and Mrk 509 the soft-excess is very broad and extends beyond that which can be fitted with a simple blackbody. In these sources I instead fitted the excess with a second power-law with a softer photon-index.

### Cold reflection

Cold reflection from large column densities of neutral or lowly ionised material outside of the sight-line can have a strong influence on the observed X-ray spectrum. The strongest observational characteristics of such reflection include the Compton-reflection hump at $\sim 30 - 40\,\mathrm{keV}$ and the almost ubiquitous Fe K$\alpha$ and Fe K$\beta$ fluorescence lines at $\sim 6.4\,\mathrm{keV}$ and $\sim 7.06\,\mathrm{keV}$ (Nandra et al. 2007; Shu, Yaqoob & Wang 2010), respectively. Compton down-scattering of both K$\alpha$ line photons and high energy continuum emission also gives rise to a 'Compton shoulder' at $\sim 6.2\,\mathrm{keV}$ (e.g., Matt 2002; Yaqoob & Murphy 2011) and resonant line emission in the soft X-ray band (e.g., Ross & Fabian 2005b; García &

Kallman 2010) which can further complicate the emergent spectrum.

Naturally, owing to the important effect it can have on the observed X-ray spectrum there are numerous models available for modelling the reflection component (e.g., `pexrav/pexriv`, Magdziarz & Zdziarski 1995; `pexmon`, Nandra et al. 2007; `reflionx`, Ross & Fabian 2005b; `xillver`[7], García & Kallman 2010; `MYTorus`[8], Murphy & Yaqoob 2009). I use a combination of `reflionx` and `pexrav` throughout this study, both of which are publicly available and extensively used in the literature. The primary reason for this is the way in which the other models compute the reflected continuum. `reflionx` interpolates the observed reflection spectrum from a pre-generated grid of table models which means that it is significantly faster at fitting spectra than, for example, `pexrav`, `pexriv` or `pexmon`, which analytically calculate the Compton reflection spectrum on the fly at each step of the fitting process, or `MYTorus` which requires the model to be tailored for each individual source. Using `reflionx` to fit the reflected spectrum ensures the least time-consuming MC simulations which is important when dealing with a large sample of objects such as that considered here. Secondly, when fitting reflection continuum without the simultaneous constraint of the Fe K$\alpha$ line the reflection fraction, $R$, reported by `pexrav` (and `pexriv`) can become degenerate with the photon-index of the primary power-law, with a hardening reflection component compensated for by a softer primary continuum. By simultaneously fitting the reflection continuum, the Fe K$\alpha$ line and the soft X-ray resonance lines, `reflionx` is able to overcome these modelling degeneracies which leads to a confident constraint on the contribution of the reflection continuum to the observed spectrum. `reflionx` also has the additional advantage of allowing the ionisation state of the reflector, $\xi$, to be a free parameter which enables it to model changes in the Fe K$\alpha$ emitted flux and Fe K-shell edge profile associated with the reflector's ionisation state. It is important to stress, however, that equivalent results are found for the detected Fe K absorbers if `pexmon` is used instead, although the resultant MC simulations take significantly longer to compute which effectively prohibits its uniform use throughout the

[7]The `xillver` reflection model is not currently available in the public domain and is therefore not considered for use in this work.

[8]The `MYTorus` model and documentation are publicly available at: www.mytorus.com

sample.

I initially fitted all sources with `pexrav` to determine the parameters of the Fe K$\alpha$ and Fe K$\beta$ lines. `pexrav` was then replaced with `reflionx` and I then systematically searched for additional atomic features in the Fe K band. A total of 11 sources have best-fitting reflector Fe abundances which are non-Solar, with 4 requiring a slight over-abundance (MCG +8-11-11, NCG 4593, NCG 7213, NCG 7469) and 7 with an under-abundance (4C +74.26, Fairall 9, IC 4329A, IGR J16185−5928, Mrk 335, Mrk 359, Mrk 841). These abundances are most likely a by-product of `reflionx` assuming a face-on reflection geometry, and is a caveat which is discussed in greater detail in §4.7.1. PDS 456 and APM 08279+5255 are not fitted with a reflection component because they lack sufficient counts in the HXD/PIN.

### 4.4.2 Searching for Fe K absorption

Once I had found a statistically acceptable fit to the broad-band continuum, i.e., all necessary absorption regions, soft X-ray emission lines and continuum components had been included in the model, I performed a thorough statistically-driven search for additional spectral features between $5 - 10$ keV. The method I used consists of inspecting the $|\Delta\chi^2|$ deviations from the best-fit continuum model using inverted contour plots in the energy-intensity plane of the Fe K band. The method of calculating the contour plots was adapted from the method outlined in Tombesi et al. (2010a), and was carried out as follows:

(i) an unresolved ($\sigma = 10$ eV) Gaussian was stepped across the entire $5 - 10$ keV energy band of the baseline continuum model in 25 eV intervals, with normalisation allowed to adopt both positive and negative values to probe for spectral lines in both emission and absorption. All of the other spectral components were allowed to be free;

(ii) after each step the $\Delta\chi^2$ deviation was recorded generating a $\chi^2$ distribution of the entire Fe K band relative to the baseline continuum model;

(iii) confidence contours for the grid of $\chi^2$ values were plotted according to $\Delta\chi^2$ deviations of $-2.3$, $-4.61$, $-9.21$, $-13.82$, $-18.42$ from the baseline model, which correspond to confidence intervals of 68%, 90%, 99%, 99.9% and 99.99%, respectively. The final black contour, which was computed as $\Delta\chi^2 = +0.5$, is intended to represent a reference level for the baseline continuum model.

The energy-intensity contour plots produced with this method yield a powerful means of searching for additional emission or absorption components present in the Fe K band while also visually assessing their energy, intensity and rough statistical requirement relative to the underlying continuum model.

There are, however, a number of atomic features between $6.0 - 8.0\,\mathrm{keV}$ which can complicate the detection of absorption line systems. Such features include ionised emission lines from Fe XXV and Fe XXVI expected at $\sim 6.63 - 6.7\,\mathrm{keV}$ and $\sim 6.97\,\mathrm{keV}$, respectively, the Fe K-shell edge complex at $\sim 7.1\,\mathrm{keV}$, and any broad Fe line profile due to general relativistic or scattering effects. It is important to account for these emission residua prior to searching for absorption lines, particularly in sources which show evidence for a broad residual as the broadness of the profile can effectively mask the presence of low velocity absorption systems in the raw data. For a given continuum model I searched for highly-ionised absorption lines in the Fe K-band using the following steps:

(i) first, I generated an energy-intensity contour plot using the method outlined above;

(ii) I then inspected the contour plot to determine whether there were any intense ionised emission and absorption lines present in the data with confidence contours of $> 99\%$;

(iii) where there was evidence for a broad emission residual at an F-test significance of at least $P_{\mathrm{F}} > 99\%$ I fitted them with either a broadened Gaussian (with $\sigma$-width a free parameter) or a `diskline`[9] depending on the asymmetry of the observed

[9]For simplicity, the `diskline` was fitted with an assumed rest-frame energy of $E = 6.4\,\mathrm{keV}$, and the emissivity profile of the broad emission (i.e., how centrally concentrated it is) was assumed to follow a power-law with a slope of $q = -2.5$ (e.g., Patrick et al. 2011b). The inner emission radius ($R_{\mathrm{in}}$), outer radius ($R_{\mathrm{out}}$) and disc inclination ($i$), were left free to vary.

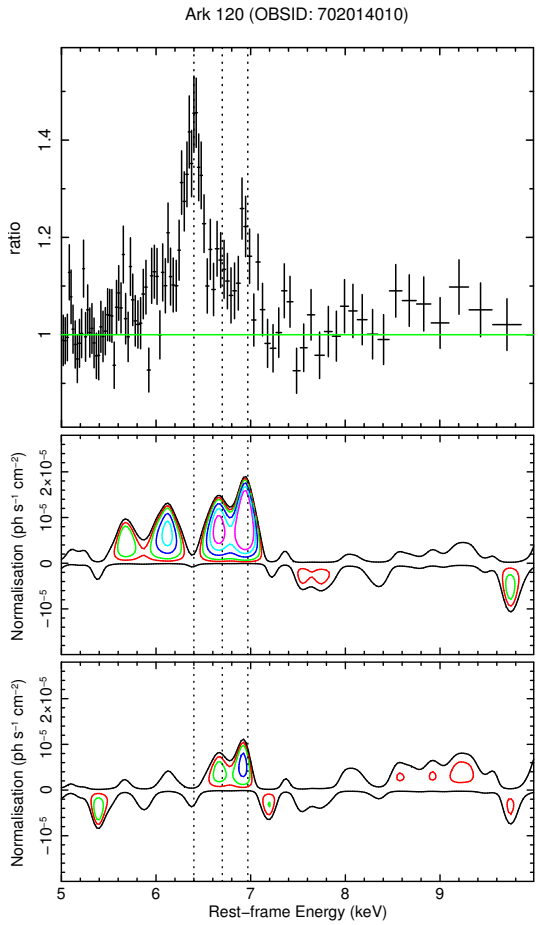


Figure 4.3: *Top panel:* Ratio plot showing the residuals remaining in the Fe K band of Ark 120 (OBSID 702014010) once all atomic lines have been removed and reflection fitted with `pexrav`; *Middle panel:* confidence contours showing deviations from the best-fit model when the Fe K$\alpha$ and Fe K$\beta$ lines have been fitted with `reflionx` and a narrow Gaussian respectively. The closed significance contours corresponding (from outer to inner) to $\Delta\chi^2$ improvements of $-2.3$ ($P_{\rm F} = 68\%$), $-4.61$ ($P_{\rm F} = 90\%$), $-9.21$ ($P_{\rm F} = 99\%$), $-13.82$ ($P_{\rm F} = 99.9\%$) and $-18.42$ ($P_{\rm F} = 99.99\%$) relative to the best-fit continuum model are shown in red, green, blue, cyan and magenta, respectively. The magenta contours in the middle panel indicate that the broad emission residual is significant at the $> 99.99\%$ level and that an additional component is required in the model; *Bottom panel:* the remaining confidence contours once the broad profile has been fitted. The broad residua are no longer detected but an additional Fe XXVI emission line is present at $E \sim 6.97$ keV which is significant at $> 99\%$. In all panels the dashed vertical lines indicate the expected rest-frame energies of (from left to right) the Fe K$\alpha$ fluorescence line, Fe XXV He$\alpha$ and Fe XXVI Ly$\alpha$, respectively.

profile, and a second intermediate contour plot was generated to determine whether any further components were needed by the model. As before, all other model parameters were allowed to vary freely during this process. If there was no evidence for a broad profile I did not generate an additional contour plot and instead moved directly onto the next step;

(iv) where narrow emission profiles were detected with a resolved confidence contour of $> 99\%$ they were fitted with unresolved ($\sigma = 10\,\mathrm{eV}$ fixed) Gaussian profiles provided they were required by the data at $P_{\mathrm{F}} > 99\%$ (i.e., corresponding to $\Delta\chi^2 < -9.21$ for two parameters of interest);

(v) once all emission profiles had been accounted for I again checked for the presence of any blue-shifted Fe K absorption lines at $E > 6.7\,\mathrm{keV}$. If no absorption lines were present the search was ended at this step and I reported the best-fit continuum and Fe K emission line parameters in the relevant tables of Appendix B, and moved onto the next observation in the sample;

(vi) otherwise, where absorption troughs were clearly detected with a confidence contour of $> 99\%$ I parametrised the line(s) using inverted Gaussians with $\sigma$-width initially fixed at either 10 eV, 30 eV or 100 eV depending on which provided the greatest improvement to $\Delta\chi^2$. While initially fixed, the line widths were allowed to vary where appropriate leading to four sources with resolved absorption profiles. The key parameters of all detected absorption lines are reported in Table 4.3

This process was carried out on each individually fitted spectrum in the sample; including those which were included in simultaneous fits. In Figures 4.3 and 4.4 I show some examples of this process applied to Ark 120 (OBSID 702014010), which shows evidence for a broad asymmetric emission profile and no absorption lines, and Mrk 766 (OBSID 701035020), which is dominated by a pair of Fe XXV He$\alpha$ and Fe XXVI Ly$\alpha$ absorption lines. The top panel in each figure shows the residuals that remain in the Fe K band when all atomic lines have been removed from the best-fit continuum model and the reflection component is fitted with `pexrav` to highlight the presence of the neutral

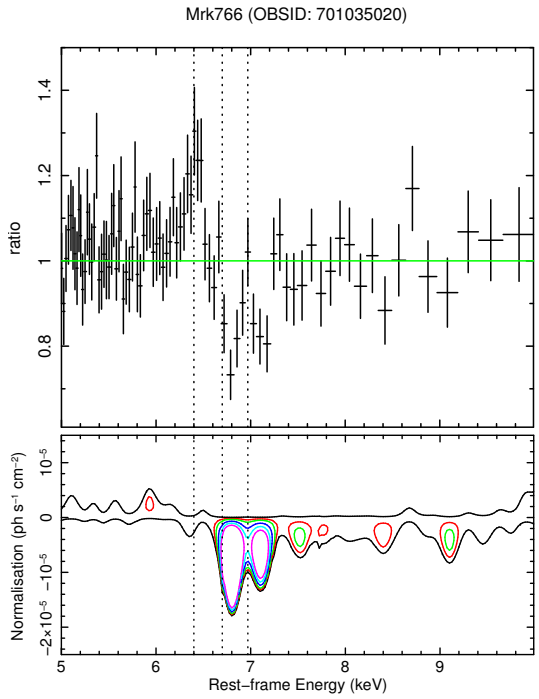


Figure 4.4: *Top Panel*: As in the case of Fig. 4.3, but this time for Mrk 766 (OBSID 701035020); *Bottom Panel*: As in the corresponding panel of Fig. 4.3. There are no ionised emission lines required in Mrk 766 however two highly significant (each required at $P_{\rm F} > 99.99\%$) absorption profiles are clearly detected. The energy of these lines is consistent with Fe XXV He$\alpha$ and Fe XXVI Ly$\alpha$, respectively, outflowing at $v_{\rm out} \sim 6,000\,{\rm km\,s^{-1}}$).

Fe K$\alpha$/Fe K$\beta$ fluorescence lines. The subsequent contour plots show the significances of the remaining residuals when the Fe K$\alpha$ and Fe K$\beta$ lines have been fitted with `reflionx` and a narrow Gaussian line. The continuous outer contour corresponds to the $\Delta\chi^2 = +0.5$ residual as mentioned previously. From outer to inner the closed significance contours corresponding to $\Delta\chi^2$ improvements of $-2.3$ ($P_{\rm F} = 68\%$), $-4.61$ ($P_{\rm F} = 90\%$), $-9.21$ ($P_{\rm F} = 99\%$), $-13.82$ ($P_{\rm F} = 99.9\%$) and $-18.42$ ($P_{\rm F} = 99.99\%$) relative to the best-fit continuum model are shown in red, green, blue, cyan and magenta, respectively.

There are clear residual profiles present in both sources, particularly Ark 120 where a asymmetric positive residual and additional Fe XXVI emission line are apparent in the middle and bottom panels of Fig. 4.3, respectively. The two absorption profiles in Mrk 766 — which have previously been identified as Fe XXV He$\alpha$ and Fe XXVI Ly$\alpha$ by Miller et al. (2007) — are statistically distinguishable at $> 99.99\%$ confidence by the F-test and are self-consistently fitted with a single highly-ionised region of photo-ionised absorption (see §4.5). Energy-intensity contour plots for all fitted spectra in this sample are included in Figures A.1 and A.2 in Appendix A. The $\Delta\chi^2$ of individual lines and their corresponding significances according to the F-Test, as listed in Table 4.3, are taken from a direct spectral fitting of the line profiles themselves, and are not determined from the contour plots.

It is also important to note that while I use the F-test to roughly gauge the significance of any line-like profiles in the Fe K band *I do not claim that the lines are robustly detected based solely on their measured $\Delta\chi^2$ and corresponding F-test significances.* All suspected absorption lines which yield an F-test significance of $P_{\rm F} > 99\%$ were followed up with extensive MC simulations following the process outlined in §2.2.6, with the resultant MC significances ($P_{\rm MC}$) noted in column 10 of Table 4.3. Absorption complexes with a total $P_{\rm MC} \geq 99\%$ are conservatively identified as robustly detected, while those with $95\% \leq P_{\rm MC} < 99\%$ are only listed as marginal detections. The overall detection rate and global significance of Fe K-band absorption lines is further discussed in §4.6.1.

It is worth noting that there are two possible caveats associated with the MC process I use, and both of these warrant further discussion. First and foremost, the MC simulations implicitly assume that the null-hypothesis model is the correct representation of the continuum in a given source, and therefore the MC probabilities do not account for the possibility of continuum mis-modelling. Given this possibility it is important to stress that I have tried to achieve a statistically acceptable representation of the broad-band spectrum (i.e., $\chi^2_{\rm red} \approx 1.0$) so that no obvious broad residuals are present. I have taken care when modelling the Fe K band in particular, such that any broad residuals are minimised prior to searching for absorption lines. Moreover, and as is apparent from the

Table 4.3: Gaussian parameters for detected Fe K band absorption lines. *Columns*: (1) Source name; (2) *Suzaku* observation ID; (3) Absorption line identification; (4) Measured line energy in the source rest-frame, in units of keV; (5) Measured line energy-width, in units of eV. Unresolved lines were fit with widths fixed at 10 eV, 30 eV or 100 eV depending upon which yielded the best statistical improvement to the fit; (6) Line intensity, in units of $10^{-6}\,\mathrm{erg\,cm^{-2}\,s^{-1}}$; (7) Line equivalent width, in units of eV; (8) Change in fit statistic (and degrees of freedom) when line is removed from the best-fit model; (9) Line significance according to the F-test, in per cent; (10) MC significance of individual lines, in per cent; (11) MC significance of observing a pair of lines with energy separation corresponding to a He$\alpha$–Ly$\alpha$ pair (see text for details), in per cent.

| Source | OBSID | Line ID | Energy | $\sigma$-width | Intensity | EW | $\Delta\chi^2/\Delta\nu$ | $P_{\rm F}$ | $P^1_{\rm MC}$ | $P^2_{\rm MC}$ |
|---|---|---|---|---|---|---|---|---|---|---|
| (1) | (2) | (3) | (4) | (5) | (6) | (7) | (8) | (9) | (10) | (11) |
| 3C 111 | 703034010 | Ly$\alpha$ | $7.24^{+0.04}_{-0.04}$ | $10^*$ | $-5.6^{+2.1}_{-2.1}$ | $-26^{+9}_{-9}$ | 16.4/2 | $>99.99$ | 99.8 | |
| | 705040020 | Ly$\alpha$ | $7.76^{+0.07}_{-0.04}$ | $10^*$ | $-15.2^{+5.1}_{-5.1}$ | $-20^{+10}_{-10}$ | 11.1/2 | 99.60 | 97.8 | |
| 3C 390.3 | 701060010 | Ly$\alpha$ | $8.08^{+0.06}_{-0.05}$ | $10^*$ | $-5.6^{+2.6}_{-2.6}$ | $-21^{+10}_{-10}$ | 12.1/2 | $>99.99$ | 98.7 | |
| 4C +74.26 | 702057010 | Ly$\alpha$ | $8.38^{+0.05}_{-0.07}$ | $10^*$ | $-7.2^{+3.4}_{-3.4}$ | $-29^{+14}_{-14}$ | 12.4/2 | 99.80 | 96.6 | |
| APM 08279+5255 | stacked | He$\alpha$–Ly$\alpha$ (1) | $7.76^{+0.11}_{-0.11}$ | $100^f$ | $-6.9^{+2.5}_{-2.3}$ | $-24^{+8}_{-8}$ | 23.8/2 | $>99.99$ | 99.7 | |
| | | He$\alpha$–Ly$\alpha$ (2) | $10.97^{+0.16}_{-0.16}$ | $100^f$ | $-4.4^{+1.9}_{-1.8}$ | $-30^{+15}_{-15}$ | 18.4/2 | $>99.99$ | 97.3 | |
| CBS 126 | 705042010 | Ly$\alpha$ | $7.04^{+0.04}_{-0.05}$ | $30^*$ | $-3.3^{+1.0}_{-1.0}$ | $-77^{+22}_{-22}$ | 27.5/2 | $>99.99$ | $>99.9$ | |
| ESO 103-G035 | 703031010 | Ly$\alpha$ | $7.26^{+0.05}_{-0.05}$ | $104^{+61}_{-55}$ | $-14.7^{+4.8}_{-4.1}$ | $-40^{+14}_{-14}$ | 35.0/3 | $>99.99$ | $>99.9$ | |
| MCG -6-30-15 | stacked[all] | Fe XXVHe$\alpha$ | $6.72^{+0.02}_{-0.01}$ | $10^*$ | $-7.8^{+1.2}_{-1.2}$ | $-18^{+3}_{-3}$ | 81.6/2 | $>99.99$ | $>99.9$ | $>99.9$ |
| | | Ly$\alpha$ | $7.05^{+0.02}_{-0.02}$ | $10^*$ | $-5.1^{+1.2}_{-1.2}$ | $-14^{+3}_{-3}$ | 25.7/2 | $>99.99$ | $>99.9$ | |
| MR 2251−178 | 704055010 | Fe L–He$\alpha$ | $7.55^{+0.12}_{-0.12}$ | $193^{+84}_{-62}$ | $-12.9^{+4.1}_{-4.1}$ | $-32^{+10}_{-10}$ | 26.9/3 | $>99.99$ | 99.6 | |
| Mrk 279 | 704031010 | Ly$\alpha$ | $8.88^{+0.06}_{-0.06}$ | $10^f$ | $-2.5^{+1.0}_{-1.0}$ | $-73^{+30}_{-30}$ | 15.1/2 | 99.95 | 99.6 | |
| Mrk 766 | 701035010 | Fe XXVHe$\alpha$ | $7.11^{+0.07}_{-0.07}$ | $10^f$ | $-2.8^{+1.6}_{-1.6}$ | $-27^{+15}_{-15}$ | 7.0/2 | 96.27 | 71.0 | 99.8 |
| | | Ly$\alpha$ | $7.42^{+0.06}_{-0.06}$ | $10^f$ | $-3.9^{+1.6}_{-1.6}$ | $-40^{+17}_{-17}$ | 15.3/2 | 99.92 | 98.4 | |
| | 701035020 | Fe XXVHe$\alpha$ | $6.80^{+0.02}_{-0.02}$ | $10^f$ | $-7.7^{+1.8}_{-1.8}$ | $-60^{+14}_{-14}$ | 50.0/2 | $>99.99$ | $>99.9$ | $>99.9$ |
| | | Ly$\alpha$ | $7.12^{+0.04}_{-0.04}$ | $10^f$ | $-5.0^{+1.9}_{-1.9}$ | $-44^{+17}_{-17}$ | 18.9/2 | $>99.99$ | 99.8 | |
| NGC 1365 | 702047010 | Fe XXVHe$\alpha$ | $6.77^{+0.01}_{-0.01}$ | $65^{+8}_{-8}$ | $-29.9^{+1.6}_{-1.6}$ | $-156^{+8}_{-8}$ | 1123.8/3 | $>99.99$ | $>99.9$ | $>99.9$ |
| | | Ly$\alpha$ | $6.97^{+0.03}_{-0.03}$ | $65^*$ | $-8.7^{+1.7}_{-1.7}$ | $-69^{+13}_{-13}$ | 77.0/3 | $>99.99$ | $>99.9$ | |
| | | He$\beta$ | $7.94^{+0.01}_{-0.01}$ | $65^*$ | $-26.1^{+1.5}_{-1.5}$ | $-164^{+10}_{-10}$ | 964.5/3 | $>99.99$ | $>99.9$ | |
| | | Ly$\beta$ | $8.38^{+0.03}_{-0.03}$ | $65^*$ | $-10.6^{+1.8}_{-1.8}$ | $-87^{+15}_{-15}$ | 94.3/3 | $>99.99$ | $>99.9$ | |
| | 704031010 | Fe XXVHe$\alpha$ | $6.71^{+0.02}_{-0.02}$ | $30^*$ | $-16.1^{+2.4}_{-2.4}$ | $-67^{+10}_{-10}$ | 134.9/2 | $>99.99$ | $>99.9$ | $>99.9$ |

Continued on next page...

Table 4.3: Parameters for detected Fe K absorption lines (continued)

| Source (1) | OBSID (2) | Line ID (3) | Energy (4) | $\sigma$-width (5) | Intensity (6) | EW (7) | $\Delta\chi^2/\Delta\nu$ (8) | $P_{\rm F}$ (9) | $P^1_{\rm MC}$ (10) | $P^2_{\rm MC}$ (11) |
|---|---|---|---|---|---|---|---|---|---|---|
| | | Ly$\alpha$ | $7.00^{+0.02}_{-0.02}$ | 30* | $-13.4^{+2.0}_{-2.0}$ | $-85^{+14}_{-14}$ | 90.7/2 | $> 99.99$ | $> 99.9$ | |
| | | He$\beta$ | $7.87^{+0.08}_{-0.08}$ | 30* | $-4.7^{+2.5}_{-2.5}$ | $-34^{+20}_{-20}$ | 7.2/2 | 96.77 | ... | |
| | | Ly$\beta$ | $8.37^{+0.11}_{-0.11}$ | 30* | $-5.3^{+2.7}_{-2.7}$ | $-45^{+24}_{-24}$ | 8.5/2 | 98.23 | ... | |
| NGC 3227 | 703022010 | Fe XXVHe$\alpha$ | $6.69^{+0.04}_{-0.04}$ | 10* | $-9.9^{+3.7}_{-3.7}$ | $-21^{+7}_{-7}$ | 17.5/2 | 99.99 | $> 99.9$ | $> 99.9$ |
| | | Ly$\alpha$ | $6.95^{+0.03}_{-0.03}$ | 10* | $-15.5^{+3.7}_{-3.7}$ | $-38^{+9}_{-9}$ | 42.4/2 | $> 99.99$ | $> 99.9$ | |
| | 703022030 | Fe XXVHe$\alpha$ | $6.76^{+0.03}_{-0.04}$ | 10* | $-8.5^{+3.5}_{-3.5}$ | $-24^{+9}_{-9}$ | 16.2/2 | 99.94 | 99.8 | $> 99.9$ |
| | | Ly$\alpha$ | $7.04^{+0.05}_{-0.05}$ | 10* | $-6.6^{+3.6}_{-3.6}$ | $-22^{+11}_{-11}$ | 9.3/3 | 98.64 | 91.8 | |
| | 703022050 | Fe XXVHe$\alpha$ | $6.76^{+0.07}_{-0.07}$ | 10* | $-5.8^{+2.8}_{-2.8}$ | $-19^{+9}_{-8}$ | 12.0/2 | 99.74 | 96.2 | $> 99.9$ |
| | | Ly$\alpha$ | $7.05^{+0.03}_{-0.03}$ | 10* | $-11.0^{+2.8}_{-2.8}$ | $-41^{+9}_{-9}$ | 41.2/2 | $> 99.99$ | $> 99.9$ | |
| NGC 3516 | 100031010 | Fe XXVHe$\alpha$ | $6.74^{+0.02}_{-0.02}$ | $10^f$ | $-9.1^{+1.6}_{-1.6}$ | $-25^{+5}_{-5}$ | 65.6/2 | $> 99.99$ | $> 99.9$ | $> 99.9$ |
| | | Ly$\alpha$ | $7.00^{+0.02}_{-0.02}$ | $10^f$ | $-6.0^{+1.7}_{-1.7}$ | $-20^{+6}_{-6}$ | 66.7/2 | $> 99.99$ | $> 99.9$ | |
| NGC 3783 | 701033010 | Fe XXVHe$\alpha$ | $6.69^{+0.04}_{-0.04}$ | 10* | $-10.0^{+3.2}_{-3.0}$ | $-16^{+5}_{-6}$ | 30.2/2 | $> 99.99$ | $> 99.9$ | |
| | 704063010 | Fe XXVHe$\alpha$ | $6.71^{+0.02}_{-0.02}$ | 10* | $-14.0^{+3.1}_{-3.1}$ | $-20^{+3}_{-5}$ | 56.7/2 | $> 99.99$ | $> 99.9$ | |
| NGC 4051 | 700004010 | Fe XXVHe$\alpha$ | $6.77^{+0.04}_{-0.04}$ | $10^f$ | $-2.2^{+1.0}_{-1.0}$ | $-21^{+10}_{-10}$ | 9.9/2 | 99.39 | 89.4 | $> 99.9$ |
| | | Ly$\alpha$ | $7.08^{+0.03}_{-0.03}$ | $10^f$ | $-3.3^{+1.1}_{-1.1}$ | $-38^{+13}_{-13}$ | 22.7/2 | $> 99.99$ | $> 99.9$ | |
| | 703023010 | Fe XXVHe$\alpha$ | $6.82^{+0.03}_{-0.03}$ | $10^f$ | $-4.8^{+1.3}_{-1.3}$ | $-22^{+6}_{-6}$ | 26.4/2 | $> 99.99$ | $> 99.9$ | $> 99.9$ |
| | | Ly$\alpha$ | $7.11^{+0.02}_{-0.02}$ | $10^f$ | $-6.4^{+1.3}_{-1.3}$ | $-33^{+7}_{-7}$ | 57.5/2 | $> 99.99$ | $> 99.9$ | |
| NGC 4151 | 701034010 | Ly$\alpha$ | $7.17^{+0.04}_{-0.04}$ | $92^{+51}_{-41}$ | $-15.9^{+4.7}_{-4.3}$ | $-28^{+8}_{-8}$ | 43.7/3 | $> 99.99$ | $> 99.9$ | |
| NGC 4395 | 702001010 | Fe XXVHe$\alpha$ | $6.63^{+0.07}_{-0.05}$ | 10* | $-2.2^{+1.1}_{-1.1}$ | $-35^{+19}_{-19}$ | 10.4/2 | $> 99.99$ | 74.5 | $> 99.9$ |
| | | Ly$\alpha$ | $6.91^{+0.06}_{-0.06}$ | 10* | $-2.9^{+1.1}_{1.1}$ | $-55^{+20}_{-20}$ | 18.3/2 | $> 99.99$ | 86.8 | |
| NGC 5506 | stacked[all] | Ly$\alpha$ | $9.23^{+0.06}_{-0.06}$ | 10* | $-11.1^{+4.7}_{-4.7}$ | $-16^{+5}_{-5}$ | 16.2/2 | $> 99.99$ | 99.8 | |
| PDS 456 | 701056010 | He$\alpha$–Ly$\alpha$ (1) | $9.07^{+0.06}_{-0.06}$ | 100* | $-2.5^{+0.8}_{-0.8}$ | $-108^{+35}_{-35}$ | 29.5/2 | $> 99.99$ | $> 99.9$ | |
| | | He$\alpha$–Ly$\alpha$ (2) | $9.57^{+0.09}_{-0.09}$ | 100* | $-2.0^{+0.8}_{-0.8}$ | $-99^{+41}_{-41}$ | 15.7/2 | $> 99.99$ | 99.8 | |
| | 705041010 | He$\alpha$–Ly$\alpha$ (1) | $8.58^{+0.09}_{-0.09}$ | 100* | $-2.8^{+1.0}_{-1.0}$ | $-118^{+46}_{-46}$ | 19.5/2 | $> 99.99$ | 96.2 | |
| | | He$\alpha$–Ly$\alpha$ (2) | $9.03^{+0.09}_{-0.09}$ | 100* | $-3.5^{+1.1}_{-1.1}$ | $-169^{+51}_{-51}$ | 78.6/2 | $> 99.99$ | $> 99.9$ | |
| S J2127.4+5654 | 702122010 | Ly$\alpha$ | $9.04^{+0.05}_{-0.05}$ | $10^f$ | $-10.0^{+4.7}_{-4.7}$ | $-60^{+28}_{-28}$ | 11.9/2 | 99.78 | 98.9 | |

[f] Indicates a parameter was frozen during spectral fitting.

plots in Appendix A.1, the vast majority of suspected absorption residuals are manifested through discrete narrow dips in the spectrum relative to the best-fit model, whereas any systematic residuals would usually be broader than the instrument resolution.

The second caveat is associated with spectral complexity in the Fe K band which can complicate both line identification and spectral interpretation. There can be significant atomic complexity between $\sim 5 - 7$ keV, e.g., the narrow Fe K$\alpha$ and Fe K$\beta$ fluorescence lines, broad underlying Fe K lines, and ionised Fe XXV–XXVI emission lines, and the detection of absorption in this regime can depend strongly on how these features are modelled. There are three sources (4C +74.26, MGC -6-30-15, SWIFT J2127.4+5654; see Figure B2) in the sample in which both a broad underlying profile and at least one absorption line have been detected. In both 4C+74.26 and SWIFT J2127.4+5654 the absorption lines are detected at high enough energies (i.e., $E > 8$ keV in the source rest-frame) that the effect of the broad Fe lines on the line detection is negligible. In MCG -6-30-15, on the other hand, the lines have also been confirmed with other X-ray observatories (Young et al. 2005; Miller, Turner & Reeves 2009) which suggests that the presence of a broad Fe line does not introduce any significant model systematics. Thus modelling of a broad emission line does not appear to affect the detections of Fe K absorption lines in these cases.

### 4.4.3 Consistency checks

To further test the robustness of the absorption lines detected in the co-added XIS-FI spectra I performed a series of consistency checks amongst the individual XIS detectors. If an absorption line is detected in two (or more, if the XIS 2 is also present) detectors the line is very likely to be a real feature intrinsic to the source spectrum rather than an artefact of background subtraction, systematic noise or an associated detector effect. The XIS-BI is not suitable for use as a consistency check as it tends to have a much lower signal-to-noise ratio above around 5 keV owing to its lower effective area and higher background. Where absorption has been detected at the $P_{\rm MC} \geq 95\%$ level I fitted each individual background-subtracted XIS 0, XIS 2 (where present) and XIS 3 spectrum with

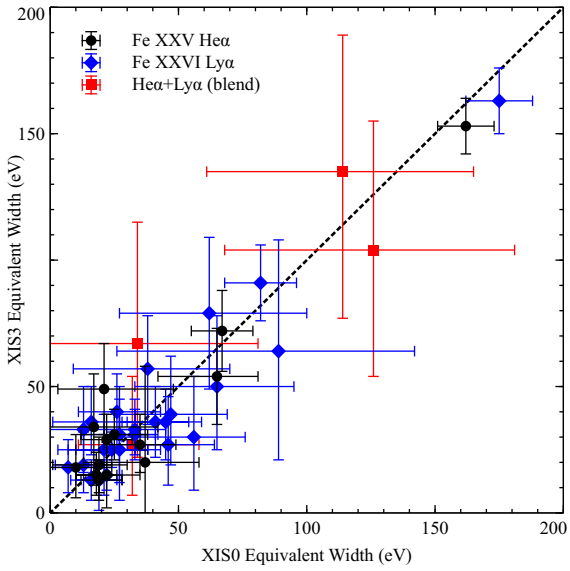


Figure 4.5: Consistency check comparing the absorption line equivalent width measured with the XIS 0 versus the XIS 3 along with the 90% error bars. The diagonal dashed line represents the location where the $EW$ is equal in both detectors. The circle (black), diamond (blue) and square (red) markers show the $EW$ of the Fe XXV He$\alpha$, Fe XXVI Ly$\alpha$ and blended Fe XXV–XXVI lines, respectively. For sources with lines detected in more than one observation the mean $EW$ for each line in each detector and associated errors are plotted. Where available this consistency check was also carried out with the XIS 2 which yielded results which are entirely consistent with those displayed here.

the best-fitting model for the full XIS-FI spectrum. I then added a Gaussian absorption line, with rest-frame energy and normalisation left free to vary, at the energy where the absorption line is detected in the XIS-FI spectrum, refitted the data, and noted the resultant line parameters for each XIS detector. Note that due to only the XIS 3 spectrum being available, this consistency check could not be conducted for SWIFT J2127.4+5654.

In all sources the residuals detected in the individual XIS spectra have Gaussian parameters consistent with those found for the co-added FI spectrum. A comparison of the absorption line equivalent width ($EW$) along with 90% error bars, as measured with the individual XIS 0 and XIS 3 detectors, is shown in Fig. 4.5. The dashed diagonal

represents the position where the *EW* is equal in each of the detectors; where the *EW* is consistent at the 90% level the error bars will overlap this line. In this plot the Fe XXV He$\alpha$, Fe XXVI Ly$\alpha$ and blended Fe XXV–XXVI lines are plotted separately, even in the cases where the lines are found to be part of an Fe XXV–XXVI pair. The mean *EW*s measured with the XIS 0 and XIS 3 detectors are consistent at the 90% level (i.e., the error bars cross the diagonal line in Fig. 4.5) in all sources. Where possible, I also carried out this analysis using the XIS 2 spectra versus both the XIS 0 and XIS 3. Again, in all cases the mean parameters of the lines are always consistent at the 90% level. The consistency check strongly suggests that the observed lines are real features and are not due to detector effects or due to background subtraction.

## 4.5 Photo-ionisation modelling

Having established the reality of the absorption lines, I proceeded to model all of the absorption complexes detected at the $P_{\rm MC} \geq 95\%$ confidence level with the XSTAR photo-ionisation code to probe the column density $N_{\rm H}$, ionisation parameter $\xi$, for the absorbing gas, and its red-shift relative to the observer $z_{\rm o}$. Probing these parameters is important as not only do they allow the mean properties of the absorbing material to be determined but, through the use of simple geometric assumptions, they also facilitate an assessment of an absorbers' likely radial distance from the ionising source, their mass outflow rate, and their global energetic output. I go on to present a detailed discussion regarding the absorber kinematics in the next chapter.

Generally, I fitted the absorption lines with an XSTAR table with an assumed illuminating continuum of $\Gamma = 2.1$ and a micro-turbulent velocity ($v_{\rm turb}$) of $1,000\,{\rm km\,s^{-1}}$, which roughly corresponds to the full-width at half-maximum (FWHM) velocity width of a $\sigma = 10\,{\rm eV}$ Fe XXVI Ly$\alpha$ absorption line at a rest-frame energy of 6.97 keV. Where the lines were resolved (i.e., $\sigma > 10\,{\rm eV}$) I instead used XSTAR tables with $v_{\rm turb}$ values which more closer matched the measured FWHM velocity width of the observed profile; tables with $v_{\rm turb}$ equal to $1,000\,{\rm km\,s^{-1}}$, $3,000\,{\rm km\,s^{-1}}$, $5,000\,{\rm km\,s^{-1}}$ and $10,000\,{\rm km\,s^{-1}}$

were sufficient to fit all systems in the sample. The XSTAR table parameters were allowed to vary freely in 17/20 sources, but in APM 08279+5255 and the multi-epoch NGC 1365 and PDS 456 models parameters were tied to prevent degeneracies between the column density and ionisation parameter (see Table 4.4). The absorber red-shift ($z_o$) as measured from the spectrum using XSTAR is given in the observer frame. This is related to the intrinsic absorber red-shift in the source rest-frame ($z_a$) and the cosmological red-shift of the source ($z_c$) through the relation

$$(1 + z_o) = (1 + z_a)(1 + z_c). \tag{4.1}$$

From this, the intrinsic velocity of the outflow relative to the source ($v_{\rm out}$) can then be calculated from the relativistic Doppler formula,

$$v_{\rm out}/c = \frac{(z_a + 1)^2 - 1}{(z_a + 1)^2 + 1} \tag{4.2}$$

which ensures that the relativistic effects associated with both high red-shift sources and high-velocity outflows are correctly taken into account when inferring absorber outflow velocities relative to the source rest-frame.

### 4.5.1 Line identifications

Before discussing the results of the XSTAR fitting it is important that I justify the *a priori* assumption that the absorption lines detected at $E \gtrsim 6.6\,{\rm keV}$ in these sources are due to the velocity shifted resonance lines of Fe XXV and Fe XXVI. Indeed, while the K$\alpha$ transitions of Fe XXV and Fe XXVI, which are expected at mean rest-frame energies of 6.697 keV and 6.966 keV, respectively, are expected to be the strongest lines in the $\approx 6.5 - 7.0\,{\rm keV}$ energy interval, there are several other atomic features at higher energies which may complicate the identification of blue-shifted absorption systems at $E > 7\,{\rm keV}$. For example, the K-shell edges from the various ionised species of Fe are found above 7 keV, with energies ranging from 7.1 keV for neutral Fe up to 9.3 keV for Fe XXVI. In the case of low-moderate ionisation Fe the K-edge is accompanied by higher order resonance line structure which can give the edge a subtle curved profile in CCD spectra rather than

it simply being an abrupt drop in flux (Kallman et al. 2004). Furthermore, given its proximity to the rest-frame energy of the Fe XXV-XXVI transitions the neutral edge at 7.1 keV could have an influence on the detection of lower velocity systems.

Of the sources included in the sample CBS 126, Mrk 766 (OBSIDs 701035010, 701035020), NGC 3227 (OBSIDs 703022010, 703022020, 703022030), NGC 4051 (OBSIDs 700004010, 703023010) and NGC 4151 all have at least one significantly detected absorption line at a rest-frame energy which is consistent at the 90% level with the neutral Fe K-shell edge from the reflection component. The absorption in Mrk 766, NGC 3227, and NGC 4051 is, however, manifested by two lines with a common velocity shift equal to that expected for Fe XXV He$\alpha$ and Fe XXVI Ly$\alpha$ and are therefore unlikely to be affected by the presence of an edge. The absorption in CBS 126 and NGC 4151, which only comprises a single detected profile, could possibly be affected. Even so, given that the K-shell edge structure is already self-consistently accounted for by the `reflionx` model and in XSTAR, this suggests that the residual profiles detected near the Fe K-shell edge in these sources are real additional component rather than the residuals left by an inadequately fitted edge. Alternatively, the residuals could be due to a partially covering absorber with a low outflow velocity. I investigate this possibility further in §4.7.1. Finally, it is important to note that while NGC 5506 shows evidence for both a highly ionised Fe XXV emission line at $\sim 6.63$ keV and an absorption trough at $\sim 9.2$ keV, the energy of the trough is not consistent with the Fe XXV K-shell edge and the two features are unlikely to be directly associated.

In addition, there are a few other complications which could have an effect on the identification of blue-shifted absorption profiles at $E > 7$ keV. In particular, because different combinations of XSTAR parameters (i.e., $N_{\rm H}$, $\log \xi$) can yield equivalent minima of the $\chi^2$ distribution at differing red-shifts there can be a level of degeneracy when identifying the ion responsible for a discrete absorption trough. This effect is not particularly significant in sources where there are two absorption lines at a common velocity shift because the absorber parameters are determined by the joint constraint of fitting both profiles, but it can become important in the instances where the absorption is manifested by a single trough. In these cases it can be difficult to determine whether an

Table 4.4: Summary of XSTAR parameters for Fe K absorbers. *Columns:* (1) Source name; (2) *Suzaku* observation ID; (3) Logarithm of absorber column density, in units of $\mathrm{cm}^{-2}$; (4) Logarithm of the ionisation parameter, in units of $\mathrm{erg\,cm\,s}^{-1}$; (5) Measured absorber outflow velocity, in units of $v/c$. Negative outflow velocities indicate a net red-shift; (6) Change in $\chi^2/\nu$ when absorber removed from the best-fit model; (7) Corresponding absorber significance according to the F-Test.

| Source (1) | OBSID (2) | $\log N_{\rm H}$ (3) | $\log \xi$ (4) | $v_{\rm out}$ (5) | $\Delta\chi/\Delta\nu$ (6) | $P_{\rm F}$ (7) |
|---|---|---|---|---|---|---|
| 3C 111 | 703034010 | $23.18^{+0.19}_{-0.24}$ | $4.63^{+0.22}_{-0.18}$ | $0.039 \pm 0.005$ | 18.7/3 | 99.97 |
| | 705040010 | $22.43^{+0.20}_{-0.31}$ | $4.13^{+0.27}_{-0.14}$ | $0.105 \pm 0.008$ | 11.6/3 | 99.08 |
| | ⟨mean⟩ | $22.95^{+0.28}_{-0.39}$ | $4.45^{+0.35}_{-0.23}$ | $0.072 \pm 0.005$ | ··· | ··· |
| 3C 390.3$^{\triangle}$ | 701060010 | $> 23.68$ | $> 5.46$ | $0.145 \pm 0.007$ | 11.7/2 | $> 99.11$ |
| 4C +74.26$^{\triangle}$ | 702057010 | $> 21.79$ | $4.06^{+0.45}_{-0.45}$ | $0.185 \pm 0.026$ | 14.6/3 | 99.76 |
| APM 08279+5255 | stacked[all] | $23.00^{+0.07}_{-0.16}$ | $3.41^{+0.08}_{-0.08}$ | $0.139 \pm 0.012$ | 27.3/3 | $> 99.99$ |
| | | $23.00^{*}$ | $3.61^{+0.23}_{-0.14}$ | $0.431 \pm 0.019$ | 14.3/2 | 99.59 |
| | ⟨mean⟩ | $23.00^{+0.12}_{-0.12}$ | $4.13^{+0.23}_{-0.17}$ | $0.285 \pm 0.011$ | ··· | ··· |
| CBS 126 | 705042010 | $> 23.73$ | $4.77^{+0.26}_{-0.17}$ | $0.012 \pm 0.006$ | 28.9/3 | $> 99.99$ |
| ESO 103-G035$^{\triangle}$ | 703031010 | $> 21.90$ | $4.36^{+1.19}_{-1.19}$ | $0.056 \pm 0.025$ | 33.2/3 | $> 99.99$ |
| MCG -6-30-15 | stacked[all] | $22.16^{+0.08}_{-0.08}$ | $3.64^{+0.05}_{-0.06}$ | $0.007 \pm 0.002$ | 103.0/3 | $> 99.99$ |
| MR 2251−178 | 705041010 | $21.54^{+0.22}_{-0.20}$ | $3.26^{+0.12}_{-0.12}$ | $0.137 \pm 0.008$ | 42.4/3 | $> 99.99$ |
| Mrk 279 | 704031010 | $23.38^{+0.25}_{-0.31}$ | $4.42^{+0.15}_{-0.27}$ | $0.220 \pm 0.006$ | 14.5/3 | 99.77 |
| Mrk 766 | 701035010 | $22.64^{+0.20}_{-0.27}$ | $4.02^{+0.21}_{-0.13}$ | $0.061 \pm 0.008$ | 14.5/3 | 99.71 |
| | 701035020 | $22.76^{+0.10}_{-0.13}$ | $3.67^{+0.06}_{-0.06}$ | $0.017 \pm 0.004$ | 63.2/3 | $> 99.99$ |
| | ⟨mean⟩ | $22.70^{+0.15}_{-0.19}$ | $3.86^{+0.13}_{-0.10}$ | $0.039 \pm 0.006$ | ··· | ··· |
| NGC 1365 | 702047010 | $23.92^{+0.03}_{-0.03}$ | $3.88^{+0.06}_{-0.07}$ | $0.014 \pm 0.001$ | 4125.1/3 | $> 99.99$ |
| | 705031010 | $23.40^{+0.10}_{-0.12}$ | $3.88^{*}$ | $0.002 \pm 0.002$ | 191.8/3 | $> 99.99$ |
| | ⟨mean⟩ | $23.73^{+0.06}_{-0.06}$ | $3.88^{+0.06}_{-0.07}$ | $0.008 \pm 0.001$ | ··· | ··· |
| NGC 3227 | 703022010 | $22.74^{+0.11}_{-0.13}$ | $3.89^{+0.08}_{-0.11}$ | $< 0.002$ | 63.1/3 | $> 99.99$ |
| | 703022030 | $22.59^{+0.16}_{-0.20}$ | $3.86^{+0.13}_{-0.14}$ | $0.007 \pm 0.004$ | 21.0/3 | $> 99.99$ |
| | 703022050 | $22.62^{+0.12}_{-0.14}$ | $3.89^{+0.11}_{-0.12}$ | $0.011 \pm 0.004$ | 37.9/3 | $> 99.99$ |
| | ⟨mean⟩ | $22.66^{+0.13}_{-0.15}$ | $3.88^{+0.19}_{-0.21}$ | $0.005 \pm 0.004$ | ··· | ··· |
| NGC 3516 | 100031010 | $22.56^{+0.14}_{-0.17}$ | $3.84^{+0.11}_{-0.10}$ | $0.004 \pm 0.002$ | 141.9/3 | $> 99.99$ |
| NGC 3783 | 701033010 | $21.75^{+0.15}_{-0.20}$ | $3.50^{+0.13}_{-0.08}$ | $< 0.005$ | 16.2/3 | 99.90 |
| | 704063010 | $21.83^{+0.09}_{-0.10}$ | $3.45^{+0.06}_{-0.04}$ | $< 0.008$ | 48.2/3 | $> 99.99$ |
| | ⟨mean⟩ | $21.79^{+0.16}_{-0.23}$ | $3.48^{+0.14}_{-0.90}$ | $< 0.007$ | ··· | ··· |
| NGC 4051 | 700004010 | $22.78^{+0.08}_{-0.09}$ | $4.05^{+0.05}_{-0.05}$ | $0.020 \pm 0.002$ | 80.3/3 | $> 99.99$ |
| | 703023010 | $22.80^{+0.11}_{-0.13}$ | $4.94^{+0.09}_{-0.09}$ | $0.015 \pm 0.002$ | 20.8/3 | 99.99 |
| | ⟨mean⟩ | $22.79^{+0.10}_{-0.11}$ | $4.00^{+0.07}_{-0.07}$ | $0.018 \pm 0.001$ | ··· | ··· |

Continued on next page...

Table 4.4: Summary of XSTAR parameters for the Fe K absorbers (continued)

| Source (1) | OBSID (2) | $\log N_{\rm H}$ (3) | $\log \xi$ (4) | $v_{\rm out}$ (5) | $\Delta\chi/\Delta\nu$ (6) | $P_{\rm F}$ (7) |
|---|---|---|---|---|---|---|
| NGC 4151$^{\triangle}$ | 701034010 | $> 21.74$ | $3.69^{+0.64}_{-0.64}$ | $0.055 \pm 0.023$ | 54.8/3 | $> 99.99$ |
| NGC 4395 | 702001010 | $22.84^{+0.21}_{-0.25}$ | $3.92^{+0.16}_{-0.15}$ | $< 0.001$ | 19.1/3 | 99.97 |
| NGC 5506 | stacked[all] | $23.22^{+0.19}_{-0.28}$ | $5.04^{+0.29}_{-0.17}$ | $0.246 \pm 0.006$ | 16.8/3 | 99.94 |
| PDS 456 | 701056010 | $23.04^{+0.08}_{-0.08}$ | $4.19^{+0.15}_{-0.14}$ | $0.253 \pm 0.008$ | 20.4/3 | $> 99.99$ |
| | | $23.04^{*}$ | $4.19^{*}$ | $0.292 \pm 0.009$ | 12.8/1 | 99.68 |
| | 705041010 | $23.04^{*}$ | $3.93^{+0.02}_{-0.02}$ | $0.253^{*}$ | 20.4/3 | $> 99.99$ |
| | | $23.04^{*}$ | $3.93^{*}$ | $0.292^{*}$ | 11.6/1 | 99.85 |
| | $\langle$mean$\rangle$ | $23.04^{+0.08}_{-0.08}$ | $4.06^{+0.15}_{-0.14}$ | $0.273 \pm 0.006$ | $\cdots$ | $\cdots$ |
| SW J2127.4+5654 | 702122010 | $22.78^{+0.23}_{-0.34}$ | $4.16^{+0.29}_{-0.13}$ | $0.231 \pm 0.006$ | 11.5/3 | 99.24 |

$^{*}$ indicates a parameter was tied during spectral fitting;
$^{\triangle}$ denotes sources with XSTAR solutions which are degenerate at the 90% level (i.e., their $\Delta\chi^2 \leq -2.71$). In these cases the reported values are averaged over the solutions and the errors are inferred as half the range between the absolute maximum and minimum values. Significances reported in columns (6) and (7) refer to the least significant of the valid solutions. See text for further details.

absorption line is due to, for example, Fe XXV He$\alpha$ or Fe XXVI Ly$\alpha$, which can therefore influence the inferred velocity of the outflow and hence any inferred absorber energetics.

There are 10 sources (11 observations) in the sample in which a single absorption trough is detected at $E > 7\,$keV at $P_{\rm MC} \geq 95\%$ significance (see Table 4.3). In each of these cases, I searched for alternative XSTAR solutions by stepping the red-shift of the highly-ionised XSTAR table through the Fe K band of each spectrum. This enables the $\chi^2$ minima for different XSTAR solutions, at different velocity-shifts and for various combinations of column density and ionisation parameter, to be mapped. This process is analogous to that used by Tombesi et al. (2011a) and is useful when it comes to ascertaining whether there were any alternative fits to the absorption lines, and to check for degeneracies between line identifications.

For each source where only a single line is detected I took the best-fitting continuum model (including any necessary soft-band absorbers) and froze all model parameters bar those of the highly-ionised absorption table and the normalisation of the primary power-law. I then stepped the highly-ionised XSTAR table in $\Delta z_o = 10^{-3}$ increments

between $-0.5 \leq z_o < 0.5$ to map both blue and red-shifted $\chi^2$ minima, and produced contour plots after each run. Example contour plots for Mrk 279 and ESO 103-G035, which illustrate the cases of non-degenerate and degenerate XSTAR solutions, respectively, are shown in Fig. 4.6. In Mrk 279 (Fig. 4.6, top panel) the stepping process yields a single valid XSTAR solution at a velocity shift corresponding to Fe XXVI Ly$\alpha$. However, in ESO 103-G035 (Fig. 4.6, middle panel) there are two degenerate $\chi^2$ minima found which are statistically equivalent at the 90% level (i.e., $\Delta\chi^2 \leq -2.71$). The measured parameters imply that the lowest velocity solution is associated with Fe XXVI Ly$\alpha$, while the higher velocity solution is likely due to Fe XXV He$\alpha$ with some contamination from lower ionised species of iron. In this scenario it is difficult to unambiguously identify the responsible Fe ion and therefore gauge the appropriate outflow velocity.

Of the 10 sources in which the Fe K absorber is manifested by a single trough, only 4 show evidence for degenerate XSTAR solutions (3C 390.3, 4C +74.26, ESO 103-G035 and NGC 4151). For these cases I have reported the mean XSTAR parameters as measured from all valid solutions in Table 4.4 to account for the uncertainty in line identifications. The associated errors are then taken as half of the range between the absolute and minimum values. The remaining 7 sources have only a single $\chi^2$ minimum which corresponds to the line identification reported in Table 4.3. In sources with degenerate XSTAR solutions I only report the most conservative one in Table 4.3 (i.e., associated with Fe XXVI Ly$\alpha$).

### 4.5.2 The influence of nickel

In principle, the presence of nickel could also complicate the identification of Fe lines above 7.1 keV. In particular, the K$\alpha$ lines of Ni XXVII and Ni XXVIII, which are expected at rest-frame energies of $E \sim 7.78$ keV and $E \sim 8.09$ keV, respectively, could offer a more energetically conservative identification for the highest energy absorption lines by virtue of requiring a lower blue-shifted velocity. A total of six sources have absorption lines detected at energies in the regime where nickel could complicate line identifications

(Table 4.3). Because of uncertainties in the atomic rates of nickel[10] its abundance is set to zero in XSTAR by default which means that any additional solutions to the $\chi^2$ distribution due to it would not be picked up during the red-shift stepping. In order to robustly search for plausible XSTAR solutions which may be associated with nickel, then, I therefore re-generated the XSTAR tables using the same assumed parameters as before (see §4.5), but this time with nickel included at Solar abundances, and again searched for alternative XSTAR solutions using the method outlined previously.

The bottom panel of Fig. 4.6 shows a comparison of the contour plots obtained for NGC 5506 when nickel is set to zero or Solar in the XSTAR table. As expected given the $Z_{\rm Ni}/Z_{\rm Fe} \sim 0.05$ abundance ratio at Solar abundances (i.e., Grevesse & Sauval 1998), in terms of valid XSTAR solutions for NGC 5506 there are no tangible differences between the two grids with Fe XXVI Ly$\alpha$ being the only valid identification in both cases. Similar is also true for the other 5 sources with absorption lines detected at $E \gtrsim 7.78$ keV, with no valid solutions corresponding to nickel being found in any of the cases. Moreover, it should be noted that in order to achieve the measured equivalent width of the absorption lines the required column density would be unreasonably large, i.e., $\log(N_{\rm H}/{\rm cm}^{-2}) > 24$, which would absorb the observed continuum far beyond that which is observed in the spectra.

Therefore, bar the extraordinary case where it is $\gtrsim 20$ times over-abundant relative to Solar values, Ni has a negligible influence on the Fe K band and identifying the observed absorption lines with K-shell resonance lines of Fe is secure. The best-fitting XSTAR parameters, including the measured outflow velocities relative to the host galaxy, are reported in Table 4.4. The statistical significances as per the $\Delta\chi^2$ and the F-test are also reported; in all cases the addition of an XSTAR grid to fit the observed lines is required at the $\geq 99\%$ confidence level. Note that since some sources have either more than one absorption complex detected in a single spectrum (i.e., APM 08279+5255 and PDS 456), or have absorption detected in more than one epoch (i.e., Mrk 766), I also note the mean absorption parameters on a per source basis. The mean values are used in

[10] http://heasarc.gsfc.nasa.gov/xstar/docs/html/node74.html

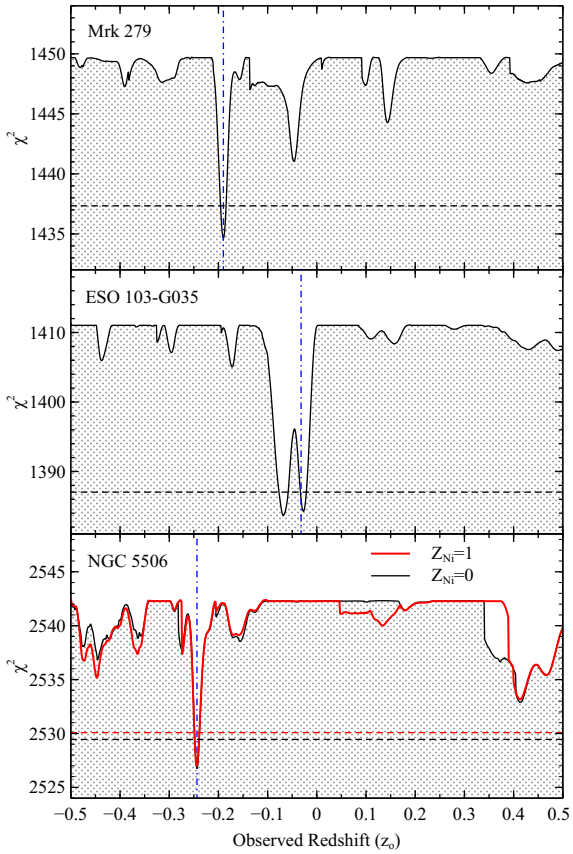


Figure 4.6: Example plots showing the $\chi^2$ statistic versus observed red-shift of the XSTAR absorber ($z_o$). Plots are shown for Mrk 279 (top panel), ESO 103-G035 (middle panel) and NGC 5506 (bottom panel). In all panels the black solid line shows the $\chi^2$ confidence contour and underlying $\chi^2$ distribution. In the bottom panel the black and red solid lines show the confidence contours for XSTAR grids both with (dot-dashed red) and without (solid black) nickel included at Solar abundances. In all panels the horizontal dashed lines show the 90% confidence level for one interesting parameter, while the vertical dash-dotted line shows the best-fitting absorber red-shift.

all subsequent analysis to prevent sources with multiple Fe K absorber detection from over-weighting the resultant parameter distributions which are discussed in §4.6.2.

## 4.6 Results

### 4.6.1 Line detection rate and phenomenology

A total of 20/51 sources (in 28/73 fitted spectra; both corresponding to $\sim 40\%$ of the total sample) show evidence for highly-ionised absorption lines in their *Suzaku* spectra at a MC significance of $P_{\rm MC} \geq 95\%$, with 18/20 of these outflows also robustly detected at $P_{\rm MC} \geq 99\%$ significance (see Table 4.3). Of the 28 observations with individually detected Fe K absorbers there are 10 which are consistent with having Fe XXVI Ly$\alpha$ as the dominant Fe ion, 3 where Fe XXV He$\alpha$ (and/or lower ionisation species of iron) is the main contributor, 12 absorbers with both Fe XXV He$\alpha$ and Fe XXVI Ly$\alpha$ lines with a common outflow velocity, and a further 3 that have two absorption components with different outflow velocities. Taking into account that some sources have absorption lines detected in more than one observation, on a per-source basis this corresponds to: 2/20 having Fe XXV He$\alpha$ absorption, 9 with Fe XXVI Ly$\alpha$ absorption[11], 7 with both Fe XXV and Fe XXVI Ly$\alpha$ absorption, and 2 having multi-$v_{\rm out}$ systems (out of 20). Interestingly, 8/9 sources with just a single Fe XXVI Ly$\alpha$ absorption line have outflow velocities which exceed the $v_{\rm out} \sim 10,000\,{\rm km\,s^{-1}}$ threshold employed by Tombesi et al. (2010a) when identifying 'Ultra-fast Outflow' (UFO) systems, while only 1 of the 6 sources with Fe XXV–XXVI absorption exhibit a mean velocity which exceed this threshold value. This is consistent with the view that higher ionised outflows originate closer to the central AGN and therefore have a higher outflow velocity, and is a point which I will be be further discussing in Chapter 5.

Histograms of *EW* for the absorption lines are shown in the top and middle panels of Fig. 4.7, respectively. Note that each of the detected line profiles is considered individually in these plots, i.e., both lines in a Fe XXV–XXVI pair are plotted separately, and that only those lines detected at $\geq 95\%$ confidence by MC simulations are included.

[11] In reality the number of Fe XXVI Ly$\alpha$ systems could be somewhat lower than this value due to the 4 AGN where the absorption is equally well fitted by Fe XXV He$\alpha$ at a slightly lower velocity (i.e., see §4.5.1).

Table 4.5: Summary of detected outflow phenomenology.

| Line(s) | Sources(spectra) |
|---|---|
| Fe XXV He$\alpha$ | 2 (3) |
| Fe XXVI Ly$\alpha$ | 9 (10) |
| Fe XXV–XXVI | 7 (12) |
| Multi $v_{\rm out}$ | 2 (3) |
| **Total** | 20 (28) |

The histogram in the bottom panel shows the *EW* distribution for *all* statistically significant absorption lines, including those which are consistent with being a blend of the Fe XXV–XXVI K$\alpha$ transitions. Measured *EW*s span from a few tens of eV up to $\sim 130 - 140$ eV (Fig. 4.7, bottom panel), in a distribution which is consistent with the curve of growth analysis conducted by Tombesi et al. (2011a). The mean *EW* of the Fe XXV He$\alpha$ and Fe XXVI Ly$\alpha$ absorption lines are $\sim 36$ eV and $\sim 38$ eV, respectively, and the total mean *EW* for all detected profiles (i.e., included blended ones) is $\sim 40$ eV. Importantly, the observed distribution of absorption line *EW*s is broadly consistent with that found by Tombesi et al. (2010a) using *XMM-Newton* (marked with a dashed black line in Fig. 4.7).

A useful quantity to calculate is the global probability that all of the observed lines are due to purely statistical shot noise, which can be done using the binomial distribution. For an event with null-probability $p$ the chance probability of the event $n$ happening in $N$ trials is given by:

$$P(n; N, p) = \frac{N!}{n!(N-n)!} p^n (1-p)^{N-n} \tag{4.3}$$

For $n = 20$ Fe K-band absorption line systems detected in $N = 51$ sources at a MC significance of $P_{\rm MC} \geq 95\%$ the probability of one of these absorption systems being due to shot noise can be taken as $p < 0.05$. On a per-source basis the probability of all of the observed absorption systems being associated with noise is then very low, with $P < 2 \times 10^{-13}$, which further reduces to $P < 5 \times 10^{-18}$ when considering the fact that

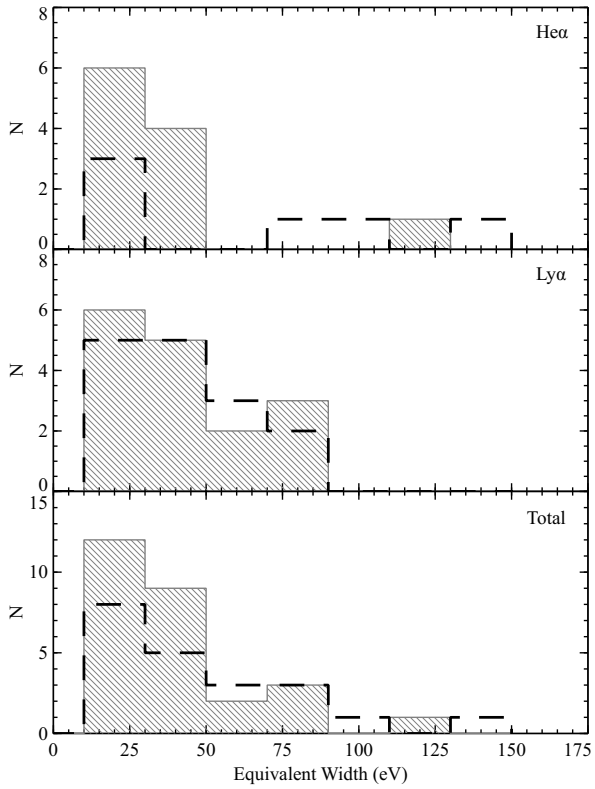


Figure 4.7: Histogram showing the mean equivalent widths of detected highly-ionised absorption lines. The top and middle panel show the distributions for Fe XXV He$\alpha$ and Fe XXVI Ly$\alpha$ transitions, respectively, while the bottom panel shows the total distribution of all detected 1s$\rightarrow$2p absorption lines including those which are detected as a blend of the two K$\alpha$ transitions. For sources with more than one line detected in multiple observations the mean equivalent widths have been used. The grey diagonally shaded area and the dashed black line show the distributions found in this work and with *XMM-Newton*, respectively. The *XMM-Newton* distributions were independently created using the values listed in table A.3 in Tombesi et al. (2010a).

some sources have lines detected in more than one epoch. This suggests that the observed lines are very unlikely to be associated with simple statistical fluctuations in the spectra. Moreover, it is important to remember that because the vast majority of absorption lines are detected at $P_{\rm MC} > 95\%$ significance these probabilities only represent conservative

lower limits on the global probability of all lines being false detections.

### 4.6.2 Absorber properties

The XSTAR parameter distributions as measured with *Suzaku*, again plotted using the mean absorber parameters averaged over all observations, are shown in Fig. 4.8. Overall, the general distributions and mean parameter values are broadly consistent with those found by Tombesi et al. (2010a) using *XMM-Newton*. The Fe K *Suzaku*-detected absorbers cover a wide range of column densities, ranging from $21.5 < \log(N_{\rm H}/{\rm cm}^{-2}) \leq 24.0$, with a peak in the distribution at $\log(N_{\rm H}/{\rm cm}^{-2}) \approx 22-23$. As shown by the dot-dashed (blue) and dotted (black) lines, which show the mean $\log(N_{\rm H}/{\rm cm}^{-2})$ value as found with *Suzaku* and *XMM-Newton*, respectively, the mean is $\log(N_{\rm H}/{\rm cm}^{-2}) \approx 23$ for both samples. From the middle panel the ionisation parameters are in the interval $2.5 < \log(\xi/{\rm erg\,cm\,s}^{-1}) \leq 6$ with the significant fraction of Fe XXV–XXVI pair systems, which persist over only a relatively narrow range in ionisation parameter (see Tombesi et al. 2011a curve of growth analysis), leading to a peak in the distribution at $\log(\xi/{\rm erg\,cm\,s}^{-1}) \approx 4$. Again, as shown by the vertical lines the mean ionisation parameter in both samples is almost identical at $\log(\xi/{\rm erg\,cm\,s}^{-1}) \approx 4.5$. The detection of relatively low-ionisation material in the Fe K band, i.e., $\log(\xi/{\rm erg\,cm\,s}^{-1}) \sim 2.5-3.0$, is particularly interesting and suggests that high velocity absorption could feasibly be detected at softer X-ray energies through weak, moderately ionised, iron lines. Moreover, the detection of a small fraction of absorbers with $\log(\xi/{\rm erg\,cm\,s}^{-1}) \geq 5$ in both my work and in that of Tombesi et al. raises the possibility that material may be present in some sources which is so highly ionised that even iron is not detectable through spectroscopy. If this is the case then the fraction of sources with Fe K absorption ($\sim 40\%$) may represent a *lower limit* on the number of sources with intrinsic nuclear outflows along the line-of-sight.

The $\log(v_{\rm out}/{\rm km\,s}^{-1})$ distribution (bottom panel) appears to be relatively continuous over a broad range of velocities; ranging from as low as $v_{\rm out} < 1,500\,{\rm km\,s}^{-1}$ up to $v_{\rm out} \approx 100,000\,{\rm km\,s}^{-1}$. The median outflow velocity is $v_{\rm out} \sim 17,000\,{\rm km\,s}^{-1}$ ($\sim 0.056\,{\rm c}$) Ninety per cent of the detected outflows have $v_{\rm out} \geq 1,500\,{\rm km\,s}^{-1}$ which makes the

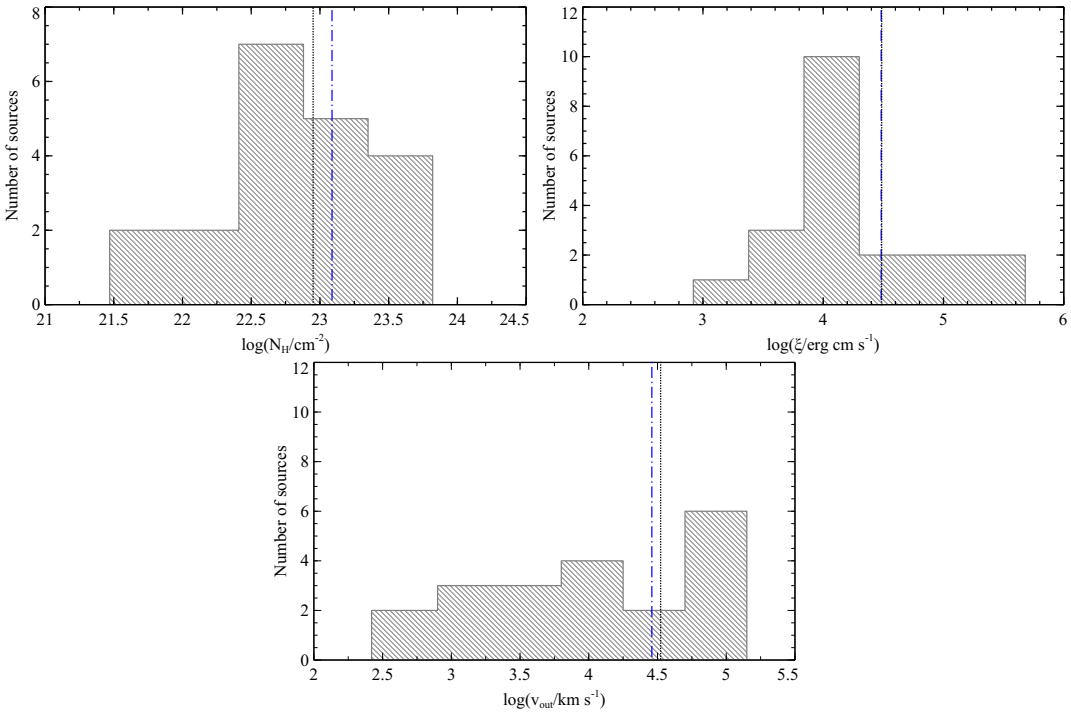


Figure 4.8: Histogram showing the overall distributions of mean absorber parameters for each source: (a) logarithm of the mean column density; (b) logarithm of the mean ionisation parameter; (c) logarithm of the mean outflow velocity. The dot-dashed (blue) and dotted (black) vertical lines indicate the mean value of the *Suzaku* and *XMM-Newton* analyses, respectively.

absorption detected at Fe K almost systematically faster than the traditional soft X-ray warm absorber. Only NGC 3227, NGC 4395 and NGC 3783 have Fe K outflows which are consistent with having no outflow velocity (i.e., $v_{\rm out} \sim 0\,{\rm km\,s^{-1}}$ at the resolution of the XIS CCDs). From Table 4.6 the distributions of outflow velocity appear to be very similar between both the *Suzaku* and *XMM-Newton* samples, with the bulk of outflows in both samples having $v_{\rm out} > 10,000\,{\rm km\,s^{-1}}$. The *Suzaku* sample does appear to have slightly more low-intermediate velocity systems but, given the low number statistics involved, the differences are probably not significant. An interesting thing to note is that both *Suzaku* and *XMM-Newton* may be subject to an instrumental bias against

Table 4.6: Outflow velocity comparison.

| Velocity ($\mathrm{km\,s^{-1}}$) | *Suzaku* | *XMM-Newton* |
|---|---|---|
| $v_{\rm out} \sim 0$ | 2/20 | 2/19 |
| $0 < v_{\rm out} \leq 10,000$ | 6/20 | 2/19 |
| $v_{\rm out} > 10,000$ | 12/20 | 15/19 |
| $v_{\rm out} \geq 30,000$ | 8/20 | 9/19 |

the detection of low-velocity absorption systems. At the energy resolution of the EPIC and XIS CCDs the presence of Fe XXV and/or Fe XXVI emission lines could mask the signature of low-velocity absorption systems and thereby introduce a selection effect against their detection. The only way to reveal the presence of such absorption systems would be through future observations with, for example, the calorimeter aboard *Astro-H*, which would have sufficient resolution to distinguish between individual emission and absorption components at low velocity.

Even so, I can quantitatively assess the similarity between all of the measured *Suzaku* and *XMM-Newton* parameter distributions using a Kolmogorov-Smirnov two-sample test (K-S Test) which uses the maximum differences between the cumulative fractional distribution of two sets of data to determine the probability that they are both drawn from the same parent sample. In this case such a test can be used to quantify the level at which the column density, ionisation parameter and outflow velocity distributions as measured with both *Suzaku* and *XMM-Newton* are in agreement. For a null hypothesis that each of the *Suzaku* and *XMM-Newton* distributions are drawn from the same parent sample I am unable to conclusively rule out the null hypothesis in any of the three cases at greater than the 90% confidence level.

## 4.7 Discussion

### 4.7.1 Modelling complexities

In the realm of complex broad-band spectral modelling, there are several modelling caveats which might have an effect on both the detection rate of Fe K-band absorbers and the measurement of their properties. Here, I offer a brief discussion to investigate whether there are any degeneracies or uncertainties in the broad-band models which could have an effect on the primary results of my work with the *Suzaku* sample.

#### The soft-excess

A total of 6/20 sources in which I have detected highly-ionised absorption also have a soft-excess. Thus far, I have taken the simplistic approach of fitting any excesses below 2 keV with a phenomenological blackbody. However there are several alternative means of fitting this component which could subtly alter the broad-band continuum model, and hence possibly influence the parameters obtained for the Fe K-band absorption lines. To assess for this possibility I also refitted the soft-excesses in each of these 6 sources with two alternative models: `diskbb` (Mitsuda et al. 1984), which integrates over the surface of the accretion disc to form a multi-colour blackbody spectrum, and `comptt` (Titarchuk 1994), which models the excess with the Comptonised emission of soft seed photons by a hot corona above the accretion disc. Both of these alternative models have been used to good effect in the literature when modelling the soft-excess (e.g., Porquet et al. 2004a; Patrick et al. 2011a,b; see Chapter 3).

In each of the 6 sources, I replaced the `bbody` component with both `diskbb` and `comptt` in turn, refitted the data in each case, and compared the resultant continuum and absorption line parameters to those obtained previously. For the `comptt` models a disc geometry was assumed and the input photon seed temperature was allowed to vary between 5 eV and 0.1 keV, while the optical depth $\tau$ and temperature $T$ of the Comptonising plasma above the disc were allowed to vary freely, as was the component

normalisation. In all cases it was apparent that fitting the soft-excess with `diskbb` or `comptt` has no significant effect on the parameters of either the absorption lines or the continuum, which were always found to be consistent with those obtained with `bbody` at the 90% level. In the heavily absorbed sources such as NCG 3783, NGC 4051 and MCG-6-30-15 there were some small variations in column density and ionisation parameter for the soft-band absorbers when fitting with `comptt`, presumably to compensate for the fact that the Comptonised emission fitted with `comptt` can extend to harder X-ray energies (i.e., $E \geq 2 - 3\,\mathrm{keV}$) than typically seen in black-body derived models. Even so, because the key parameters (i.e., those of the continuum and the hard-band absorption lines) are not affected by these subtle changes I do not regard them particularly significant in the context of my analysis. On the whole, then, the parameters measured for the highly-ionised absorption systems in these sources are largely independent of the method used to parametrise the soft-excess.

As mentioned in §4.4.1 (c.f., §1.4.3) other interpretations of the soft-excess posit that it may be due to smeared absorption or blurred reflection associated with an increase in optical depth of lowly ionised circumnuclear material. For simplicity, I do not investigate these interpretations any further as they will probably require a complete restructuring of the entire broad-band model for each source. However, it is important to note that most of the outflows detected in these sources have also been detected by Patrick et al. (2012) (also see Chapter 6 for a detailed sample comparison) who have used blurred reflection models to fit their *Suzaku* spectra which suggests that the majority of the line detections are robust regardless of the underlying assumptions made when modelling the broad-band continuum.

### Warm absorption

soft-band absorbers with intermediate ionisation states, i.e., those with $\log(\xi/\mathrm{erg\,cm\,s^{-1}}) \geq 2.5$ where Fe starts to become significantly ionised (Kallman & McCray 1982; Kallman et al. 2004) can impart weak Fe XXV and Fe XXVI absorption lines in the Fe K band which can reduce the significance of any absorption lines associated with higher ionisation

material. Absorption components with ionisation parameters in this regime are present in 4/20 sources with detected Fe K outflows. However, because all of the absorbers in the soft-band have an implicitly assumed $v_{\rm out} = 0\,{\rm km\,s^{-1}}$ throughout this work, any associated absorption lines will be limited solely to their expected rest-frame energies and only the lowest velocity absorbers in the Fe K band are likely to be affected. Moreover, even if this was not the case, the line significances through Gaussian fitting for each of the sources are very high, with $\Delta\chi^2/\Delta\nu \geq 25/2$ in all cases. This suggests that even if there is weak Fe XXV-XXVI from the soft-band absorbers present at higher energies, it is unlikely to have a significant effect on the high velocity absorption systems detected here. For these two reasons, this effect could potentially pose a problem for my detections of highly-ionised absorption lines in these sources.

### Compton reflection

The `reflionx` reflection model assumes a fixed face-on geometry with all of the reflected emission originating at the surface of the accretion disc (Ross & Fabian 2005b). This means that it is unable to account for the variations of the fluorescence line emissivity or the profile of the Compton reflection hump, both of which have a viewing angle dependence (Magdziarz & Zdziarski 1995), which can lead the model to either under- or over-predict the Fe K$\alpha$ line flux for a given reflection fraction if a source happens to have an inclined accretion disc, or has a more complex reflection geometry. In some sources this can lead to an apparent hard-excess which may be a direct result of the underlying assumptions made with the `reflionx` model rather than an intrinsic feature of the X-ray spectrum. Alternatively, the observed reflection could have an origin which is not associated with the accretion disc. For example, a strong hard-excess remains in MCG -2-58-22 when I fitted the reflection continuum with `reflionx`, while Rivers, Markowitz & Rothschild (2011) show that no such excess is present when using the more sophisticated `MYTorus` reflection model which assumes a distant toroidal reflector.

Strong hard X-ray excesses at $E \gtrsim 15\,{\rm keV}$ have been reported in a number of sources in the literature in recent years (e.g., Turner et al. 2009; Reeves et al. 2009;

Risaliti et al. 2009; Tatum et al. 2013). The weaker of these hard excesses can sometimes be accounted for by allowing the iron abundance of the reflector to adopt sub-Solar values, and thereby enhancing the prominence of the Compton-reflection hump relative to the flux of the Fe K$\alpha$ fluorescence line. However, this approach is unable to account for the observed excesses in the most extreme cases and an additional spectral component is required to supplement the neutral reflection in the hard X-ray band. There are two spectral interpretations which accomplish this: relativistically enhanced reflection (e.g., Nardini et al. 2011; Reynolds et al. 2012) and Compton-thick partial covering (e.g., Turner et al. 2009; Reeves et al. 2009; Tatum et al. 2013).

In this work I decided to exclusively fit any hard-excesses which cannot be accounted for through a variable iron abundance with Compton-thick partial covering ($N_{\rm H} \gtrsim \sigma_{\rm T}^{-1} \simeq 1.5 \times 10^{24}\,{\rm cm}^{-2}$). However, it is important to note that my decision to model hard-excesses in this manner is driven solely by the desire to construct a broad-band model which is suitable for rapidly computed MC simulations, and that the presence of a Compton-thick partial coverer in any given model does not necessarily mean that that source is intrinsically covered by a clumpy screen of Compton-thick gas. Indeed, statistically equivalent fits to the hard-excess can likely be achieved with models based on relativistically blurred reflection, but the extreme computation time that would be necessary to run MC simulations on these models makes their use impractical in the search for highly-ionised absorption lines and I therefore do not consider them a viable option in this work. Even so, I stress that because the contribution of Compton thick absorption or blurred reflection is largely limited to hard energies, i.e., $E > 10 - 15\,{\rm keV}$, the manner in which the hard-excess is fitted in these sources is unlikely to have an effect on the detection rate of highly-ionised absorption lines or the parameters of the associated Fe K absorbers.

### Partially-covering absorption

In addition to the Compton-thick partial covering gas used to supplement the reflection continuum in sources with hard-excesses, I have also used moderate columns of partial-

covering absorption ($N_{\rm H} \lesssim$ few $\times 10^{23}\,{\rm cm}^{-2}$) to fit spectral curvature and spectral variability below 10 keV. In terms of the sources with detected Fe K outflows 12/20 have at least one partially covering component (including those which are Compton-thick), with 5 of those having more than one partial coverer in a layered or clumpy geometry. The principal driver behind the inclusion of partial covering absorption in these sources is the need to account for the variability in spectral shape which is apparent when more than one observation has been simultaneously fitted, especially if those observations are separated by a number of years. The addition of a partially covering component allowed for the variability observed in Mrk 766, NGC 1365, NGC 3227, NGC 3516, NGC 3783, NGC 4051 and PDS 456 to be easily accounted for, and enables the absorption line parameters in these sources to be assessed against a self-consistently fitted underlying continuum in all observations. It is important to note, however, that regardless of the underlying continuum model the detection of highly-ionised absorption lines in these sources is largely model independent and does not affect the overall statistics reported in this work.

### 4.7.2 Evidence for complex variability and absorber structure?

In addition to broad-band spectral variability there is also compelling evidence for intricate variability in the Fe K absorber itself. In a number of cases this variability can be simultaneously and self-consistently fitted using XSTAR absorption tables which strongly implies an atomic origin rather than an association with spectral fluctuations and photon statistics. In NGC 3227, for example, transient Fe K absorption lines are detected in 3 of the 6 *Suzaku* epochs, with the line parameters varying on a $\Delta t \sim 2$ week time-scale. Similar is also true in Mrk 766, PDS 456 and NGC 1365, which all exhibit absorption line variability albeit over a longer (i.e., $\Delta t \sim$year) baseline. In both Mrk 766 and PDS 456 the absorber appears to change in ionisation state between the *Suzaku* epochs, with the outflow in Mrk 766 also showing a decrease in outflow velocity. Here, I discuss both of these sources in greater detail.

Mrk 766 and PDS 456 have both long been known to harbour Fe K absorbers

(Mrk 766: Pounds et al. 2003b; Turner et al. 2007; Miller, Turner & Reeves 2008; Risaliti et al. 2011. PDS 456: Reeves & Turner 2000; Reeves, O'Brien & Ward 2003; Reeves et al. 2009). In both cases, the range of *Suzaku* rest-frame energies which I find for the absorption profiles with are consistent with those previously published in the literature. In Mrk 766 I find a common velocity shift of $v_{\rm out} \sim 6,000 - 18,000\,{\rm km\,s^{-1}}$ for the Fe XXV He$\alpha$ and Fe XXVI Ly$\alpha$ lines, which is consistent with the $v_{\rm out,XMM} \sim 3,000 - 16,000\,{\rm km\,s^{-1}}$ reported previously in *XMM-Newton* data (Miller et al. 2007; Turner et al. 2007; Risaliti et al. 2011). Similarly, from my simultaneous analysis of the 2007 and (currently) unpublished 2011 *Suzaku* observations of PDS 456 I find two absorption troughs which persist across both sequences (see Fig. 4.9). These troughs — which are likely due to blends of the Fe XXV He$\alpha$ and Fe XXVI Ly$\alpha$ lines owing to their breadth — have a mean inferred $\langle v_{\rm out} \rangle \sim 0.3\,{\rm c}$, which is consistent with that reported by Reeves et al. (2009) in their initial analysis of the 2007 observation.

An interesting property of the outflows in both of these sources is that the parameters of the hard-band absorber appears to be linked to both the incident source flux, and to the broad-band absorption characteristics of the X-ray spectrum. On the basis of detailed time- and flux-resolved spectroscopy of Mrk 766 using *XMM-Newton*, Turner et al. (2007) noted that the *EW* of the Fe XXVI Ly$\alpha$ absorption line could be correlated with the intrinsic source flux, with the correlation not easily accounted for by simply appealing to changes in the ionisation state of a constant column density absorber in response to changes in the incident continuum. This provided evidence for complex absorber structure in Mrk 766. Further evidence for Fe K absorber complexity was suggested by Risaliti et al. (2011) who, from a re-analysis of the same *XMM-Newton* data, found that the presence of the highly-ionised absorption profiles appeared to be contingent on the source being eclipsed by a number of high column density, i.e., $\log(N_{\rm H}/{\rm cm^{-2}}) \gtrsim 23$, partially-covering clouds with a low ionisation state. This led the authors to propose a scenario where multiple 'cometary' absorption clouds with a large gradient in both column density and ionisation state were moving across the line of sight, thus giving rise to the varying absorption characteristics present in different time-slices (e.g., $v_{\rm out}$).

My analyses of their *Suzaku* spectra yield further evidence for a complex and dynamic structure in hard-band absorbers. In Mrk 766 the *EW* of the Fe XXV He$\alpha$ and Fe XXVI Ly$\alpha$ lines present in the *Suzaku* spectrum are statistically consistent at the 90% level but, as shown in the appropriate entries in Appendix A.1, there is a visual shift in the dominant iron ion of the absorber, with Fe XXVI Ly$\alpha$ ($EW_{\mathrm{Ly}\alpha} = -40 \pm 17\,\mathrm{eV}$) appearing strongest in OBSID 701035010 and Fe XXV He$\alpha$ ($EW_{\mathrm{He}\alpha} = -60 \pm 14\,\mathrm{eV}$) strongest in OBSID 701035020, which is possibly associated with the $\Delta \log(\xi/\mathrm{erg\,cm\,s^{-1}}) \sim 0.4$ change in ionisation parameter between the two observations. Furthermore, and as I have mentioned previously, the decrease in ionisation is also met with a decrease in measured outflow velocity and the onset of strong Fe XXV emission which could be associated with a cloud/clump of material moving outside of the sight-line. A similar effect is also apparent in PDS 456 where, despite there being no measurable change in the relative velocity of the two blended Fe XXV–XXVI absorption complexes, the absorber ionisation state decreases by $\Delta \log(\xi/\mathrm{erg\,cm\,s^{-1}}) \sim 0.26$ in the 2011 observation relative to 2007 which leads to a slight visual broadening of the absorption profiles due to an increased Fe XXV He$\alpha$ contribution in the blended absorption line profile.

Interestingly, the decreased ionisation state of the absorbers in both Mrk 766 and PDS 456 occurs when the covering fraction of the soft X-ray absorber is at its highest which implies a dynamic clumpy structure to the outflow. Moreover, as noted by both Turner et al. (2007) and Behar et al. (2010), respectively, the opposite is also true in both sources, i.e., when the sources are in their least absorbed state, the discrete highly-ionised absorption lines are not significantly present in the X-ray spectra of either source. This is consistent with the conclusions reached by Risaliti et al. (2011) in the context of stratified, partially-covering, absorption clumps needing to be present along the line of sight, and close to the continuum source, for highly-ionised absorption lines to be observed.

Additional evidence for this supposition is provided through consideration of my fits to the other sources in the sample. It is intriguing to note that statistically acceptable (i.e., $\chi^2_{\mathrm{reduced}} \approx 1.0$) partially covering absorption models are obtained for a curiously large fraction of the sources with detected outflows (12/20; $\sim 60\%$) which further suggests

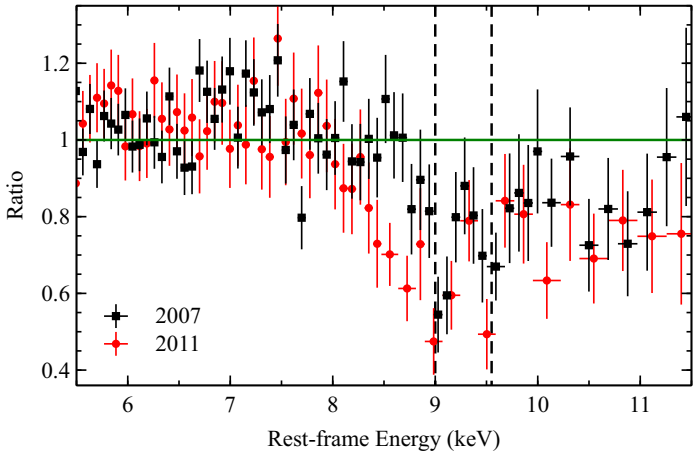


Figure 4.9: Ratio plot comparison of the 2007 (black squares) and 2011 (red circles) *Suzaku* observations of PDS 456 in the Fe K band. The dashed vertical lines indicate the position of the two blended Fe XXV–XXVI absorption troughs present in both spectra, at rest-frame energies of $\sim 9.0$ and $\sim 9.6$ keV, respectively. There is a noticeable broadening in the left hand absorption profile in the 2011 observation which is likely caused by a drop in absorber ionisation state, and an associated increase in the Fe XXV He$\alpha$ contribution to the absorption profile. See text and Reeves et al. (2013, in prep) for further details.

that there may be a link between complex absorption geometries and highly-ionised absorption lines. One possibility is where the partially covering components represent denser clumps of material in an inhomogeneous highly-ionised wind from the accretion disc, similar to the case reported in Mrk 766 (Miller et al. 2007; Turner et al. 2007; Risaliti et al. 2011). Indeed, inhomogeneous winds with stratified or filamentary ionisation and density structure are expected as a natural consequence of the accretion process and are ubiquitously seen in both hydrodynamic (e.g., Proga & Kallman 2004; Kurosawa & Proga 2009; Sim et al. 2010) and magneto-hydrodynamic (e.g., Ohsuga et al. 2009; Ohsuga & Mineshige 2011) simulations of accretion discs. It is therefore not particularly surprising to find a possible link between clumpy absorption dominated models and sources with high-velocity outflows.

### 4.7.3 On the claimed publication bias

The transient and variable nature of Fe K absorption lines has in part lead to their true veracity to be questioned in the literature. In particular, Vaughan & Uttley (2008) suggested that there may be a publication bias at play in the reporting of both red- and blue-shifted features in the Fe K band, with only those observations with the strongest line detections being reported in the literature. Through a plot of '$EW - \mathrm{error}\langle\mathrm{EW}\rangle$' Vaughan & Uttley (2008) showed that the $EW/\mathrm{error}\langle\mathrm{EW}\rangle$ ratio remained relatively constant (i.e., lines with larger $EW$ have correspondingly larger 90% errors) over a wide range of $EW$s in their sample of narrow lines in 38 sources collected from the literature. They also noted that since the vast majority of reported detections (prior to 2008, at least) were of relatively low significance (i.e., typically around $2-3\sigma$) suggesting that the lines may be spurious, and more consistent with merely being the strongest natural fluctuations in otherwise featureless spectra rather than real atomic features. Moreover, Vaughan & Uttley (2008) suggested that the conspicuous absence of any lines in the upper left quadrant of the $EW - \mathrm{error}\langle\mathrm{EW}\rangle$ plot (which would correspond to stronger lines having smaller uncertainties) implied that the detection of the narrow velocity shifted lines was in some way inversely correlated to the statistical quality of the observation. Observations with longer exposures and better photon statistics only ever showed the weakest lines, which further enforced the possibility of a bias in the published observations.

However, these points were addressed through the systematic search conducted by Tombesi et al. (2010a) using *XMM-Newton*, at least in the context of blue-shifted Fe K absorption lines. By uniformly and comprehensively searching for such features in a complete sample of AGN observations, by carefully reporting the fraction of detections to null detections, and by assessing the statistical significance of any detected absorption lines through MC simulations, Tombesi et al. (2010a) were able to robustly assess the fraction of AGN in the local universe that have Fe K outflows in a way which overcame any publication biases and accounted for the possibility of random fluctuations in the source spectra. My work with the *Suzaku* outflow sample complements the findings of

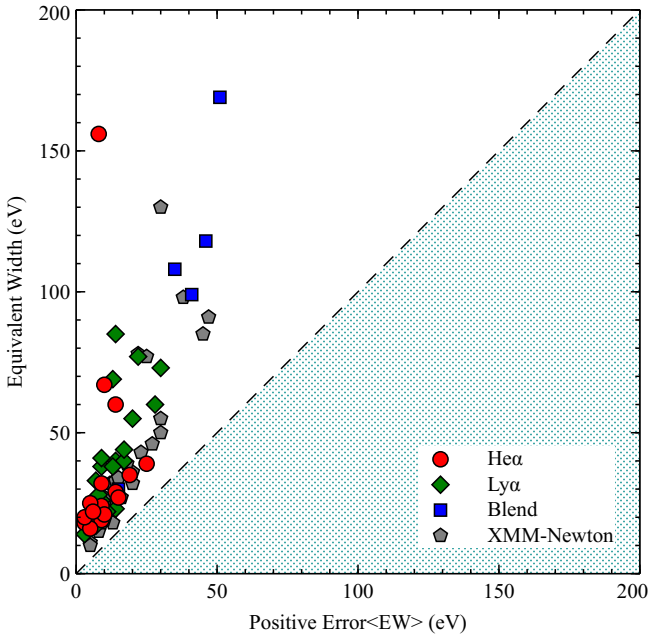


Figure 4.10: Plot of the measured equivalent width of the blue-shifted absorption lines with respect to their negative 90% error. The circles (red), diamonds (green), and squares (blue) correspond to the Fe XXV He$\alpha$, Fe XXVI Ly$\alpha$ and blended Fe XXV–XXVI lines, respectively. Analogous values for the blue-shifted absorption lines found in the Tombesi et al. (2010a) *XMM-Newton* sample are shown as pentagons (grey). The diagonal dashed line shows the expected trend if $EW = -\text{error}\langle\text{EW}\rangle$ and the dotted (dark-cyan) area shows the area of non-detection (see text for further details).

Tombesi et al. (2010a), and lends further weight to the assertion that such outflows are an important intrinsic feature of the AGN X-ray spectrum in a large fraction of sources. In Fig. 4.10 I have reproduced the Vaughan & Uttley (2008) $EW/\text{error}\langle\text{EW}\rangle$ plot[12] used by Tombesi et al. (2010a) (see their Fig. 8) to include data points corresponding to the absorption lines found in this work at a $P_{\text{MC}} \geq 95\%$ significance level. The figure concisely shows that the distribution of points from both the *Suzaku* and *XMM-Newton*

[12]Note that the axes in this plot use a linear scale rather than the logarithmic one as used by Vaughan & Uttley (2008). As noted by Tombesi et al. (2010a) the use of a logarithmic scale visually compresses the data points towards the $EW = \text{error}\langle EW\rangle$ threshold of non-detection.

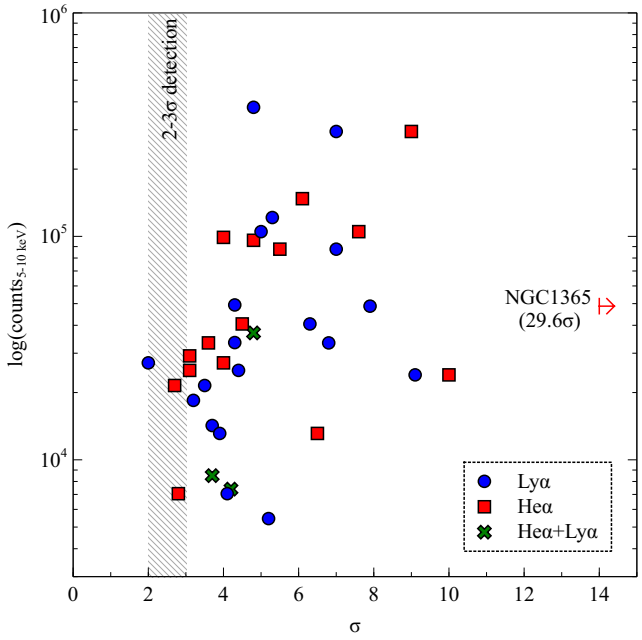


Figure 4.11: Plot of total $5-10\,\mathrm{keV}$ counts versus line significance, in units of $N\sigma$ ($\equiv \mathrm{EW}/-\mathrm{error}\langle\mathrm{EW}\rangle$). The blue circles, red squares and green crosses show the positions of Fe XXV He$\alpha$, Fe XXVI Ly$\alpha$ and blended Fe XXV–XXVI lines, respectively. Only absorption lines detected at $P_{\mathrm{MC}} \geq 95\%$ are shown. The dashed grey band shows the $2-3\sigma$ detection regime.

samples diverges from that of the $EW = \mathrm{error}\langle EW\rangle$ 'detection line', with both sets of data having a number of points which veer towards the important upper left quadrant of the diagram indicating stronger lines with smaller uncertainties. Interestingly, the overall distribution of points for the *Suzaku* lines follows a similar trend to those obtained with *XMM-Newton* which implies that all points are drawn from the same parent population, as would be expected should the two samples be tracing the same physical phenomenon which imprints real spectroscopic lines in the X-ray spectrum.

A further means of visually assessing for a publication bias, and for testing whether the absorption lines are consistent with random fluctuations or real features, is through a plot of line significance versus photon counts in the Fe K band (i.e., between $5-10\,\mathrm{keV}$).

Such a plot is shown in Fig. 4.11. For simplicity I grade line significance according to $N\sigma \equiv EW/-\text{error}\langle\text{EW}\rangle$, where it is important to recognise that in this case $-\text{error}\langle\text{EW}\rangle$ refers to the $1\sigma$ (68%) negative errors on an absorption line's $EW$, which were measured independently for each absorption line, and *not* to the 90% errors ($\approx 1.6\sigma$) reported in Table 4.3. By using the $1\sigma$ negative errors the standard Gaussian probabilities (i.e., $2\sigma = 95.5\%$, $3\sigma = 99.73\%, 4\sigma = 99.994\%$) then correspond to the statistical significance of a line relative to it having an intrinsic $EW$ of 0 eV, and thus not being detected. Fig. 4.11 shows that the detected lines typically have significances ranging from $\sim 2\sigma$ through to $\sim 10\sigma$ over a wide range in count rate; with a significance of $\sim 30\sigma$ the extremely strong Fe XXV He$\alpha$ line in NGC 1365 (OBSID 702047010) is by far the most significant line in the sample and is omitted from the main plot for clarity.

In such a plot one would expect to see a correlation between total Fe K counts and the significance of an absorption line, where observations with higher counts in the Fe K band, and therefore better photon statistics, have stronger absorption line detections. Indeed, while there is noticeable scatter in $N_{\text{counts}}$ versus $\sigma$ — as would be expected given that there is a wide dispersion in absorption properties (i.e., $N_{\text{H}}$, $\xi$, $v_{\text{out}}$) for a given total counts — a simple Spearman's rank association shows that the data are positively correlated (Spearman's rank coefficient, $r_s = 0.4406$). This is sufficient to rule out the possibility of the two parameters being completely independent at the $> 99\%$ significance for 34 matched pairs. Therefore, $\sigma$ values tend to increase in higher counts observations which causes the data to gradually diverge from the $2-3\sigma$ significance region towards the upper right quadrant of the plot. Moreover, the vast majority of the line detections are located well away from the $2-3\sigma$ 'noise' level, as would be expected if the majority of the line detections are not purely due to photon statistics.

Overall, my work with the *Suzaku* sample is consistent with those obtained using *XMM-Newton* and, combined, the two studies provide strong evidence for the presence of very highly-ionised, often high-velocity, outflows in the central region of a large fraction of not only radio-quiet AGN, but also suggests that they may be prevalent in radio-loud sources as well. The possible prevalence of very highly-ionised, high-velocity winds in AGN is consistent with theoretical models which argue that such outflows are an

important phenomenon which may play a role in Galactic-scale feedback scenarios. I return to this point in the next chapter where I probe the global energetics of the detected absorbers, assess for any correlations between the outflow parameters and those of the central SMBH, and discuss both the origins of the absorbing material and its likely launching mechanism.

# 5 Outflow sample II – wind location and energetics

## 5.1 Introduction

In the previous chapter I showed that $\sim 40\%$ (20/51) of the *Suzaku* selected AGN display statistically significant (i.e., $P_{\rm MC} \geq 95\%$) evidence for Fe XXV He$\alpha$ and/or Fe XXVI Ly$\alpha$ absorption at rest-frame energies of $E > 6.7\,{\rm keV}$. Modelling the absorption lines with XSTAR showed that the absorbing gas is typified by both large column densities and high ionisation, with $\langle \log(N_{\rm H}/{\rm cm}^{-2}) \rangle \approx 23$ and $\langle \log \xi \rangle \approx 4.5$, respectively. The lines were also substantially blue-shifted from their expected laboratory energies, corresponding to outflows with velocities in the range $v_{\rm out} \sim 10^3 - 10^5\,{\rm km\,s^{-1}}$. These parameters are substantially larger than those found for the canonical soft X-ray warm absorber (e.g., Reynolds 1997; Blustin et al. 2005; Crenshaw, Kraemer & George 2003a and references therein) which suggests that the Fe K outflows are located much closer to the central black hole. Even so, the absorber parameters made available through XSTAR modelling can only elude to the instantaneous properties of the *absorber* and, by themselves, they offer little to no insight into the *outflow* itself or the impact which it may have on the host galaxy.

In this chapter I use the XSTAR parameters in conjunction with several simple geometric relations to infer three key parameters for the highly-ionised outflows. These are: (1) their projected distance from the central source, (2) the rate at which they expel mass into the host galaxy, and (3) the associated mechanical power (kinetic luminosity) imparted into the host galaxy due to the ejected mass. These parameters enable how much energy the outflows inject into their local environment to be estimated which therefore allows assessment as to their significance when it comes to AGN feedback. Following on from this analysis, I perform a correlation analysis to assess whether there are any global trends amongst the highly-ionised outflows, and to see whether the outflow properties are at all correlated with those fundamental to the AGN itself.

## 5.2 Outflow parameters

### 5.2.1 Projected distance

The column density $N_{\rm H}$ of gas along the line of sight is given by $N_{\rm H} = \int_r^{r+\delta r} n(r)dr$, where $r$ is the distance of the absorber from the central source and $\delta r$ is the observed thickness of the flow along the line of sight. Should the absorber occupy a thin spherically-symmetric shell with a net thickness which is less than its distance from the source, i.e., $\delta r/r < 1$, this equation can then be approximated to good accuracy by $N_{\rm H} \sim n\delta r$. Combining this relation with the definition of the ionisation parameter $\xi = L_{\rm ion}/nr^2$ (Tarter, Tucker & Salpeter 1969), where $L_{\rm ion}$ is the source ionising luminosity integrated between $1 - 1000$ Rydberg and $n$ is the average absorber number density, the maximum distance that the absorber can be located from the ionising source given its measured $N_{\rm H}$ and $\xi$ is

$$r < r_{\rm max} = \frac{L_{ion}}{\xi N_H} \tag{5.1}$$

Conversely, a lower limit on $r$ can be inferred by considering the escape radius of the gas given its observed velocity. For a simple Keplerian disc orbiting a black hole the escape velocity at distance $r$ is $v_{esc} = \sqrt{2GM_{\rm BH}/r}$. In the limit that $v_{\rm out} = v_{\rm esc}$, i.e., assuming that the measured outflow velocity across the line of sight is equal to the escape velocity at observed radius $r$, a lower limit on $r$ can be estimated by

$$r > r_{\rm min} = \frac{2GM_{\rm BH}}{v_{\rm out}^2}. \tag{5.2}$$

These relations then allow upper and lower limits to be placed on the absorber location, given the observed parameters.

### 5.2.2 Mass outflow rate

Simulations of accretion discs have shown that AGN winds are likely to be inhomogeneous in structure, and form a bi-cone-like geometry (e.g., Proga & Kallman 2004; Ohsuga et al. 2009; Ohsuga & Mineshige 2011). Krongold et al. (2007) derive an angle-dependent

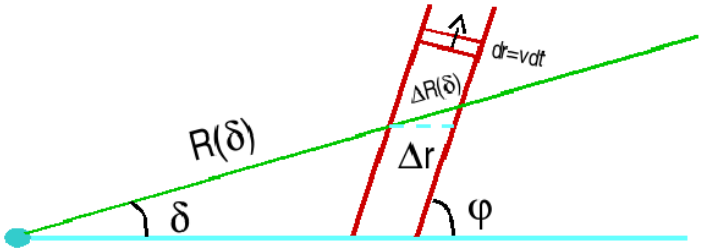


Figure 5.1: Schematic diagram of the bi-conical outflow geometry used by Krongold et al. (2007). A wind of thickness $\Delta r$, launched at an angle $\phi$ with respect to the accretion disc, is observed at an angle $\delta$ from the accretion disc plane. See text for further details. Image taken from Krongold et al. (2007).

mass outflow rate for bi-conical winds, however an equivalent equation can be achieved by assuming spherical symmetry and retrospectively using the Krongold et al. results to correct for the geometry.

In general, the mass outflow rate $dM/dt = \dot{M}_{\rm out}$ for an arbitrary wind is given by

$$\dot{M}_{\rm out} = A(r)\rho(r)v(r), \tag{5.3}$$

where $\rho(r)$ and $v(r)$ are the density and velocity profile of the wind, and $A(r)$ is a factor which accounts for the geometry of the outflow. Assuming that the flow has constant terminal velocity $v(r) = v_{\rm out}$ and that the absorbing gas has cosmic elemental abundances (i.e., $\sim 75\%$ of its mass by hydrogen and $\sim 25\%$ by helium), $\rho(r) = 1.23 m_{\rm p} n$ where $m_{\rm p}$ is the proton mass and $n$ is the gas number density. Substituting these into eq. (5.3) then gives $\dot{M}_{\rm out} \propto A(r) m_{\rm p} n v_{\rm out}$, with the remaining uncertainty being the outflow geometry. For a spherically symmetric isotropic wind $A(r) = \Omega b r^2$, where the product $\Omega b \leq 1$ is known as the *global filling factor* and accounts for both the solid angle occupied by the flow ($\Omega$) and how much of the flow volume is filled by gas ($b$). This then leads to $\dot{M}_{\rm out} \propto \Omega b r^2 m_{\rm p} n v_{\rm out}$.

The value $b$ is extremely difficult to determine observationally so it is useful to re-write it in terms of observable parameters. At low–intermediate ionisation states the flow is likely to be clumpy/filamentary, while at high ionisation states it can be considered largely smooth and of low density because the vast majority of elements

are stripped of electrons. In the clumpy case, the column density of the wind can be given by $N_{\rm H} \sim bn\delta r$, with $b < 1$ implicitly allowing for inhomogeneities in the flow. Alternatively, at high ionisation states $b \simeq 1$ and $r \rightarrow r_{\rm max}$. Substituting these relations into equations 5.1 and 5.2 yields upper and lower limits:

$$\dot{M}_{\rm out} = 1.23\Omega m_{\rm p} N_{\rm H} v_{\rm out} r \equiv \begin{cases} 2.46 G \Omega m_{\rm p} M_{\rm BH} N_{\rm H} v_{\rm out}^{-1} & \text{(lower limit)} \quad (5.4a) \\ 1.23\Omega m_{\rm p} L_{\rm ion} \xi^{-1} v_{\rm out} & \text{(upper limit)} \quad (5.4b) \end{cases}$$

This quick derivation is directly equivalent to the more complex one by Krongold et al. (2007) because all of the angle-dependencies and constants invoked by those authors are folded into our $\Omega$ parameter, e.g.,

$$\dot{M}_{\rm out} = 1.23 \times \underbrace{0.8 f(\delta,\phi)\pi}_{\Omega=(6/5)\pi} m_{\rm p} N_{\rm H} v_{\rm out} r, \quad (5.5)$$

the $f(\delta,\phi)$ function collects all of the $\delta$ and $\phi$ angle dependencies associated with the bi-conical geometry into a single calculable function; $f(\delta,\phi) \simeq 1.5$ is assumed, which corresponds to a wind launched vertically from the accretion disc (i.e., $\phi = \pi/2$) and viewed at a mean line-of-sight viewing angle of $\delta = 30°$, leading to $\Omega = (6/5)\pi$ (see Fig. 5.1). This corresponds to a global wind covering of $\Omega/4\pi = 0.3$, which is comparable to the $\sim 40\%$ detection rate for Fe K winds in the *Suzaku* sample. The viewing angle has only a small effect on the value of $\dot{M}_{\rm out}$, with all real values of $\delta$ appropriate for type 1.0–1.9 AGN leading to inferred mass outflow rates which differ by only a factor of $\sim 2$. Therefore, whilst the estimated $\dot{M}_{\rm out}$ values in Table 5.1 are reported under the caveat that they could differ by a factor of $\sim 2$ depending on the true source inclination, the noted values will still give a suitable indication of the mass outflow rate to within an order of magnitude.

The Krongold et al. bi-conical geometry yields more conservative mass outflow rates than alternative methods which initially consider a fully spherical flow and later correct for the geometry. This is because the $f(\delta,\phi)$ function already takes into account the solid angle occupied by the flow which means that any *a posteriori* corrections for geometry and covering fraction are not strictly necessary. It also only deals with the net observed thickness of the flow which means that the flow can be clumped and/or filamentary

without appealing to difficult to determine volume-filling factors. Equations 5.4a and 5.4b highlight the need for tight constraints on the other parameters — and on $r$ in particular via the upper and lower bounds — when one is estimating both the mass outflow rate and the consequent kinetic luminosity. Should there be large uncertainties on either $N_{\rm H}$, $v_{\rm out}$, $\xi$ or $r$ the estimated $\dot{M}_{\rm out}$ will be similarly uncertain. The XIS CCDs provide both high throughput and good energy resolution at Fe K so the uncertainty in both $N_{\rm H}$ and $v_{\rm out}$ is relatively low in most cases. The dominant source of uncertainty is therefore the inferred constraint on $r$ (c.f., the left hand side of eq. 5.4a and 5.4b).

### 5.2.3 Kinetic power

For a wind that has already reached its constant terminal velocity the mechanical power imparted by a wind expelling mass at a rate $\dot{M}_{\rm out}$ with velocity $v_{\rm out}$ is simply equal to its kinetic power

$$L_{\rm kin} = \frac{1}{2}\dot{M}_{\rm out}v_{\rm out}^2 = \begin{cases} 1.23G\Omega m_{\rm p}M_{\rm BH}N_{\rm H}v_{\rm out} & \text{(lower limit)} \quad (5.6a) \\ (1.23/2)\Omega m_{\rm p}L_{\rm ion}\xi^{-1}v_{\rm out}^3 & \text{(upper limit)} \quad (5.6b) \end{cases}$$

Similarly, the rate at which the outflow transports momentum to its environment $dp/dt \equiv \dot{p}_{\rm out}$. This is given by

$$\dot{p}_{\rm out} = \dot{M}_{\rm out}v_{\rm out} = \begin{cases} 2.46G\Omega m_{\rm p}M_{\rm BH}N_{\rm H} & \text{(lower limit)} \quad (5.7a) \\ 1.23\Omega m_{\rm p}L_{\rm ion}\xi^{-1}v_{\rm out}^2 & \text{(upper limit)} \quad (5.7b) \end{cases}$$

The $L_K \propto v_{\rm out}^3$ and $\dot{p}_{\rm out} \propto v_{\rm out}^2$ dependencies in the unclumped case (where $b \sim 1$) highlights that the outflow velocity is the dominant term in these parameters, with faster outflows expected to expel more kinetic energy and more momentum into the surrounding galaxy.

## 5.3 Black hole masses

The minimum radius (in units of cm) to the absorbing gas, $r_{\rm min}$, is proportional to the mass of the black hole, $M_{\rm BH}$. Consequently, the minimum estimate on $\dot{M}_{\rm out}$ also has an

implicit dependence upon the black hole mass, and as such an estimate on $M_{\rm BH}$ is needed before any useful assessment of the source energetics can be obtained via the above method. These estimates were gathered from the literature and are noted in Table 5.1 along with the appropriate references. Most of the $M_{\rm BH}$ values were obtained through the numerous reverberation mapping studies (i.e., Peterson et al. 2004; Bentz et al. 2009a,b; Edri et al. 2012) which tend to offer tight constraints on the mass of the central object; in the cases where an AGN has been reverberation mapped multiple times the most recent estimate on $M_{\rm BH}$ is used. For non-reverberation mapped sources $M_{\rm BH}$ is inferred from one of the various scaling relations between $M_{\rm BH}$ and the properties of the host galaxy (see Chapter 1).

Multiple $M_{\rm BH}$ estimates are available in the literature for 3C 111, ESO 103-G035, NGC 1365, NGC 5506 and PDS 456, and these estimates are subtly different depending upon which scaling has been used. In these cases the mean value is listed in Table 5.1 with the associated errors taken as half of the range between the minimum and maximum values to account for the uncertainty in the individual mass estimates. In the case of CBS 126, for which there are no robust estimates on $M_{\rm BH}$ available in the literature, the value listed in Table 5.1 is based upon the BLR line width and luminosity scaling relation (Kaspi et al. 2000) using the appropriate values listed in Grupe et al. (2004). In all other sources $M_{\rm BH}$ is taken directly from the reference listed in the table footnote.

Overall, the heterogeneously selected outflow sample span almost 6 orders of magnitude in black hole mass. Log $M_{\rm BH}$ ranges from $\sim 4.7$ in the dwarf-Seyfert galaxy NGC 4395 (Edri et al. 2012), all the way up to an estimated $\sim 10$ in the high luminosity BAL quasar APM 08279+5255 (Saez, Chartas & Brandt 2009).

## 5.4 Calculations

The outflow parameters are listed in Table 5.1. The absorption corrected ionising luminosity, $L_{\rm ion}$, and the appropriate $v_{\rm out}$ values are also listed for completeness. For each of the Fe K absorbers $r_{\rm min}$ and $r_{\rm max}$ were calculated first, followed by the minimum

Table 5.1: Summary of inferred wind parameters.

| | Source | $\log M_{\rm BH}$ ($M_\odot$) | $\log L_{\rm ion}$ (erg s$^{-1}$) | $v_{\rm out}$ (c) | $\log r_{\rm min}$ (cm) | $\log r_{\rm max}$ (cm) | $\log \dot{M}_{\rm out}^{\rm min}$ (g s$^{-1}$) | $\log \dot{M}_{\rm out}^{\rm max}$ (g s$^{-1}$) | $\log L_{\rm kin}^{\rm min}$ (erg s$^{-1}$) | $\log L_{\rm kin}^{\rm max}$ (erg s$^{-1}$) |
|---|---|---|---|---|---|---|---|---|---|---|
| 1 | 3C 111[3,4,*] | $8.1^{+0.5}_{-0.5}$ | 44.7 | $0.072 \pm 0.005$ | $15.86^{+0.06}_{-0.06}$ | $17.27^{+0.62}_{-0.63}$ | $24.94^{+0.06}_{-0.06}$ | $26.35^{+0.62}_{-0.63}$ | $43.31^{+0.06}_{-0.06}$ | $44.72^{+0.62}_{-0.63}$ |
| 2 | 3C 390.3[1,5] | $8.5^{+0.1}_{-0.1}$ | 44.7 | $0.145 \pm 0.007$ | $15.65^{+0.04}_{-0.04}$ | $< 16.73$ | $> 25.52$ | $< 26.64$ | $> 44.49$ | $< 45.61$ |
| 3 | 4C +74.26[16] | 9.6[†] | 47.0 | $0.185 \pm 0.026$ | $16.54^{+0.13}_{-0.11}$ | $< 20.02$ | $> 24.76$ | $27.90^{+0.45}_{-0.45}$ | $> 43.95$ | $47.09^{+0.45}_{-0.65}$ |
| 4 | APM 08279[17,a] | 10.0[†] | 45.4 | $0.285 \pm 0.011$ | $16.56^{+0.03}_{-0.03}$ | $19.83^{+0.33}_{-0.30}$ | $26.29^{+0.03}_{-0.03}$ | $29.56^{+0.33}_{-0.30}$ | $45.86^{+0.03}_{-0.03}$ | $49.12^{+0.33}_{-0.30}$ |
| 5 | CBS 126[15] | $7.8^{+0.1}_{-0.1}$ | 44.2 | $0.012 \pm 0.006$ | ··· | $< 15.91$ | ··· | $24.83^{+0.17}_{-0.26}$ | ··· | $41.64^{+0.17}_{-0.26}$ |
| 6 | ESO 103-G035[14,*] | $7.4^{+0.1}_{-0.1}$ | 43.9 | $0.056 \pm 0.025$ | $15.38^{+0.51}_{-0.32}$ | $< 18.84$ | $> 22.98$ | $25.58^{+1.19}_{-1.19}$ | $> 41.13$ | $43.73^{+1.19}_{-1.19}$ |
| 7 | MCG -6-30-15[7] | $6.7^{+0.2}_{-0.2}$ | 43.2 | $0.007 \pm 0.002$ | $16.48^{+0.29}_{-0.22}$ | $17.40^{+0.14}_{-0.13}$ | $23.76^{+0.29}_{-0.22}$ | $24.68^{+0.14}_{-0.13}$ | $40.11^{+0.29}_{-0.21}$ | $41.03^{+0.14}_{-0.13}$ |
| 8 | MR 2251−178[6] | $8.7^{+0.1}_{-0.1}$ | 45.2 | $0.137 \pm 0.008$ | $15.90^{+0.05}_{-0.05}$ | $20.44^{+0.32}_{-0.34}$ | $24.32^{+0.05}_{-0.05}$ | $27.81^{+0.50}_{-0.75}$ | $43.25^{+0.05}_{-0.05}$ | $46.74^{+0.50}_{-0.75}$ |
| 9 | Mrk 279[5] | $7.5^{+0.1}_{-0.1}$ | 43.4 | $0.220 \pm 0.006$ | $14.29^{+0.02}_{-0.02}$ | $15.56^{+0.58}_{-0.40}$ | $24.29^{+0.02}_{-0.02}$ | $25.56^{+0.58}_{-0.40}$ | $43.63^{+0.02}_{-0.02}$ | $44.90^{+0.58}_{-0.40}$ |
| 10 | Mrk 766[8] | $6.2^{+0.3}_{-0.6}$ | 43.2 | $0.039 \pm 0.006$ | $14.49^{+0.15}_{-0.12}$ | $16.66^{+0.29}_{-0.28}$ | $23.06^{+0.15}_{-0.12}$ | $25.23^{+0.29}_{-0.28}$ | $40.89^{+0.15}_{-0.12}$ | $43.06^{+0.29}_{-0.28}$ |
| 11 | NGC 1365[13,*] | $7.6^{+0.7}_{-0.7}$ | 42.8 | $0.008 \pm 0.001$ | ··· | $15.16^{+0.13}_{-0.12}$ | ··· | $24.07^{+0.13}_{-0.12}$ | ··· | $40.53^{+0.13}_{-0.12}$ |
| 12 | NGC 3227[1] | $7.6^{+0.2}_{-0.2}$ | 42.5 | $0.005 \pm 0.004$ | ··· | $15.96^{+0.36}_{-0.32}$ | ··· | $23.59^{+0.36}_{-0.32}$ | ··· | $39.65^{+0.36}_{-0.32}$ |
| 13 | NGC 3516[1] | $7.6^{+0.1}_{-0.2}$ | 43.6 | $0.004 \pm 0.002$ | ··· | $17.18^{+0.30}_{-0.27}$ | ··· | $24.62^{+0.30}_{-0.27}$ | ··· | $40.48^{+0.30}_{-0.27}$ |
| 14 | NGC 3783[1] | $7.5^{+0.1}_{-0.2}$ | 43.6 | $< 0.007$ | $> 17.28$ | $18.35^{+0.27}_{-0.30}$ | $> 24.19$ | $< 25.53$ | $< 40.54$ | $< 41.88$ |
| 15 | NGC 4051[1] | $6.3^{+0.2}_{-0.2}$ | 42.5 | $0.018 \pm 0.001$ | $15.26^{+0.05}_{-0.05}$ | $15.70^{+0.18}_{-0.17}$ | $23.58^{+0.05}_{-0.05}$ | $24.02^{+0.18}_{-0.17}$ | $40.74^{+0.05}_{-0.05}$ | $41.19^{+0.18}_{-0.17}$ |
| 16 | NGC 4151[1] | $7.1^{+0.1}_{-0.2}$ | 42.9 | $0.055 \pm 0.023$ | $15.09^{+0.47}_{-0.30}$ | $< 18.12$ | $> 22.55$ | $25.24^{+0.64}_{-0.64}$ | $> 40.68$ | $43.37^{+0.64}_{-0.64}$ |
| 17 | NGC 4395[2] | $4.7^{+0.2}_{-0.2}$ | 40.7 | $< 0.001$ | ··· | $13.94^{+0.43}_{-0.37}$ | ··· | $< 21.49$ | ··· | $< 36.14$ |
| 18 | NGC 5506[6,9,10,*] | $7.3^{+0.6}_{-0.7}$ | 43.7 | $0.246 \pm 0.006$ | $13.99^{+0.02}_{-0.02}$ | $15.39^{+0.45}_{-0.48}$ | $23.88^{+0.02}_{-0.02}$ | $25.28^{+0.45}_{-0.48}$ | $43.31^{+0.02}_{-0.02}$ | $44.71^{+0.45}_{-0.48}$ |
| 19 | PDS 456[11,*] | $9.4^{+0.4}_{-0.5}$ | 45.3 | $0.273 \pm 0.006$ | $16.00^{+0.02}_{-0.02}$ | $18.18^{+0.22}_{-0.23}$ | $25.75^{+0.02}_{-0.02}$ | $27.93^{+0.22}_{-0.23}$ | $45.28^{+0.02}_{-0.02}$ | $47.46^{+0.22}_{-0.23}$ |
| 20 | SW J2127[12,b] | 7.2[†] | 43.7 | $0.231 \pm 0.006$ | $13.94^{+0.02}_{-0.02}$ | $16.75^{+0.47}_{-0.52}$ | $23.37^{+0.02}_{-0.02}$ | $26.17^{+0.47}_{-0.52}$ | $42.75^{+0.02}_{-0.02}$ | $45.55^{+0.47}_{-0.52}$ |

[*] $M_{\rm BH}$ is taken as the mean of extreme values found in the literature; [†]Errors on $M_{\rm BH}$ not present in literature; [a]Full designation APM 08279+5255; [b]Full designation SWIFT J2127.4+5654;

REFERENCES:– [1]Peterson et al. (2004); [2]Edri et al. (2012); [3]Chatterjee et al. (2011); [4]Tombesi et al. (2012b); [5]Bentz et al. (2009a); [6]Khorunzhev et al. (2012); [7]McHardy et al. (2005); [8]Bentz et al. (2009b); [9]Papadakis (2004); [10]Nikołajuk, Czerny & Gurynowicz (2009); [11]Reeves et al. (2009); [12]Malizia et al. (2008); [13]Risaliti et al. (2007); [14]Czerny et al. (2001); [15]Grupe et al. (2004); [16]Woo & Urry (2002); [17]Saez, Chartas & Brandt (2009).

and maximum values for $\dot{M}_{\rm out}$, $L_{\rm kin}$ and $\dot{p}_{\rm out}$ which were calculated using the appropriate equations outlined in the previous section. In CBS 126, NGC 1365, NGC 3227, NGC 3516 and NGC 4395, which all have relatively slow outflows with $v_{\rm out} < 0.005\,{\rm c}$, the kinematically inferred $r_{\rm min}$ exceeds that for $r_{\rm max}$ which suggests that the outflow has not been accelerated to its full escape speed. In these cases the absorbing material will remain in the system, likely falling back onto the accretion disc eventually, unless it is subject to an additional acceleration mechanism once it has crossed the line of sight. For these sources, only the upper limits to $r$, $\dot{M}_{\rm out}$ and $L_{\rm kin}$ are reported in Table 5.1. The errors on all $\dot{M}_{\rm out}$ and $L_{\rm kin}$ values were determined by propagating the error on the input XSTAR values, e.g., $\dot{M}_{\rm out}^{\rm max} \propto (N_{\rm H}, v_{\rm out}, r_{\rm max})$, where $r_{\rm max} = L_{\rm ion}/N_{\rm H}\xi$ and hence $\dot{M}_{\rm out}^{\rm max} \propto (L_{\rm ion}/\xi)v_{\rm out}$. In this way, errors in the individual XSTAR parameters are already accounted for in the reported $\dot{M}_{\rm out}^{\rm min,max}$ and $L_{\rm kin}^{\rm min,max}$ values.

$\dot{M}_{\rm out}$ and $L_{\rm kin}$ are a function of $r$, and $r_{\rm min}$ (in cgs units) is then itself proportional to $M_{\rm BH}$. As shown in equations 5.4a–5.7a $\dot{M}_{\rm out}$, $L_{\rm kin}$ and $\dot{p}_{\rm out}$ hence scale with $M_{\rm BH}$, which could have an adverse influence on any subsequent correlation analyses performed in §5.6. For this reason, and to enable a uniform physical analysis throughout the sample, all of the outflow parameters were normalised to the equivalent values appropriate for a given black hole. The distance $r$ was normalised to the Schwarzschild radius $r_s = 2GM_{\rm BH}/c^2$, the kinetic luminosity $L_{\rm kin}$ to the Eddington luminosity $L_{\rm edd} = 4\pi GM_{\rm BH}m_p c/\sigma_T$, and the mass outflow rate $\dot{M}_{\rm out}$ to the Eddington accretion rate $\dot{M}_{\rm edd} = \eta L_{\rm edd}/c^2$ (assuming $\eta = 0.06$). The momentum rate $\dot{p}_{\rm out}$ was normalised to the Eddington momentum rate $\dot{p}_{\rm edd} = L_{\rm edd}/c$. The normalised parameters are listed in Table 5.2. A particular advantage of normalising $r$ to $r_{\rm s}$ is that it alleviates the implicit correlation between $r_{\rm min}$ and $M_{\rm BH}$, i.e., $r_{\rm min} = 2GM_{\rm BH}/c^2 = (c/v_{\rm out})^2\, r_{\rm s}$.

The Eddington ratio of each AGN, $\lambda$, defined in this case as the ratio of a source's bolometric luminosity to its inferred Eddington luminosity, $\lambda = L_{\rm bol}/L_{\rm edd}$, was also estimated to gauge source power. The bolometric luminosities for each source, $L_{\rm bol}$, were estimated from the relation $L_{\rm bol} = \kappa_{\rm bol} L_{2-10\,{\rm keV}}$, where $L_{2-10\,{\rm keV}}$ is the absorption-corrected source luminosity integrated between $2-10\,{\rm keV}$ and $\kappa_{\rm bol}$ is the bolometric correction factor. The spread of $\kappa_{\rm bol}$ factors for individual AGN is believed to be quite

large (Elvis et al. 1994) and studies have shown that the correction appropriate for a particular AGN can be a function of luminosity (Marconi et al. 2004; Hopkins, Richards & Hernquist 2007), Eddington ratio (Vasudevan & Fabian 2007; Lusso et al. 2010), or both (Lusso et al. 2010). The uniform application of a bolometric correction factor to a sample of AGN with differing properties could therefore over- or under-estimate the total luminosity in a minority of sources. For this reason, the $\kappa_{\rm bol}$ values reported in the works of Vasudevan & Fabian (2007, 2009) and Vasudevan et al. (2010) have preferentially been adopted because they have been calculated individually for each AGN. Where $\kappa_{\rm bol}$ has not been calculated in these works it was instead estimated from the correlation between $\Gamma - \kappa_{\rm bol}$ (Zhou & Zhao 2010), where $\Gamma$ is the photon-index of the primary power-law continuum as measured in the broad-band models of each source. Values for $L_{2-10\,\rm keV}$ (denoted $L_*$ for brevity), $\kappa_{\rm bol}$ and the inferred $L_{\rm bol}$ for AGN are also listed in Table 5.2.

## 5.5 Parameter constraints

A constraint diagram for the location of the Fe K outflows is given in Fig. 5.2; the raw calculated values (from Table 5.1) are shown in the upper panel while the normalised ones (from Table 5.2) are shown in the bottom panel. In both panels the black bars denote the limits on $r$ and span $r_{\rm min}$ to $r_{\rm max}$ in each AGN. The blue shaded area shows the mean range of $r$ between $\langle r_{\rm min} \rangle$ and $\langle r_{\rm max} \rangle$ across the whole sample. These upper and lower bounds correspond to the geometric mean of the available values, as shown at the bottom of Tables 5.1 and 5.2. As reasonable lower values are not available for CBS 126, NGC 1365, NGC 3227, NGC 3516 and NGC 4395 these sources were not included when calculating the mean lower bound, and the plotted range can thus be considered as restrictive.

The absorbers are clearly distributed across several orders of magnitude in absolute distance from the black hole, with $r$ typically ranging from $\sim 10^{14-20}$ cm ($\sim 10^{1-6}\,r_{\rm s}$). On average the outflows are located at distances of between $\langle r \rangle \sim 10^{15-17}$ cm ($\sim 10^{2-4}\,r_{\rm s}$). The constraint diagram implies that while there may be some limited overlap between the

Table 5.2: Summary of normalised wind parameters.

| | Source | $\log L_*/L_{\rm bol}$ | $\kappa_{\rm bol}$ | $\log\lambda$ | $\log\frac{r_{\rm min}}{r_s}$ | $\log\frac{r_{\rm max}}{r_s}$ | $\log\frac{\dot{M}_{\rm out}^{\rm min}}{\dot{M}_{\rm edd}}$ | $\log\frac{\dot{M}_{\rm out}^{\rm max}}{\dot{M}_{\rm edd}}$ | $\log\frac{L_{\rm kin}^{\rm min}}{L_{\rm edd}}$ | $\log\frac{L_{\rm kin}^{\rm max}}{L_{\rm edd}}$ |
|---|---|---|---|---|---|---|---|---|---|---|
| 1 | 3C 111 | 44.4/45.7 | $20.8^{6}$ | $-0.52$ | $2.29^{+0.06}_{-0.06}$ | $3.70^{+0.62}_{-0.63}$ | $-1.31^{+0.06}_{-0.06}$ | $0.11^{+0.62}_{-0.63}$ | $-2.89^{+0.06}_{-0.06}$ | $-1.48^{+0.62}_{-0.63}$ |
| 2 | 3C 390.3 | 44.4/45.5 | $13.3^{3}$ | $-1.13$ | $1.68^{+0.04}_{-0.04}$ | $< 2.76$ | $> -1.05$ | $< -0.01$ | $> -2.11$ | $< -2.81$ |
| 3 | 4C +74.26 | 44.9/46.5 | $39.7^{6}$ | $-1.17$ | $1.47^{+0.13}_{-0.11}$ | $< 4.95$ | $> -2.77$ | $0.16^{+0.45}_{-0.45}$ | $> -3.75$ | $-0.61^{+0.45}_{-0.45}$ |
| 4 | APM 08279[a] | $-/47.4^{1}$ | ··· | $-0.67$ | $1.09^{+0.03}_{-0.03}$ | $4.36^{+0.33}_{-0.30}$ | $-1.85^{+0.03}_{-0.03}$ | $1.41^{+0.33}_{-0.30}$ | $-2.25^{+0.03}_{-0.03}$ | $1.02^{+0.33}_{-0.30}$ |
| 5 | CBS 126 | 43.8/45.5 | $47.5^{6}$ | $-0.43$ | ··· | $< 2.64$ | ··· | $-1.12^{+0.17}_{-0.26}$ | ··· | $-4.26^{+0.17}_{-0.26}$ |
| 6 | ESO 103-G035 | 43.4/45.1 | $45.2^{6}$ | $-0.41$ | $2.50^{+0.51}_{-0.32}$ | $< 5.97$ | $> 2.57$ | $0.03^{+1.19}_{-1.19}$ | $> -4.37$ | $-1.78^{+1.19}_{-1.19}$ |
| 7 | MCG -6-30-15 | 42.8/44.0 | $16.1^{5}$ | $-0.79$ | $4.31^{+0.29}_{-0.22}$ | $5.23^{+0.14}_{-0.13}$ | $-1.08^{+0.29}_{-0.22}$ | $-0.17^{+0.14}_{-0.13}$ | $-4.69^{+0.29}_{-0.22}$ | $-3.78^{+0.14}_{-0.13}$ |
| 8 | MR 2251−178 | 44.6/46.0 | $22.0^{3}$ | $-0.84$ | $1.73^{+0.05}_{-0.05}$ | $5.23^{+0.14}_{-0.13}$ | $-2.53^{+0.05}_{-0.05}$ | $0.97^{+0.50}_{-0.75}$ | $-3.55^{+0.05}_{-0.05}$ | $0.06^{+0.51}_{-0.75}$ |
| 9 | Mrk 279 | 43.0/44.0 | $10.1^{5}$ | $-1.65$ | $1.32^{+0.02}_{-0.02}$ | $2.59^{+0.58}_{-0.40}$ | $-1.36^{+0.02}_{-0.02}$ | $-0.09^{+0.58}_{-0.40}$ | $-1.98^{+0.02}_{-0.02}$ | $-0.70^{+0.58}_{-0.40}$ |
| 10 | Mrk 766 | 42.7/44.1 | $48.9^{5}$ | 0.11 | $2.82^{+0.15}_{-0.12}$ | $4.99^{+0.29}_{-0.28}$ | $-1.29^{+0.15}_{-0.12}$ | $0.88^{+0.29}_{-0.28}$ | $-3.41^{+0.15}_{-0.12}$ | $-1.24^{+0.29}_{-0.28}$ |
| 11 | NGC 1365 | 42.4/44.1 | $101.6^{5}$ | $-1.30$ | ··· | $2.09^{+0.13}_{-0.12}$ | ··· | $-1.68^{+0.13}_{-0.12}$ | ··· | $-5.17^{+0.13}_{-0.12}$ |
| 12 | NGC 3227 | 42.1/43.3 | $15.3^{5}$ | $-2.39$ | ··· | $2.89^{+0.36}_{-0.32}$ | $-0.44^{+1.40}_{-0.51}$ | $-2.15^{+0.36}_{-0.32}$ | ··· | $-6.06^{+0.36}_{-0.32}$ |
| 13 | NGC 3516 | 43.0/44.1 | $14.0^{5}$ | $-1.59$ | ··· | $4.11^{+0.30}_{-0.27}$ | ··· | $-1.13^{+0.30}_{-0.27}$ | ··· | $-5.23^{+0.30}_{-0.27}$ |
| 14 | NGC 3783 | 43.1/44.5 | $23.7^{5}$ | $-1.14$ | $> 4.31$ | $5.38^{+0.27}_{-0.30}$ | $> -1.45$ | $< -0.12$ | $< -5.06$ | $< -4.30$ |
| 15 | NGC 4051 | 41.6/43.2 | $41.1^{4}$ | $-1.19$ | $3.49^{+0.05}_{-0.05}$ | $3.93^{+0.18}_{-0.17}$ | $-0.86^{+0.05}_{-0.05}$ | $-0.43^{+0.18}_{-0.17}$ | $-3.65^{+0.05}_{-0.05}$ | $-3.22^{+0.18}_{-0.17}$ |
| 16 | NGC 4151 | 42.3/43.6 | $18.3^{4}$ | $-1.63$ | $2.52^{+0.47}_{-0.30}$ | $< 5.55$ | $> -2.70$ | $-0.01^{+0.64}_{-0.64}$ | $> -4.52$ | $-1.83^{+0.64}_{-0.64}$ |
| 17 | NGC 4395 | 40.4/41.7 | $22.5^{3}$ | $-1.09$ | ··· | $3.77^{+0.43}_{-0.37}$ | ··· | $< -1.36$ | ··· | $< -7.46$ |
| 18 | NGC 5506 | 43.2/44.4 | $16.8^{5}$ | $-1.02$ | $1.22^{+0.02}_{-0.02}$ | $2.62^{+0.45}_{-0.48}$ | $-1.57^{+0.02}_{-0.02}$ | $-0.17^{+0.45}_{-0.48}$ | $-2.09^{+0.02}_{-0.02}$ | $-0.69^{+0.45}_{-0.48}$ |
| 19 | PDS 456 | $-/47.0^{2}$ | ··· | $-0.50$ | $1.13^{+0.02}_{-0.02}$ | $3.31^{+0.22}_{-0.23}$ | $-1.80^{+0.02}_{-0.02}$ | $0.39^{+0.22}_{-0.23}$ | $-2.22^{+0.02}_{-0.02}$ | $-0.04^{+0.22}_{-0.23}$ |
| 20 | SW J2127[b] | 43.2/44.9 | $41.8^{6}$ | $-0.45$ | $1.27^{+0.02}_{-0.02}$ | $4.08^{+0.47}_{-0.52}$ | $-1.98^{+0.02}_{-0.02}$ | $0.82^{+0.47}_{-0.52}$ | $-2.56^{+0.02}_{-0.02}$ | $0.25^{+0.47}_{-0.52}$ |
| | $\langle$**mean**$\rangle$ | | | | 2.12 | 4.27 | −1.81 | 0.17 | −3.91 | −1.96 |

[a]Full designation APM 08279+5255; [b]Full designation SWIFT J2127.4+5654;

NOTES:– [1]The bolometric luminosity of APM 08279+5255 is taken as $L_{\rm bol} = 7\times10^{15}\mu_L^{-1}\,L_\odot$ (Lewis et al. 1998; Riechers et al. 2009; Saez & Chartas 2011), and assuming a conservative magnification factor of $\mu_L = 100$ (Egami et al. 2000); [2]$L_{\rm bol}$ for PDS 456 taken from Reeves & Turner (2000); [3,4,5]$\kappa_{\rm bol}$ correction factors taken from Vasudevan & Fabian (2007, 2009) or Vasudevan et al. (2010), respectively; [6]$\kappa_{\rm bol}$ estimated from the $\Gamma-\kappa_{\rm bol}$ correlation of Zhou & Zhao (2010) using the $\Gamma$ values listed in the previous chapter.

Fe K outflows and the traditional soft X-ray warm absorber (which is usually inferred to be on parsec-scale distances, e.g., Blustin et al. (2005); Kaastra et al. (2012); Crenshaw, Kraemer & George (2003a) and references therein), the former are generally thought to be located much closer to the central black hole. This is consistent with the view that the base of these highly-ionised flows originates in a wind from the inner regions of the accretion disc itself (i.e., $10^{2-4}\,r_{\rm s}$), rather than being associated with more distant phenomena such as a wind from the putative torus.

An analogous plot showing the constraints on $\dot{M}_{\rm out}$ is shown in Fig. 5.3. Estimates on $\dot{M}_{\rm out}$ also vary significantly across the sample, and span nearly 8 orders of magnitude in absolute mass outflow rate. $\dot{M}_{\rm out}$ ranges from $< 10^{22}\,{\rm g\,s^{-1}}$ in the dwarf Seyfert galaxy NGC 4395, all the way up to $\sim 10^{30}\,{\rm g\,s^{-1}}$ in the massive quasar APM 08279+5255, with the other sources having $\dot{M}_{\rm out}$ estimates distributed between these two extremes with a mean range of minimum and maximum values $\langle \dot{M}_{\rm out} \rangle \sim 10^{24-26}\,{\rm g\,s^{-1}}$ ($\sim 0.01 - 1\,M_{\odot}\,{\rm yr}$). Interestingly, and while there is still considerable uncertainty in each case, the overall mean outflow rate normalised to the Eddington rate is $\langle \dot{M}_{\rm out} \rangle \sim 0.1 \dot{M}_{\rm edd}$, while $\langle \dot{M}_{\rm out}^{\rm max} \rangle$ is actually of the order of the Eddington rate: $\langle \dot{M}_{\rm out}^{\rm max} \rangle \sim \dot{M}_{\rm edd}$. This implies that on average the Fe K winds have a mass outflow rate which is comparable to the Eddington rate, a fact which further suggests that they are likely to be energetically significant. Indeed, their energetic significance is further suggested by the distribution of kinetic power $L_{\rm kin}$, shown in Fig. 5.4. The range of $L_{\rm kin}$ once again spans several orders of magnitude, but the mean kinetic power of the sample is tightly constrained to between $\langle L_{\rm kin} \rangle \sim 10^{43}$ and $10^{44}\,{\rm erg\,s^{-1}}$. The normalised values show $\langle L_{\rm kin} \rangle$ is $< L_{\rm edd}$, with a mean range of $\langle L_{\rm kin} \rangle \sim (0.1 - 1\%) L_{\rm edd}$. Thus, these plots show that both the mass outflow rate and kinetic power of these winds are comparable to a significant fraction of their Eddington limited values. The net energetic output suggests that they are very likely to be significant in terms of feedback. This is further discussed in §6.3, where additional diagnostics are performed.

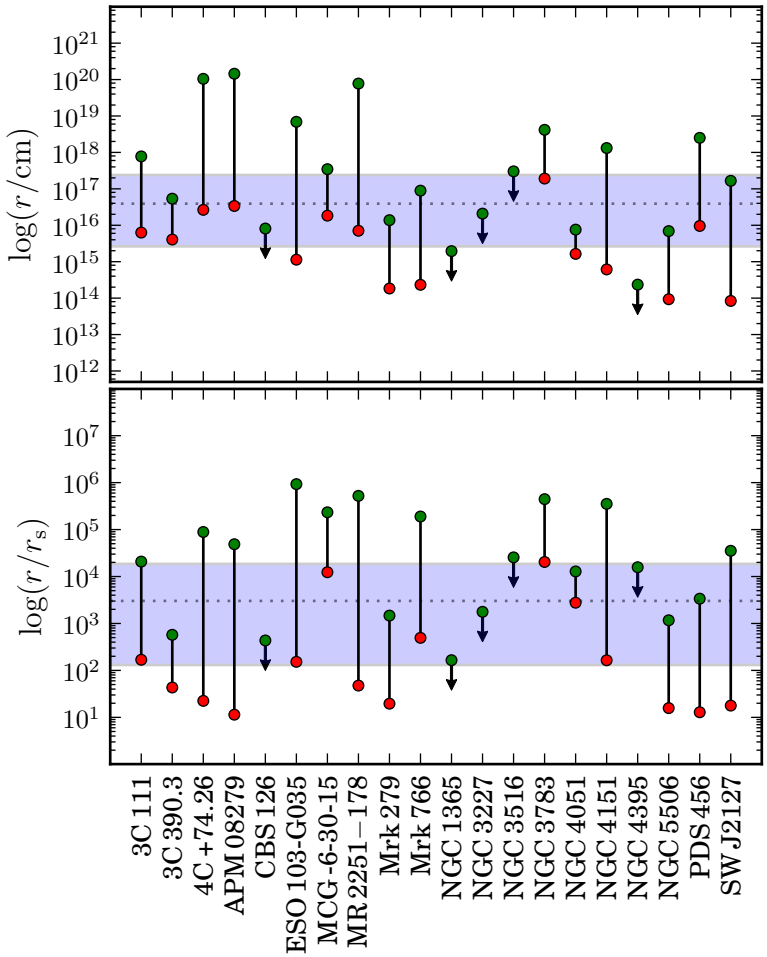


Figure 5.2: Radial distance constraint diagram. The top panel shows the location constraints for each absorber in units of cm, while the bottom panel shows the normalised location in units of Schwarzschild radii ($r_{\rm s}$). The red and green circles in both panels denote the lower and upper limits on $r$, respectively, while the black bars show the range in distance that each outflow can occupy. The blue/shaded horizontal region spans between the geometric means of the lower and upper limits, respectively, and is intended to indicate the mean range in outflow distance. The dotted horizontal line is the overall mean distance.

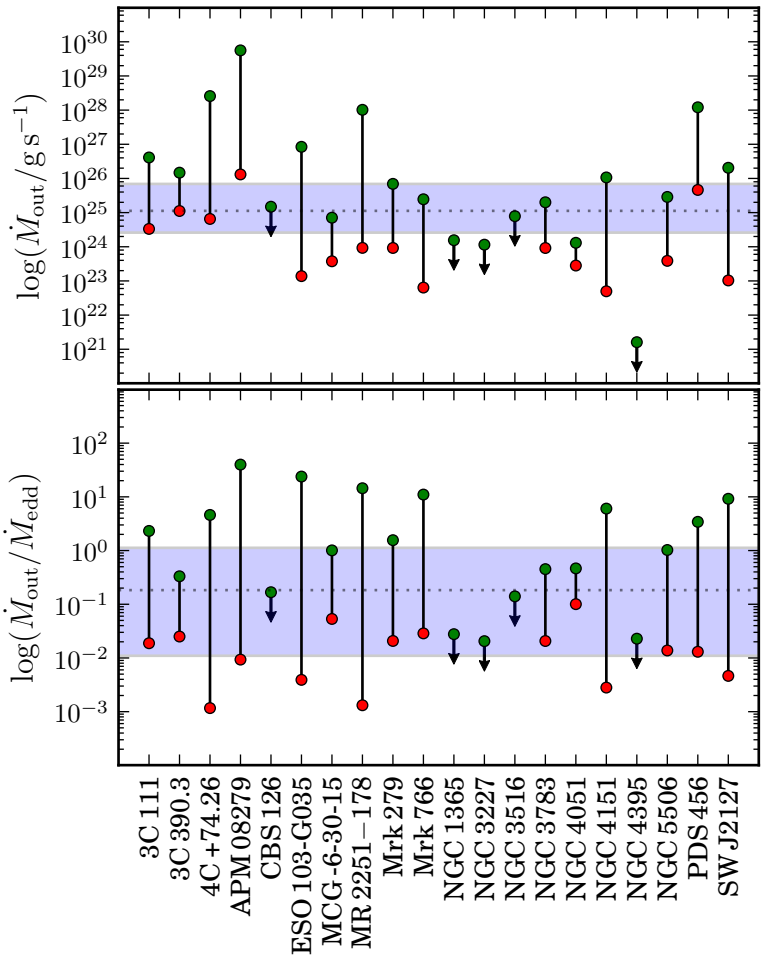


Figure 5.3: Mass outflow rate constraint diagram. As in Fig. 5.2, the top panel shows the mass outflow rate of the absorbers in units of $\mathrm{g\,s^{-1}}$, while the bottom panel shows the normalised mass outflow rate in Eddington units ($\dot{M}_{\rm edd}$). The other components have the same meaning as in Fig. 5.2, except this time they correspond to the limits on $\dot{M}_{\rm out}$.

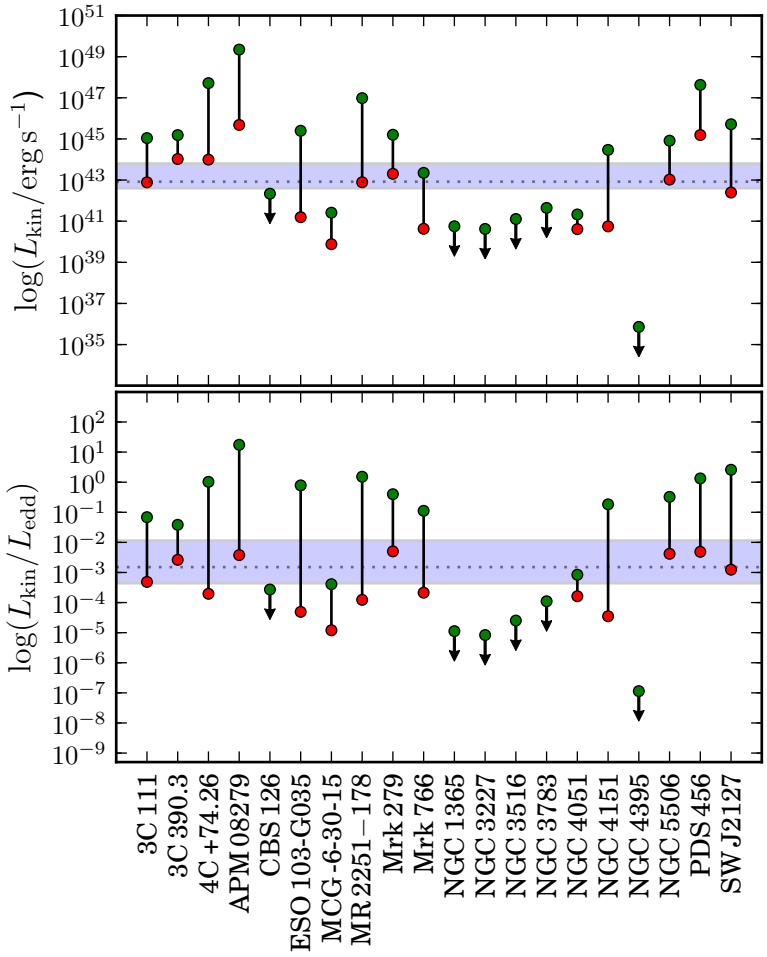


Figure 5.4: Constraint diagram for the absorber kinetic luminosity, $L_{\rm kin}$. The top and bottom panel show the range of $L_{\rm kin}$ in units of erg s$^{-1}$ and $L_{\rm edd}$, respectively. The various components have the same meaning as before, except this time they correspond to the limits on $L_{\rm kin}$.

## 5.6 Correlation analyses

Supplementing the constraint diagrams I also carried out correlation analysis to look for any fundamental relationships between the absorbers and the associated outflows. This analysis bares notable similarities to the one conducted by Tombesi et al. (2013) for their *XMM-Newton* outflow sample. There, the authors combined the hard-band absorption

parameters as measured in their Fe K absorption survey with soft X-ray warm absorption parameters collated from the literature in an effort to search for general trends amongst the global X-ray absorber population. While the individual warm absorbers in each source were modelled in my broad-band *Suzaku* analysis, their obtained parameters are not suitable for inclusion in the regression analysis. This is because the energy resolution offered by the XIS CCDs aboard *Suzaku* is insufficient to constrain the outflow velocity of the soft-band absorber in the majority of cases which means that the energetics of the lowly ionised flow cannot be gauged. For this reason, the correlation analysis presented here focuses only on the highly-ionised Fe K absorbers.

In all subsequent plots the regression lines represent a straight line fit to the data points of the form $\log y = a \log x + b$. The significance of each regression was calculated using the Pearson coefficient $R_p$, with the resultant line parameters being reported in Table 5.3. $P_{\rm null}$ values are given in reference to the null-hypothesis that the two considered parameters are unrelated; a standard 95% confidence interval ($\alpha = 0.05$) is adopted when determining whether a correlation may be statistically significant. To ensure that any mutual dependencies on $M_{\rm BH}$ are minimised the normalised outflow parameters are considered, and all error bars denote the 90% limits on a given parameter.

### 5.6.1 Primary absorber parameters

First, I considered the parameters of the Fe K absorber. Panels (a), (b) and (c) of Fig. 5.5 show the $\log N_{\rm H} - \log \xi$, $\log N_{\rm H} - \log v_{\rm out}$, and $\log \xi - \log v_{\rm out}$ permutations, respectively. From Fig. 5.5 (panel a) there is a positive correlation between column and ionisation, with a slope of $a \simeq 0.59$. This relationship is most likely an observational bias induced by how the curves of growth for Fe XXV He$\alpha$ and Fe XXVI Ly$\alpha$ absorption behaves: larger column densities of material are able to give rise to observable absorption lines across a wider range of ionisation states. This is especially true of Fe XXVI Ly$\alpha$ which can persist right through the $\log(\xi/{\rm erg\,cm\,s^{-1}}) \sim 3-6$ ionisation range at $N_{\rm H} = 10^{24}\,{\rm cm^{-2}}$, whilst Fe XXV He$\alpha$ becomes completely ionised at only $\log(\xi/{\rm erg\,cm\,s^{-1}}) \sim 4.5$ (see Figure 2 and the discussion of Tombesi et al. 2011a for further details). As a result, Fe XXVI Ly$\alpha$

Table 5.3: Results of linear regression analysis.

| Relation | | $a$ | $b$ | $R_p$ | $P_{\rm null}$ |
|---|---|---|---|---|---|
| $(x)$ | $(y)$ | | | | |
| $\log N_{\rm H}$ | $\log \xi$ | 0.59 | −9.18 | 0.65 | $1.49 \times 10^{-3}$ |
| $\log N_{\rm H}$ | $\log v_{\rm out}$ | 0.09 | 1.92 | 0.08 | $7.22 \times 10^{-1}$ |
| $\log \xi$ | $\log v_{\rm out}$ | 0.57 | 1.68 | 0.43 | $5.78 \times 10^{-2}$ |
| $\log(r_{\rm max}/r_s)$ | $\log N_{\rm H}$ | −0.48 | 24.54 | −0.84 | $2.12 \times 10^{-6}$ |
| | $\log \xi$ | −0.31 | 5.36 | −0.73 | $1.81 \times 10^{-4}$ |
| | $\log v_{\rm out}$ | 0.02 | 3.92 | 0.02 | $9.19 \times 10^{-1}$ |
| | $\log(\dot{M}_{\rm out}/\dot{M}_{\rm edd})$ | 0.41 | −1.78 | 0.53 | $1.63 \times 10^{-2}$ |
| | $\log(L_{\rm kin}/L_{\rm edd})$ | 0.28 | −3.34 | 0.15 | $5.37 \times 10^{-1}$ |
| | $\log(\dot{p}_{\rm out}/\dot{p}_{\rm edd})$ | 0.35 | −1.91 | 0.26 | $2.61 \times 10^{-1}$ |
| $\log \lambda$ | $\log N_{\rm H}$ | 0.09 | 22.77 | 0.08 | $7.34 \times 10^{-1}$ |
| | $\log \xi$ | 0.14 | 4.27 | 0.19 | $4.17 \times 10^{-1}$ |
| | $\log v_{\rm out}$ | 0.35 | 4.43 | 0.27 | $2.45 \times 10^{-1}$ |
| | $\log(r/r_{\rm s})$ | −0.02 | 3.18 | −0.01 | $9.67 \times 10^{-1}$ |
| | $\log(\dot{M}_{\rm out}/\dot{M}_{\rm edd})$ | 0.47 | −0.44 | 0.64 | $2.51 \times 10^{-3}$ |
| | $\log(L_{\rm kin}/L_{\rm edd})$ | 1.17 | −1.81 | 0.40 | $8.15 \times 10^{-2}$ |
| | $\log(\dot{p}_{\rm out}/\dot{p}_{\rm edd})$ | 0.82 | −0.47 | 0.47 | $3.44 \times 10^{-2}$ |
| $\log L_{\rm bol}$ | $\log L_{\rm kin}$ | 1.69 | −32.75 | 0.89 | $1.82 \times 10^{-7}$ |
| $\log L_{\rm bol}$ | $\log(L_{\rm kin}/L_{\rm edd})$ | 0.87 | −42.07 | 0.72 | $3.36 \times 10^{-4}$ |

*Notes*: $a$ and $b$ are the gradient and intercept of the straight line fit; $R_p$ is the Pearson correlation coefficient. For reference, $R_p = \pm 1$ represents a perfect positive/negative correlation. $R_p = 0$ means that there is no discernible correlation in the data points.

absorption lines are more likely to be observed in higher column density material, as per the observed correlation.

There is no correlation between $\log N_{\rm H} - \log v_{\rm out}$ and a marginal one between $\log \xi - \log v_{\rm out}$ ($a \simeq 0.57$) which suggests that higher ionisation winds may tend to be faster; this is consistent with the findings of Blustin et al. (2005) who also found that these parameter permutations followed no clear trend in their small sample of soft X-ray warm absorbers. However, in contrast to this the Tombesi et al. (2013) analysis found

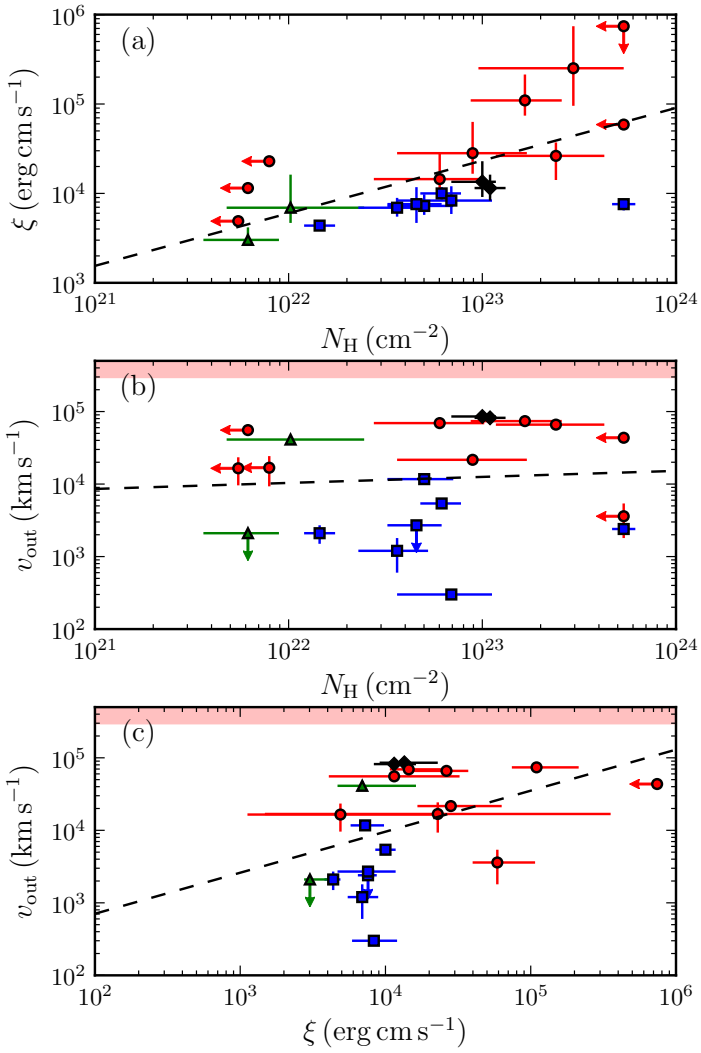


Figure 5.5: Scatter plots showing: (a) $\log N_{\rm H} - \log \xi$, (b) $\log N_{\rm H} - \log v_{\rm out}$ and (c) $\log \xi - \log v_{\rm out}$. The data-points correspond to Fe XXV He$\alpha$ (green triangles), Fe XXVI Ly$\alpha$ (red circles), Fe XXV–XXVI pair (blue squares) and blended (black diamonds) absorption line systems, respectively. In panels (b) and (c) the shaded red area shows the region where $v_{\rm out} > c$. The dashed black line shows the best fitting linear regression.

that both $\log N_{\rm H} - \log v_{\rm out}$ and $\log \xi - \log v_{\rm out}$ are strongly correlated when the soft- and hard-band absorbers are considered together. The lack of significantly detected correlations between these parameters in both this work and in that of Blustin et al. (2005) may therefore be a symptom of narrow dynamic range considered, and does not rule out the possibility of a relationship amongst the global outflow population.

Despite there being no clear relationships between the parameters, the regression lines in both panels (b) and (c) do appear to bisect the absorbers into two sub-groups. Independent of their ionisation or column, the Fe XXVI Ly$\alpha$ absorption line systems tend to have $v_{\rm out} \gtrsim 10^4\,{\rm km\,s^{-1}}$, while the lower ionisation lines, i.e., those containing Fe XXV He$\alpha$ occupy the $v_{\rm out} \lesssim 10^4\,{\rm km\,s^{-1}}$ range. This indicates that while the absorber parameters are not themselves correlated, the phenomenology of the absorption lines is still in some way linked to the physical properties of the outflowing wind.

### 5.6.2 Scaling with distance

Next, I considered how the distance of the absorber from the black hole affects the outflow parameters (Fig. 5.6). Such an analysis is analogous to that recently performed by Tombesi et al. (2013), although only the Fe K absorbers are considered here. In this regard, the dynamic range is significantly smaller in terms of the outflow parameters. For instance, I am limited to probing correlations at relatively small distances from the black hole, i.e., $r < 10^6\,r_{\rm s}$, while the inclusion of the soft X-ray warm absorber in Tombesi et al.'s analysis enables them to probe out to distances of $r \sim 10^{10}\,r_{\rm s}$.

Before conducting this analysis, however, there is a significant caveat which needs to be addressed. The minimum distance to the absorbers, $r_{\rm min}$, was estimated under the assumption that the observed outflow velocity exceeds the local escape velocity. Normalising $r_{\rm min}$ to the Schwarzschild radius therefore introduces an implicit inverse correlation between distance and velocity, such that $r_{\rm min}/r_{\rm s} = (c/v_{\rm out})^2$, which will induce a strong artificial correlation in the $v_{\rm out}$ regression. By extension of this, correlations will also be induced in the $L_{\rm kin}$ and $\dot{p}_{\rm out}$ regressions as well because they also scale with $v_{\rm out}$ and $r_{\rm min}$. Moreover, the outflows in CBS 126, NGC 1365, NGC 3227, NGC 3516 and

NGC 4395 are observed with $v_{\rm out} < v_{\rm esc}$ which means that the assumption of the outflow velocity being equal to the local escape speed does not hold universally across the sample anyway. All parameters are therefore compared solely to $\log(r_{\rm max}/r_s)$ – which is estimated independently of $v_{\rm out}$. For consistency, the upper values for the other parameters, i.e., $\log(\dot{M}_{\rm out}^{\rm max}/\dot{M}_{\rm edd})$, $\log(L_{\rm kin}^{\rm max}/L_{\rm edd})$, are considered as well. The error bars then correspond to the uncertainty in the maximum values by virtue of the input XSTAR parameters only (see equations in §5.2). Errors on the black hole mass are not included in the calculations, but will typically lead to an uniform additional error of $\sim 0.5$ dex on all parameters.

Figures 5.6a and 5.6b show that the measured column density and ionisation are strongly related to the location of the wind; the column density varies with a slope of $a \simeq -0.48$ while the ionisation varies with a slope $a \simeq -0.31$, both at the $> 99\%$ confidence level. Larger column density and higher ionisation winds are thus located closer to the black hole, as is expected by virtue of the $r_{\rm max} \propto (N_{\rm H}\xi)^{-1}$ relation. Extrapolating these fits to smaller radii suggests that any absorber present at, for example, $\sim 10\,r_{\rm s}$, is likely to be both Compton-thick (i.e., $N_{\rm H} > \sigma_T^{-1} \sim 1.5 \times 10^{24}\,{\rm cm}^{-2}$) and very highly ionised ($\xi > 10^{5-6}\,{\rm erg\,cm\,s}^{-1}$). Such material could be stripped of all of its electrons and is therefore unlikely to be detectable through spectroscopy, although could still be driven through Thompson scattering at the base of the wind (see Chapter 6). The outflow velocity, kinetic power and momentum rate do not correlate significantly with distance (Fig. 5.6c,e,f).

The only outflow parameter which varies significantly with distance is the mass outflow rate (Fig. 5.6d) which increases with a slope of $a \simeq 0.41$ at the 98.4% confidence level. This is consistent with the findings of Tombesi et al. (2013) although the slope found here is roughly a factor of two steeper than the one found by those authors. Utilising their larger dynamic range Tombesi et al. (2013) find that the outflow velocity, the kinetic power and the momentum rate of X-ray absorbers in general decrease significantly with distance, in contrast to what has been found in this work. However, given the limited dynamic range occupied by the data the results of this analysis are not necessarily at odds with those reported in Tombesi et al. (2013). The only way to overcome these limitations is to include the parameters of the soft X-ray warm absorbers as well which

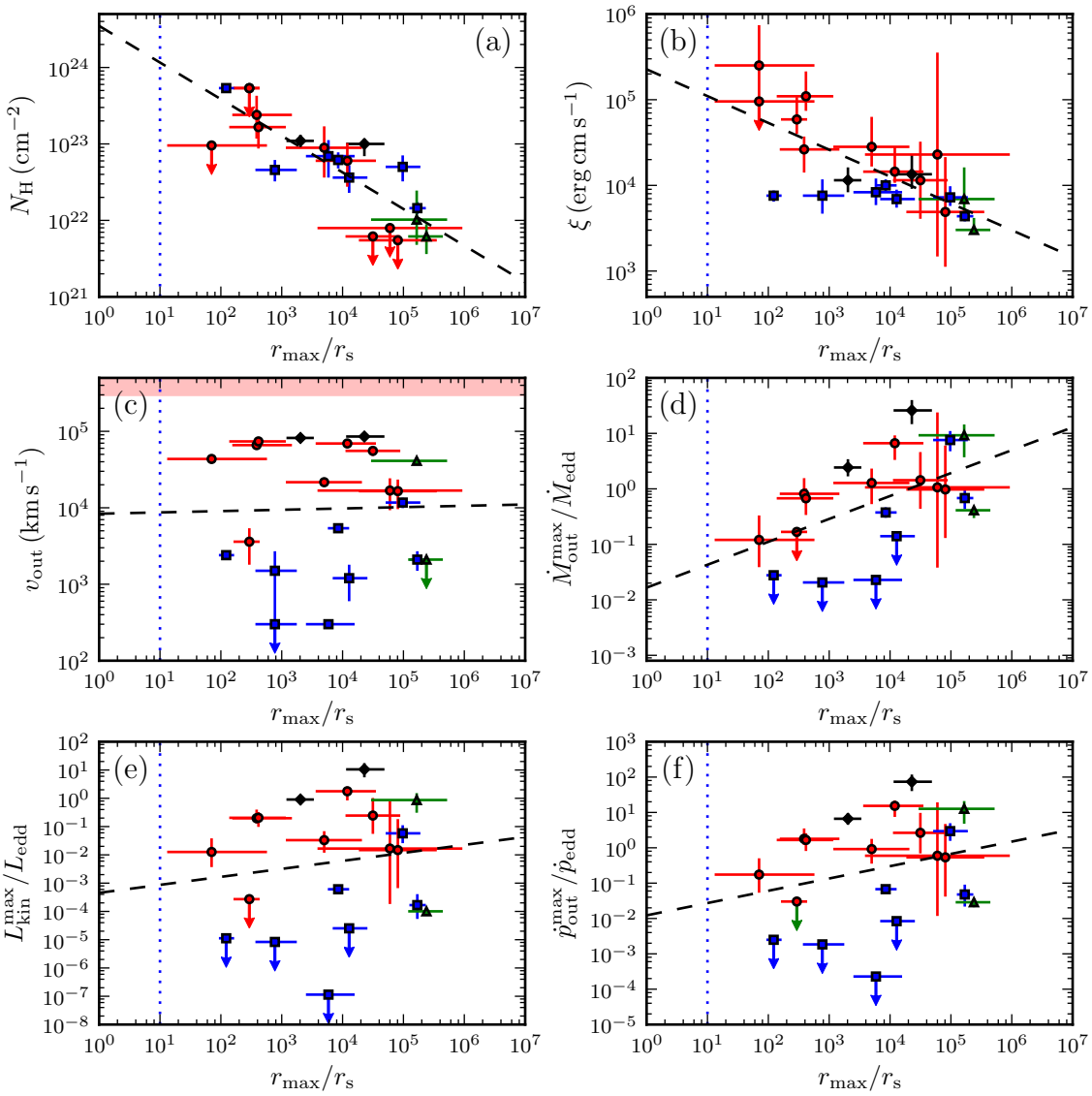


Figure 5.6: Scatter plots showing $\log(r/r_{\rm s})$ versus: (a) $\log N_{\rm H}$, (b) $\log\xi$, (c) $\log v_{\rm out}$, (d) $\log(\dot{M}_{\rm out}/\dot{M}_{\rm edd})$, (e) $\log(L_{\rm kin}/L_{\rm edd})$ and (f) $\log(\dot{p}_{\rm out}/\dot{p}_{\rm edd})$. As in Fig. 5.5, the plotted points correspond to Fe XXV He$\alpha$ (green triangles), Fe XXVI Ly$\alpha$ (red circles), Fe XXV–XXVI pair (blue squares) and blended (black diamonds) absorption line systems, respectively. In all panels, the dotted vertical line corresponds to $r = 10r_{\rm s}$, which is the expected launching radius of an Fe K wind, while in panel (c) the red shaded area denotes the region where $v_{\rm out} > c$. The black dashed lines are the best-fit linear regressions.

would require collating all of the soft X-ray grating observations, which is well beyond the scope of this thesis and is instead deferred to future work.

### 5.6.3 Scaling with Eddington ratio ($\lambda$)

Whilst the *XMM-Newton* outflow study was flux limited to sources with $F_{2-10\,\mathrm{keV}} \gtrsim 10^{-11}\,\mathrm{erg\,cm^{-2}\,s^{-1}}$ and had a red-shift cut-off of $z < 0.1$ (see Tombesi et al. 2010a), the heterogeneously selected *Suzaku* study is solely counts limited and hence includes both low flux (low-luminosity) nearby AGN, and highly-luminous ones at higher red-shifts. The inclusion of both the dwarf Seyfert galaxy NGC 4395 and the lensed quasar APM 08279+5255, for example, means that the range of bolometric luminosity, $L_{\mathrm{bol}}$, in the *Suzaku* sample spans approximately 6 decades in luminosity, $L_{\mathrm{bol}} \sim 10^{41} - 10^{47}\,\mathrm{erg\,s^{-1}}$. The Eddington ratio, $\lambda$, then also spans several decades across the sample due to the inclusion of low accretion rate AGN such as NGC 3227, e.g., $\lambda \simeq 10^{-3} - 1$. The available data therefore cover a significant fraction of the available parameter space in terms of $L_{\mathrm{bol}}$ and $\lambda$, which means that the *Suzaku* sample could perhaps be better suited to search for correlations between the absorber/outflow parameters and source power. I therefore performed an exploratory study of whether the outflow parameters correlate with the power of the host AGN; noting that it is simply $L_{\mathrm{bol}}$ normalised to $L_{\mathrm{edd}}$, the principal power metric considered is the Eddington ratio, $\lambda$.

Scatter plots and regression lines for $\log L_{\mathrm{edd}}$ against the various wind parameters are presented in Fig. 5.7. $\mathrm{Log}L_{\mathrm{edd}}$ was also compared to $N_{\mathrm{H}}$ and $\xi$, but these are not included as no significant correlations were found (see Table 5.3). As there are no implicit correlations between $\lambda$ and the other parameters the mean points can be considered; each plotted point then corresponds to the geometric mean of the upper and lower limits of each parameter (as presented in Table 5.2), with the errors denoting the range between the maximum/minimum values, including the errors. The plotted points are then analogous to those presented in Figures 5.2–5.4.

There are no significant correlations found with $\log\lambda$ versus $\log N_{\mathrm{H}}$ or $\log\xi$; the linear fits have $|a| < 0.15$ (see Table 5.3) indicating that the column density and ionisation

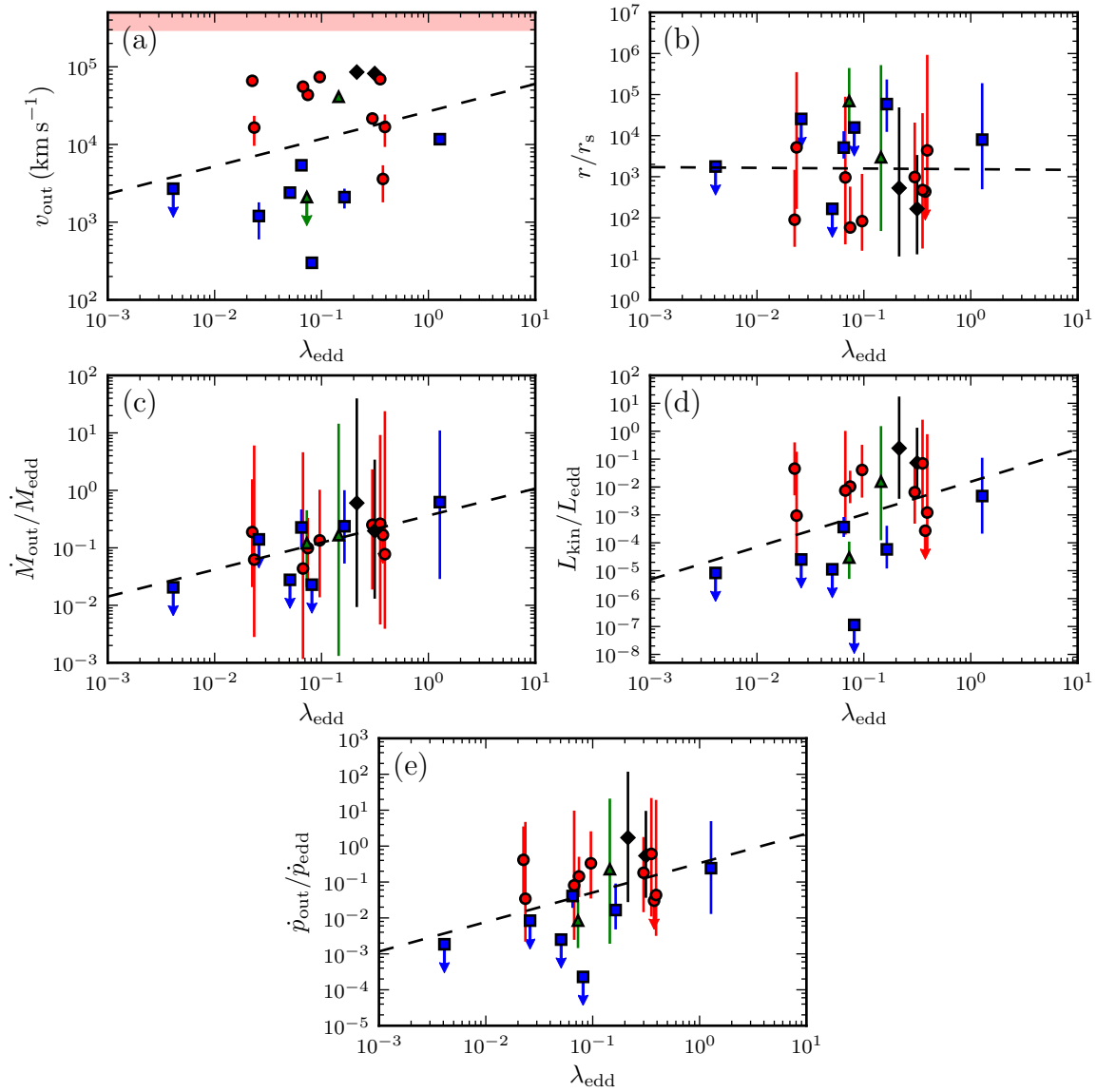


Figure 5.7: As in Fig. 5.6, but this time showing scatter plots of Eddington ratio ($\log\lambda$) versus: (a) $\log v_{\rm out}$, (b) $\log(r/r_{\rm s})$, (c) $\log(\dot{M}_{\rm out}/\dot{M}_{\rm edd})$, (d) $\log(L_{\rm kin}/L_{\rm edd})$ and (e) $\log(\dot{p}_{\rm out}/\dot{p}_{\rm edd})$. The plotted points again correspond to Fe XXV He$\alpha$ (green triangles), Fe XXVI Ly$\alpha$ (red circles), Fe XXV–XXVI pair (blue squares) and blended (black diamonds) absorption line systems, respectively, while the red shaded area once again denotes the region where $v_{\rm out} > c$.

of the absorbers are largely independent of source power. Likewise, both the velocity (Fig. 5.7a) and location (Fig. 5.7b) of the outflows appear to be independent of $\lambda$. This seemingly suggests that the Fe K winds are typically observed at the same relative distance from the SMBH regardless of source power, and with a wide range of velocities. Conversely, $\log(\dot{M}_{\rm out}/\dot{M}_{\rm edd})$ (Fig. 5.7c), $\log(L_{\rm kin}/L_{\rm edd})$ (Fig. 5.7d) and $\log(\dot{p}_{\rm out}/\dot{p}_{\rm edd})$ (Fig 5.7e) have plausible correlations versus $\lambda$, with slopes of $a \simeq 0.47$, $a \simeq 1.17$ and $a \simeq 0.82$, respectively, similar to what is expected for a wind driven by Thompson scattering (see Chapter 6). The correlations for $\log(\dot{M}_{\rm out}/\dot{M}_{\rm edd})$ and $\log(\dot{p}_{\rm out}/\dot{p}_{\rm edd})$ in particular are significant at the $> 95\%$ level, while the one for $\log(L_{\rm kin}/L_{\rm edd})$ is only marginally detected at $\sim 90\%$. Overall, these relationships seem to convey a picture where the relative power of Fe K winds is proportional to the Eddington rate of the AGN — sources at higher $\lambda$ driving winds with $\dot{M}_{\rm out}$, $\dot{p}_{\rm out}$ and maybe $L_{\rm kin}$ at larger fractions of their respective Eddington limited values.

However, while the analysis thus far has identified that Fe K winds are frequently observed there are a few fundamental open questions which still remain unanswered. Amongst these is the question of what principal driving mechanism is responsible for accelerating the winds to their large velocities, and whether they are in fact energetically significant in terms of feedback. In the next chapter I use the insights offered by the *Suzaku* sample to probe this important question.

# 6 General discussion[1]

The analysis presented thus far has identified that Fe K winds are frequently observed in local AGN. However, there are a few fundamental open questions which still remain unanswered. Amongst these are the questions of what driving mechanism is responsible for accelerating the winds to their large velocities, and whether the resultant winds are energetically significant in terms of feedback. In this chapter I will attempt to address these important points using the information gleaned from the *Suzaku* outflow sample.

## 6.1 Comparison with previous work

### 6.1.1 Tombesi et al. (2010+)

Substantial parallels can be drawn between the research that I have presented in this thesis and the works of Tombesi et al. (2010a, 2011a, 2012a, 2013) who analyse a flux-limited sample of 42 nearby (i.e., $z < 0.1$) AGN with *XMM-Newton*. Indeed, both studies employ similar quantitative techniques to both assess for the presence of highly-ionised Fe XXV He$\alpha$ and/or Fe XXVI Ly$\alpha$ absorption lines, and hence deduce their statistical significance. Given these similarities, an obvious step is to compare my results with those obtained by Tombesi et al. to ascertain whether there are any notable differences between the two bodies of work.

[1]This chapter is partly based on published work entitled '*The Suzaku view of highly ionized outflows in AGN – I. Statistical detection and global absorber properties*'; Gofford, J.; Reeves, J. N.; Tombesi, F.; Braito, V.; Turner, T. J.; Miller, L.; Cappi, M.; MNRAS, **430**, 60-80.

All work was conducted by myself.

### Radio-quiet sources

In the *Suzaku* outflow sample of 51 AGN I have detected Fe K outflows in 17 radio-quiet AGN and 3 in radio-loud AGN. Of the radio-quiet detections, 9/17 sources are also included in the *XMM-Newton* outflow sample with 6/9 of these cases having their Fe K outflows directly confirmed by Tombesi et al. (2010a) (i.e., Mrk 766, NGC 4051, NGC 3516, NGC 3783, NGC 4151, Mrk 279). In NGC 5506, MCG -6-30-15 and NGC 3227 the *Suzaku*-detected outflows are, unfortunately, not confirmed by *XMM-Newton*. Even so, given that in the case of NGC 3227 the Fe K absorption is detected at $P_{\rm MC} > 99.9\%$ significance in 3 separate *Suzaku* epochs, and that both the Fe XXV He$\alpha$ and Fe XXVI Ly$\alpha$ absorption lines in MCG -6-30-15 are each statistically detected at $P_{\rm MC} > 99.9\%$ confidence, the *Suzaku* line detections alone still imply very robust absorber detections in both of these sources. There are a further 3 sources with *Suzaku*-detected absorption which have had statistically significant absorption detected in *XMM-Newton* observations which were not included in the Tombesi et al. (2010a) outflow sample: NGC 1365, (Risaliti et al. 2005), PDS 456 (Reeves, O'Brien & Ward 2003; Reeves et al. 2009) and APM 08279+5255 (Chartas et al. 2009). Furthermore, weak hard-band absorption has been noted in the *XMM-Newton* spectra of MCG -6-30-15 by several authors (e.g., Fabian et al. 2002; Vaughan & Fabian 2004; Nandra et al. 2007; Miller, Turner & Reeves 2008). Nandra et al. (2007) in particular found moderately significant (i.e., just below 99% confidence) Fe XXV He$\alpha$ absorption but this detection was not significantly replicated by Tombesi et al. (2010a) due to differences in the continuum model.

Therefore, 9/17 ($\sim 53\%$) of the AGN have had Fe K outflows detected independently by both *Suzaku* and *XMM-Newton*. In addition to these, the absorbers in MR 2251−178 and MCG -6-30-15 are corroborated on the basis of their *Chandra* HETG data. Gibson et al. (2005) found a resolved Fe XXV He$\alpha$ absorption line at $E \sim 7.25\,{\rm keV}$ in the HETG spectrum of MR 2251−178 ($v_{\rm out} \sim 13,000\,{\rm km\,s^{-1}}$), while Young et al. (2005) found variable absorption lines due to Fe XXV He$\alpha$ and Fe XXVI Ly$\alpha$ in MCG 6-30-15 with $v_{\rm out} \sim 2,000\,{\rm km\,s^{-1}}$. In both of these cases the reported outflow velocities are consistent with those that I have measured in their *Suzaku* spectra, with the detection in the HETG

spectrum of MCG -6-30-15 overcoming any ambiguities which remained on the basis of the *XMM-Newton* observation. Fe K absorption has also been reported in the *Chandra* spectrum of APM 08279+5255 (Chartas et al. 2002), which makes it the only source in the sample to have its Fe K outflow independently detected by all 3 of the major X-ray observatories at a high significance level.

Thus, in total 11/17 ($\sim 65\%$) of the radio-quiet AGN with *Suzaku*-detected Fe K outflows have also has similar features reported elsewhere in the literature via either *XMM-Newton* or *Chandra*. Of the remaining 6 sources, SWIFT J2127.4+5654 has been observed by *XMM-Newton* twice: once in 2009 ($\sim 24$ ks) and once in 2010 ($\sim 131$ ks), but neither observation has been published at the time of writing. CBS 126 has not been observed by either *XMM-Newton* or *Chandra*, while ESO 103-G035 only has a 13 ks *XMM-Newton* observation available which is insufficient to test for Fe K absorption. This leaves only 3 AGN — NGC 5506, NGC 3227 and NGC 4395 — with sufficient observations available which do not have independent confirmations with other observatories; although, as I noted previously, NGC 3227 does have multiple *Suzaku* detections implying a robust detection overall.

### Radio-loud sources

There are 6 Broad-line radio galaxies (BLRGs) in the *Suzaku* outflow sample. This includes all of the sources which were part of the Tombesi et al. (2010b) radio-loud 'UFO' case study (i.e., 3C 111, 3C 120, 3C 445, 3C 390.3 and 3C 382), in addition to 4C +74.26 which was not part of their analysis. Tombesi et al. (2010b) report that 3/5 of the BLRGs in their sample, namely 3C 111, 3C 120 and 3C 390.3, show evidence for highly-ionised absorption lines in their *Suzaku* spectra, with that found in 3C 111 also being confirmed in subsequent observations (Tombesi et al. 2011b).

Through my analysis I am able confirm the Fe K absorption lines in both 3C 111 and 3C 390.3 at a similar confidence level but I am not able to confirm their reported detection in 3C 120. In this latter case, however, it is worth noting that adding two narrow ($\sigma = 10$ eV) Gaussians at the rest-frame energies for the Fe XXV He$\alpha$ and Fe XXVI Ly$\alpha$

lines reported by Tombesi et al. (2010b) (i.e., 7.25 keV and 7.54 keV, respectively) yields lower limits of $EW_{\mathrm{He}\alpha} > -8$ eV and $EW_{\mathrm{Ly}\alpha} > -9$ eV for the Fe XXV He$\alpha$ and Fe XXVI Ly$\alpha$ absorption lines, which are entirely consistent with those reported by Tombesi et al. (2010b) at the 90% level. Furthermore, I also find that the BLRG 4C +74.26 harbours a statistically significant high-velocity outflow, which supplements that also reported in the *Chandra* LETG data for 3C 445 (Reeves et al. 2010; see also Braito et al. 2011).

Thus the number of BLRGs with high-velocity outflows could tentatively rise to 4/6 if observations from multiple observatories are included, which suggests that such Fe K outflows could well be an important component in radio-loud sources as well. It is important to note, however, that the current sample size of 6 *Suzaku* observed radio-loud AGN is insufficient for a reliable statistical study into the prevalence of Fe K absorption in radio-loud sources.

**On the absorber and outflow properties**

In Chapter 4 I showed that $\sim 40\%$ of the AGN in the *Suzaku* sample exhibit evidence for highly-ionised outflows in their Fe K band. This is consistent with the detection fraction reported by Tombesi et al. (2010a) for *XMM-Newton*, and implies that the winds have a large covering fraction. Moreover, the distributions of measured column densities and ionisation parameter for the *Suzaku*-detected outflows are also entirely consistent between the two samples, covering ranges of $21 \lesssim \log(N_{\mathrm{H}}/\mathrm{cm}^{-2}) \leq 24$ and $2 \lesssim \log(\xi/\mathrm{erg\,cm\,s}^{-1}) \leq 6$ in both, respectively. The *Suzaku* distribution of outflow velocities is subtly different, lacking the pronounced peak at $v_{\mathrm{out}} \sim 0.1\,\mathrm{c}$ which was found with *XMM-Newton*, however this could be a by-product of the fitting method (e.g., I have used broad-band models whilst Tombesi et al. take a simplistic phenomenological approach) and instrumental differences such as the XIS resolution at Fe K.

The next thing to consider is whether the parameters of the *outflow*, i.e., its radial location, mass outflow rate and kinetic power, are also similar between the two samples. In § 5.2 I derived these quantities for the *Suzaku* sample and showed that while there can be

large differences between the individual cases, the principle outflow parameters have mean ranges of $r \sim 10^{2-4}\,r_{\rm s}$, $\dot{M}_{\rm out} \sim 0.01 - 1 M_{\odot}\,{\rm yr}^{-1}$ and $L_{\rm kin} \sim 10^{42-44}\,{\rm erg\,s}^{-1}$, respectively. These ranges are entirely in agreement with those reported for the *XMM-Newton* detected Fe K outflows (Tombesi et al. 2012a). The Fe K absorbers detected in both studies are therefore typified by the same physical parameters and occupy the same parameter space in terms of overall energetics, as would be expected if they are probing the same real physical phenomenon.

In general, then, my analysis of the *Suzaku* outflow sample provides robust and independent confirmation that Fe K winds are a real physical component of AGN spectra in the X-rays, that these winds likely have a large covering fraction with respect to the central black hole, and that they are typified by large column densities and high ionisation. Furthermore, the range of outflow velocities as found for the Fe K winds in the *Suzaku* sample — which are typically around $v_{\rm out} \geq 10,000\,{\rm km\,s}^{-1}$, but can be as low as $\lesssim 1,000\,{\rm km\,s}^{-1}$ in some cases — suggests that the highly-ionised winds share an overlap in velocity space with the traditional soft X-ray warm absorber. This is consistent with the findings of Tombesi et al. (2013) who argue that the soft X-ray warm absorber may simply be the remnants of an accretion disc wind seen at greater distance from the black-hole along the line of sight.

Tombesi et al. (2013) also conducted a detailed investigation of how the properties of both the absorber and the outflow vary with how far the absorbing gas is located from the black hole. In §5.6.2 I attempted to replicate their analysis using data for the *Suzaku* detected Fe K winds but, unfortunately, their limited dynamic range meant that I was unable to confirm their results. In particular, I cannot confirm the global trends of both the outflow velocity and kinetic power decreasing with distance which are reported by Tombesi et al. (2013). Even so, I *am* able to confirm that the larger column density and higher ionisation winds tend to be located closer to the black hole at a high confidence level.

### 6.1.2 Patrick et al. (2012)

I can also compare and contrast my results against those reported by Patrick et al. (2012), who have recently published the analysis of another large sample of *Suzaku* selected AGN. While the primary aims of the Patrick et al. (2012) study was to assess the properties of Fe K emission lines and black hole spin, they also note the presence of Fe XXV He$\alpha$ and/or Fe XXVI Ly$\alpha$ absorption lines in 14/46 ($\sim 30\%$) of their objects. The two samples have 43 AGN in common, including 15 of the AGN in which I have detected Fe K absorption. Of these, 11 of the detections are confirmed by the Patrick et al. (2012) analysis. The four objects where the outflow detections are not corroborated by Patrick et al. (2012) are 3C 390.3, 4C+74.26, NGC 5506 and SWIFT J2127.4+5654, of which three are only marginal detections from Monte Carlo simulations. Indeed, the outflows which I have detected in 3C 390.3, 4C+74.26 and SWIFT J2127.4+5654 are only significant at the $95\% \leq P_{MC} < 99\%$ level, which suggests that the lines may not be visually apparent in the raw data without a statistically driven analysis. The outflow in NGC 5506, on the other hand, is detected with $P_{\rm MC} = 99.8\%$ which suggests that the discrepancy is likely a result of the method by which the datasets were analysed. For example, my detection of a Fe XXVI Ly$\alpha$ absorption line in this source is taken from the time-averaged (stacked) *Suzaku* spectrum while Patrick et al. (2012) analysed the observations separately. The outflow in NGC 5506 may then be intrinsically weak in the individual *Suzaku* epochs, only becoming apparent when they are time-averaged due to higher $S/N$.

An interesting contrast with the Patrick et al. (2012) analysis is that they claim outflow detections in three sources (3C 445, NGC 5548 and PG 1211+143) which I am not able to confirm despite employing a more rigorous statistical analysis. Highly-ionised outflows in 3C 445 and PG 1211+143 have been detected with other observatories previously (3C 445: Reeves et al. 2010, PG 1211+143: Pounds et al. 2003a) and they are known to be intrinsically variable, being weakest in their respective *Suzaku* observations (Braito et al. 2011; Reeves et al. 2008b; Reeves & Pounds 2012). In NGC 5548 there appears to be a weak absorption trough detected at the energy expected for Fe XXV He$\alpha$

(see appropriate entry in Appendix A.1), but it falls below my chosen selection criteria. Similar is also true for the *Suzaku* line detection in PG 1211+143, which is only detected at 90% significance.

Even so, the broader results of Patrick et al. (2012) in the context of highly-ionised absorption are entirely consistent with my own analysis. Indeed, both analyses confirm that there is a strong peak in the ionisation parameter distribution at $\log(\xi/\mathrm{erg\,cm\,s^{-1}}) \sim 4-4.5$, with the associated absorber outflow velocities spanning a continuous range from $\sim 0 \lesssim v_{\rm out} \lesssim 100,000\,\mathrm{km\,s^{-1}}$. The two samples are therefore in complete agreement when it comes to the overall properties of the Fe K absorbers, despite the minor discrepancies at the level of individual sources.

### 6.1.3 King et al. (2013)

In § 5.6.3 I investigated how the properties of both the absorber and the outflow vary with source power, and, more specifically, how they varied with Eddington ratio, $\lambda$. There are a number of similar studies already in the literature. In particular King et al. (2013) have used *Chandra* grating spectra to compare the kinetic power of slow X-ray winds (i.e., the warm absorber) in both Black-Hole binaries (BHBs) and AGN to the bolometric luminosity of their host system. By virtue of considering both BHBs and AGN the King et al. (2013) study samples an extremely broad spectrum of both black hole mass [$0.8 \lesssim \log(M_{\rm BH}/M_{\odot}) < 10$] and bolometric luminosity [$37 \lesssim \log L_{\rm bol} < 47$]. These ranges have notable overlap with the parameters of the *Suzaku* outflow sample that I have presented in this thesis, especially at the high mass/high luminosity end. In fact, the two samples actually have several AGN in common, with MCG -6-30-15, NGC 3516, NGC 3783, NGC 4051, NGC 4151, 3C 111 and APM 08279+5255 all appearing in both samples at some point.

However, because the bulk of the outflows considered by King et al. (2013) are taken from literary *Chandra* observations, their analysis primarily deals with the relatively low-velocity soft X-ray warm absorber and not the highly-ionised, high-velocity, Fe K winds which are the focus of my *Suzaku* study. Even so, they do include a few 'Ultra-Fast

Outflows' (which they define as those with $v_{\rm out} \geq 0.01\,{\rm c}$) as a matter of comparison, although they do not fit them directly as part of their regression analysis. Two of these 'UFO' sources, namely 3C 111 and APM 08279+5255, are also included in the *Suzaku* sample considered in this thesis. In principle, then, the *Suzaku*-detected outflows could be compared directly with the King et al. results to determine if the high velocity winds scale in a similar way as the slow ones. However, this is not possible in practice because the two studies compute the wind power according to different underlying assumptions (i.e., King et al. give their quantities in units of per-covering-fraction) which means that the data are normalised to different scales, and any linear regressions will have an intrinsically offset intercept. Even so, the *slope* of any linear fit — which is the important parameter as it measures how the wind power varies with bolometric luminosity — is independent of the normalisation and so can still be compared.

King et al. find the kinetic power of slow X-rays winds to be strongly correlated with $L_{\rm bol}$. They find that their kinetic power scales with a global slope of $\log L_{\rm kin} \propto (1.58 \pm 0.07) \log L_{\rm bol}$, while those in AGN have a much flatter slope of $0.63 \pm 0.30$ when considered in isolation (although note that this could be driven by there being a smaller number of AGN). Fig. 6.1a shows a plot of $\log L_{\rm bol} - \log L_{\rm kin}$ for the *Suzaku* sample. The kinetic power of the *Suzaku*-detected winds are strongly correlated with the bolometric luminosity of the host AGN ($P_{\rm null} = 1.82 \times 10^{-7}$); the data follow a slope of $a \simeq 1.69$ ($R_p = 0.89$), which is largely consistent with that found by King et al. in their global sample and suggests that the highly-ionised winds scale with bolometric luminosity in a similar manner to their global sample. Moreover, and as was suggested by King et al., the fact that the slope of the regression is greater than unity rather than exactly 1 implies that the radiation in more luminous sources couples more efficiently with the local gas. In fact, evidence in support of this claim is already provided by Fig. 5.7d-e, which all show that the higher Eddington ratio (higher luminosity) sources impart a larger fraction of their maximum radiative output to mechanical power, and is further enforced here by Fig. 6.1b which shows the ratio of kinetic power to Eddington luminosity is strongly correlated with $L_{\rm bol}$ (with $a \simeq 0.87$, $P_{\rm null} = 3.36 \times 10^{-4}$). Therefore, higher Eddington ratio (higher luminosity) sources appear to drive overall stronger winds, which

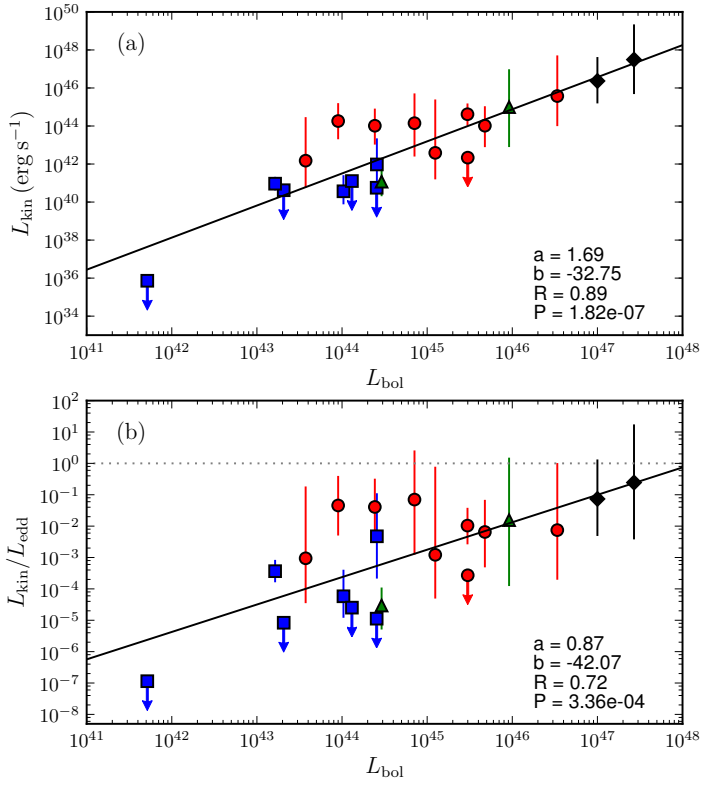


Figure 6.1: Scatter plots showing how wind kinetic power varies with source luminosity. Panel (a) shows a regression of $\log L_{\rm kin} - \log L_{\rm bol}$. There is a clear linear correlation between the two parameters, with more luminous sources harbouring winds with greater kinetic power. Panel (b) shows $\log(L_{\rm kin}/L_{\rm edd}) - \log(L_{\rm bol})$. The steady gradient of $a \simeq 0.87$ in the normalised data shows that the winds in more luminous AGN contain a larger fraction of $L_{\rm edd}$.

is consistent with a wind accelerated by radiation pressure.

## 6.2 Wind driving mechanisms

The physical and kinematic characteristics of Fe K winds strongly indicates an association with material located near the inner regions of the accretion disc. However, the precise nature of their acceleration remains largely ambiguous. In general, astrophysical winds around accreting black holes are driven by one of three mechanisms: (1) they can be *radiatively driven* by gaining momentum from an incident photon field; (2) they can be *magnetically driven* by interactions between charged material and local magnetic fields; or (3) they can be *thermally driven* by kinetic motions in the gas as it is heated. Regardless of the driving mechanism, a wind will only be launched if the induced pressure acting on the gas exceeds the strength of the local gravitational field; in general, the closer material is to the SMBH, the higher the necessary pressure to effectively launch a wind.

With existing instrumentation it is not possible to observationally distinguish between which of these mechanisms is acting on a given absorber and, in reality, a full explanation of winds in AGN will likely require a cohesive combination of the three. In the remainder of this section, I will provide an outline of the three driving mechanisms and discuss what, if any, new insights can be gleaned from my results with the *Suzaku* outflow sample.

### 6.2.1 Thermal driving

A mass outflow can be launched if the low-density outer layers of the accretion disc are heated. In AGN the outer disc atmosphere is Compton heated by the incident radiation field and the resultant thermal pressure can be sufficient to launch a wind if thermal velocity exceeds the local escape velocity; in general, this is only possible at large radii from the black hole where the escape velocity is relatively small. The UV and X-ray radiation from a typical quasar spectrum can heat an accretion disc atmosphere to an equilibrium Compton temperature of the order a few $\times 10^7$ K (Sazonov et al. 2005), corresponding to a thermal velocity in the disc atmosphere of $v_{\rm th} \simeq 540\,{\rm km\,s^{-1}}$— roughly

equal to the escape velocity at a distance of $\sim 3\,\mathrm{pc}$ from a fiducial $M_{\mathrm{BH}} = 10^8 M_{\odot}$ black hole. Thermally driven winds can only achieve maximum terminal velocities of the order $\sim 1,000\,\mathrm{km\,s^{-1}}$ and while they are capable of matching the observed characteristics of both soft X-ray and UV warm absorbers (e.g., Krolik & Kriss 1995, 2001; Chelouche & Netzer 2005) they are unable to account for the high-velocity X-ray (and UV) winds and one must therefore invoke either radiative or magnetic driving to explain them.

### 6.2.2 Radiative driving

AGN are prodigious emitters of electromagnetic radiation which makes radiation pressure an appealing means of explaining how winds are accelerated to their high velocities. Indeed, when the source luminosity exceeds the Eddington limit the continuum radiation pressure exceeds gravity, accretion halts and, by definition, one expects an episodic outflow of material to be launched. However, powerful winds can also be driven at $L_{\mathrm{bol}} < L_{\mathrm{edd}}$ when the momentum associated with the radiation field is transferred to circumnuclear gas, hence accelerating it away from the continuum source. The precise nature of this process depends upon the primary source of opacity to the radiation, e.g., bound-bound spectral lines ('line-driven'), bound-free absorption or Thomson/Compton scattering ('continuum-driven'), and which of these dominates depends upon its ionisation state (e.g., Stevens & Kallman 1990; Arav, Li & Begelman 1994).

#### Line-driving

Line-driven winds are expected to be prevalent at low–moderate ionisation states where the opacity due to bound-bound absorption can exceed that of continuum scattering by several orders of magnitude (i.e., $\sigma_{\mathrm{line}} \gg \sigma_T$). The quantity which expresses their relative contribution to the total opacity is called the *force multiplier* (Castor, Abbott & Klein 1975), and is typically largest for material which interacts at UV wavelengths — the opacity due to resonant UV absorption can exceed that for electron scattering by of the order a few $\times 10^3$ (Castor 1974; Stevens & Kallman 1990; Proga, Stone & Kallman 2000)

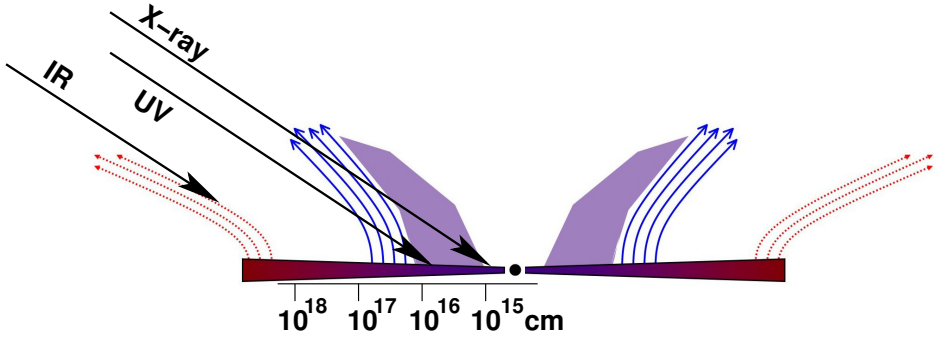


Figure 6.2: Cartoon showing a schematic of the wind geometry necessary for efficient line-driving at UV wavelengths. The UV gas needs to be shielded from the intense ionising continuum radiation; this necessitates the presence of a thick layer of X-ray absorbing gas. One plausible identification for the highly-ionised Fe K winds is with this shielding gas. Figure taken directly from Gallagher & Everett (2007).

— and several numerical studies have shown that UV line-driving can give rise to winds with properties similar to those seen in BALQSOs, i.e., outflow velocities of $\sim 0.1\,c$ and covering fractions of $\sim 0.2$ (e.g., Murray & Chiang 1995; Proga, Stone & Kallman 2000; Proga & Kallman 2004). However, these results are contingent on the presence of a thick layer of X-ray absorbing gas [$\log(N_{\rm H}/{\rm cm}^{-2}) \gtrsim 23-24$] which is required to prevent the over-ionisation of the UV absorbing gas and hence allow it to maintain conditions which favour a large force multiplier (Murray & Chiang 1995). A schematic of the necessary geometry for efficient line-driving in the UV, as presented by Gallagher & Everett (2007), is shown in Fig. 6.2.

Indeed, because efficient line driving is dependent upon the ionisation state of the material it is highly sensitive to the ratio of UV disc radiation to Comptonised X-ray emission; the former can only launch and accelerate a UV wind via line-driving if there are sufficient bound electrons in the gas, and these are removed by energetic X-ray photons. Thus, in order for a UV wind to be driven solely by radiation pressure there must either be a deficit of X-rays relative to UV photons, or the UV absorbing gas must be 'shielded' from the incident high energy X-ray photons. Detailed hydrodynamic

simulations by Proga, Stone & Kallman (2000); Proga & Kallman (2004) and Proga (2005) of a wind accelerated by UV line opacity around a $M_{\rm BH} = 10^8 M_{\odot}$ ($\lambda = 0.5$) black hole have demonstrated that radiatively driven winds in this vein can become self-shielded from continuum radiation by a region of dense material which accumulates at the inner part of the flow.

There are three main components to their simulated wind. At angles close to the pole ($\theta \lesssim 55^{\circ}$) the gas is hot, of low density, and has an extremely high ionisation parameter, i.e., $\log(\xi/{\rm erg\,cm\,s^{-1}}) \sim 8$, meaning that it will not be detectable through spectroscopy. At angles close to the equatorial plane (i.e., $\theta \gtrsim 67^{\circ}$), on the other hand, the flow is dominated by a dense, warm and rapidly outflowing equatorial disc wind where the strong line force accelerates material to velocities of the order a few $\times 10^4\,{\rm km\,s^{-1}}$, consistent with the velocities seen in BALQSOs. Separating the two extremes, at angles of $55^{\circ} \lesssim \theta < 65^{\circ}$, the wind has an embedded warm transitional 'surface layer'. In this region the gas is high density, clumpy, and composed of highly-ionised (but not completely) gas, and is important for shielding the outer portions of the flow from X-rays, preventing its over-ionisation, and thereby allowing it to be launched by UV resonant line-driving (e.g., Proga & Kallman 2004).

Schurch, Done & Proga (2009) simulated the resultant X-ray spectra one would expect to observe when viewing the disc-wind simulated by Proga & Kallman (2004) at different angles. They found that when sight-lines intercept the 'transition layer' the X-ray spectrum is imprinted with a plethora of absorption lines from the ionised material. In fact, they found the majority of material in this region to be characterised by $\log(N_{\rm H}/{\rm cm^{-2}}) \sim 23 - 25$ and $\log(\xi/{\rm erg\,cm\,s^{-1}}) \sim 3.5 - 4.5$, which is completely consistent with the *Suzaku*-detected highly-ionised outflows and implies that they could be associated with the X-ray shielding layer. Sim et al. (2010) later significantly extended this analysis by employing a powerful Monte Carlo radiative transfer code to include a sophisticated treatment of X-ray reprocessing and scattering both in and through the wind. Figs 6.3a, 6.3b and 6.3c show the temperature, density and mean Fe ion charge (a proxy for the ionisation state) in the Proga & Kallman (2004) disc-wind as calculated via their Monte Carlo code. The wind clearly has a complex topology, with an inhomogeneous

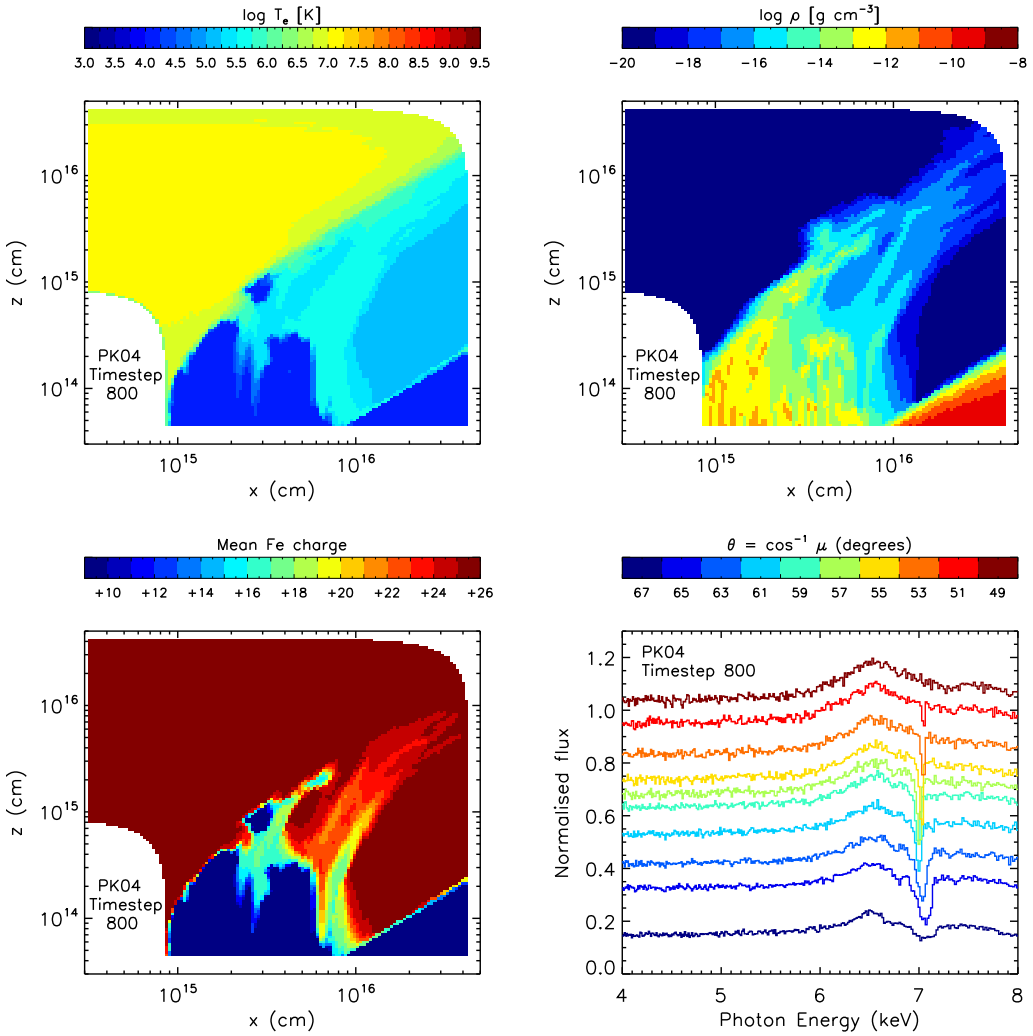


Figure 6.3: Example plots showing some of the key properties of the Proga & Kallman (2004) hydrodynamic wind model, as calculated by Sim et al. (2010) using a Monte Carlo radiative-transfer code. Clockwise from top left, the panels show (a) the distribution in temperature across the flow; (b) the wind density; (c) the mean charge of Fe ions, a proxy for the ionisation state; and (d) synthetic absorption line spectra for different viewing angles. See text for further discussion. All panels taken directly from Sim et al. (2010).

and clumpy distribution of density (and hence column density), and also has a complex temperature distribution across the flow which is consistent with a stratified ionisation structure. Both Fe XXV He$\alpha$ and Fe XXVI Ly$\alpha$ are prevalent on the face and in the outer extremities of the wind, which can imprint modestly blue-shifted Fe K absorption features in the output spectra at intermediate inclination angles (see Fig. 6.3d).

However, while the analyses of both Schurch, Done & Proga (2009) and Sim et al. (2010) concisely show that whilst the X-ray shielding gas found in the Proga & Kallman (2004) hydrodynamic simulation has physical properties (i.e., $N_{\rm H}$, $\log \xi$) which are reminiscent of the winds seen in Fe K, they are typically unable to account for the full range of observed outflow velocities. Indeed, the resultant line blue-shifts as inferred by these authors for the line-driven flow are all on the relatively slow side in the X-rays — the maximum possible velocity which could be achieved was $v_{\rm out} \sim 0.1\,{\rm c}$, but they were more typically around $\sim 0.01\,{\rm c}$ — and it is therefore unlikely that line-driving alone is responsible for launching the fastest outflows which can have semi-relativistic velocities in the $v_{\rm out} \gtrsim 0.2 - 0.3\,{\rm c}$ range (e.g., PDS 456 and APM 08279+5255), or even if the line-driven X-ray outflows can achieve escape velocity at all. Both Proga & Kallman (2004); Proga (2005) and Schurch, Done & Proga (2009) note, however, that it is possible that some clumps or clouds of gas in the flow may not escape the system because they, for instance, may be over-ionised to bona-fide line-driving but still be subject to other radiative acceleration mechanisms such as bound-free absorption which are less efficient.

In the X-ray regime where most absorption is characterised by ions in their He- or H-like charge states the opacity to line-driving is very small and in these cases a 'failed wind' may instead develop where material is driven to large scale-heights above the disc but, because its line opacity is insufficient for it to achieve an escape velocity, will eventually fall back onto the disc at larger radii (Proga 2005; see Fig. 6.4). Even so, this material can still impart significant absorption features in the X-ray spectrum while it has a large height above the disc, and could therefore give rise to Fe K features at the right ionisation. Such clouds could be a reasonable explanation for why the winds in CBS 126, NGC 1365, NGC 3227, NGC 3516 and NGC 4395 are observed with $v_{\rm out} < v_{\rm esc}$, but an alternative initial driving mechanism is probably necessary to explain how the

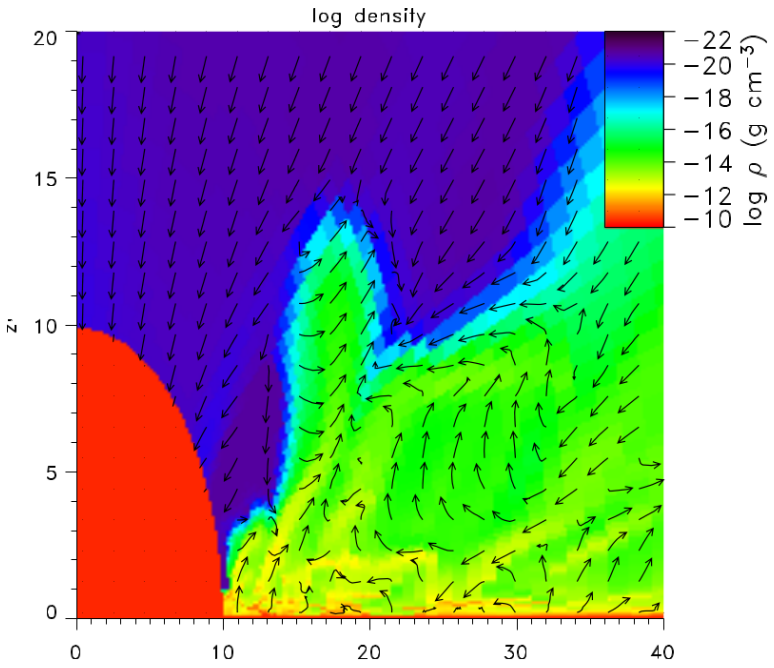


Figure 6.4: A sample panel from the Proga (2005) hydrodynamic simulation of a failed X-ray wind; the intense X-ray irradiation over-ionises the UV-shielding gas leading to a turbulent 'failed wind' in the X-rays which is unable to escape the system. A failed X-ray wind in this vein is a plausible explanation for the *Suzaku*-detected Fe K outflows in CBS 126, NGC 1365, NGC 3227, NGC 3516 and NGC 4395, which are all observed with $v_{\rm out} < v_{\rm esc}$. Note that the $x$-axis corresponds to distance from the black hole, see Proga (2005) for more details. Figure taken from Proga (2005).

outflows in the remaining AGN are accelerated to beyond their local escape speed.

### Continuum-driving

Whilst the need for low–moderate ionisation absorbing gas rules against efficient line-driving in the X-ray regime, the highly ionised material can still be radiatively accelerated via the momentum transfer associated with Thomson/Compton scattering. In this scenario, the significantly reduced interaction cross-section compared to line-driving means that the resultant winds have much less efficient energy-coupling than their

line-driven counterparts and, as a consequence, require much larger source luminosities to achieve equivalent outflow velocities. A general characteristic of momentum-driven winds is that they are accelerated by photons scattering off free electrons in the wind which transfers a portion of their momentum to the material. This scenario has been considered extensively by King & Pounds (2003) and King (2005, 2010) in the literature and below I outline their base derivation.

The efficiency through which momentum is transferred to the wind depends upon its optical depth to electron scattering, $\tau$, which determines how many times each electron scatters in the flow. Mathematically, the total electron scattering optical depth of a homogeneous (i.e., un-clumped) wind viewed from infinity down to radius $R$ is given by

$$\tau = N_{\rm H}\sigma_{\rm T} = \sigma_{\rm T}\int_{R}^{\infty} n \cdot dr = \frac{\sigma_{\rm T}\dot{M}_{\rm out}}{4\pi b m_{\rm p} v_{\rm out} R} \tag{6.1}$$

where $\sigma_{\rm T}$ is the Thomson cross-section for electron-scattering and $n = \dot{M}_{\rm out}/4\pi b m_{\rm p} v_{\rm out} r^2$ is the electron number density as estimated by imposing the limit of a mass-conserving spherical flow (c.f., §5.2.2). Here $b$ is the geometrical factor which takes into account the global covering of the flow. It is useful to eliminate the Thomson cross-section by normalising the above quantity to the Eddington mass-accretion rate, $\dot{M}_{\rm edd} = L_{\rm edd}/\eta c^2 = 4\pi G M_{\rm BH} m_{\rm p}/\sigma_{\rm T}\eta c$, yielding

$$\tau = \frac{1}{b\eta c}\frac{1}{v_{\rm out}}\frac{GM_{\rm BH}}{R}\frac{\dot{M}_{\rm out}}{\dot{M}_{\rm edd}}, \tag{6.2}$$

Up to this point the above derivation is equivalent to the one presented by King & Pounds (2003) (see also King 2010 for a recent review). It is important to note, however, that the $\tau$ above is the *observed* optical depth of the outflow as inferred from the measured column density. Indeed, as it is unlikely for our sight line to be viewing directly down the wind flow direction (i.e., we are more likely viewing across or through the wind), the observed $\tau$ is probably an underestimate of the total opacity in the wind from the view of the continuum source. It is therefore useful to denote $\tau = \tau'$, were $\tau'$ denotes the total optical depth in the outflow during its initial acceleration phase. Extrapolating the measured $N_{\rm H}$ regression back to typical escape radii, i.e., $r_{\rm esc} \sim 100\, r_{\rm s}$ for a $v_{\rm out} \sim 0.1\,{\rm c}$

wind, implies that the base of the flow is likely characterised by $N_{\rm H} \sim 10^{24}\,{\rm cm}^{-2}$, and that hence $\tau' \simeq 1$. This is consistent with the assertions of King et al. who infer $\tau = 1$ from the highly-ionised outflow in PG 1211+143 (Pounds et al. 2003a), but I will be leaving it as a free parameter to allow for the possibility of more (fewer) scattering events in the wind and therefore more (less) efficient energy coupling.

Substituting $\tau = \tau'$ into eq. (6.2), and further assuming that the measured flow velocity roughly corresponds to the escape velocity at the radius where the wind was launched, i.e., $R = R_{\rm esc} = 2GM_{\rm BH}/v^2$, then gives

$$\tau' = \frac{1}{2b\eta}\frac{v_{\rm out}}{c}\frac{\dot{M}_{\rm out}}{\dot{M}_{\rm edd}}, \tag{6.3}$$

which, after substituting for $\dot{M}_{\rm edd} = L_{\rm edd}/\eta c^2$ and re-arranging, becomes

$$\dot{M}_{\rm out}v_{\rm out} = 2b\frac{\tau' L_{\rm edd}}{c} \simeq \frac{\tau' L_{\rm edd}}{c} \simeq \frac{\tau'}{\lambda}\frac{L_{\rm bol}}{c}. \tag{6.4}$$

Here, I have assumed a global covering fraction of $b \sim 0.5$ which is close to that observed (see Chapter 4, Tombesi et al. 2010a), and I have exploited the $\lambda = L_{\rm bol}/L_{\rm edd}$ definition to express the relation in terms of solely observable quantities. Eq. (6.4) therefore shows that a momentum-driven wind accelerated by electron scattering will have an outward momentum-rate which is proportional to that of the incident radiation field. As I have mentioned previously, this result (and the associated derivation) is largely equivalent to the one presented by King & Pounds (2003). Indeed, in the specific case of an Eddington-limited black hole ($\lambda = L_{\rm edd}/L_{\rm bol} \simeq 1$) launching a Compton-thick wind ($\tau' \simeq 1$), as is considered by those authors, the above equation reduces to their exact equation. The additional $\tau'/\lambda$ factor, however, allows for the further possibility of momentum-driven winds in sub-Eddington AGN and also allows for subtle differences in coupling efficiency. Indeed, it is important to note that whilst $\tau'$ has thus far been described as the optical depth to electron scattering in the above equations, it can also account for additional sources of opacity to continuum radiation such as bound-free or free-free absorption as well which can provide additional momentum to the flow, and it can also be further boosted by multiple scattering events.

From eq. (6.4) an obvious way of testing for momentum-driving is to plot the calculated wind momentum rate against that of the radiation field to see whether they follow the expected 1 : 1 correlation; Fig. 6.5a shows a scatter plot of $\log \dot{p}_{\rm out}$ versus $\log \dot{p}_{\rm bol}$ to this effect. There is clearly a strong correlation between the two quantities ($P_{\rm null} = 6.43 \times 10^{-9}$), with a best-fitting slope of $a \simeq 1.32$ ($R_{\rm p} = 0.92$). Importantly, whilst the overall slope appears to be slightly steeper than expected, possibly reflecting subtle changes in $\tau'/\lambda$, the vast majority of sources are consistent with unity within the errors: this certainly suggests that the winds may, indeed, by accelerated by radiative momentum-driving. The largest discrepancy is for the left-most point which corresponds to the unusually small AGN NGC 4395 ($M_{\rm BH} = 10^{4.5} M_{\odot}$; Edri et al. 2012) and falls a few orders of magnitude below the expected 1 : 1 relation. Excluding this unusual AGN, and therefore only considering those with $M_{\rm BH} \gtrsim 10^6 M_{\odot}$ softens the slope slightly to $a \simeq 1.16$ and strengths the notion that the winds in 'typical' AGN could be momentum-driven.

One thing which is apparent from Fig. 6.5a is that whilst most of the higher ionisation Fe XXVI Ly$\alpha$ absorption systems are consistent with a $\dot{p}_{\rm out}/\dot{p}_{\rm bol}$ slope of unity within the errors, most of the lower-ionisation Fe XXV–XXVI systems (blue squares) fall below the relation. Kinematically, the main difference between the Fe XXVI Ly$\alpha$ and Fe XXV–XXVI systems is their outflow velocity — i.e., most of the Fe XXVI Ly$\alpha$ systems have $v_{\rm out} > 10,000\,{\rm km\,s^{-1}}$ while the Fe XXV–XXVI flows are systematically slower, with $v_{\rm out}$ of the order of a few thousand $\rm km\,s^{-1}$— and so one possibility is that the two velocity sub-groups follow subtly different local relations. Indeed, such a scenario might be expected if the radiation field is coupled more efficiently with the Fe XXVI (and vice-versa for the Fe XXV–XXVI lines), which would also be consistent with their systematically larger outflow velocities. Indeed, taking logarithms of eq. (6.4) yields $\log(\dot{p}_{\rm out}) = \log(\dot{p}_{\rm bol}) + \log(\tau'/\lambda)$ and therefore any systematic offset for a given slope of unity corresponds to a change in $\tau'/\lambda$, and therefore reflects the efficiency through which the radiation couples to the gas. Unfortunately, however, the range of $\dot{p}_{\rm out}$ is too narrow to robustly assess this possibility in the lower velocity systems; fixing the slope to unity and fitting for an offset in intercept yields $\log(\tau'/\lambda) = -0.76$ and therefore implies $\tau'_{\rm max} \lesssim 0.2$ (with $\lambda \leq 1$), i.e., a maximum coupling efficiency of 20% in the slower systems.

The higher velocity systems with $v_{\rm out} > 10,000\,{\rm km\,s^{-1}}$, on the other hand, span a much wider range and can be fit with a slope of $a \simeq 1.04$ ($R_{\rm P} = 0.90$; $P_{\rm null} = 6.55 \times 10^{-5}$) in isolation which is almost exactly the $a = 1$ expected from eq. (6.4). Fixing $a = 1$ in this case (which is consistent with the measured regression, within the errors) yields $\log(\tau'/\lambda) = 0.14$, implying $\tau'_{\rm max} \lesssim 1.4$ for $\lambda \lesssim 1$, i.e., in the fast winds the incident photons can transfer almost all of their momentum to the flow via one (or more) electron scattering events, as suggested by King & Pounds (2003) and King (2005, 2010). The mean coupling efficiency is $\tau'_{\rm max} \lesssim 0.6$ when the entire sample is considered together. This analysis, while tentative, certainly suggests that efficient momentum-driving is plausible for the high-velocity outflows in particular, but that it becomes less effective for systems with lower velocities. Indeed, the latter could also have a different origin, e.g., with the shielding gas required for line-driving, as discussed previously, or with magnetic processes (see below), or it may simply be the highest ionisation end of a more distant warm absorber component.

Even so, one startling conclusion of the momentum-driving scenario, assuming that it is correct, is that it seemingly suggests that the measured outflow velocity should directly trace the accretion efficiency of the central black hole. Indeed, re-arranging eq. (6.3) gives

$$\frac{v_{\rm out}}{c} = 2b\eta\tau' \left(\frac{\dot{M}_{\rm out}}{\dot{M}_{\rm edd}}\right)^{-1}, \tag{6.5}$$

where $b \sim 0.4 - 0.5$ from the detection fraction of highly ionised outflows. This then implies that $v_{\rm out}/c \propto \eta\tau'(\dot{M}_{\rm out}/\dot{M}_{\rm edd})$. The total electron scattering depth of the wind $\tau'$ is, by definition, proportional to the mass contained in the wind, i.e., $\tau' \propto (\dot{M}_{\rm out}/\dot{M}_{\rm edd})$, with higher mass flows having larger optical depths to scattering and vice-versa. Note that while $\tau'$ is also sensitive to the ionisation state of the material, with lower ionisation material having boosted momentum coupling via bound transitions, most of the outflows have $\log(\xi/{\rm erg\,cm\,s^{-1}}) \gtrsim 4$ which implies that most of the gas in the majority of cases is approaching complete ionisation with the effects of bound-free opacity being negligible. In general then, the ratio of $\tau'/(\dot{M}_{\rm out}/\dot{M}_{\rm edd})$ for the highly-ionised winds is largely expected to be $\sim 1$ for a spherical flow, which hence implies that $v_{\rm out}/c \propto \eta$. This raises the

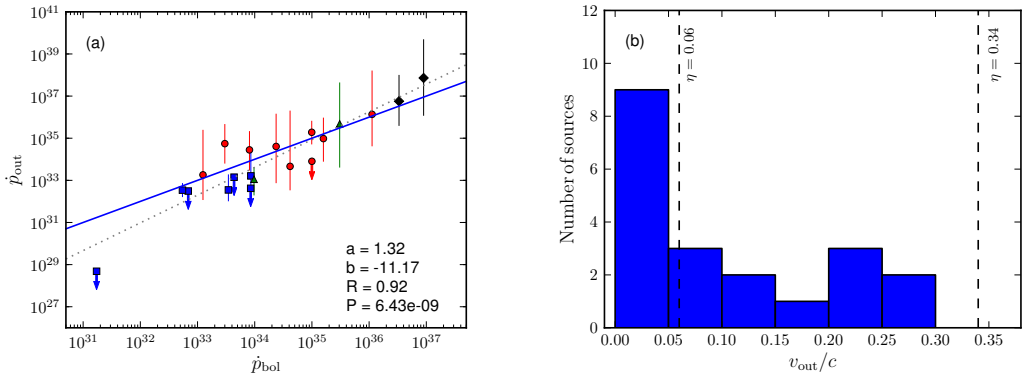


Figure 6.5: Panel (a) compares the momentum rate of the wind ($\dot{p}_{\rm out}$) against the outward momentum rate of the radiation field ($\dot{p}_{\rm bol}$). For a momentum-driven wind scenario a $1:1$ correlation would be expected, as is observed. Panel (b) shows the linear distribution of wind outflow velocities. Over-plotted are the maximum accretion efficiencies for a Schwarzschild ($\eta = 0.06$; Salpeter 1964) and a Kerr ($\eta = 0.34$; Thorne 1974) black hole. Should the momentum-driving scenario prove to be correct, one possibility is that the observed wind velocities trace the accretion efficiency of the black hole. See text for further details.

tantalising possibility of probing the accretion efficiency of black holes (and hence their spin) by measuring the velocity of their highly-ionised X-ray winds.

Indeed, Fig. 6.5b shows a histogram of $v_{\rm out}/c$, as measured for the Fe K winds in the *Suzaku* sample, over-plotted with the maximum accretion efficiencies associated with non-rotating Schwarzschild ($\eta = v_{\rm out}/c = 0.06$; Salpeter 1964) and rotating Kerr ($\eta = v_{\rm out}/c = 0.34$; Thorne 1974) black holes. It is immediately apparent that all of the outflows have velocities below $\sim 0.34\,$c, while just over half of the sample have velocities below $\sim 0.06\,$c. If the outflow velocities are, indeed, proportional to $\eta$ this may imply that over half of the AGN in the sample harbour Schwarzschild black holes, while others have some degree of spin. However, even though the current winds do appear to be largely consistent with the framework of momentum-driving it does not rule out the possibility of their being accelerated by other means, such as magnetic driving. Even so, should the winds be accelerated by continuum-scattering, the possibility of measuring the

black hole accretion efficiency via the velocities of highly-ionised winds which originate near the ISCO is certainly an interesting one.

To conclude the discussion on radiation driving, the data suggest that radiation pressure is a plausible means of accelerating the *Suzaku*-detected Fe K winds. The highest velocity winds (i.e., $v_{\rm out} \gtrsim 10,000\,{\rm km\,s^{-1}}$) have an outward momentum-rate which is directly proportional to the radiation field which suggests that they could be accelerated by scattering processes, as per the suggestion of King & Pounds (2003) King (2005, 2010). The slower winds, on the other hand, might still be accelerated through scattering processes provided the photons couple less efficiently with the gas, although their kinematic and physical properties are also consistent with the expected properties of a failed line-driven wind (Proga 2005; see Fig. 6.4).

### 6.2.3 Magnetic driving

The presence of the magneto-rotational instability (MRI; Balbus & Hawley 1991, 1998; Hawley, Gammie & Balbus 1995; Krolik, Hawley & Hirose 2005) — that is, theoretically robust mechanism through which accretion discs are believed to dissipate their angular momentum — pre-supposes the presence of magnetic fields in accreting systems and implies that magnetism could play a key role in the accretion process. Theoretical studies have shown that magnetic forces could also be important in the mediation and acceleration of winds (e.g., Blandford & Payne 1982; Emmering, Blandford & Shlosman 1992; Contopoulos & Lovelace 1994; Bottorff et al. 1997; Proga 2003 and references therein), and the possibility of the winds being magnetically accelerated should also be considered.

There are numerous magnetohydrodynamic (MHD) prescriptions of AGN winds available in the literature (e.g., Konigl & Kartje 1994; Everett 2005; Ohsuga & Mineshige 2011; Kazanas et al. 2012), and they all share the fundamental property of intense magnetic field lines which are threaded through the accretion disc. In a pure MHD system (i.e., neglecting radiation pressure) ionised material is channelled along the magnetic field lines as the disc rotates and it is magneto-centrifugally accelerated away from the disc

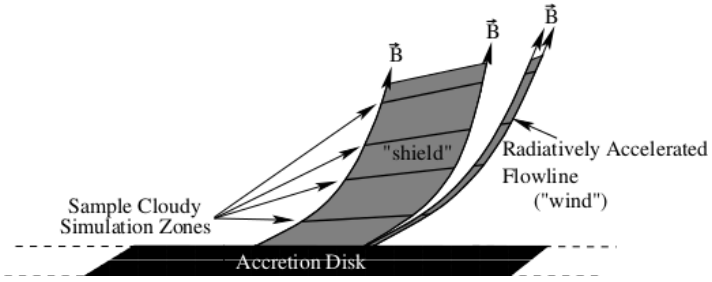


Figure 6.6: The hybrid MHD-radiation wind geometry as suggested by Everett (2005). The inner MHD wind shields an outer wind from over-ionisation, allowing it to be driven by UV radiation pressure. Figure taken directly from Everett (2005).

surface as a wind; the field lines are anchored to this disc surface which means that the wind removes angular momentum from the system and ultimately helps mediate the accretion process (Blandford & Begelman 1999). Notably, these winds do not require radiation pressure to be launched (Proga 2007) and can therefore be an important mechanism in low-luminosity sources, in circumstances where the material is over-ionised with regard line-driving (i.e., close to the black hole) or it is of too low column density to be dominated by continuum-scattering. Indeed, it is possible that the 'shielding gas' necessary for efficient line driving in the UV (see §6.2.2) may be mediated by magnetic fields close to the black hole (e.g., Everett 2005; Fig. 6.6), whilst the channelling of material along tightly wound field lines is postulated as being responsible for the strong relativistic jets in radio-loud sources (Blandford & Payne 1982).

Generically, magneto-centrifugally driven winds differ from those which are radiatively driven in several fundamental aspects. For instance, the wind stream lines are different: while radiatively driven winds are lifted from the accretion disc and accelerated radially which leads to convex streamlines, magneto-centrifugally driven winds are lifted towards the polar axis by the rotationally-collimated magnetic field and hence have concave streamlines. A magnetically launched wind can have substantial transverse velocities due to the anchored field-lines co-rotating with the disc, and these are difficult

to replicate via radiation driving which tends to act radially. In principle, these properties offer a means of observationally distinguishing between winds which are magnetically driven from those that are radiatively driven. In practice, however, magnetic forces are usually only invoked in the literature when radiation driving is unable to account for the observations. For example, Kraemer et al. (2005) and Crenshaw & Kraemer (2007) invoke magnetic wind driving in NGC 4151 on the basis of absorption clouds with strong tangential velocities, while Miller et al. (2006, 2008, see also Neilsen & Homan 2012) argue that the wind in the black hole X-ray binary GRO J1655-40 is probably magnetically driven only after ruling out both radiative and thermal driving mechanisms.

Whilst magnetism is undoubtedly important in accreting black hole systems, it is currently difficult, if not impossible, to definitively test whether the *Suzaku*-detected Fe K winds are associated with a magnetically-driven flow. Indeed, and as I have remarked previously, the models which describe MHD winds currently lack clear and unambiguous quantitative predictions for the wind properties. Even so, it is still possible to gain some insight by qualitatively comparing the properties of the *Suzaku*-detected outflows with those predicted for MHD winds. The recent model outlined by Fukumura et al. (2010a,b) and Kazanas et al. (2012) is particularly useful in this regard as they derive several MHD scaling laws and use them to describe how the ionisation, ionic column density and outflow velocity of their simulated MHD wind vary as a function of distance from the black hole (see Kazanas et al. 2012 for detailed discussion); Fig. 6.7 shows an excerpt of how these parameters vary in a fiducial Seyfert galaxy (left panel) and a BALQSO (right panel). A general property of their model is that the outflow velocity, column density and ionisation of the wind are inversely proportional to their launching radius, with the fastest, largest column, and most ionised winds being located closest to the black hole. The wind velocity is itself also sensitive to the total column density (Fig. 6.7, right hand panel), with larger column densities of material capable of achieving greater velocities. The dynamic range of their simulated MHD winds are qualitatively similar to those measured for the *Suzaku*-detected winds, while the model also naturally explains the observed trends of decreasing wind column density and ionisation with distance (see §5.6.2). This certainly suggests that the winds could have an magnetic origin, at least at

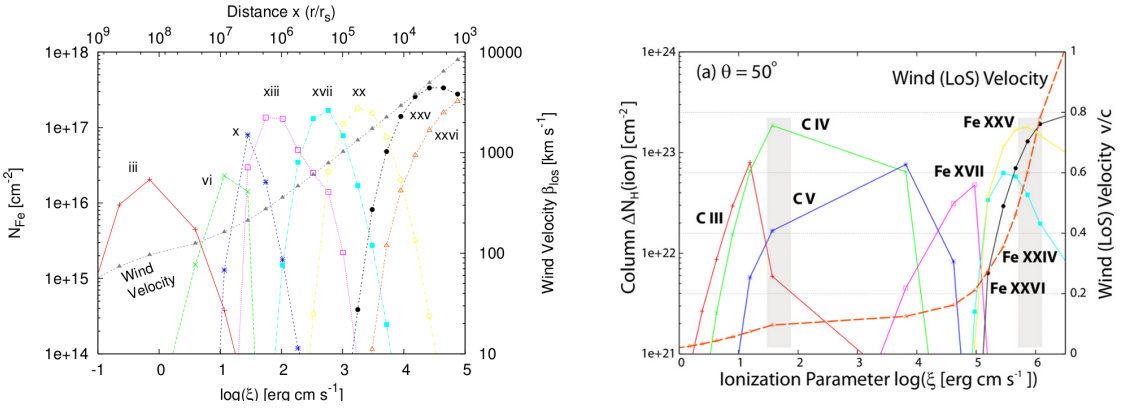


Figure 6.7: Plots showing the parameter space achieved with the Kazanas et al. (2012) MHD wind model. The left hand panel shows the wind parameters obtained for a typical Seyfert galaxy, while the right shows those obtained for a BALQSO. There is a significant overlap in the simulated MHD wind parameters and those found in the *Suzaku*-observed AGN. Both figures taken from Kazanas et al. (2012).

the qualitative level.

However, it should be noted that the Kazanas et al. wind model is a pure MHD system, which is an idealistic case which is unlikely to be realised in real sources. Indeed, because AGN are highly luminous objects a contribution from radiation pressure should generally be expected, even if the wind is primarily launched or accelerated via magnetic processes. Any attempts to understand winds around accreting objects will need to incorporate both radiative- and magnetic-driving mechanisms close to the black hole, which is by no means a simple task. A significant step in this direction has, nevertheless, been presented by Ohsuga et al. (2009); Ohsuga & Mineshige (2011) and Ohsuga (2012) (see also Proga 2003) who use radiation-magnetohydrodynamic (R-MHD) simulations to find unified inflow–outflow solutions for accretion discs close to a black hole. The Ohsuga et al. simulations — which are probably the most numerically sophisticated simulations of accretion disc-winds to date — showed that in the presence of a black hole an input toroidal reservoir of gas threaded with weak self-similar poloidal magnetic fields naturally forms a dynamic accretion disc, and that this accretion disc has both inflowing and

outflowing components. The simulations are performed in a computational domain of $\sim 100\, r_{\rm s}$ and consider continuum opacity from Thompson/Compton scattering, free-free absorption and bound-free absorption, as well as any associated general relativistic effects. In this sense, their simulations are directly applicable to the very innermost regions of an AGN where the material is likely to be very highly ionised and the effects of spectral line-driving can confidently be neglected.

One of the most fundamental outcomes of the Ohsuga et al. simulations is that outflows/winds are a ubiquitous feature despite their presence not being included *a priori* in their prescription of the accretion process. Furthermore, the simulated winds could be either radiatively or magnetically driven depending upon the input gas density (which influences the accretion rate, and hence the source luminosity). In general, Ohsuga et al. found that they could reproduce three distinct modes of accretion simply by adjusting the gas density in the initial toroidal gas reservoir. These modes are shown in Fig. 6.8. Unfortunately, the Ohsuga et al. R-MHD model does not provide any quantitative predictions with which to test the properties of the *Suzaku*-detected winds, but it is still interesting to compare the two qualitatively. The accretion modes are as follows:

1. **Model A**: At high initial input densities ($\rho = 10^{-2} - 10^{-1}\,{\rm g\,cm^{-3}}$) the mass accretion-rate through the disc exceeds the local Eddington rate of the disc yielding a disc which is optically-thick to continuum radiation; this traps photons inside the disc structure, causing it to puff up and become geometrically thick. The resultant disc is extremely luminous, with $L_{\rm disc} \gtrsim L_{\rm edd}$ from certain sight lines due to beaming effects associated with the optically-thick disc/wind geometry, and the strong radiation pressure launches highly-ionised winds with velocities of the order $v_{\rm out} \sim 0.25\,{\rm c}$. Because opacity due to line-driving is neglected in the simulation the radiatively driven wind is reminiscent of the momentum-driven winds proposed by King & Pounds (2003, see also Zubovas & King 2013). These authors argue that a powerful Compton-thick wind will be accelerated via scattering processes when the source approaches the Eddington limit, which is qualitatively similar to what is found by Ohsuga et al.'s simulations. This accretion mode also harbours a radiatively accelerated but magnetically collimated jet

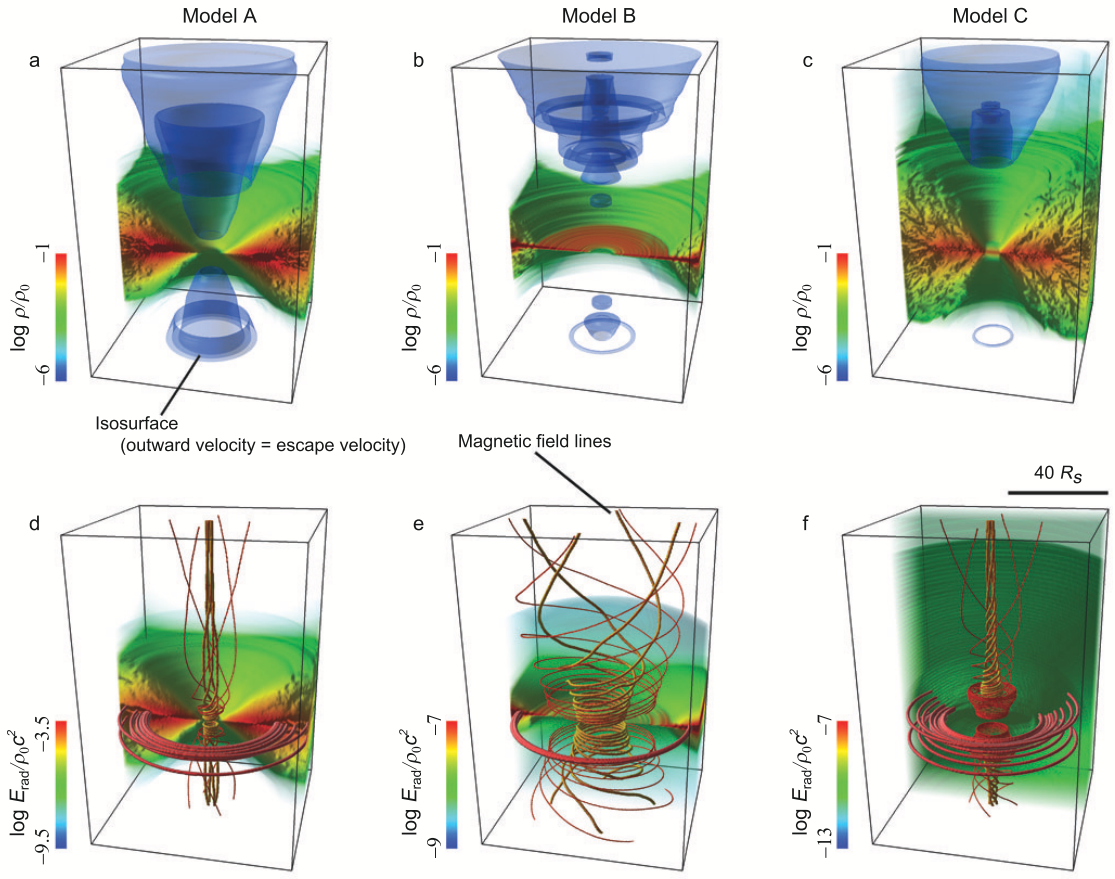


Figure 6.8: Plot showing the three radiation-magnetohydrodynamic accretion discs as simulated by Ohsuga & Mineshige (2011). Three different modes of accretion disc can be obtained by varying the density of the accreting gas, all of which are characterised by various forms of outflow. See text for further details. Figure taken from Ohsuga & Mineshige (2011).

which extends perpendicularly to the rotation axis.

2. **Model B**: At moderate input densities ($\rho = 10^{-5}\,\mathrm{g\,cm^{-3}}$), on the other hand, the accreting gas is able to cool efficiently by emitting radiation and it settles into a geometrically-thin (but still optically-thick) disc which is an analogue of the Shakura & Sunyaev (1973) standard disc. In this case, a relatively slow, rotating, and wide

opening angle wind with $v_{\rm out} \sim 0.01\,{\rm c}$ can be launched along the loosely twisted magnetic field lines in the system. Such a wind might explain the observed transverse velocities observed in NGC 4151 by Kraemer et al. (2005) and Crenshaw & Kraemer (2007), or the slower velocity systems observed with *Suzaku*.

3. **Model C**: Finally, at low densities ($\rho = 10^{-10}\,{\rm g\,cm^{-3}}$) a hot and geometrically thick, but optically-thin, radiatively inefficient accretion flow (RIAF) forms. In this case there is no wind, but there is a strongly magnetically collimated and accelerated jet.

From the Ohsuga et al. simulations it is clear that both radiation-pressure and magnetic forces are important when it comes to describing accretion disc–black hole systems, and that no single mechanism is likely to be universally responsible for the winds observed across the black hole mass spectrum. The strong UV winds observed in BALQSOs are almost certainly accelerated by resonant line-driving in the moderately-ionised gas; the wealth of both observational (e.g., Foltz et al. 1987; Weymann et al. 1991; Arav et al. 1995; Arav 1996; Laor & Brandt 2002, see also Chelouche & Netzer 2003) and theoretical (e.g., Proga & Kallman 2004; Proga 2005; Schurch, Done & Proga 2009; Sim et al. 2010, and references therein) evidence in favour of this acceleration mechanism is approaching saturation. However, the situation is evidently much less clear-cut for highly-ionised X-ray winds, with both radiative and magnetic processes appearing capable of providing the requisite driving. One possibility which is alluded to by the Ohsuga et al. simulations is that there is actually an interplay between radiation and magnetism, with radiation pressure/magnetism dominating at high/low accretion rates. One could therefore envision a scenario where the fastest winds were launched by continuum radiation pressure when the source had a high accretion rate, while the slower ones are magneto-centrifugal in nature and launched from lower accretion rate AGN. Indeed, this appears to be consistent with the main finding of this thesis: higher luminosity sources drive winds which contain a larger fraction of their Eddington-limited maximum values in terms of their mass outflow rate, kinetic power and outward momentum rate.

## 6.3 Energetic significance and feedback implications

In this thesis, I have shown that highly ionised Fe K winds are both frequently observed in AGN, and that they contain a large amount of mechanical energy. But a fundamental question still remains: is the energy imparted by the mass flow likely to play a role in terms of AGN–host-galaxy feedback scenarios? An informative qualitative diagnostic of energetic significance is to compare the total radiative output of the AGN to the mechanical output of the outflow.

Canonically, AGN feedback models have postulated that $\sim 5\%$ of an AGN's bolometric radiative output needs to be converted to mechanical power in order to have a notable effect on the growth of a central SMBH and the bulge of its host galaxy (e.g., Di Matteo, Springel & Hernquist 2005). However, recent numerical simulations have shown that should the effects of 'secondary' feedback such as cloud ablation be taken into account, the required energy is significantly lower, of the order $\sim 0.5\%$ of $L_{\rm bol}$ (e.g., Hopkins & Elvis 2010). Indeed, hydrodynamic simulations have shown that even relatively modest Fe K outflows (e.g., those with only $v_{\rm out} \sim 0.01\,{\rm c}$, $\dot{M}_{\rm out} \sim 0.01 M_{\odot}$ yr$^{-1}$ and $L_{\rm kin} \sim 10^{44}\,{\rm erg\,s^{-1}}$; see Wagner, Umemura & Bicknell 2013) can impart significant feedback upon the host galaxy on ∼kpc scales should these effects be taken into account. Investigating what fraction of an AGNs' bolometric output is also conveyed through mechanical power therefore provides a means of qualitatively assessing the likely energetic significance of the mass flow. A plot of $L_{\rm bol} - (L_{\rm kin}/L_{\rm bol})$ to this effect is shown in Fig. 6.9a.

It is clear that a large fraction of the outflows have a kinetic luminosity in excess of 0.5% of $L_{\rm bol}$, with 7/20 also exceeding the 5% limit as well. The geometric mean is $\langle L_{\rm kin}/L_{\rm bol}\rangle = 1.05 \times 10^{-2} \approx 1\%$ (or $\approx 1.5\%$ with NGC 4395 excluded). In this context, it is important to also remember that the Fe K outflows considered here are probably just one component of a much larger scale outflow which is spectroscopically identifiable across multiple wave-bands (e.g., at UV and optical wavelengths as well). Therefore, even in those AGN where the Fe K outflow itself is unlikely to provide the necessary energy to be energetically significant in terms of feedback, the seemingly crucial 0.5%

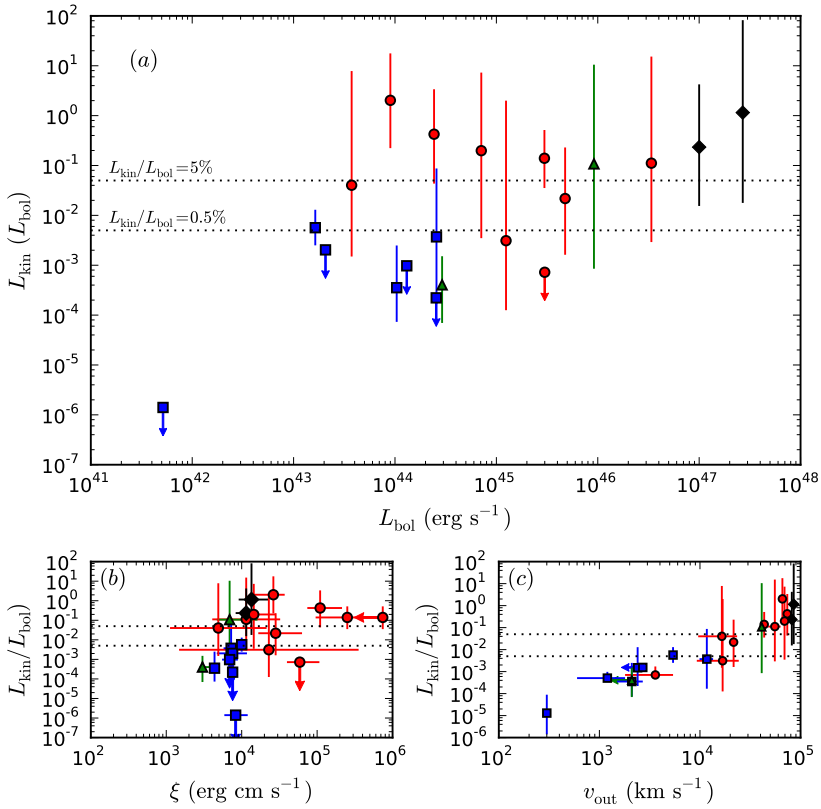


Figure 6.9: Plots comparing ($L_{\rm kin}/L_{\rm bol}$) of the detected Fe K outflows to (a) $L_{\rm bol}$ of each AGN, (b) $\log(\xi/{\rm erg\,cm\,s^{-1}})$ of each outflow and (c) their outflow velocity. The horizontal lines in each plot correspond to $L_{\rm kin}/L_{\rm bol}$ fractions of 0.5% and 5%. The plotted points again correspond to Fe XXV He$\alpha$ (green triangles), Fe XXVI Ly$\alpha$ (red circles), Fe XXV–XXVI pair (blue squares) and blended (black diamonds) absorption line systems, respectively. A significant fraction of the Fe XXVI Ly$\alpha$ absorption systems have kinetic powers in excess of 0.5% of $L_{\rm bol}$ by virtue of their high outflow velocities, which suggests that they are likely to be significant in terms of AGN-host galaxy feedback scenarios. In contrast, the lower ionisation Fe XXV He$\alpha$ and Fe XXVI Ly$\alpha$ pair systems tend to be below the 0.5% threshold.

threshold could still be exceeded if the kinetic power is integrated across all of the outflowing components (e.g., Crenshaw & Kraemer 2012). The $L_{\rm kin}/L_{\rm bol}$ fractions noted in Fig. 6.9 can therefore be taken as *lower limits* on the global outflow energetics in these AGN. Importantly, these estimates are derived solely from the wind kinematics and are

therefore independent of the initial driving mechanism.

There is an interesting trend in the distribution of $L_{\rm kin}/L_{\rm bol}$ values across the sample, with the Fe XXVI Ly$\alpha$ outflows typically having a larger $L_{\rm kin}/L_{\rm bol}$ fraction than their lower ionisation counterparts. Eight of the nine Fe XXVI Ly$\alpha$ outflows (red circles) have kinetic powers which are consistent with exceeding $\sim 5\%$ of $L_{\rm bol}$ at the 90% level, while those absorbers which comprise both Fe XXV He$\alpha$ and Fe XXVI Ly$\alpha$ absorption lines at a common velocity shift (blue squares) only tend to be $\lesssim 0.5\%$ of $L_{\rm bol}$. This trend is quantified when the geometric means of the two populations are considered; the Fe XXVI Ly$\alpha$-only absorbers have $\langle L_{\rm kin}/L_{\rm bol}\rangle_{{\rm Ly}\alpha} = 5.58 \times 10^{-2} \simeq 5\%$, while those that have a contribution from Fe XXV He$\alpha$ have $\langle L_{\rm kin}/L_{\rm bol}\rangle_{{\rm He}\alpha} = 8.37 \times 10^{-4} \simeq 0.08\%$ (or $\approx 0.1\%$ without NGC 4395). A comparison of $\xi - (L_{\rm kin}/L_{\rm bol})$ shown in Fig. 6.9b makes this even more apparent, with the Fe XXVI Ly$\alpha$ outflows occupying the upper right quadrant of the plot indicating that the highest ionisation outflows are the most energetic. The fundamental driver underlying this trend is the higher ionisation absorbers having larger outflow velocities, as is evidenced in Fig. 6.9c.

## 6.4 Relation to $M_{\rm BH} - \sigma_*$ in quiescent galaxies

To conclude this chapter it is propitious to highlight the recent work presented by McQuillin & McLaughlin (2013, in press) who have inferred the distribution of outflow velocities required to lock a sample of 51 'normal' (i.e., non-active) galaxies onto the observed $M_{\rm BH} - \sigma_*$ relation. The authors consider the case of self-regulated energy-driven feedback. Note that there is an important distinction to be made between *momentum*-driven outflows, as I have considered throughout this thesis thus far, and the *energy*-driven outflows which are considered by McQuillin & McLaughlin (see also King 2010 and references therein). The difference is related to the rate of cooling and energy injection in the swept-up shell of gas: momentum-driven flows are able to cool efficiently, are therefore geometrically thin, and require a continuous injection of momentum to be pushed outwards (e.g., Fabian 1999; King & Pounds 2003; McQuillin & McLaughlin 2012),

as per the case that I considered in §6.2.2. Conversely, *energy*-driven flows are unable to cool efficiently, leading to a geometrically thick shell that is pushed outwards by thermal pressure exerted by the hot gas (King 2010). Momentum-driven shells are Compton cooled which means that an initially momentum-driven shell of gas will transition to an energy-driven phase when the rate of incident X-ray photons is no longer sufficient to enable efficient cooling; this can occur on distances of the order $\simeq 10\,{\rm pc}$ from the SMBH for a fiducial $M_{\rm BH}=10^8 M_\odot$ black hole with a $v_{\rm out}\sim 0.03\,{\rm c}$ wind (McQuillin & McLaughlin 2013).

Generally, and as has been shown in the literature (e.g., Silk & Rees 1998; King 2005, 2010; Zubovas & King 2012a), an energy-driven flow is expected to yield an $M_{\rm BH}-\sigma_*$ relation of the form $M_{\rm BH}\propto\sigma_*^5$. McQuillin & McLaughlin build upon these results. Assuming that $\tau=1$ and the gas-to-dark matter mass fraction is $\sim 0.2$, they derive an $M_{\rm BH}-\sigma_*$ relation for an energy-driven flow of the form:

$$\left(\frac{M_{\rm BH}}{10^8 M_\odot}\right)\left(\frac{v_{\rm out}}{c}\right)=6.68\times10^{-2}\left(\frac{\sigma_*}{200\,{\rm km\,s^{-1}}}\right)^5, \tag{6.6}$$

i.e., the velocity of the initial wind, $v_{\rm out}$, is also important, such that $M_{\rm BH}v_{\rm out}\propto\sigma_*^5$. Using the above equation [their eq. (15)] the authors go on to estimate the outflow velocities which would be needed to match a sample of 51 quiescent galaxies taken from Gültekin et al. (2009) onto the observed $M_{\rm BH}-\sigma_*$ relation, and compared them to the distributions measured in local AGN with *XMM-Newton* Tombesi et al. (2010a) and *Suzaku* (chapters 4 and 5).

Fig. 6.10 compares the distribution of velocities, as inferred by McQuillin & McLaughlin (2013), to that which I have found for the *Suzaku*-detected Fe K outflows. As noted by the authors, there is a startling resemblance between the two, with both samples tracing a similar overall distribution. Their overall range (i.e., their maxima) are similar, as is their median: $v_{\rm out}\sim 0.035\,{\rm c}$ in the quiescent galaxies, and $\sim 0.056\,{\rm c}$ for the *Suzaku*-detected outflows. Formally, the two distributions cannot be distinguished: a Kolmogorov-Smirnov (KS) test only rules their being from the same parent population at $\sim 75\%$ confidence.

The fact that there are similarities between the inferred and measured $v_{\rm out}$ distri-

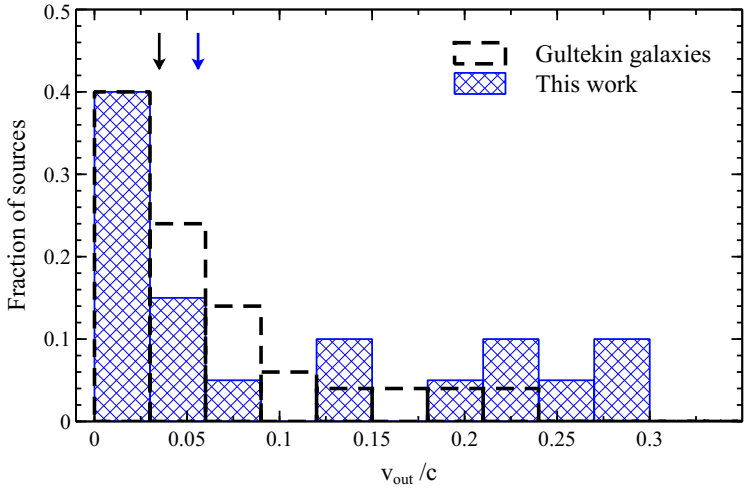


Figure 6.10: Histogram comparing the *Suzaku*-observed distribution of outflow velocities (blue cross-hatched area) to those inferred from local quiescent galaxies by McQuillin & McLaughlin (2013) who assume that their observed $M_{\rm BH} - \sigma_*$ relation (c.f., Gültekin et al. 2009) is induced by energy-driven feedback (black dashed line). The blue and black arrows correspond to the median outflow velocities of $v_{\rm out} \sim 0.056\,{\rm c}$ and $v_{\rm out} \sim 0.035\,{\rm c}$ in the AGN and quiescent sub-samples, respectively. Overall, there are some intriguing similarities between the two distributions, particularly at the low-velocity end, despite their being drawn from completely independent sub-samples of galaxy. The two samples are formally indistinguishable by the Kolmogorov-Smirnov (KS) test. See text for further details.

butions at all is in itself extremely interesting, if only because the quiescent and AGN samples are entirely independent and drawn from two different sub-populations of galaxy. Overall, the work of McQuillin & McLaughlin (2013) is extremely encouraging for the general notion that high-velocity outflows — which, on the basis of my work and that of Tombesi et al. (2010a), are becoming established as routinely present in local AGN — contribute to the feedback which is invoked to explain the $M_{\rm BH} - \sigma_*$ relationship in local quiescent galaxies, and, more importantly, for the idea that AGN play a key role in galaxy formation and evolution.

# 7 Conclusions and future work

## 7.1 Overall conclusions

In this thesis I have presented two bodies of independent work. chapter 3 encapsulates my work on the radio-quiet quasar MR 2251−178, and outlines a deep and systematic analysis of the warm absorber using data from an extensive observing campaign with the *Suzaku*, *XMM-Newton* and *Chandra* observatories; this chapter is relatively self-contained with a summary of results presented in §3.7 and, as such, I will not repeat them here. The remaining chapters (4 – 6) are concerned with the *Suzaku* outflow sample. The main results of this study are listed below.

### 7.1.1 Line detection and absorber properties

In chapter 4 I described the creation and primary analysis of the *Suzaku* outflow sample.

- Highly-ionised Fe XXV He$\alpha$ and / or Fe XXVI Ly$\alpha$ absorption lines are robustly detected ($P_{\rm MC} \geq 99\%$) in 20/51 of the AGN in the sample, corresponding to a $\approx 40\%$ detection fraction. Visually, most of the outflows are either: (1) an Fe XXV He$\alpha$ *and* Fe XXVI Ly$\alpha$ pair at a common velocity shift, or (2) an isolated Fe XXVI Ly$\alpha$ line. These make up 7/20 and 9/20 of the line detections, respectively, with the rest being either just an Fe XXV He$\alpha$ line (2/20) or an un-resolved blend of the two (2/20). A key feature of this analysis is that several of the absorption systems yield multiple *Suzaku* detections in different epochs, with them often showing signs of inter-observation variability which is most plausibly explained through subtle changes in properties of a photo-ionised absorber (see below).

- Modelling the absorbers with XSTAR revealed the gas to by typified by column densities and ionisation parameters which ranged between $21.5 <$

$\log(N_{\rm H}/{\rm cm}^{-2}) \leq 24$ and $2.5 < \log(\xi/{\rm erg\,cm\,s}^{-1}) \leq 6$, with means of $\log(N_{\rm H}/{\rm cm}^{-2}) \approx 23$ and $\log(\xi/{\rm erg\,cm\,s}^{-1}) \approx 4.5$, respectively. The distribution of outflow velocities covers a continuous range from $v_{\rm out} < 1,500\,{\rm km\,s}^{-1}$ up to $v_{\rm out} \sim 100,000\,{\rm km\,s}^{-1}$, with a median velocity of the order $\sim 0.056\,{\rm c}$. Most of the Fe XXVI Ly$\alpha$-only absorption systems have $v_{\rm out} \geq 10,000\,{\rm km\,s}^{-1}$ and therefore constitute 'Ultra-Fast Outflows' (UFOs; Tombesi et al. 2010a), while the lines which have a contribution from Fe XXV He$\alpha$ as well (i.e., line-pairs or solitary lines) are systematically slower. This can be interpreted in the context of a stratified disc-wind (see Tombesi et al. 2013) , where the Fe XXVI Ly$\alpha$-only systems originate in the inner portion of the flow while the slower systems bridge the gap between the disc-wind and the canonical warm absorber. These properties are, on the whole, consistent with the framework established for Fe K absorption by Tombesi et al. (2012a, 2011b) using *XMM-Newton*.

### 7.1.2 Outflow parameters and correlation analyses

In chapter 5 I used several simple geometric relations in conjunction with the physical properties of the *Suzaku*-detected Fe K winds to probe the wind energetics.

- On average, the winds appear to be located $\langle r \rangle \sim 10^{2-4}\,r_{\rm s}$ ($\leq 0.1\,{\rm pc}$) from the central source, have mean mass outflow rates of $\langle \dot{M}_{\rm out} \rangle \sim 0.01 - 1 M_{\odot}\,{\rm yr}^{-1}$, and mean kinetic luminosities of $\langle L_{\rm kin} \rangle \sim 10^{42-44}\,{\rm erg\,s}^{-1}$. It also became apparent that 5 of the 20 winds are observed at a radius inside the escape radius for their observed velocity (i.e., $v_{\rm out} < v_{\rm esc}$). This suggests that they are unlikely to escape the system. In general, these parameters are entirely consistent with those reported by Tombesi et al. (2010a) for the *XMM-Newton*-detected Fe K winds, and they strongly imply a direct origin with the accretion disc.

- Using these inferred quantities I then investigated how the wind parameters vary with both their distance from the source of ionising continuum, and with Eddington ratio ($\lambda$) of their host AGN. While the limited dynamic range of the

data in terms of $r$ meant that I was unable to corroborate recent claims that $v_{\rm out}$, $L_{\rm kin}$ and $\dot{p}_{\rm out}$ decrease with distance (see Tombesi et al. 2013), the data do confirm that higher ionisation and larger column density outflows are indeed observed closer to the black hole at the $> 99.9\%$ confidence level (Tombesi et al. 2013), which is consistent with the idea of a stratified wind.

- The strongest result in this chapter is that the wind parameters are correlated with $\lambda$. The normalised $\dot{M}_{\rm out}$ and $\dot{p}_{\rm out}$ quantities in particular are both positively correlated with $\lambda$ at the $\gtrsim 95\%$ confidence level. $L_{\rm kin}$ could also be positively correlated as well, although such a relation is only required at the $\sim 90\%$ confidence level in the current data. Overall, the correlations with $\lambda$ mean that more powerful AGN (higher $\lambda$) have Fe K winds with parameters which are a larger fraction of their theoretical maximum Eddington-limited quantities. This, in itself, suggests that the winds may be accelerated by radiation pressure, as has been suggested in the literature many times (e.g., Arav, Li & Begelman 1994; Murray & Chiang 1995; Proga, Stone & Kallman 2000; Proga & Kallman 2004; Sim et al. 2008, 2010).

### 7.1.3 Potential driving mechanisms

In the first half of chapter 6 I discussed the likely acceleration / launching mechanisms for the observed outflows. By comparing the wind properties to models and simulations available in the literature it is clear that they could feasibly be accelerated via either radiation pressure or magnetic pressure.

- In favour of radiative acceleration I showed that the highest velocity winds (i.e., $v_{\rm out} \gtrsim 10,000\,{\rm km\,s^{-1}}$) have an outward momentum-rate which is directly proportional to that of the radiation field. This is consistent with acceleration by electron scattering, as per the continuum-driving scenario developed by King & Pounds (2003) and King (2005, 2010). I also showed that the slower winds could be continuum-driven as well provided the photons couple less efficiently with the

gas, or they could simply represent the X-ray phase of a failed line-driven wind in the UV (e.g., Proga 2005). I argued that the latter scenario could be a likely explanation for the outflows with $v_{\rm out} < v_{\rm esc}$.

- However, it was also apparent that the dynamic range of the outflows, along with the trends of decreasing column density and ionisation parameter with distance from the black hole, were qualitatively consistent with the recent MHD wind model presented by Fukumura et al. (2010a) and Kazanas et al. (2012). Therefore, while radiation pressure does appear to be a favourable explanation for the observed flows, a magnetic origin cannot be ruled out on the basis of the current data.

- If the winds *are* accelerated by continuum-driving I argued that the terminal velocity of the wind should then be proportional to the accretion efficiency of the black hole, i.e., $v_{\rm out}/c \propto \eta$. Hence, I raised the interesting possibility of indirectly studying black hole spin through the outflow velocity of highly-ionised winds which emanate from the inner regions of the disc.

### 7.1.4 Significance for AGN–host-galaxy feedback

In the latter half of chapter 6 I showed that the Fe K outflows are likely to be energetically significant, and that their measured distribution of velocities is similar to one inferred from local quiescent galaxies via the $M_{\rm BH} - \sigma_*$ relation.

- By comparing the wind kinetic power ($L_{\rm kin}$) to the bolometric luminosity ($L_{\rm bol}$) of their host AGN I showed that 8 of the 9 fast Fe XXVI Ly$\alpha$ outflows exceeded the conservative $L_{\rm kin} > 5\%\, L_{\rm bol}$ threshold (Di Matteo, Springel & Hernquist 2005) required for feedback, while those slower outflows with a Fe XXV He$\alpha$ contribution are noticeably less significant due to their lower velocities. This suggests that the fastest UFO-type winds may be directly significant in terms of feedback, although I note that the slower flows may still contribute to feedback if their

total kinetic power is integrated over all outflowing components in all wave-bands. Ultimately, these relationships imply that the mechanical energy imparted by Fe K winds may be capable inducing significant feedback on galaxy-wide scales.

- I compared my results to the recent work of McQuillin & McLaughlin (2013) who, in the framework of an energy-driven feedback model, have inferred the distribution of outflow velocities required to lock a sample of quiescent galaxies onto their observed $M_{\rm BH} - \sigma_*$ relation. I showed that their inferred velocity distribution is remarkably similar to the one obtained for the *Suzaku*-observed outflows, with their covering a similar range and sharing a similar median velocity. I argued that these similarities imply that outflows in AGN may be an underlying cause of the observed $M_{\rm BH} - \sigma_*$ relation, and that it hence offers compelling support for the idea that winds may play an important role in shaping how galaxies grow and evolve.

## 7.2 The way forward...

### 7.2.1 Disc-wind models

X-ray observations of AGN remain the best way to learn about the complex physical processes which occur in the innermost regions of accretion flows around black holes. However, what can be learnt about the underlying physical system is limited by the sophistication of the applied models. The current generic approach for studying absorption in AGN is to measure the properties of individual absorption lines using Gaussian fitting before attempting to deduce the ionisation / density structure of the absorber using a phenomenological model constructed from photo-ionisation codes such as XSTAR. However, in addition to implicitly adopting a simplifying assumption that the absorbing gas is a spherically symmetric, continuous, homogeneous, and isotropic flow at constant velocity, this approach does not take into account the full physics of the system. A

significant caveat associated with the XSTAR code, for instance, is that it does not calculate the effects of Compton-scattering in the flow and is thus not appropriate at Compton-thick column densities (Miller & Turner 2013).

In light of these limitations Sim et al. (2008, 2010) have developed a Monte Carlo code for calculating Compton-thick disc-wind spectra. The Monte Carlo simulations include the effects of scattering and reflection and, through a detailed 3-D radiative transfer treatment, predict that winds may play a strong role in shaping the emergent X-ray spectrum in AGN. A particularly interesting outcome is that the wind itself can give rise to Fe K emission, with line widths of the order FWHM $\sim 1$ keV. As the line is formed by the wind it is broadened by a combination of both the velocity-shear in the flow and the down-scattering of Fe K$\alpha$ line photons but, since the launch radius of the wind is assumed to be of the order a few tens of $r_{\rm s}$ (see Sim et al. 2008, 2010), no relativistic blurring is required. A follow-up study by Tatum et al. (2012) (see also Turner, Miller & Tatum 2012) has shown that the broad Fe K$\alpha$ profile in several seemingly 'bare' (i.e., un-absorbed) Seyfert galaxies can be fitted as the scattered emission from a Compton-thick wind and hence raises the possibility of studying winds indirectly through their scattered spectra.

Despite the complexity and sophistication of the model it is now possible to generate disc-wind models which can be applied to spectra within XSPEC. These models need to be generated from simulations specific to the spectral properties of a given object, and are currently only geared towards fitting the Fe K band rather than full broad-band spectra. Even so, Sim et al. (2008) and Sim et al. (2010) have successfully applied the disc-wind model to case studies of Mrk 766 and PG 1211-143 (see Fig. 7.1), respectively. In the case of PG 1211+143, they found that a single Compton-thick wind with $\dot{M}_{\rm out} \sim 0.53 M_{\odot}$ yr$^{-1}$ was capable of simultaneously describing both the broad Fe K$\alpha$ emission complex and the highly-ionised Fe XXV He$\alpha$ absorption line.

More recently, the model has been adapted for fitting PDS 456 which is the archetype for an extreme wind. Fig. 7.2 shows that the model is able to replicate the fast $v_{\rm out} \sim 0.25$ c outflow which is present in the 2011 *Suzaku* spectrum quite well, requiring $\dot{M}_{\rm out} \sim \dot{M}_{\rm edd}$ ($\approx 50 M_{\odot}$ yr$^{-1}$) and an inclination angle of $\sim 25^{\circ}$. A partial-covering

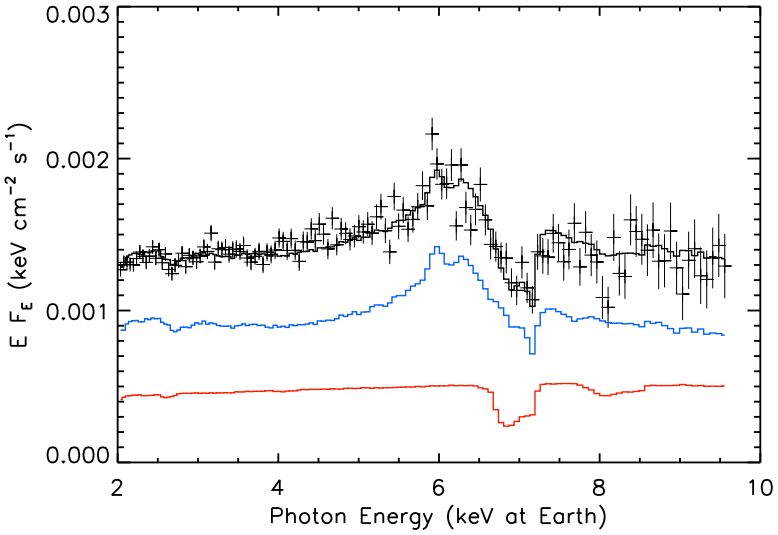


Figure 7.1: The wind model of Sim et al. (2010) applied to the PG 1211+143 data of Pounds & Reeves (2009).The data and model are shown in black, while the red and blue lines show the contribution from the direct and scattered / reprocessed emission, respectively. Figure taken from Sim et al. (2010).

component is still required to fit the soft X-ray absorber in this case, but the Fe K band is fitted solely by the disc-wind model. Notably, the disc-wind is able to replicate both the absorption profile, and its asymmetric extent. These results suggest that winds may play a significant role in shaping the emergent X-ray spectrum, with the re-processing of incident X-ray photons potentially giving rise to both broad Fe K$\alpha$ profiles and highly-ionised absorption lines in a self-consistent way. While the model is still actively being developed the early results are certainly promising.

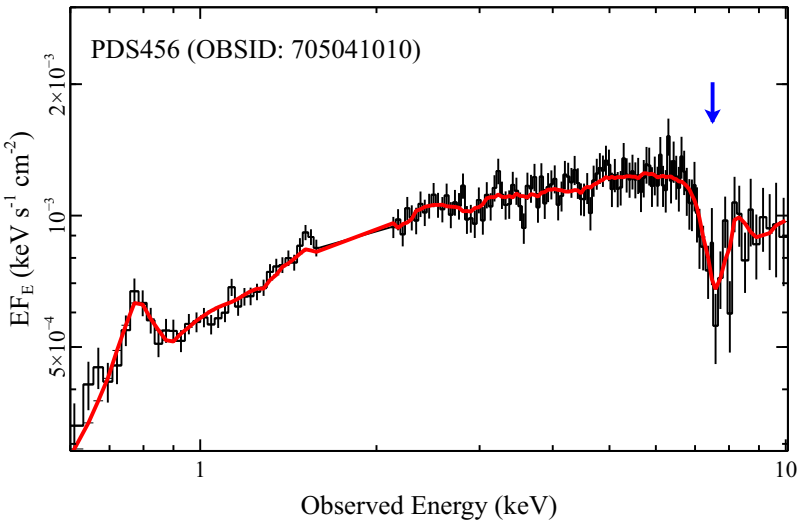


Figure 7.2: The Sim et al. (2010) wind model applied to the PDS 456 *Suzaku* observation (OBSID: 705041010). The data and model are shown in black and red, respectively, while the blue arrow highlights the position of the absorption trough. It is clear that the model is able to replicate both the absorption trough between $7-8$ keV (observed frame) and the asymmetric spectral complexity which surrounds the profile.

### 7.2.2 Future observatories

#### *Astro-H*

The *Astro-H* orbital X-ray telescope is the direct successor to *Suzaku*, and is the 6$^{\rm th}$ Japanese-led X-ray observatory mission. It is an international mission which, whilst headed by JAXA, is also developed in collaboration with both the NASA/GSFC and ESA. In terms of in-orbit operation, *Astro-H* will be similar to *Suzaku* in many respects. For instance, the spacecraft is intended to occupy a circular orbit with an altitude of $\sim 550$ km, and have a pointing of $\sim 30^{\circ}$ with respect to the equator. However, the scientific payload aboard *Astro-H* will represent significant improvements over *Suzaku* in every respect. It will offer a combination of wide-band X-ray spectroscopy and imaging ($E \sim 0.4-80$ keV) via both soft and hard X-ray imaging telescopes (SXI and HXI,

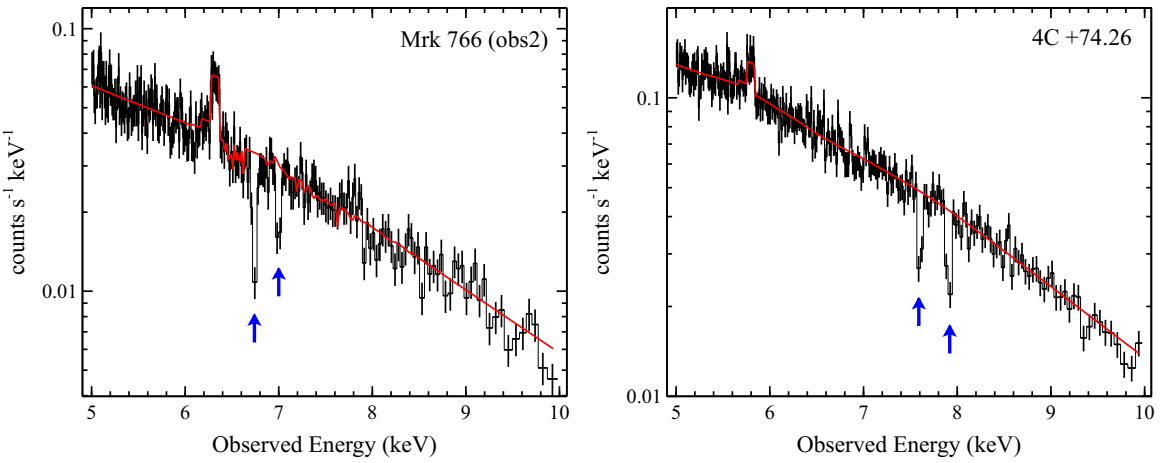


Figure 7.3: Simulations of how the *Suzaku*-detected absorption lines in Mrk 766 (OBSID: 701035020) and 4C +74+26 (OBSID: 702057010) would look with the *Astro-H* SXS micro-calorimeter. Both spectra were simulated from the best-fit continuum model for the *Suzaku* observation (red line, see Appendix B), with the absorption line parameters taken from Table 4.3. The $\Delta E = 4$ eV energy resolution is easily able to separate the individual absorption components, and resolve the degenerate line identification in 4C +74.26. See text for further details.

respectively), and high energy-resolution X-ray spectroscopy ($E \sim 0.3 - 12$ keV) via an X-ray micro-calorimeter array known as the Soft X-ray Spectrometer (SXS). These X-ray detectors are also joined by a Soft $\gamma$-ray detector (SGD), which extends the energy sensitivity of *Astro-H* up to $\sim 600$ keV. The simultaneous broad bandpass, coupled with the high spectral resolution offered in the Fe K-band by the SXS will represent a crucial improvement to all branches of X-ray astronomy.

This is especially true for the study of winds which are manifest in the Fe K band, an energy range where the spectral resolution and effective area of traditional CCD-based detectors begins to degrade. The SXS will offer an effective area of $\sim 225$ cm$^2$ at 6 keV and, more importantly, an unprecedented minimum (goal) FWHM spectral resolutions of $\Delta E \sim 7$ eV ($\Delta E \sim 4$ eV) in the $E \sim 0.3 - 12.0$ keV energy interval. In Fig. 7.3 I

simulated two SXS observations of the Fe K winds in Mrk 766 (OBSID: 701035020) and 4C +74.26 (OBSID: 702057010). Both simulations are for a 100 ks SXS observation, assume the goal FWHM resolution of $\Delta E \sim 4$ eV, and are generated from the best-fitting continuum model reported in Appendix B using the Fe K absorber parameters listed in Table 4.4. It is clear that the wind in both absorbers is resolved into its constituent Fe XXV He$\alpha$ and Fe XXVI Ly$\alpha$ components; this is particularly interesting for 4C +74.26 because the *Suzaku* XIS was unable to distinguish between the two components leading to a degenerate line identification (see §4.5.1).

In general, the SXS will be able to resolve Fe K absorption lines to within a FWHM velocity broadening of $\sim 300\,\mathrm{km\,s^{-1}}$, with errors of the order $\pm 10\%$. This, in turn, will then allow much tighter constraints on both the column density and the ionisation parameter to be obtained, as well as improving measurements of line $EWs$ by a factor of $\sim 5$, while errors on the outflow velocity $v_{\rm out}$ could plausibly be reduced by a factor of $\sim 10$. These improved constraints, in addition to the possibility of detailed time-resolved spectroscopy of the absorption line profiles themselves, will allow deeper diagnostics of both the properties of the wind material and its subsequent energetics to be performed, which is key to furthering our understanding of how the winds interact with their host galaxies. *Astro-H* is currently set to be launched in the $\sim 2015$ fiscal year.

### ATHENA+

*ATHENA+*, or Advanced Telescope for High ENergy Astrophysics+, is an X-ray observatory which is to be proposed as a large mission for the ESA science program with an intended launch in $\sim 2028$. In its current iteration the satellite is planned to house a single X-ray telescope and a payload of two interchangeable scientific instruments in the focal plane. These are (1) the Wide Field Imager (WFI), a solid-state spectrometer with a large $40'$ FOV which operates between $\sim 0.1 - 15$ keV, and (2) the X-ray Integral Field Unit (X-IFU), a micro-calorimeter which has a very high effective area ($\simeq 0.65\,\mathrm{m^2}$ at 6 keV) coupled with a minimum (goal) energy resolution of FWHM $\simeq 2.5$ eV ($\simeq 1.5$ eV) from $\sim 0.1$ keV through to $\sim 12 - 13$ keV. This unprecedented sensitivity, which would be of

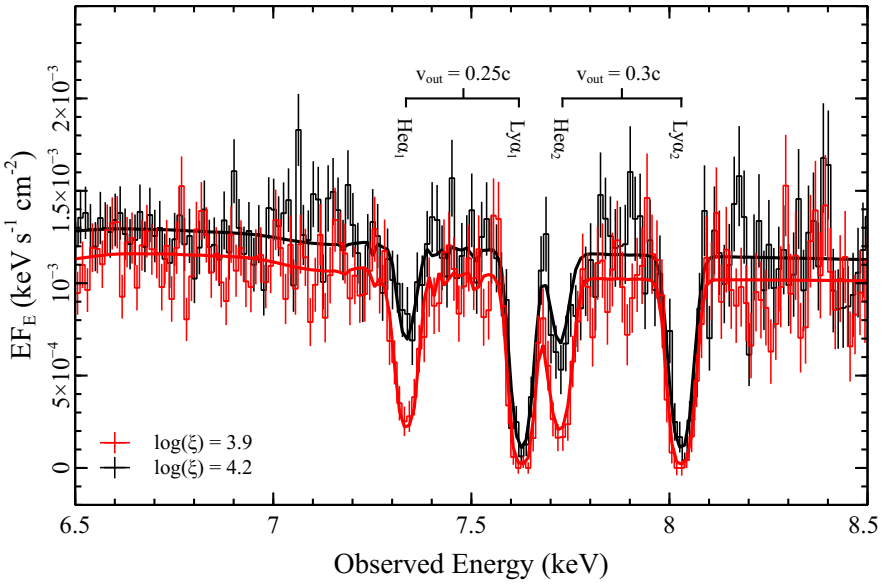


Figure 7.4: Simulation of how the *Suzaku* spectra of PDS 456 will look in a 100 ks *ATHENA+* X-IFU observation. The black and red spectra correspond to the 2007 (OBSID: 701056010) and 2011 (OBSID: 705041010) observations, respectively, while the black and red solid lines show the best-fitting spectral models to the two datasets. The spectra were simulated from the best-fit continuum model found for the *Suzaku* spectra, as listed in Appendix B, with the absorption line parameters noted in Table 4.3. The simulation was assuming an X-IFU energy resolution of $\Delta E = 2.5$ eV, which corresponds to the minimum specification of the instrument. The mission goal of $\Delta E = 1.5$ eV will yield even more precise results. These simulated spectra were made available courtesy of J. Reeves and V. Braito on behalf of the *ATHENA+* co-ordination group.

the order $3-5$ times greater than can be achieved with *Astro-H*, would represent a huge improvement for high resolution X-ray spectroscopy in the Fe K band, and revolutionise the way in which Fe K winds could be studied.

If *ATHENA+* is selected by ESA and performs to specification the X-IFU in particular will make it possible to study individual line profiles in detail, and to directly measure their velocity broadening down to as low as $\sim 50-100\,\mathrm{km\,s^{-1}}$ at $\sim 6$ keV. The $\Delta E \sim 1.5$ keV spectral resolution at Fe K will make the fine structure components

of the iron lines discernible (e.g., the Fe K$\alpha_1$ and Fe K$\alpha_2$ doublet) and, furthermore, potentially resolve the intricate atomic structure around the Fe K edge (Kallman et al. 2004), which will be a crucial test for reflection and partial-covering continuum models. The combination of large effective area and high spectral resolution means that detailed spectroscopy will be able to be performed on even relatively faint, or extreme objects. For example, the X-IFU will be able to resolve the multi-phase and blended (at CCD resolution) absorber in PDS 456 (c.f., §4.7.2; Reeves, O'Brien & Ward 2003; Reeves et al. 2009) into its constituent lines (see Fig. 7.4), whilst also allow for a sensitive time-resolved analysis of the absorber's ionisation state. This latter diagnostic is an important diagnostic for the gas density, and hence its location, which is one of the key parameters when it comes to discerning their energetic output (see §5.2.1). If it is selected by the ESA Cosmic Visions program *ATHENA+* would be the next big advancement in X-ray astronomy after *Astro-H*.

## 7.3 Final remarks

Arguably one of the most important results from this work is the frequency with which Fe XXV He$\alpha$ and/or Fe XXVI Ly$\alpha$ absorption lines have been detected in the AGN sample. The detection fraction of $\approx 40\%$ is not only consistent with previous studies of Fe K winds (e.g., Tombesi et al. 2010a), but it is also similar to the fraction of AGN in the local universe which have warm absorbers (Reynolds 1997; Crenshaw, Kraemer & George 2003b; Blustin et al. 2005; McKernan, Yaqoob & Reynolds 2007; Turner et al. 2009). This, coupled with the recent finding that similar highly-ionised outflows are frequently observed in BHXBs as well (Ponti et al. 2012), observationally affirms the theoretical expectation that winds may be a common — and possibly even ubiquitous — property of accreting black holes.

Ultimately, however, this work is just a small step on the road to understanding AGN winds and the role they may play in shaping their host galaxies. The impending launch of micro-calorimeters aboard *Astro-H* in $\sim$ 2015, and hopefully also *ATHENA+* in

2028, should usher in a new era of unprecedented high precision dynamical studies in the Fe K band. Such future studies will be crucial if we are to fully understand the complex interplay between accretion and outflow processes in AGN, and for firmly establishing whether AGN winds are as important to galactic evolution as recent results suggest.

# A Supplementary figures

## A.1 Ratio and contour plots 1: narrow Fe K$\alpha$ line

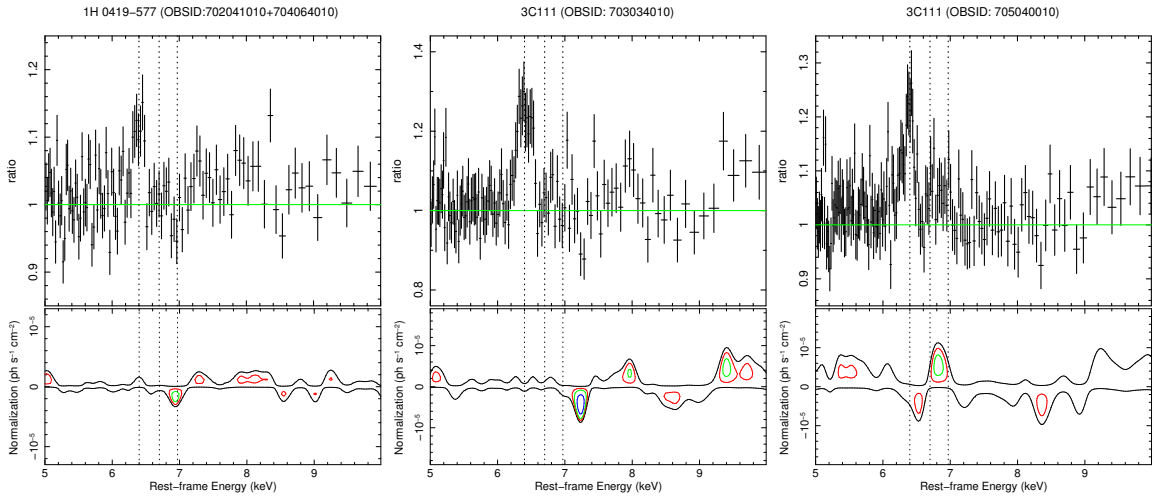


Figure A.1: Ratio and contour plots for sources which do not require a broadened component in the Fe K band. In each plot the data/model residuals (top panel) show the residuals which remain in the Fe K band when all atomic lines have been removed and the reflection component is fitted with `pexrav` to highlight the presence of the neutral Fe K$\alpha$/K$\beta$ fluorescence lines. The contour plot (bottom panel) show the F-test significances of the remaining residuals when the Fe K$\alpha$ and K$\beta$ lines are fitted with `reflionx` and a narrow Gaussian line. The continuous outer contour corresponds to a $\Delta\chi^2 = +0.5$ worse fit and is intended to indicate the level of the continuum baseline. The closed coloured contours correspond to $\Delta\chi^2$ improvements of $-2.3$ (red), $-4.61$ (green), $-9.21$ (blue), $-14.52$ (cyan) and $-18.42$ (magenta), which translate to F-test significances of 68%, 90%, 99%, 99.9% and 99.99%, respectively. The dashed vertial lines indicate the expected rest-frame energies of the Fe K$\alpha$, Fe XXV He$\alpha$ and Fe XXVI Ly$\alpha$ transitions.

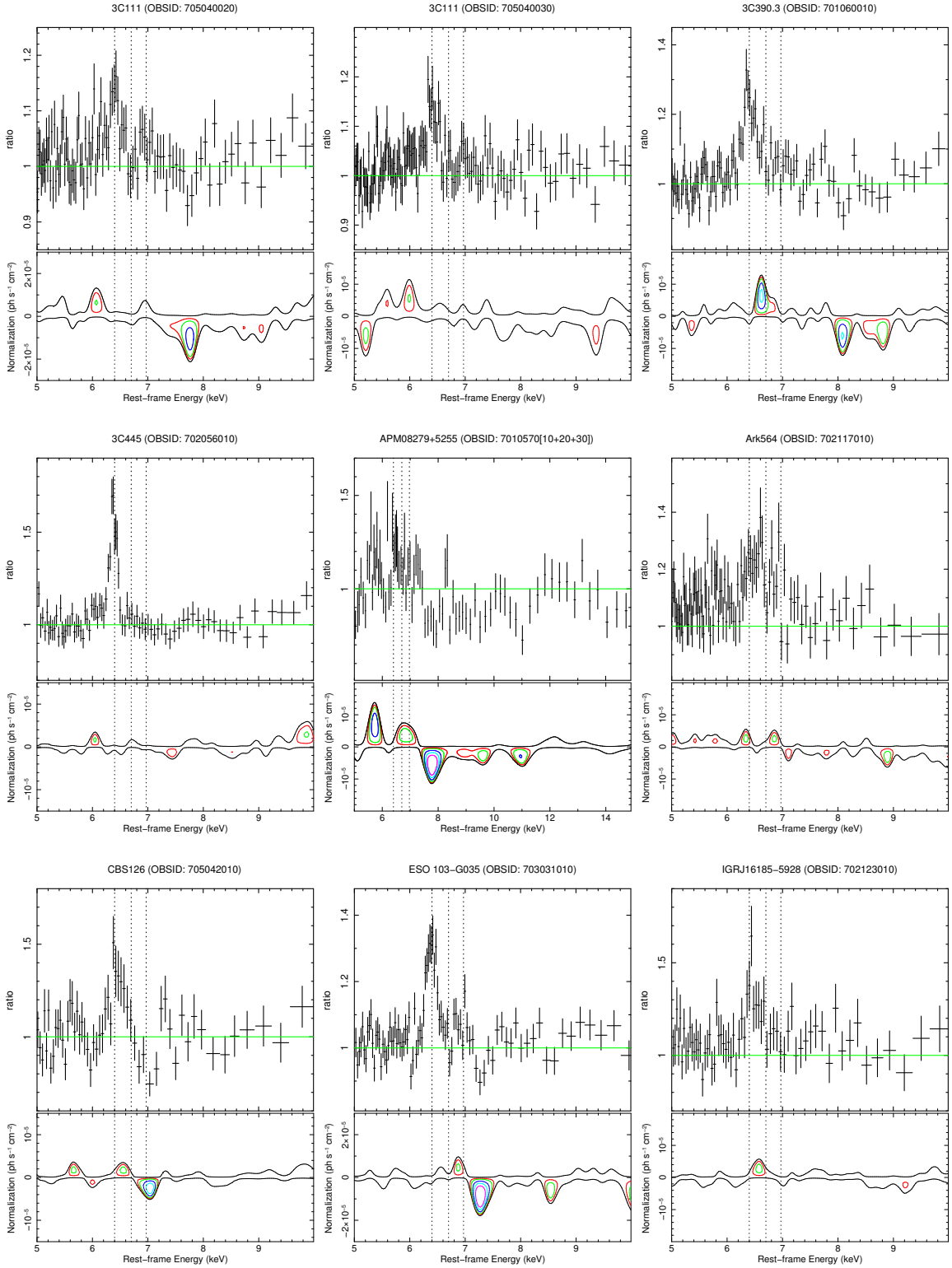


Figure A.1: – *Continued*

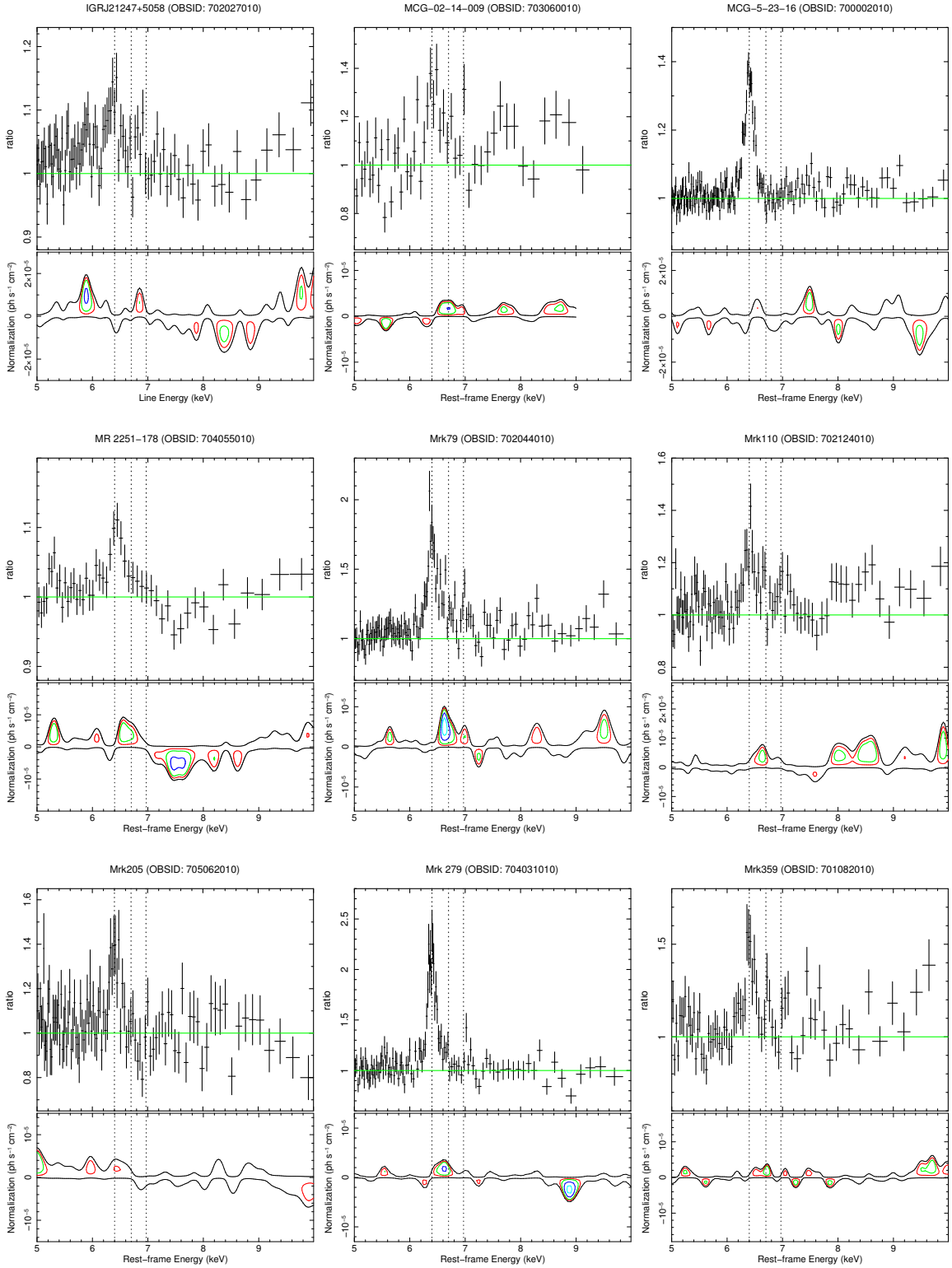


Figure A.1: – *Continued*

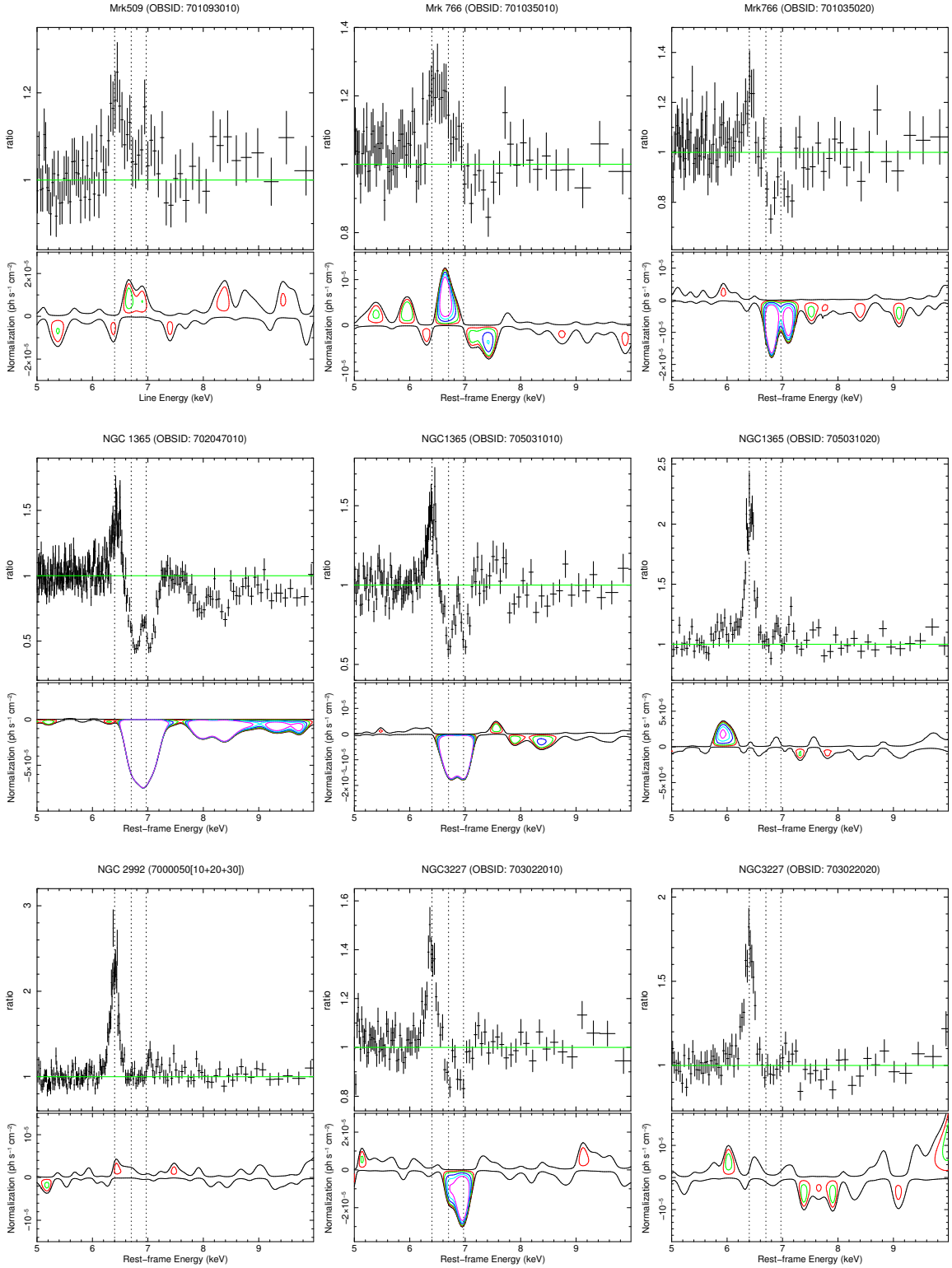


Figure A.1: – *Continued*

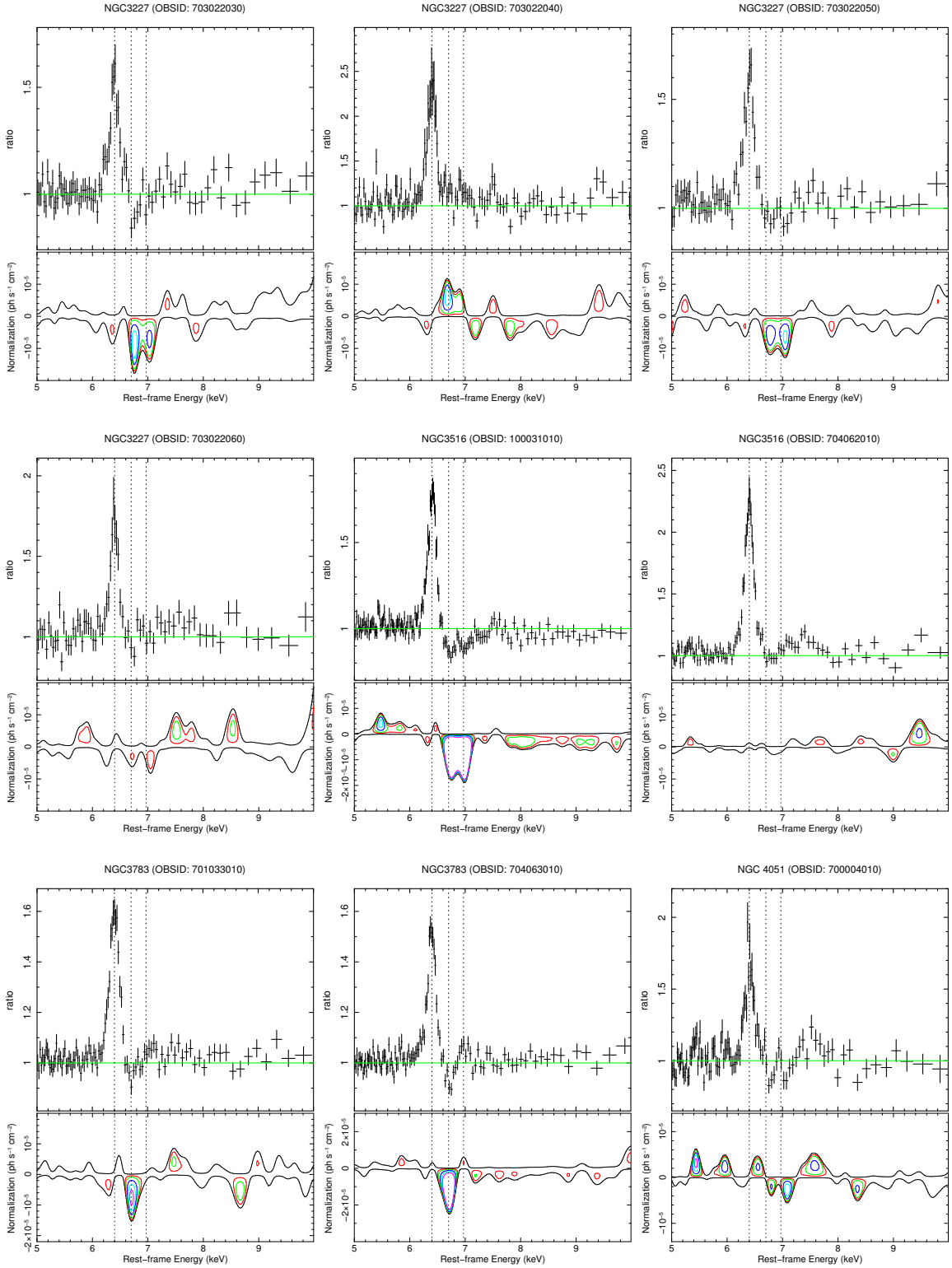


Figure A.1: – *Continued*

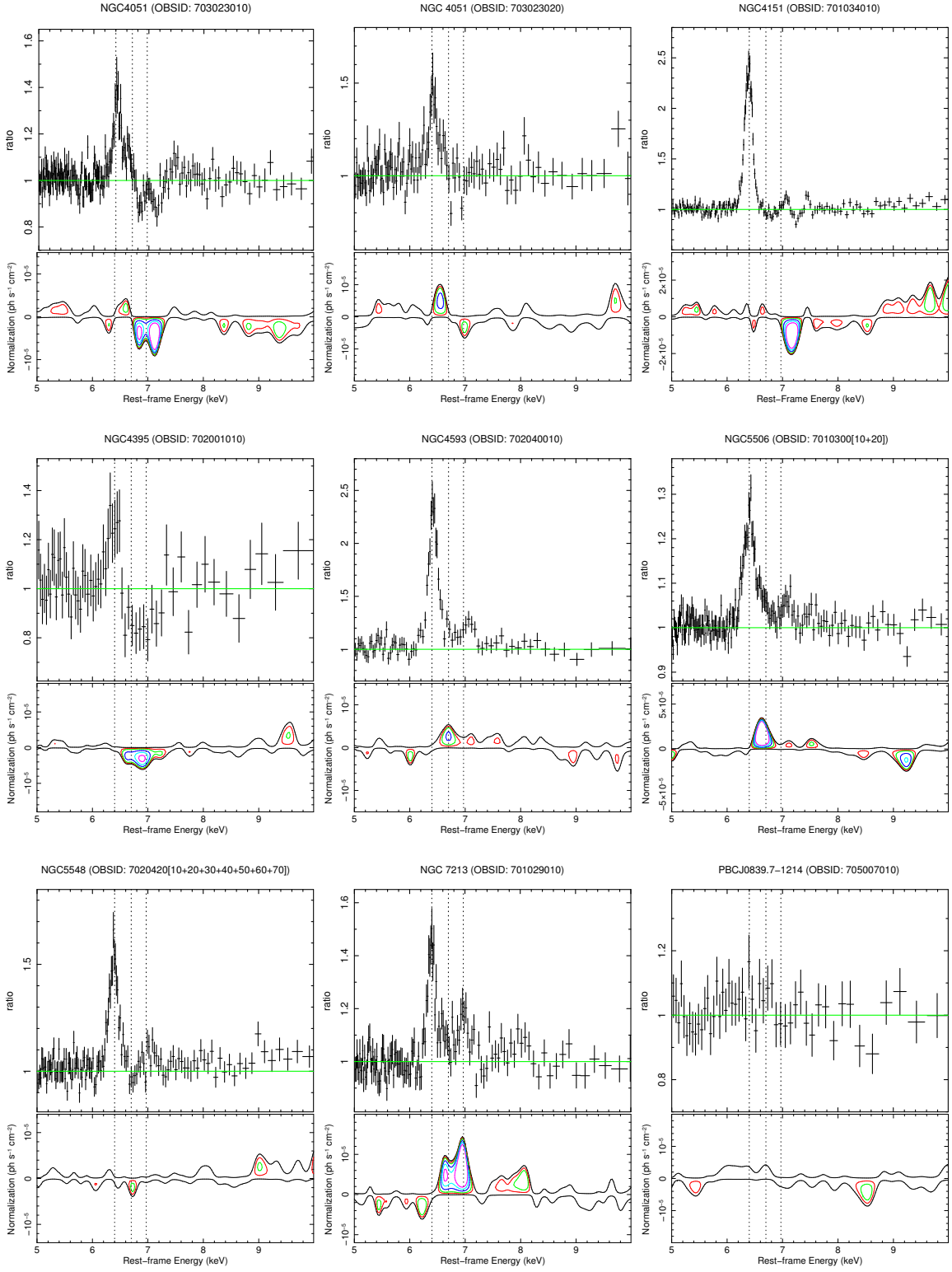


Figure A.1: – *Continued*

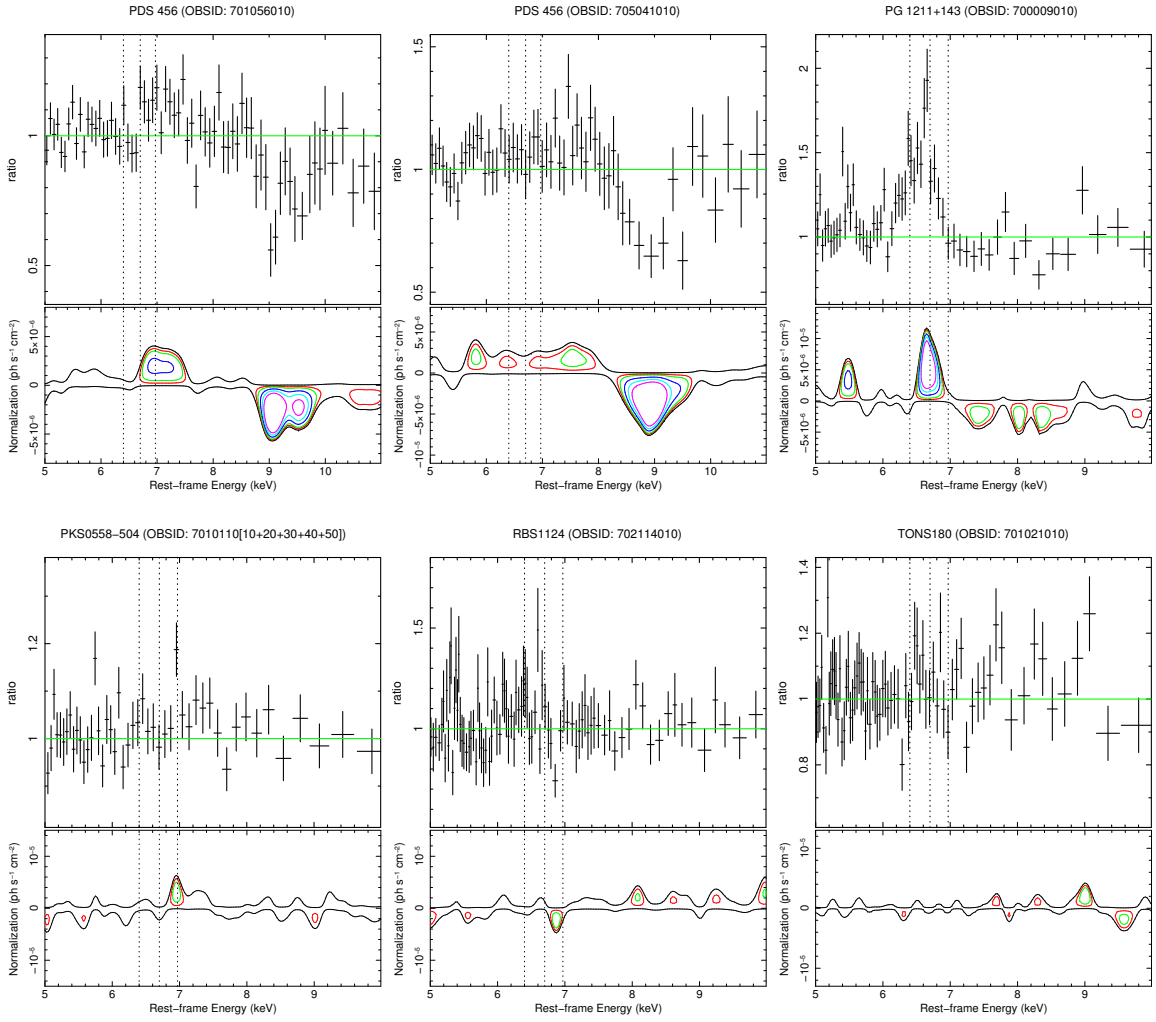


Figure A.1: – *Continued*

## A.2 Ratio and contour plots 2: broad Fe K$\alpha$ line

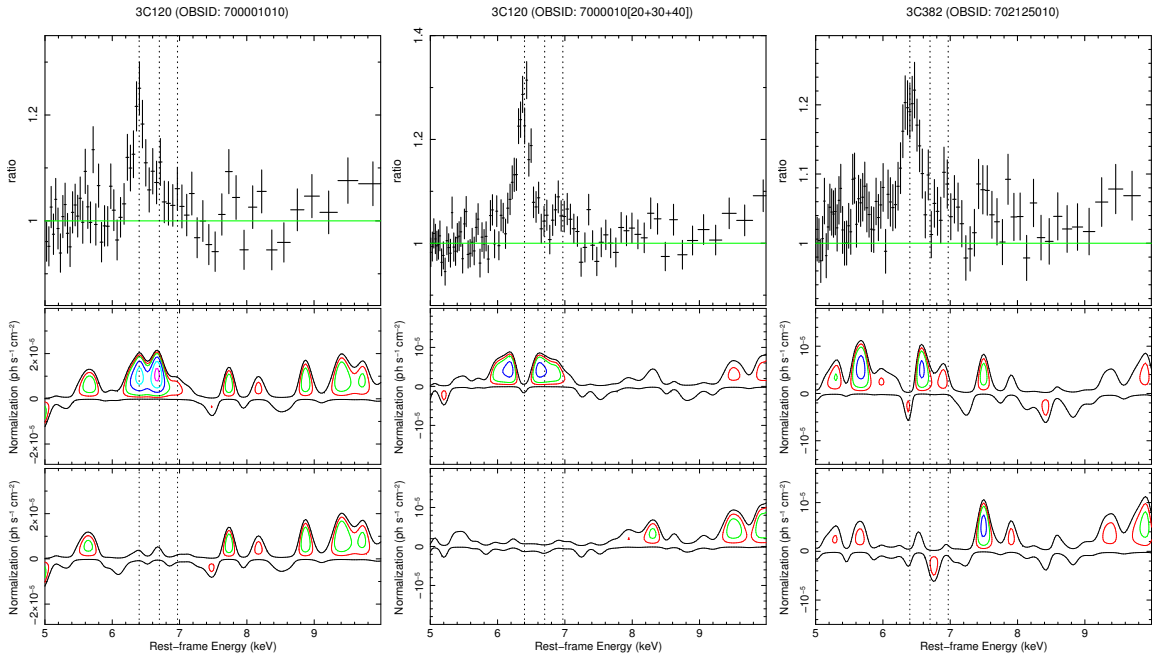


Figure A.2: Ratio and contour plots for sources which *do* require an additional broad component at Fe K. The top and middle panels again show the primary residuals at Fe K and their significances according to the F-test, respectively. The remaining residua after the additon of this broadened component (i.e., a broadened Gaussian or a `diskline`) are shown in the bottom panel. The confidence contours and dashed vertial lines have the same meaning as in Fig. A.1.

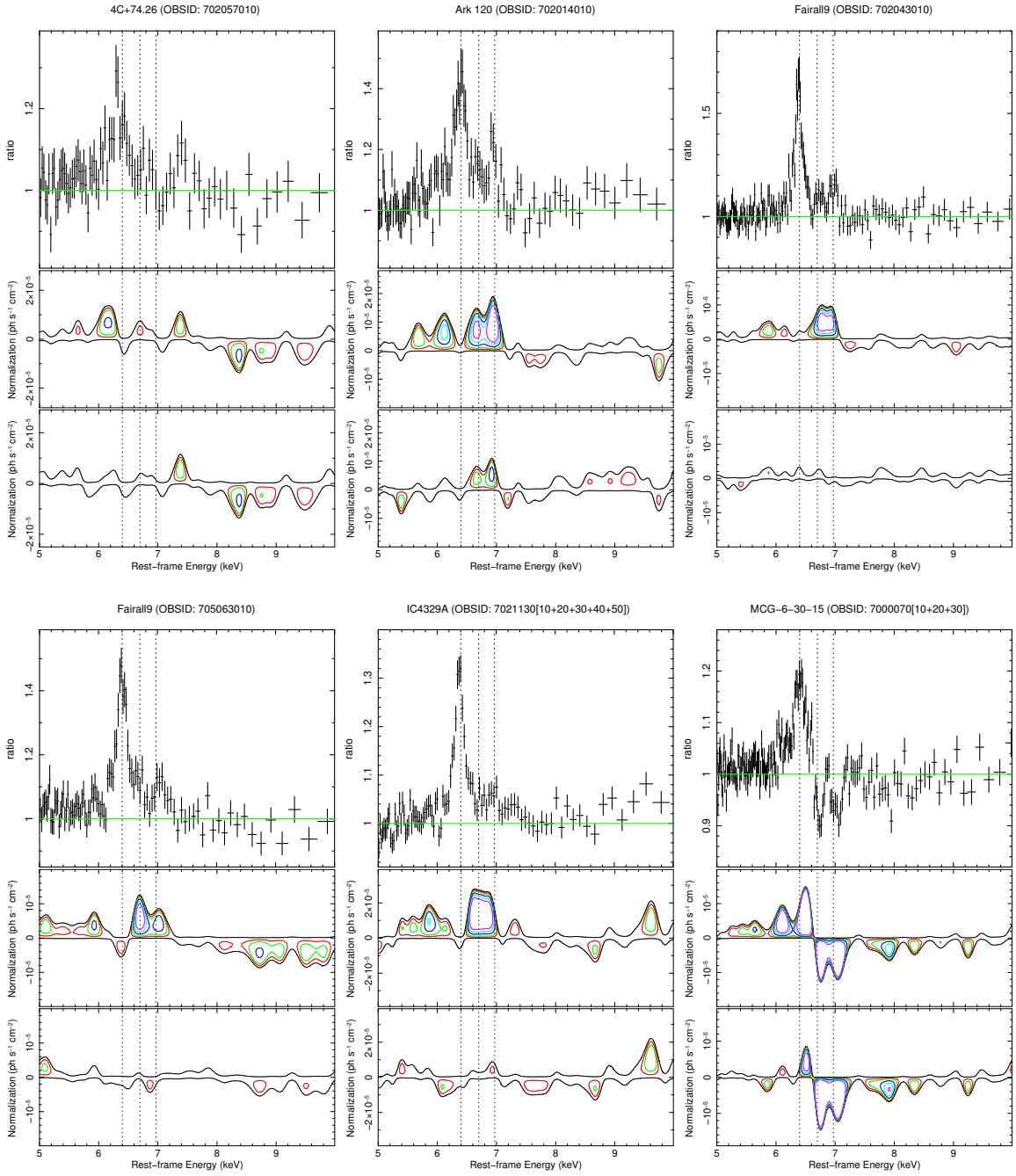


Figure A.2: – *Continued*

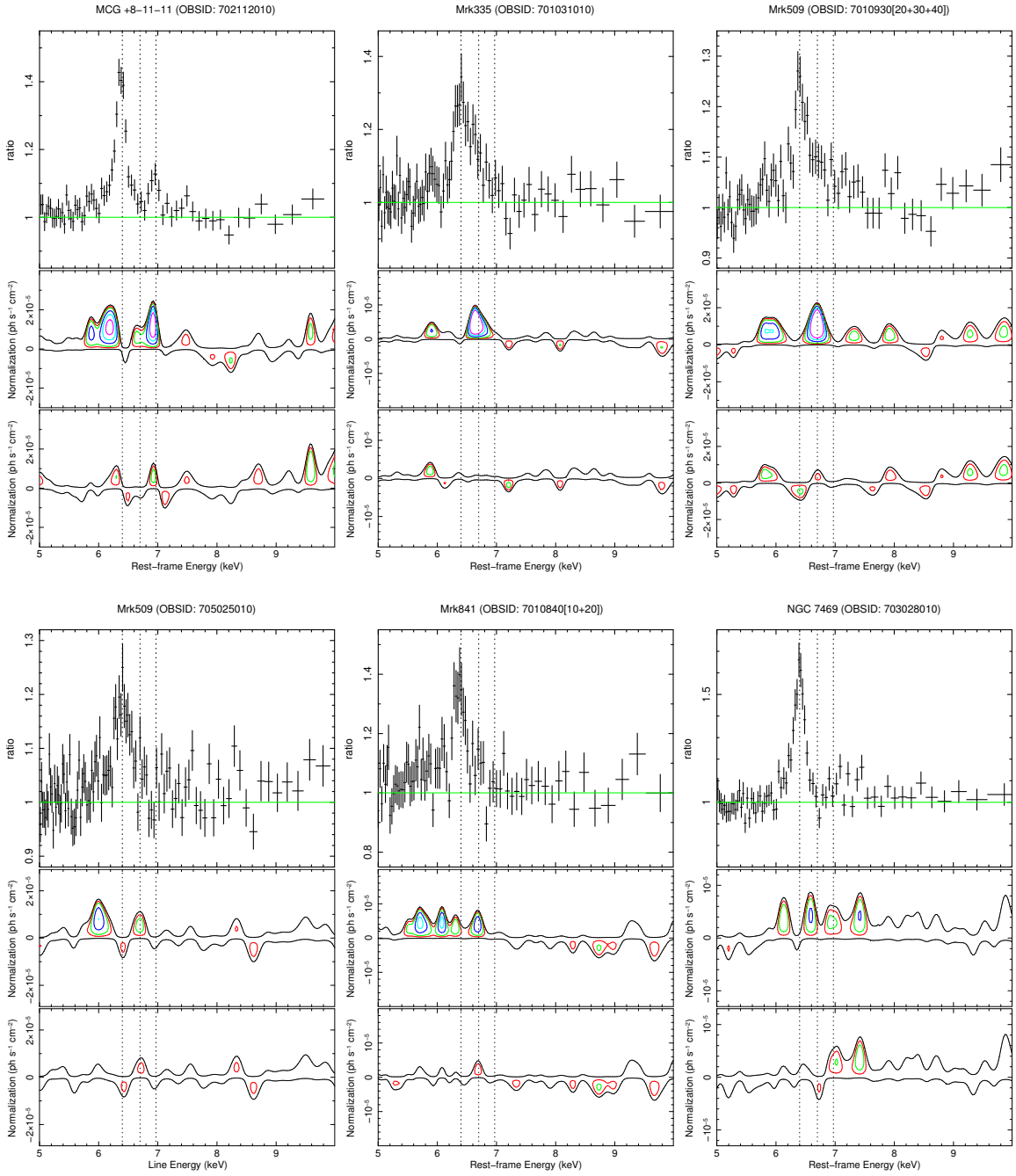


Figure A.2: – *Continued*

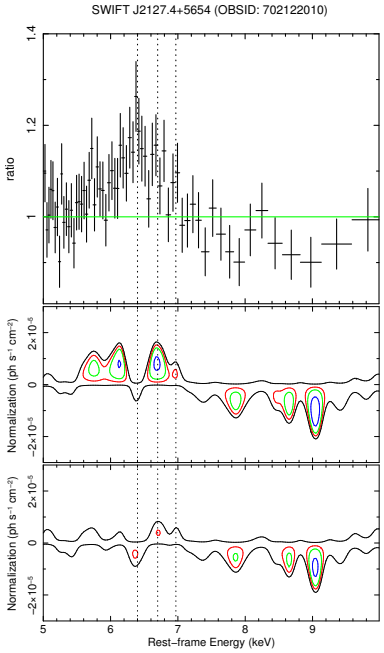


Figure A.2: – *Continued*

# B Supplementary tables

Table B.1: Summary of broad-band continuum models. *Columns*: (1) Source name; (2) *Suzaku* observation ID. See table 4.4 for details on stacked spectra; (3) Power-law photon index; (4) Power-law component normalisation in units of $10^{-3}$ ph keV$^{-1}$ cm$^{-2}$ s$^{-1}$ at 1 keV; (5) Blackbody thermal temperature in units of eV; (6) Blackbody normalisation in units of $10^{-5} \times (L_{39}/D_{10}^2)$, where $L_{39}$ is the source luminosity in units of $10^{39}$ erg s$^{-1}$ and $D_{10}$ is the distance to the source in units of 10 kpc; (7) Ionisation parameter of the `reflionx` X-ray reflection component, where $\xi = 4\pi F/n$; (8) Iron abundance for the X-ray reflector, in Solar units; (9) Reference for warm absorption parameters table (if present). A $^{\diamond}$ indicates that a highly-ionised outflow is also detected, with parameters listed in Table 4.4 of the main text; (10) Reduced $\chi^2$ and number of degrees of freedom ($\nu$) for the final best-fit model.

| | | Power-law | | bbody | | Reflection | | Abs. | $\chi^2_r(\nu)$ |
|---|---|---|---|---|---|---|---|---|---|
| Source | OBSID | $\Gamma$ | norm | $k_BT$ | norm | $\xi$ | $Z_{\rm Fe}$ | | |
| (1) | (2) | (3) | (4) | (5) | (6) | (7) | (8) | (9) | (10) |
| 1H 0419−577 | stacked[all] | $2.36 \pm 0.02$ | $33.71^{+1.06}_{-1.06}$ | ··· | ··· | $< 1.03$ | 1.00* | B.2 | 1.08(3070) |
| 3C 111$^{\diamond}$ | 703034010$^{j}$ | $1.74^{+0.01}_{-0.01}$ | $4.98^{+0.04}_{-0.04}$ | ··· | ··· | $< 3.21$ | 1.00* | B.3 | 1.07(7218) |
| | 705040010$^{j}$ | 1.74* | $12.29^{+0.10}_{-0.10}$ | ··· | ··· | $< 3.21$ | 1.00* | | |
| | 705040020$^{j}$ | 1.74* | $16.44^{+0.13}_{-0.13}$ | ··· | ··· | $< 3.21$* | 1.00* | | |
| | 705040030$^{j}$ | 1.74* | $16.73^{+0.13}_{-0.13}$ | ··· | ··· | $< 3.21$* | 1.00* | | |
| 3C 120 | 700001010$^{j}$ | (1)$1.58^{+0.04}_{-0.05}$ | $7.15^{+0.07}_{-0.07}$ | ··· | ··· | $30.02^{+2.02}_{-1.89}$ | 1.00* | B.3 | 1.02(3841) |
| | | (2)$2.56^{+0.09}_{-0.08}$ | $5.07^{+0.08}_{-0.07}$ | | | | | | |
| | Stacked[bcd]$^{j}$ | (1)1.58* | $7.69^{+0.08}_{-0.09}$ | ··· | ··· | 30.02* | 1.00* | | |
| | | (2)2.56* | $8.77^{+0.09}_{-0.08}$ | | | | | | |
| 3C 382 | 702125010 | $1.86^{+0.01}_{-0.01}$ | $12.42^{+0.09}_{-0.07}$ | $95^{+8}_{-8}$ | $1.39^{+0.50}_{-0.32}$ | $< 1.38$ | 1.00* | B.2 | 1.06(3020) |
| 3C 390.3$^{\diamond}$ | 701060010 | $1.72^{+0.01}_{-0.02}$ | $7.45^{+0.10}_{-0.12}$ | $149^{+26}_{-31}$ | $1.07^{+0.35}_{-0.36}$ | $< 5.11$ | 1.00* | ··· | 1.02(2666) |
| 3C 445 | 702056010 | $1.85^{+0.05}_{-0.05}$ | $4.69^{+0.31}_{-0.31}$ | ··· | ··· | $< 22.65$ | 1.00* | B.2 | 1.05(530) |
| 4C +74.26$^{\diamond}$ | 702057010 | $1.99^{+0.02}_{-0.02}$ | $11.50^{+0.32}_{-0.32}$ | ··· | ··· | $1.91^{+0.36}_{-0.71}$ | $0.28^{+0.10}_{-0.09}$ | B.2 | 1.01(2271) |
| APM 08279+5255$^{\diamond}$ | stacked | $1.89^{+0.04}_{-0.04}$ | $0.14^{+0.01}_{-0.01}$ | ··· | ··· | ··· | ··· | B.2 | 1.08(351) |
| Ark 120 | 702014010 | $2.06^{+0.01}_{-0.01}$ | $11.87^{+0.15}_{-0.15}$ | $150^{+5}_{-5}$ | $9.50^{+0.72}_{-0.71}$ | $< 3.5$ | 1.00* | ··· | 1.06(2543) |
| Ark 564 | 702117010 | $2.56^{+0.01}_{-0.01}$ | $25.95^{+0.36}_{-0.36}$ | $146^{+1}_{-1}$ | $40.22^{+0.13}_{-0.13}$ | $< 1.20$ | 1.00* | B.2 | 1.02(1967) |
| CBS 126 $^{\diamond}$ | 705042010 | $2.06^{+0.03}_{-0.03}$ | $1.75^{+0.07}_{-0.06}$ | $71^{+5}_{-5}$ | $22.39^{+9.72}_{-6.44}$ | $< 2.96$ | 1.00* | B.2 | 1.03(1003) |

Continued on next page...

Table B.1: Summary of broad-band continuum models (continued)

| Source | OBSID | Power-law | | bbody | | Reflection | | Abs. | $\chi^2_r(\nu)$ |
|---|---|---|---|---|---|---|---|---|---|
| | | $\Gamma$ | norm | $k_BT$ | norm | $\xi$ | $Z_{\rm Fe}$ | | |
| (1) | (2) | (3) | (4) | (5) | (6) | (7) | (8) | (9) | (10) |
| ESO 103-G035$^{\diamond}$ | 703031010 | $2.04^{+0.02}_{-0.02}$ | $28.99^{+0.95}_{-0.95}$ | ··· | ··· | $< 52.01$ | 1.00* | B.2 | 0.97(1444) |
| Fairall 9 | 702043010$^{j}$ | $2.04^{+0.01}_{-0.01}$ | $8.32^{+0.04}_{-0.04}$ | $104^{+1}_{-1}$ | $7.08^{+0.72}_{-0.72}$ | $< 1.01$ | $0.59^{+0.04}_{-0.04}$ | ··· | 1.09(3706) |
| | 705063010$^{j}$ | $2.11^{+0.01}_{-0.01}$ | $10.20^{+0.05}_{-0.05}$ | 104* | $11.71^{+0.09}_{-0.09}$ | $< 1.01$* | 0.59* | | |
| IC 4329A | Stacked[all] | $1.95^{+0.01}_{-0.01}$ | $37.18^{+0.11}_{-0.11}$ | ··· | ··· | $< 1.02$ | $0.40^{+0.03}_{-0.03}$ | B.2 | 1.03(3336) |
| IGR J16185−5928 | 702123010 | $1.97^{+0.01}_{-0.01}$ | $2.84^{+0.03}_{-0.03}$ | ··· | ··· | $< 2.29$ | $0.51^{+0.27}_{-0.17}$ | B.2 | 0.97(1004) |
| IGR J21247+5058 | 702027010 | $1.61^{+0.01}_{-0.01}$ | $18.49^{+0.18}_{-0.18}$ | ··· | ··· | $< 1.17$ | 1.00* | B.2 | 1.06(2778) |
| MCG -02-14-009 | 703060010 | $1.84^{+0.04}_{-0.04}$ | $1.21^{+0.06}_{-0.06}$ | $187^{+32}_{-40}$ | $0.45^{+0.17}_{-0.17}$ | $< 11.14$ | 1.00* | ··· | |
| MCG -2-58-22 | 704032010 | $1.85^{+0.01}_{-0.01}$ | $20.78^{+0.05}_{-0.05}$ | ··· | ··· | $< 3.07$ | 1.00* | B.2 | 1.06(2991) |
| MCG -5-23-16 | 700002010 | $2.13^{+0.01}_{-0.01}$ | $88.08^{+0.04}_{-0.04}$ | $752^{+41}_{-84}$ | $5.78^{+0.56}_{-0.56}$ | $< 4.63$ | 1.00* | B.2 | 1.03(3250) |
| MCG -6-30-15$^{\diamond}$ | stacked[all] | $2.06^{+0.01}_{-0.01}$ | $20.72^{+0.41}_{-0.41}$ | $115^{+3}_{-3}$ | $23.65^{+1.04}_{-1.04}$ | $< 1.05$ | 1.00* | B.2 | 1.03(2334) |
| MCG +8-11-11 | 702112010 | $1.72^{+0.01}_{-0.01}$ | $16.85^{+0.06}_{-0.06}$ | ··· | ··· | $< 2.61$ | $1.60^{+0.23}_{-0.23}$ | B.2 | 1.04(3030) |
| MR 2251−178$^{\diamond}$ | 704055010 | $1.65^{+0.01}_{-0.01}$ | $10.21^{+0.04}_{-0.04}$ | $64^{+3}_{-3}$ | $9.79^{+3.12}_{-2.30}$ | $14.17^{+7.65}_{-4.63}$ | 1.00* | B.2 | 1.05(3117) |
| Mrk 79 | 702044010 | $1.94^{+0.02}_{-0.02}$ | $5.18^{+0.13}_{-0.13}$ | ··· | ··· | $< 1.34$ | 1.00* | B.2 | 0.94(1791) |
| Mrk 110 | 702124010 | $1.81^{+0.01}_{-0.01}$ | $5.93^{+0.10}_{-0.10}$ | $153^{+12}_{-13}$ | $2.65^{+0.38}_{-0.38}$ | $20.19^{+5.25}_{-8.75}$ | 1.00* | ··· | 0.96(1994) |
| Mrk 205 | 705062010 | $1.94^{+0.02}_{-0.02}$ | $7.85^{+0.13}_{-0.15}$ | $115^{+17}_{-18}$ | $2.33^{+1.18}_{-0.58}$ | $9.85^{+0.68}_{-1.42}$ | 1.00* | B.2 | 1.05(1344) |
| Mrk 279$^{\diamond}$ | 704031010 | $1.76^{+0.01}_{-0.01}$ | $1.10^{+0.01}_{-0.01}$ | ··· | ··· | $1.3^{+0.9}_{-0.3}$ | 1.0* | B.2 | 0.99(1442) |
| Mrk 335 | 701031010 | $2.17^{+0.01}_{-0.01}$ | $6.94^{+0.07}_{-0.07}$ | $123^{+1}_{-1}$ | $2.09^{+0.06}_{-0.06}$ | $< 3.00$ | $0.51^{+0.16}_{-0.10}$ | B.2 | 1.09(2423) |
| Mrk 359 | 701082010 | $1.81^{+0.03}_{-0.03}$ | $1.39^{+0.04}_{-0.04}$ | $207^{+22}_{-18}$ | $0.73^{+0.19}_{-0.19}$ | $2.72^{+0.22}_{-0.22}$ | $0.54^{+0.22}_{-14}$ | ··· | 1.11(1126) |
| Mrk 509 | 701093010$^{j}$ | (1)$1.67^{+0.03}_{-0.03}$ | $8.92^{+0.57}_{-0.53}$ | ··· | ··· | $4.12^{+0.25}_{-0.25}$ | 1.00* | B.3 | 1.01(5502) |
| | | (2)$2.67^{+0.05}_{-0.05}$ | $7.15^{+0.57}_{-0.60}$ | | | | | | |
| | stacked[bcd]$^{j}$ | (1)1.67* | $8.43^{+0.60}_{-0.56}$ | ··· | ··· | 4.12* | 1.00* | | |
| | | (2)2.67* | $10.52^{+0.58}_{-0.62}$ | | | | | | |
| | 705025010$^{j}$ | (1)1.67* | $9.54^{+0.70}_{-0.65}$ | ··· | ··· | 4.12* | 1.00* | | |
| | | (2)2.67* | $12.66^{+0.66}_{-0.72}$ | | | | | | |

Continued on next page...

Table B.1: Summary of broad-band continuum models (continued)

| Source | OBSID | Power-law | | bbody | | Reflection | | Abs. | $\chi^2_r(\nu)$ |
|---|---|---|---|---|---|---|---|---|---|
| | | $\Gamma$ | norm | $k_BT$ | norm | $\xi$ | $Z_{\rm Fe}$ | | |
| (1) | (2) | (3) | (4) | (5) | (6) | (7) | (8) | (9) | (10) |
| Mrk 766$^{\diamond}$ | 701035010$^{j}$ | $2.10^{+0.01}_{-0.01}$ | $7.19^{+0.06}_{-0.06}$ | ··· | ··· | $1.95^{+0.26}_{-0.45}$ | 1.00$^{*}$ | B.3 | 1.05(2258) |
| | 701035020$^{j}$ | 2.10$^{*}$ | $5.92 \pm 0.03$ | ··· | ··· | 1.95$^{*}$ | 1.00$^{*}$ | | |
| Mrk 841 | stacked[all] | $1.91^{+0.01}_{-0.01}$ | $4.25^{+0.04}_{-0.04}$ | $84^{+7}_{-8}$ | $9.58^{+4.42}_{-2.42}$ | $< 1.03$ | $0.46^{+0.09}_{-0.08}$ | B.2 | 1.02(1892) |
| NGC 1365$^{\diamond}$ | 702047010$^{j}$ | $1.87^{+0.02}_{-0.02}$ | $11.92^{+0.23}_{-0.23}$ | ··· | ··· | $1.34^{+0.08}_{-0.08}$ | 1.00$^{*}$ | B.3 | 1.06(2323) |
| | 705031010$^{j}$ | 1.87$^{*}$ | $10.43^{+0.33}_{-0.33}$ | ··· | ··· | 1.34$^{*}$ | 1.00$^{*}$ | | |
| | 705031020 | $1.87^{+0.03}_{-0.03}$ | $7.92^{+0.55}_{-0.55}$ | ··· | ··· | $1.14^{+0.18}_{-0.10}$ | 1.00$^{*}$ | B.2 | 1.04(978) |
| NGC 2992 | stacked[all] | $1.85^{+0.02}_{-0.02}$ | $3.35^{+0.07}_{-0.07}$ | ··· | ··· | $< 5.1^{+0.09}_{-0.09}$ | 1.00$^{*}$ | B.2 | 1.05(1610) |
| NGC 3227$^{\diamond}$ | 703022010$^{j}$ | $1.83^{+0.01}_{-0.01}$ | $13.92^{+0.49}_{-0.49}$ | ··· | ··· | $< 1.22$ | 1.00$^{*}$ | B.3 | 1.04(5803) |
| | 703022020$^{j}$ | 1.83$^{*}$ | $9.71^{+0.37}_{-0.37}$ | ··· | ··· | $< 1.22^{*}$ | 1.00$^{*}$ | | |
| | 703022030$^{j}$ | 1.83$^{*}$ | $11.47^{+0.29}_{-0.37}$ | ··· | ··· | $< 1.22^{*}$ | 1.00$^{*}$ | | |
| | 703022040$^{j}$ | 1.83$^{*}$ | $4.94^{+0.17}_{-0.17}$ | ··· | ··· | $< 1.22^{*}$ | 1.00$^{*}$ | | |
| | 703022050$^{j}$ | 1.83$^{*}$ | $10.27^{+0.24}_{-0.24}$ | ··· | ··· | $< 1.22^{*}$ | 1.00$^{*}$ | | |
| | 703022060$^{j}$ | 1.83$^{*}$ | $7.60^{+0.21}_{-0.21}$ | ··· | ··· | $< 1.22^{*}$ | 1.00$^{*}$ | | |
| NGC 3516$^{\diamond}$ | 100031010 | $2.11^{+0.03}_{-0.03}$ | $27.81^{+0.75}_{-0.75}$ | ··· | ··· | $2.24^{+0.14}_{-0.10}$ | 1.00$^{*}$ | B.3 | 1.01(3820) |
| | 704062010 | 2.11$^{*}$ | $9.79^{+0.61}_{-0.61}$ | ··· | ··· | 2.24$^{*}$ | 1.00$^{*}$ | | |
| NGC 3783$^{\diamond}$ | 701033010$^{j}$ | $1.85^{+0.01}_{-0.01}$ | $18.48^{+0.40}_{-0.40}$ | $82^{+1}_{-1}$ | $26.40^{+3.32}_{-3.29}$ | $< 1.20$ | 1.00$^{*}$ | B.3 | 1.04(4219) |
| | 704063010$^{j}$ | 1.85$^{*}$ | $22.39^{+0.20}_{-0.19}$ | 82$^{*}$ | $107.72^{+12.01}_{-10.24}$ | 1.20$^{*}$ | 1.00$^{*}$ | | |
| NGC 4051$^{\diamond}$ | 700004010 | $2.18^{+0.01}_{-0.01}$ | $13.20^{+0.07}_{-0.07}$ | $79^{+1}_{-1}$ | $4.33^{+0.56}_{-0.56}$ | $< 1.01$ | 1.00$^{*}$ | B.3 | 1.01(4551) |
| | 703023010 | 2.18$^{*}$ | $26.43^{+0.09}_{-0.09}$ | 79$^{*}$ | $57.36^{+4.34}_{-4.09}$ | $< 1.01^{*}$ | 1.00$^{*}$ | | |
| | 703023020 | 2.18$^{*}$ | $21.44^{+0.14}_{-0.13}$ | 79$^{*}$ | $33.74^{+2.73}_{-2.98}$ | $< 1.01^{*}$ | 1.00$^{*}$ | | |
| NGC 4151$^{\diamond}$ | 701034010 | $2.02^{+0.01}_{-0.01}$ | $22.65^{+0.95}_{-0.93}$ | ··· | ··· | $< 1.02$ | 1.00$^{*}$ | B.2 | 1.00(3052) |
| NGC 4395$^{\diamond}$ | 702001010 | $1.65^{+0.02}_{-0.02}$ | $1.82^{+0.05}_{-0.05}$ | ··· | ··· | $< 2.18^{+1.46}_{-1.02}$ | 1.00$^{*}$ | B.2 | 1.00(590) |
| NGC 4593$^{c}$ | 702040010 | $1.64^{+0.01}_{-0.01}$ | $2.20^{+0.02}_{-0.02}$ | ··· | ··· | $< 1.04$ | $1.67^{+0.19}_{-0.19}$ | B.2 | 1.03(1863) |
| NGC 5506 | stacked[all] | $2.04^{+0.01}_{-0.01}$ | $83.98^{+0.64}_{-0.62}$ | ··· | ··· | $6.86^{+0.37}_{-0.35}$ | 1.00$^{*}$ | B.3 | 1.06(2376) |
| NGC 5548 | stacked[all] | $1.75^{+0.01}_{-0.01}$ | $4.80^{+0.25}_{-0.25}$ | ··· | ··· | $< 1.42$ | 1.00$^{*}$ | B.2 | 1.05(1854) |

Continued on next page...

Table B.1: Summary of broad-band continuum models (continued)

| Source | OBSID | Power-law | | bbody | | Reflection | | Abs. | $\chi^2_r(\nu)$ |
|---|---|---|---|---|---|---|---|---|---|
| | | $\Gamma$ | norm | $k_BT$ | norm | $\xi$ | $Z_{\rm Fe}$ | | |
| (1) | (2) | (3) | (4) | (5) | (6) | (7) | (8) | (9) | (10) |
| NGC 7213 | 701029010 | $1.78^{+0.01}_{-0.01}$ | $6.39^{+0.02}_{-0.02}$ | ··· | ··· | $5.01^{+0.24}_{-0.51}$ | $1.83^{+0.47}_{-0.27}$ | ··· | 1.02(2686) |
| NGC 7469 | 703028010 | $1.83^{+0.01}_{-0.01}$ | $2.21^{+0.02}_{-0.02}$ | ··· | ··· | $< 1.3$ | $1.61^{+0.16}_{-0.16}$ | B.2 | 1.00(2377) |
| PBC J0839.7−1214 | 705007010 | $1.74^{+0.01}_{-0.01}$ | $2.66^{+0.04}_{-0.04}$ | ··· | ··· | $134.15^{+8.32}_{-7.81}$ | 1.00* | ··· | 1.06(1267) |
| PDS 456◇ | 701056010 | $2.47^{+0.01}_{-0.01}$ | $3.19^{+0.05}_{-0.05}$ | ··· | ··· | ··· | ··· | B.3 | 1.08(1238) |
| | 705041010 | 2.47* | $3.07^{+0.06}_{-0.06}$ | ··· | ··· | ··· | ··· | | |
| PG 1211+143 | 700009010 | $1.88^{+0.02}_{-0.02}$ | $1.18^{+0.02}_{-0.02}$ | $80^{+4}_{-4}$ | $1.16^{+0.29}_{-0.22}$ | $< 71.87$ | 1.00* | B.2 | 1.04(831) |
| PKS 0558−504 | Stacked[all] | $2.30^{+0.01}_{-0.01}$ | $13.08^{+0.18}_{-0.18}$ | $133^{+4}_{4}$ | $10.28^{+0.57}_{-0.57}$ | $< 155.36$ | 1.00* | B.2 | 0.99(1868) |
| RBS 1124 | 702114010 | $1.75^{+0.03}_{-0.03}$ | $2.77^{+0.06}_{-0.06}$ | $105^{+17}_{-17}$ | $0.99^{+0.86}_{-0.38}$ | $< 27.41$ | 1.00* | B.2 | 0.94(764) |
| SW J2127.4+5456◇ | 702122010 | $2.01^{+0.02}_{-0.02}$ | $13.27^{+0.39}_{-0.39}$ | $271^{+24}_{-24}$ | $3.72^{+1.01}_{-1.02}$ | $20^{+5}_{-13}$ | 1.00* | B.2 | 0.97(2063) |
| TON S180 | 701021010 | $2.41^{+0.02}_{-0.02}$ | $9.94^{+0.25}_{-0.25}$ | $124^{+6}_{-6}$ | $6.00^{+0.79}_{-0.77}$ | $566.39^{+212.12}_{-142.11}$ | 1.00* | B.2 | 1.05(922) |

* Parameter was tied during fitting;
f Parameter was frozen at this value during fitting;
c Indicates that spectra were fit simultaneously;
◇ indicates that a highly-ionised outflow is detected in this source.

Table B.2: Warm absorber parameters for single-epoch sources. *Columns:* (1) Source name; (2) *Suzaku* observation ID; (3) Absorption zone; (4) Logarithm of absorber column density, in units of $\mathrm{cm}^{-2}$; (5) Logarithm of the ionisation parameter, in units of $\mathrm{erg\,cm\,s}^{-1}$; (6) Per cent (%) covering fraction of absorption component. All warm absorption components are required with $P_{\mathrm{F}} > 99\%$.

| Source (1) | OBSID (2) | Zone (3) | $\log(N_{\mathrm{H}})$ (4) | $\log(\xi)$ (5) | $f_{\mathrm{cov}}$ (6) |
|---|---|---|---|---|---|
| 1H 0419−577 | stacked[all] | 1 | $24.33^{+0.01}_{-0.01}$ | $0.51^{+0.44}_{-0.08}$ | $65^{+5}_{-5}$ |
| | | 2 | $23.27^{+0.01}_{-0.01}$ | $2.03^{+0.01}_{-0.01}$ | $17^{+2}_{-2}$ |
| 3C 382 | 702125010 | 1 | $21.10^{+0.03}_{-0.46}$ | $2.73^{+0.16}_{-0.31}$ | 100 * |
| 3C 445 | 702056010 | 1 | $23.28^{+0.01}_{-0.01}$ | $1.12^{+0.07}_{-0.16}$ | $\gtrsim 98$ |
| 4C +74.26$^{\diamond}$ | 702057010 | 1 | $21.57^{+0.10}_{-0.10}$ | $1.61^{+0.08}_{-0.09}$ | 100 * |
| | | 2 | $20.96^{+0.05}_{-0.05}$ | neutral | 100 * |
| APM 08279+5255$^{\diamond}$ | stacked[all] | 1 | $22.67^{+0.09}_{-0.10}$ | neutral | 100 * |
| Ark 564 | 702117010 | 1 | $24.48^{+0.01}_{-0.01}$ | $2.46^{+0.04}_{-0.19}$ | $41 \pm 1$ |
| | | 2 | $22.73^{+0.03}_{-0.02}$ | $0.95^{+0.10}_{-0.09}$ | 100 * |
| CBS 126$^{\diamond}$ | 705042010 | 1 | $22.48^{+0.05}_{-0.05}$ | $2.97^{+0.02}_{-0.02}$ | 100 * |
| ESO 103-G035$^{\diamond}$ | 703031010 | 1 | $23.07^{+0.02}_{-0.02}$ | neutral | $98 \pm 1$ |
| | | 2 | $23.02^{+0.02}_{-0.02}$ | $0.82^{+0.23}_{-0.22}$ | 98* |
| | | 3 | $21.74^{+0.04}_{-0.04}$ | neutral | 100 * |
| IC 4329A | stacked[all] | 1 | $21.17^{+0.17}_{-0.09}$ | $1.98^{+0.16}_{-0.10}$ | 100 * |
| | | 2 | $21.24^{+0.01}_{-0.01}$ | $-1.27^{+0.01}_{-0.01}$ | 100 * |
| | | 3 | $21.75^{+0.05}_{-0.05}$ | $1.24^{+0.13}_{-0.18}$ | 100 * |
| | | 4 | $21.15^{+0.03}_{-0.02}$ | $2.52^{+0.07}_{-0.03}$ | 100 * |
| IGR J21247+5058 | 702027010 | 1 | $22.54^{+0.13}_{-0.12}$ | neutral | $< 21$ |
| | | 2 | $21.94^{+0.02}_{-0.02}$ | neutral | 100 * |
| MR 2251−178$^{\diamond}$ | 704055010 | 1 | $20.98^{+0.10}_{-0.09}$ | $0.96^{+0.13}_{-0.11}$ | 100 * |
| | | 2 | $21.43^{+0.36}_{-0.75}$ | $2.21^{+0.08}_{-0.08}$ | 100 * |
| Mrk 79 | 702044010 | 1 | $23.19^{+0.03}_{-0.03}$ | $2.13^{+0.07}_{-0.09}$ | $37 \pm 6$ |
| | | 2 | $21.62^{+0.04}_{-0.04}$ | $1.44^{+0.06}_{-0.04}$ | 100 * |
| Mrk 205 | 705062010 | 1 | $> 24.68$ | neutral | $59 \pm 2$ |
| Mrk 279$^{\diamond}$ | 704031010 | 1 | $20.68^{+0.12}_{-0.10}$ | $1.26^{+0.28}_{-0.68}$ | 100 * |
| Mrk 335 | 701031010 | 1 | $20.43^{+0.02}_{-0.02}$ | $0.52^{+0.20}_{-0.18}$ | 100 * |
| Mrk 841 | stacked[all] | 1 | $20.39^{+0.39}_{-0.24}$ | $1.84^{+0.41}_{-0.43}$ | 100 * |
| MCG -2-58-22 | 704032010 | 1 | $24.15^{+0.03}_{-0.04}$ | $2.33^{+0.20}_{-0.13}$ | $35 \pm 2$ |
| MCG -5-23-16 | 700002010 | 1 | $24.18^{+0.01}_{-0.01}$ | $1.71^{+0.06}_{-0.06}$ | $49 \pm 1$ |
| | | 2 | $22.68^{+0.01}_{-0.01}$ | $0.58^{+0.01}_{-0.01}$ | 100 * |
| MCG -6-30-15$^{\diamond}$ | stacked[all] | 1 | $23.73^{+0.02}_{-0.02}$ | $2.21^{+0.05}_{-0.05}$ | $< 18$ |

Continued on next page...

Table B.2: Summary of broad-band continuum models (continued)

| Source (1) | OBSID (2) | Zone (3) | $\log(N_{\rm H})$ (4) | $\log(\xi)$ (5) | $f_{\rm cov}$ (6) |
|---|---|---|---|---|---|
| | | 2 | $21.42^{+0.02}_{-0.02}$ | $0.72^{+0.02}_{-0.03}$ | $100^{*}$ |
| | | 3 | $21.79^{+0.01}_{-0.01}$ | $1.74^{+0.02}_{-0.02}$ | $100^{*}$ |
| MCG +8-11-11 | 702112010 | 1 | $20.52^{+0.05}_{-0.02}$ | $< 0.18$ | $100^{*}$ |
| | | 2 | $21.02^{+0.13}_{-0.13}$ | $2.35^{+0.10}_{-0.14}$ | $100^{*}$ |
| NGC 1365$^{\diamond}$ | 705031020 | 1 | $24.17^{+0.13}_{-0.09}$ | neutral | $31 \pm 1$ |
| | | 2 | $23.79^{+0.01}_{-0.01}$ | $1.32^{+0.06}_{-0.07}$ | $> 0.96$ |
| NGC 2992 | stacked[all] | 1 | $21.80^{+0.02}_{-0.02}$ | neutral | $95 \pm 1$ |
| | | 2 | $22.12^{+0.05}_{-0.04}$ | $1.79^{+0.08}_{-0.08}$ | $95^{*}$ |
| NGC 4151$^{\diamond}$ | 701034010 | 1 | $22.21^{+0.06}_{-0.14}$ | $2.57^{+0.14}_{-0.18}$ | $\gtrsim 98$ |
| | | 2 | $23.00^{+0.01}_{-0.01}$ | $0.63^{+0.02}_{-0.02}$ | $\gtrsim 98^{*}$ |
| | | 3 | $23.69^{+0.01}_{-0.01}$ | $1.86^{+0.07}_{-0.06}$ | $68 \pm 5$ |
| NGC 4395$^{\diamond}$ | 702001010 | 1 | $23.91^{+0.08}_{-0.06}$ | neutral | $38 \pm 2$ |
| | | 2 | $22.34^{+0.03}_{-0.03}$ | $0.56^{+0.14}_{-0.13}$ | $83 \pm 1$ |
| | | 3 | $21.58^{+0.14}_{-0.17}$ | $1.64^{+0.17}_{-0.27}$ | $100^{*}$ |
| NGC 4593 | 702040010 | 1 | $21.99^{+0.28}_{-0.15}$ | $2.96^{+0.18}_{-0.09}$ | $100^{*}$ |
| | | 2 | $21.79^{+0.24}_{-0.20}$ | $2.28^{+0.06}_{-0.09}$ | $100^{*}$ |
| NGC 5506$^{\diamond}$ | stacked[all] | 1 | $21.51^{+0.02}_{-0.02}$ | neutral | $100^{*}$ |
| | | 2 | $22.39^{+0.03}_{-0.02}$ | $1.55^{+0.05}_{-0.07}$ | $> 99$ |
| | | 3 | $22.29^{+0.02}_{-0.02}$ | neutral | $> 99$ |
| | | 4 | $24.01^{+0.01}_{-0.01}$ | neutral | $35 \pm 1$ |
| NGC 5548 | stacked[all] | 1 | $22.15^{+0.07}_{-0.12}$ | $2.78^{+0.06}_{-0.09}$ | $100^{*}$ |
| | | 2 | $21.44^{+0.21}_{-0.05}$ | $2.20^{+0.09}_{-0.11}$ | $> 92$ |
| | | 3 | $21.84^{+0.03}_{-0.03}$ | $0.38^{+0.12}_{-0.14}$ | $46 \pm 2$ |
| NGC 7314 | 702015010 | 1 | $21.62^{+0.06}_{-0.06}$ | neutral | $100^{*}$ |
| | | 2 | $21.94^{+0.03}_{-0.03}$ | $1.22^{+0.15}_{-0.12}$ | $100^{*}$ |
| NGC 7469 | 703028010 | 1 | $21.82^{+0.10}_{-0.09}$ | $2.85^{+0.07}_{-0.08}$ | $100^{*}$ |
| PG 1211+143 | 700009010 | 1 | $22.49^{+0.13}_{-0.12}$ | $2.88^{+0.07}_{-0.09}$ | $100^{*}$ |
| PKS 0558−504 | stacked[all] | 1 | $24.28^{+0.04}_{-0.04}$ | $1.94^{+0.09}_{-0.27}$ | $38 \pm 2$ |
| RBS 1124 | 702114010 | 1 | $24.62^{+0.22}_{-0.14}$ | neutral | $56 \pm 1$ |
| TON S180 | 701021010 | 1 | $24.14^{+0.03}_{-0.07}$ | $1.92^{+0.10}_{-0.73}$ | $64 \pm 1$ |
| SW J2127.4+5456$^{\diamond}$ | 702122010 | 1 | $21.12^{+0.03}_{-0.03}$ | $0.83^{+0.50}_{-0.54}$ | $100^{*}$ |

$^{*}$ Indicates a parameter was tied during spectral fitting;
$^{f}$ Indicates a parameter was frozen during spectral fitting;
$^{\diamond}$ Indicates that a highly-ionised outflow is detected in this source.

Table B.3: Warm absorber parameters for multi-epoch spectra. *Columns*: (1) Source name; (2) *Suzaku* observation ID; (3) Absorption zone; (4) Logarithm of absorber column density, in units of $\mathrm{cm}^{-2}$; (5) Logarithm of absorber ionisation parameter, in units of $\mathrm{erg\,cm\,s}^{-1}$; (6) Absorber covering fraction, in per cent. All absorption components are required at $P_{\mathrm{F}} > 99\%$ significance.

| Source (1) | OBSID (2) | Zone (3) | $\log(N_{\mathrm{H}})$ (4) | $\log(\xi)$ (5) | $f_{\mathrm{cov}}$ (6) |
|---|---|---|---|---|---|
| 3C 111$^{\diamond}$ | 703034010 | 1 | $21.83^{+0.01}_{-0.01}$ | neutral | $100^{\,*}$ |
| | 705040010 | 1 | $21.83^{*}$ | neutral$^{*}$ | $100^{*}$ |
| | 705040020 | 1 | $21.83^{*}$ | neutral$^{*}$ | $100^{*}$ |
| | 705040030 | 1 | $21.83^{*}$ | neutral$^{*}$ | $100^{*}$ |
| 3C 120 | 700001010 | 1 | $20.96^{+0.06}_{-0.06}$ | neutral | $100^{\,*}$ |
| | stacked[bcd] | 1 | $20.96^{*}$ | neutral$^{*}$ | $100^{*}$ |
| Mrk 509 | 705025010 | 1 | $21.40^{+0.04}_{-0.03}$ | $2.19^{+0.04}_{-0.05}$ | $100^{\,*}$ |
| | stacked[bc] | 1 | $21.40^{*}$ | $2.19^{*}$ | $100^{*}$ |
| | 705025010 | 1 | $21.40^{*}$ | $2.19^{*}$ | $100^{*}$ |
| Mrk 766$^{\diamond}$ | 701035010 | 1 | $22.66^{+0.03}_{-0.02}$ | $2.19^{+0.03}_{-0.03}$ | $94 \pm 4$ |
| | | 2 | $21.86^{+0.06}_{-0.06}$ | $1.80^{+0.04}_{-0.04}$ | $100^{\,*}$ |
| | 701035020 | 1 | $22.66^{*}$ | $2.19^{*}$ | $< 14$ |
| | | 2 | $21.86^{*}$ | $1.80^{*}$ | $100^{*}$ |
| NGC 1365$^{\diamond}$ | 702047010 | 1 | $24.11^{+0.02}_{-0.03}$ | $2.42^{+0.24}_{-0.24}$ | $55^{+5}_{-4}$ |
| | | 2 | $23.02^{+0.01}_{-0.01}$ | neutral | $42^{+4}_{-3}$ |
| | | 3 | $22.82^{+0.06}_{-0.06}$ | $3.21^{+0.04}_{-0.04}$ | $42*$ |
| | 705031010 | 1 | $24.11^{*}$ | $2.42^{*}$ | $40^{+2}_{-3}$ |
| | | 2 | $23.02^{+0.01}_{-0.01}$ | neutral$^{*}$ | $58 \pm 2$ |
| | | 3 | $23.82^{+0.06}_{-0.06}$ | $3.21^{*}$ | $58*$ |
| NGC 3227$^{\diamond}$ | 703022010 | 1 | $22.16^{+0.01}_{-0.01}$ | $0.81 \pm 0.05$ | $100^{\,*}$ |
| | | 2 | $23.06^{+0.01}_{-0.01}$ | $2.34 \pm 0.02$ | $55 \pm 5$ |
| | 703022020 | 1 | $22.16^{*}$ | $1.00^{+0.05}_{-0.13}$ | $100^{*}$ |
| | | 2 | $23.06^{*}$ | $-0.11 \pm 0.04$ | $86 \pm 8$ |
| | 703022030 | 1 | $22.16^{*}$ | $0.67^{+0.11}_{-0.11}$ | $100^{*}$ |
| | | 2 | $23.06^{*}$ | $1.53 \pm 0.05$ | $87 \pm 4$ |
| | 703022040 | 1 | $22.16^{*}$ | $1.13^{+0.09}_{-0.08}$ | $100^{*}$ |
| | | 2 | $23.06^{*}$ | $-1.15^{+0.19}_{-0.18}$ | $83 \pm 6$ |
| | 703022050 | 1 | $22.16^{*}$ | $0.66^{+0.16}_{-0.16}$ | $100^{*}$ |
| | | 2 | $23.06^{*}$ | $1.24 \pm 0.04$ | $91 \pm 4$ |
| | 703022060 | 1 | $22.16^{*}$ | $0.51^{+0.23}_{-0.17}$ | $100^{*}$ |
| | | 2 | $23.06^{*}$ | $0.67^{+0.12}_{-0.11}$ | $90 \pm 5$ |
| NGC 3516$^{\diamond}$ | 100031010 | 1 | $24.22^{+0.02}_{-0.02}$ | $2.00^{+0.02}_{-0.04}$ | $46 \pm 4$ |

Continued on next page...

Table B.3: Warm absorber parameters for multi-epoch spectra (continued)

| Source (1) | OBSID (2) | Zone (3) | $\log(N_{\rm H})$ (4) | $\log(\xi)$ (5) | $f_{\rm cov}$ (6) |
|---|---|---|---|---|---|
| | | 2 | $23.27^{+0.01}_{-0.01}$ | $1.89^{+0.04}_{-0.04}$ | $> 93$ |
| | | 3 | $21.32^{+0.01}_{-0.01}$ | $1.01^{+0.07}_{-0.05}$ | $> 99$ |
| | | 4 | $21.50^{+0.10}_{-0.09}$ | $< 0.14$ | $> 99^{*}$ |
| | 704062010 | 1 | $24.22^{*}$ | $2.00^{*}$ | $48^{+9}_{-8}$ |
| | | 2 | $23.27^{*}$ | $1.89 \pm 0.04$ | $58 \pm 11$ |
| | | 3 | $21.32^{*}$ | $1.01^{*}$ | $> 77$ |
| | | 4 | $21.50^{*}$ | $< 0.14^{*}$ | $> 77^{*}$ |
| NGC 3783$^{\diamond}$ | 701033010 | 1 | $23.76^{+0.02}_{-0.02}$ | $1.92^{+0.04}_{-0.12}$ | $27 \pm 3$ |
| | | 2 | $22.23^{+0.01}_{-0.01}$ | $1.56^{+0.01}_{-0.01}$ | $100^{*}$ |
| | | 3 | $22.10^{+0.09}_{-0.09}$ | $2.77^{+0.07}_{-0.07}$ | $100^{*}$ |
| | 704063010 | 1 | $23.76^{*}$ | $2.41^{+0.06}_{-0.06}$ | $22 \pm 1$ |
| | | 2 | $22.23^{*}$ | $1.92^{*}$ | $100^{*}$ |
| | | 3 | $22.10^{*}$ | $2.77^{*}$ | $100^{*}$ |
| NGC 4051$^{\diamond}$ | 100004010 | 1 | $24.36^{+0.01}_{-0.01}$ | $2.11^{+0.02}_{-0.02}$ | $26 \pm 2$ |
| | | 2 | $23.14^{+0.02}_{-0.02}$ | $1.65^{+0.05}_{-0.05}$ | $< 14$ |
| | | 3 | $21.41^{+0.01}_{-0.01}$ | $1.46^{+0.03}_{-0.03}$ | $100^{*}$ |
| | 703023010 | 1 | $24.36^{*}$ | $2.11^{*}$ | $50 \pm 6$ |
| | | 2 | $23.14^{*}$ | $1.65^{*}$ | $40 \pm 2$ |
| | | 3 | $20.54^{+0.05}_{-0.04}$ | $1.46^{*}$ | $100^{*}$ |
| | 703023020 | 1 | $24.36^{*}$ | $2.11^{*}$ | $< 10$ |
| | | 2 | $23.14^{*}$ | $1.65^{*}$ | $32 \pm 3$ |
| | | 3 | $21.41^{*}$ | $1.46^{*}$ | $100^{*}$ |
| PDS 456$^{\diamond}$ | 701056010 | 1 | $22.98^{+0.03}_{-0.04}$ | $2.15^{+0.04}_{-0.04}$ | $28 \pm 2$ |
| | | 2 | $22.00^{+0.08}_{-0.08}$ | $3.13^{+0.10}_{-0.11}$ | $100^{*}$ |
| | 705041010 | 1 | $22.98^{*}$ | $2.15^{*}$ | $56 \pm 3$ |
| | | 2 | $22.00^{*}$ | $1.65^{+0.11}_{-0.12}$ | $100^{*}$ |

$^{*}$ Indicates a parameter was tied during spectral fitting;
$^{f}$ Indicates a parameter was frozen during spectral fitting;
$^{\diamond}$ Indicates that a highly-ionised outflow is detected in this source.

Table B.4: Principal emission components in the 5-10 keV band. *Columns*: (1) Source name; (2) *Suzaku* observation ID; (3) Absorption line identification. In cases where a broad component is required G and DL refer to a broad Gaussian or `diskline`, respectively; (4) Measured line energy in the source rest-frame, in units of keV; (5) Measured line energy-width, in units of eV. Unresolved lines were fit with widths fixed at 10 eV; (6) Line intensity, in units of $10^{-6}\,\mathrm{erg\,cm^{-2}\,s^{-1}}$; (7) Line equivalent width, in units of eV; (8) Change in fit statistic (and degrees of freedom) when line is removed from the best-fit model; (9) Line significance according to the F-test.

| Source (1) | OBSID (2) | Line ID (3) | Energy (4) | $\sigma$-width (5) | Intensity (6) | EW (7) | $\Delta\chi^2/\Delta\nu$ (8) | $P_{\rm F}$ (9) |
|---|---|---|---|---|---|---|---|---|
| 1H 0419−577 | stacked[all] | Fe K$\alpha$[$\beta$] | $6.39^{+0.02}_{-0.02}$ | 10* | $4.6^{+1.1}_{-1.1}$ | $21^{+4}_{-4}$ [$3\pm1$] | 35.4 | $>99.99$ |
| 3C 111$^{\diamond}$ | 703034010 | Fe K$\alpha$[$\beta$] | $6.39^{+0.02}_{-0.02}$ | 10* | $17.1^{+3.1}_{-3.0}$ | $87^{+8}_{-12}$ [$10^{+2}_{-2}$] | 102.2/2 | $>99.99$ |
| | 705040010 | Fe K$\alpha$[$\beta$] | $6.38^{+0.02}_{-0.02}$ | 10* | $26.1^{+4.0}_{-4.0}$ | $46^{+8}_{-7}$ [$6\pm1$] | 93.0/2 | $>99.99$ |
| | | Fe XXVI? | $6.85^{+0.10}_{-0.09}$ | 10* | $8.5^{+3.8}_{-3.8}$ | $17^{+5}_{-6}$ | 13.0 | $>99.99$ |
| | 705040020 | Fe K$\alpha$[$\beta$] | $6.38^{+0.04}_{-0.04}$ | 10* | $14.3^{+4.4}_{-4.4}$ | $19^{+6}_{-6}$ [$4\pm1$] | 49.0 | $>99.99$ |
| | 705040030 | Fe K$\alpha$[$\beta$] | $6.40^{+0.03}_{-0.03}$ | 10* | $20.6^{+4.4}_{-4.4}$ | $29^{+5}_{-6}$ [$5\pm1$] | 68.7 | $>99.99$ |
| 3C 120 | 700001010 | Fe K$\alpha$[$\beta$] | $6.39^{+0.03}_{-0.03}$ | 10* | $18.0^{+4.4}_{-4.4}$ | $31^{+8}_{-8}$ [$5^{+1}_{-1}$] | 37.5/2 | $>99.99$ |
| | | broad(G) | $6.54^{+0.12}_{-0.12}$ | $300^{+162}_{-86}$ | $32.2^{+8.8}_{-8.8}$ | $58^{+36}_{-40}$ | 13.4/3 | 99.62 |
| | stacked[bcd] | Fe K$\alpha$[$\beta$] | $6.39^{+0.01}_{-0.01}$ | 10* | $19.9^{+2.4}_{-2.4}$ | $38^{+4}_{-4}$ [$6^{+2}_{-2}$] | 162.5/2 | $>99.99$ |
| | | broad(G) | $6.40^{+0.09}_{-0.10}$ | $432^{+100}_{-84}$ | $34.9^{+6.4}_{-6.2}$ | $70^{+13}_{-13}$ | 106.4/3 | $>99.99$ |
| 3C 382 | 702125010 | Fe K$\alpha$[$\beta$] | $6.35^{+0.03}_{-0.03}$ | 10* | $11.8^{+2.7}_{-2.7}$ | $23^{+5}_{-5}$ [$4^{+1}_{-1}$] | 46.6/2 | $>99.99$ |
| | | broad(DL) | 6.4* | ⋯ | $32.1^{+6.3}_{-6.3}$ | $105^{+11}_{-11}$ | 38.2/4 | $>99.99$ |
| | | Ni K$\alpha$ | $7.50^{+0.05}_{-0.05}$ | 10* | $5.0^{+2.6}_{-2.6}$ | $14^{+6}_{-6}$ | 9.8/2 | 99.24 |
| 3C 390.3$^{\diamond}$ | 701060010 | Fe K$\alpha$[$\beta$] | $6.38^{+0.02}_{-0.02}$ | $87^{+32}_{-29}$ | $26.9^{+4.6}_{-4.3}$ | $69^{+10}_{-10}$ [$11^{+2}_{-2}$] | 105.5/3 | $>99.99$ |
| | | Fe XXV | $6.62^{+0.04}_{-0.04}$ | 10* | $7.6^{+2.7}_{-2.7}$ | $19^{+7}_{-7}$ | 20.8/2 | $>99.99$ |
| 3C 445 | 702056010 | Fe K$\alpha$[$\beta$] | $6.38^{+0.01}_{-0.01}$ | $<47$ | $21.3^{+2.8}_{-2.6}$ | $104^{+14}_{-13}$ [$18^{+2}_{-2}$] | 212.5/3 | $>99.99$ |
| 4C +74.26$^{\diamond}$ | 702057010 | Fe K$\alpha$[$\beta$] | $6.33^{+0.06}_{-0.06}$ | 10* | $6.2^{+3.5}_{-3.5}$ | $13^{+7}_{-7}$ [$2^{+1}_{-1}$] | 9.5/2 | 99.07 |
| | | broad(G) | $6.21^{+0.12}_{-0.13}$ | $274^{+216}_{-117}$ | $24.8^{+7.8}_{-7.8}$ | $47^{+15}_{-15}$ | 13.4/3 | $>99.59$ |
| APM 08279+5255$^{\diamond}$ | stacked | Fe K$\alpha$[$\beta$] | $6.52^{+0.12}_{-0.09}$ | 10* | $5.1^{+2.4}_{-2.4}$ | $13^{+6}_{6}$ [$\cdots$] | 9.8/2 | 99.03 |
| Ark 120 | 702014010 | Fe K$\alpha$[$\beta$] | $6.40^{+0.02}_{-0.02}$ | 10* | $50.0^{+6.6}_{-6.6}$ | $18^{+3}_{-3}$ [$13^{+3}_{-3}$] | 108.3/2 | $>99.99$ |

Continued on next page...

Table B.4: Principal emission components in the 5-10 keV band (continued)

| Source (1) | OBSID (2) | Line ID (3) | Energy (4) | $\sigma$-width (5) | Intensity (6) | EW (7) | $\Delta\chi^2/\Delta\nu$ (8) | $P_{\rm F}$ (9) |
|---|---|---|---|---|---|---|---|---|
| | | broad(G) | $6.26^{+0.14}_{-0.14}$ | $564^{+136}_{-111}$ | $42.4^{+8.9}_{-8.5}$ | $113^{+24}_{-23}$ | 39.7/3 | $>99.99$ |
| | | Fe XXVI | $6.94^{+0.04}_{-0.04}$ | $10^*$ | $7.4^{+2.6}_{-2.6}$ | $26^{+9}_{-9}$ | 17.9/2 | $>99.99$ |
| Ark 564 | 702117010 | Fe XXV | $6.59^{+0.06}_{-0.06}$ | $10^*$ | $5.2^{+1.8}_{-1.8}$ | $31^{+12}_{-12}$ | 21.1/2 | $>99.99$ |
| CBS 126$^\diamond$ | 705042010 | Fe K$\alpha$[$\beta$] | $6.44^{+0.05}_{-0.04}$ | $10^*$ | $4.3^{+1.2}_{-1.2}$ | $85^{+22}_{-22}$ [$15^{+4}_{-4}$] | 30.7/2 | $>99.99$ |
| ESO 103-G035$^\diamond$ | 703031010 | Fe K$\alpha$[$\beta$] | $6.40^{+0.02}_{-0.02}$ | $69^{+22}_{-22}$ | $64.5^{+6.1}_{-5.9}$ | $52^{+5}_{-5}$ [$8^{+1}_{-1}$] | 397.7/3 | $>99.99$ |
| | | broad(G) | $6.46^{+0.10}_{-0.10}$ | $546^{+90}_{-90}$ | $95.5^{+13.9}_{-13.9}$ | $76^{+11}_{-11}$ | 89.8/3 | $>99.99$ |
| Fairall 9 | 702043010 | Fe K$\alpha$[$\beta$] | $6.39^{+0.01}_{-0.01}$ | $10^*$ | $25.0^{+1.9}_{-1.9}$ | $91^{+8}_{-8}$ | 401.9/2 | $>99.99$ |
| | | broad(DL) | $6.36^{+0.04}_{-0.04}$ | ... | $28.1^{+4.3}_{-4.3}$ | $112^{+37}_{-37}$ | 52.6/5 | $>99.99$ |
| | 705063010 | Fe K$\alpha$[$\beta$] | $6.40^{+0.01}_{-0.01}$ | $10^*$ | $22.8^{+2.1}_{-2.1}$ | $76^{+14}_{-14}$ | 296.1/2 | $>99.99$ |
| | | broad(DL) | $6.36^*$ | ... | $20.8^{+4.6}_{-4.6}$ | $75^{+60}_{-60}$ | 84.8/5 | $>99.99$ |
| IC 4329A | stacked[all] | Fe K$\alpha$[$\beta$] | $6.38^{+0.01}_{-0.01}$ | $45^{+17}_{-20}$ | $74.1^{+8.4}_{-8.1}$ | $59^{+7}_{-7}$ [$9^{+1}_{-1}$] | 314.6/3 | $>99.99$ |
| IGR J16185−5928 | 702123010 | Fe K$\alpha$[$\beta$] | $6.44^{+0.04}_{-0.04}$ | $10^*$ | $6.2^{+1.9}_{-1.9}$ | $68^{+21}_{-21}$ [$10^{+4}_{-4}$] | 26.4/2 | $>99.99$ |
| IGR J21274+5058 | 702027010 | Fe K$\alpha$[$\beta$] | $6.37^{+0.03}_{-0.03}$ | $10^*$ | $19.1^{+5.1}_{-5.1}$ | $20^{+5}_{-5}$ [$3^{+1}_{-1}$] | 39.7/2 | $>99.99$ |
| | | ? | $5.89^{+0.05}_{-0.05}$ | $10^*$ | $10.9^{+5.1}_{-5.1}$ | $10^{+5}_{-5}$ | 11.9/2 | 99.65 |
| MCG -02-14-009 | 703060010 | Fe K$\alpha$[$\beta$] | $6.43^{+0.04}_{-0.04}$ | $10^*$ | $4.4^{+1.1}_{-1.1}$ | $92^{+27}_{-27}$ [$14^{+4}_{-4}$] | 35.7/2 | $>99.99$ |
| MCG -2-58-22 | 704032010 | Fe K$\alpha$[$\beta$] | $6.41^{+0.02}_{-0.02}$ | $10^*$ | $21.1^{+3.0}_{-3.0}$ | $37^{+5}_{-5}$ [$6^{+1}_{-1}$] | 119.4/2 | $>99.99$ |
| MCG -5-23-16 | 700002010 | Fe K$\alpha$[$\beta$] | $6.40^{+0.01}_{-0.01}$ | $54^{+11}_{-11}$ | $85.8^{+5.7}_{-5.7}$ | $76^{+5}_{-5}$ [$12^{+1}_{-1}$] | 804.3/3 | $>99.99$ |
| MCG -6-30-15$^\diamond$ | stacked[all] | Fe K$\alpha$[$\beta$] | $6.38^{+0.01}_{-0.01}$ | $10^*$ | $11.6^{+1.3}_{-1.3}$ | $25^{+3}_{-3}$ [$3^{+1}_{-1}$] | 145.0/2 | $>99.99$ |
| | | broad(G) | $6.03^{+0.12}_{-0.12}$ | $646^{+97}_{-83}$ | $35.6^{+5.1}_{-4.9}$ | $70^{+10}_{-10}$ | 32.9/3 | $>99.99$ |
| | | ? | $6.55^{+0.03}_{-0.03}$ | $10^*$ | $5.3^{+1.5}_{-1.5}$ | $12^{+3}_{-3}$ | 29.6/2 | $>99.99$ |
| MCG +8-11-11 | 702112010 | Fe K$\alpha$[$\beta$] | $6.38^{+0.01}_{-0.01}$ | $41^{+19}_{-24}$ | $54.3^{+6.0}_{-5.8}$ | $68^{+8}_{-7}$ [$11^{+1}_{-1}$] | 303.5/3 | $>99.99$ |
| | | broad(G) | $6.17^{+0.13}_{-0.14}$ | $462^{+182}_{-156}$ | $55.1^{+14.9}_{-14.3}$ | $60^{+16}_{-16}$ | 50.9/3 | $>99.99$ |
| | | Fe XXVI | $6.95^{+0.03}_{-0.03}$ | $10^*$ | $14.2^{+4.3}_{-4.3}$ | $21^{+6}_{-6}$ | 15.6/2 | 99.95 |
| MR 2251−178$^\diamond$ | 704055010 | Fe K$\alpha$[$\beta$] | $6.44^{+0.03}_{-0.03}$ | $10^*$ | $11.9^{+2.7}_{-2.7}$ | $22^{+5}_{-5}$ [$3^{+1}_{-1}$] | 52.2/2 | $>99.99$ |
| Mrk 79 | 702044010 | Fe K$\alpha$[$\beta$] | $6.39^{+0.01}_{-0.01}$ | $<58$ | $23.7^{+2.8}_{-2.8}$ | $133^{+17}_{-17}$ [$22^{+3}_{-3}$] | 232.5/3 | $>99.99$ |

Continued on next page...

Table B.4: Principal emission components in the 5-10 keV band (continued)

| Source (1) | OBSID (2) | Line ID (3) | Energy (4) | $\sigma$-width (5) | Intensity (6) | EW (7) | $\Delta\chi^2/\Delta\nu$ (8) | $P_{\rm F}$ (9) |
|---|---|---|---|---|---|---|---|---|
| | | Fe XXV | $6.63^{+0.04}_{-0.04}$ | 10 * | $6.5^{+2.2}_{-2.0}$ | $34^{+10}_{-10}$ | 15.9/2 | 99.98 |
| Mrk 110 | 702124010 | Fe K$\alpha[\beta]$ | $6.41^{+0.03}_{-0.03}$ | 10 * | $12.0^{+2.6}_{-2.6}$ | $51^{+12}_{-12}$ $[8^{+2}_{-2}]$ | 52.4/2 | > 99.99 |
| Mrk 205 | 705062010 | Fe K$\alpha[\beta]$ | $6.40^{+0.03}_{-0.03}$ | < 108 | $9.3^{+2.8}_{-2.5}$ | $80^{+24}_{-24}$ $[13^{+3}_{-3}]$ | 43.9/3 | > 99.99 |
| Mrk 279$^{\diamond}$ | 704031010 | Fe K$\alpha[\beta]$ | $6.40^{+0.01}_{-0.01}$ | 10 * | $12.4^{+1.1}_{-1.2}$ | $205^{+20}_{-20}$ $[33^{+3}_{-3}]$ | 326.6/2 | > 99.99 |
| | | Fe XXV | $6.63^{+0.07}_{-0.07}$ | 10 * | $1.7^{+0.9}_{-0.9}$ | $23^{+13}_{-13}$ | 9.4/2 | 99.14 |
| Mrk 335 | 703034010 | Fe K$\alpha[\beta]$ | $6.39^{+0.03}_{-0.03}$ | < 89 | $7.5^{+1.8}_{-1.7}$ | $45^{+10}_{-10}$ $[8^{+2}_{-2}]$ | 63.9/3 | > 99.99 |
| | | broad(DL) | 6.4 * | ... | $22.1^{+3.4}_{-3.2}$ | $172^{+22}_{-28}$ | 146.7/4 | > 99.99 |
| Mrk 359 | 701082010 | Fe K$\alpha[\beta]$ | $6.42^{+0.03}_{-0.03}$ | $96^{+55}_{-55}$ | $7.0^{+1.8}_{-1.8}$ | $119^{+27}_{-26}$ $[17^{+4}_{-4}]$ | 44.3/3 | > 99.99 |
| Mrk 509 | 701093010 | Fe K$\alpha[\beta]$ | $6.44^{+0.04}_{-0.04}$ | 10 * | $23.3^{+5.4}_{-5.4}$ | $45^{+11}_{-11}$ $[7^{+1}_{-1}]$ | 37.4/2 | > 99.99 |
| | stacked[bcd] | Fe K$\alpha[\beta]$ | $6.42^{+0.02}_{-0.02}$ | $68^{+48}_{-62}$ | $26.9^{+5.4}_{-4.9}$ | $50^{+10}_{-10}$ $[7^{+1}_{-1}]$ | 122.5/3 | > 99.99 |
| | | broad(G) | $6.73^{+0.20}_{-0.20}$ | $606^{+183}_{-175}$ | $37.6^{+10.1}_{-9.8}$ | $74^{+19}_{-19}$ | 48.4/3 | > 99.99 |
| | 705025010 | Fe K$\alpha[\beta]$ | $6.41^{+0.02}_{-0.02}$ | $67^{+25}_{-30}$ | $34.0^{+4.8}_{-4.7}$ | $57^{+9}_{-9}$ $[9^{+1}_{-1}]$ | 169.72/3 | > 99.99 |
| | | broad(G) | $6.33^{+0.15}_{-0.15}$ | $517^{+166}_{-113}$ | $43.0 \pm 8.8$ | $67^{+14}_{-13}$ | 24.9/3 | > 99.99 |
| Mrk 766$^{\diamond}$ | 701035010 | Fe K$\alpha[\beta]$ | $6.41^{+0.03}_{-0.03}$ | 10 * | $5.68^{+1.82}_{-1.82}$ | $39^{+12}_{-12}$ $[7^{+2}_{-2}]$ | 28.6/2 | > 99.99 |
| | | Fe XXV | $6.62^{+0.03}_{-0.03}$ | 10 * | $8.80^{+1.95}_{-1.95}$ | $63^{+13}_{-13}$ | 61.6/2 | > 99.99 |
| | 701035020 | Fe K$\alpha[\beta]$ | $6.43^{+0.03}_{-0.03}$ | 10 * | $8.02^{+2.32}_{-2.32}$ | $52^{+17}_{-17}$ $[9^{+3}_{-3}]$ | 32.5/2 | > 99.99 |
| Mrk 841 | stacked[all] | Fe K$\alpha[\beta]$ | $6.37^{+0.02}_{-0.02}$ | < 75 | $10.7^{+2.4}_{-2.3}$ | $63^{+14}_{-14}$ $[3^{+1}_{-1}]$ | 58.9/3 | > 99.99 |
| | | broad(G) | $5.92^{+0.22}_{-0.23}$ | $570^{+241}_{-162}$ | $18.1^{+10.0}_{-10.0}$ | $101^{+56}_{-56}$ | 34.8/3 | > 99.99 |
| NGC 1365$^{\diamond}$ | 702047010 | Fe K$\alpha[\beta]$ | $6.42^{+0.02}_{-0.02}$ | < 59 | $12.6^{+2.6}_{-2.5}$ | $45^{+9}_{-9}$ $[4^{+1}_{-1}]$ | 83.1/3 | > 99.99 |
| | 705031010 | Fe K$\alpha[\beta]$ | $6.39^{+0.02}_{-0.02}$ | $53^{+30}_{-41}$ | $27.9^{+3.9}_{-3.7}$ | $137^{+15}_{-18}$ $[22^{+4}_{-3}]$ | 135.8/3 | > 99.99 |
| | 705031020 | Fe K$\alpha[\beta]$ | $6.41^{+0.01}_{-0.01}$ | < 43 | $40.8^{+2.6}_{-2.5}$ | $251^{+17}_{-17}$ $[45^{+2}_{-2}]$ | 828.9/3 | > 99.99 |
| | | broad(G) | $5.92^{+0.06}_{-0.05}$ | 10 * | $2.2^{+0.7}_{-0.7}$ | $37^{+12}_{-12}$ | 27.2/2 | > 99.99 |
| NGC 2992 | stacked[all] | Fe K$\alpha[\beta]$ | $6.40^{+0.01}_{-0.01}$ | $39^{+11}_{-13}$ | $36.7^{+2.2}_{-2.2}$ | $260^{+13}_{-15}$ $[40^{+3}_{-1}]$ | 871.0/3 | > 99.99 |
| NGC 3227$^{\diamond}$ | 703022010 | Fe K$\alpha[\beta]$ | $6.38^{+0.01}_{-0.01}$ | $54^{+33}_{-40}$ | $42.9^{+6.9}_{-6.1}$ | $92^{+12}_{-12}$ $[15^{+2}_{-2}]$ | 201.9/3 | > 99.99 |
| | 703022020 | Fe K$\alpha[\beta]$ | $6.40^{+0.01}_{-0.01}$ | $52^{+19}_{-23}$ | $47.3^{+5.0}_{-4.9}$ | $173^{+16}_{-18}$ $[26^{+3}_{-3}]$ | 306.4/3 | > 99.99 |

Continued on next page...

Table B.4: Principal emission components in the 5-10 keV band (continued)

| Source (1) | OBSID (2) | Line ID (3) | Energy (4) | $\sigma$-width (5) | Intensity (6) | EW (7) | $\Delta\chi^2/\Delta\nu$ (8) | $P_{\rm F}$ (9) |
|---|---|---|---|---|---|---|---|---|
| | 703022030 | Fe K$\alpha$[$\beta$] | $6.40^{+0.01}_{-0.01}$ | $71^{+24}_{-26}$ | $46.2^{+5.9}_{-5.8}$ | $127^{+16}_{-16}$ [$19^{+3}_{-3}$] | 194.8/3 | $>99.99$ |
| | 703022040 | Fe K$\alpha$[$\beta$] | $6.40^{+0.01}_{-0.01}$ | $39^{+17}_{-25}$ | $40.9^{+3.7}_{-3.6}$ | $270^{+32}_{-25}$ [$42^{+3}_{-3}$] | 454.4/3 | $>99.99$ |
| | | Fe XXV | $6.68^{+0.05}_{-0.04}$ | $10^{*}$ | $5.8^{+2.5}_{-2.4}$ | $30^{+12}_{-12}$ | 15.2/2 | $>99.99$ |
| | 703022050 | Fe K$\alpha$[$\beta$] | $6.40^{+0.01}_{-0.01}$ | $52^{+20}_{-23}$ | $40.9^{+4.4}_{-4.3}$ | $128^{+14}_{-14}$ [$22^{+2}_{-2}$] | 332.9/3 | $>99.99$ |
| | 703022060 | Fe K$\alpha$[$\beta$] | $6.40^{+0.01}_{-0.01}$ | $<53$ | $34.4^{+4.5}_{-4.4}$ | $145^{+17}_{-17}$ [$22^{+2}_{-2}$] | 213.9/3 | $>99.99$ |
| NGC 3516$^{\diamond}$ | 100031010 | Fe K$\alpha$[$\beta$] | $6.40^{+0.01}_{-0.01}$ | $40^{+9}_{-9}$ | $55.7^{+2.6}_{-2.6}$ | $149^{+7}_{-7}$ [$25^{+1}_{-1}$] | 1416.7/3 | $>99.99$ |
| | 704062010 | Fe K$\alpha$[$\beta$] | $6.40^{+0.01}_{-0.01}$ | $39^{+12}_{-12}$ | $42.2^{+2.0}_{-2.0}$ | $262^{+13}_{-13}$ [$40^{+2}_{-2}$] | 1318.4/3 | $>99.99$ |
| | | Ni ? | $7.43^{+0.05}_{-0.04}$ | $10^{*}$ | $4.8^{+1.5}_{-1.5}$ | $40^{+12}_{-12}$ | 24.0/2 | $>99.99$ |
| NGC 3783$^{\diamond}$ | 701033010 | Fe K$\alpha$[$\beta$] | $6.40^{+0.01}_{-0.01}$ | $50^{+13}_{-14}$ | $72.8^{+5.1}_{-4.7}$ | $131^{+9}_{-10}$ [$20^{+1}_{-1}$] | 1005.5/3 | $>99.99$ |
| | 704063010 | Fe K$\alpha$[$\beta$] | $6.39^{+0.01}_{-0.01}$ | $10^{*}$ | $68.4^{+3.5}_{-3.5}$ | $97^{+5}_{-5}$ [$15^{+1}_{-1}$] | 1057.8/3 | $>99.99$ |
| NGC 4051$^{\diamond}$ | 700004010 | ? | $5.44^{+0.03}_{-0.03}$ | $10^{*}$ | $2.7^{+1.1}_{-1.1}$ | $19^{+8}_{-8}$ | 13.8/2 | 99.85 |
| | | Fe K$\alpha$[$\beta$] | $6.40^{+0.01}_{-0.01}$ | $43^{+17}_{-22}$ | $15.4^{+1.6}_{-1.6}$ | $140^{+15}_{-15}$ [$12^{+1}_{-1}$] | 273.2/3 | $>99.99$ |
| | | Fe XXV | $6.63^{*}$ | $10^{*}$ | $3.3^{+1.2}_{-1.2}$ | $25^{+11}_{-11}$ | 12.6/2 | 99.82 |
| | | Ni K$\alpha$ | $7.58^{+0.09}_{-0.09}$ | $10^{*}$ | $2.4^{+1.3}_{-1.3}$ | $33^{+17}_{-17}$ | 9.8/2 | 99.02 |
| | 703023010 | Fe K$\alpha$[$\beta$] | $6.41^{+0.01}_{-0.01}$ | $10^{*}$ | $17.4^{+1.6}_{-1.6}$ | $70^{+5}_{-5}$ [$12^{+1}_{-1}$] | 254.5/2 | $>99.99$ |
| | | Fe XXV | $6.61^{+0.03}_{-0.03}$ | $10^{*}$ | $5.5^{+1.4}_{-1.4}$ | $22^{+5}_{-5}$ | 67.8/2 | $>99.99$ |
| | 703023020 | Fe K$\alpha$[$\beta$] | $6.42^{+0.02}_{-0.02}$ | $<108$ | $18.6^{+3.7}_{-3.7}$ | $100^{+15}_{-20}$ | 108.4/3 | $>99.99$ |
| | | Fe XXV | $6.59^{+0.04}_{-0.04}$ | $10^{*}$ | $7.2^{+2.4}_{-2.4}$ | $37^{+1}_{-1}$ | 25.4/2 | $>99.99$ |
| NGC 4151$^{\diamond}$ | 701034010 | Fe K$\alpha$[$\beta$] | $6.39^{+0.01}_{-0.01}$ | $28^{+5}_{-5}$ | $169.5^{+4.8}_{-4.7}$ | $294^{+8}_{-8}$ [$40^{+1}_{-1}$] | 4185.4/3 | $>99.99$ |
| NGC 4395$^{\diamond}$ | 701001010 | Fe K$\alpha$[$\beta$] | $6.38^{+0.05}_{-0.05}$ | $10^{*}$ | $3.4^{+1.3}_{-1.3}$ | $55^{+22}_{-22}$ [$9^{+3}_{-3}$] | 18.2/2 | $>99.99$ |
| NGC 4593 | 702040010 | Fe K$\alpha$[$\beta$] | $6.43^{+0.01}_{-0.01}$ | $50^{+11}_{-12}$ | $34.0^{+2.4}_{-2.3}$ | $271^{+19}_{-19}$ [$41^{+3}_{-3}$] | 623.6/3 | $>99.99$ |
| | | Fe XXV | $6.70^{+0.06}_{-0.06}$ | $10^{*}$ | $4.4^{+1.8}_{-2.0}$ | $23^{+9}_{-10}$ | 12.7/2 | 99.80 |
| NGC 5506$^{\diamond}$ | stacked[all] | Fe K$\alpha$[$\beta$] | $6.40^{+0.01}_{-0.01}$ | $75^{+12}_{-12}$ | $96.4^{+6.5}_{-6.5}$ | $66^{+5}_{-5}$ [$11^{+1}_{-1}$] | 677.7/3 | $>99.99$ |
| | | Fe XXV | $6.62^{+0.03}_{-0.03}$ | $10^{*}$ | $19.2^{+4.5}_{-4.5}$ | $13^{+3}_{-3}$ | 31.0/2 | $>99.99$ |
| NGC 5548 | stacked[all] | Fe K$\alpha$[$\beta$] | $6.38^{+0.01}_{-0.01}$ | $51^{+15}_{-16}$ | $23.4^{+2.2}_{-2.1}$ | $110^{+10}_{-10}$ [$17^{+1}_{-1}$] | 439.5/3 | $>99.99$ |

Continued on next page...

Table B.4: Principal emission components in the 5-10 keV band (continued)

| Source (1) | OBSID (2) | Line ID (3) | Energy (4) | $\sigma$-width (5) | Intensity (6) | EW (7) | $\Delta\chi^2/\Delta\nu$ (8) | $P_{\rm F}$ (9) |
|---|---|---|---|---|---|---|---|---|
| NGC 7213 | 701029010 | Fe K$\alpha[\beta]$ | $6.40^{+0.01}_{-0.01}$ | $< 38$ | $20.3^{+2.3}_{-2.2}$ | $79^{+9}_{-9}$ $[12^{+1}_{-1}]$ | 270.0/3 | $> 99.99$ |
| | | Fe XXV | $6.64^{+0.04}_{-0.03}$ | $10^{*}$ | $5.2^{+1.8}_{-1.8}$ | $19^{+6}_{-6}$ | 22.5/2 | $> 99.99$ |
| | | Fe XXVI | $6.95^{+0.03}_{-0.03}$ | $10^{*}$ | $7.5^{+1.8}_{-1.8}$ | $33^{+8}_{-8}$ | 43.2/2 | $> 99.99$ |
| NGC 7469 | 703028010 | Fe K$\alpha[\beta]$ | $6.40^{+0.01}_{-0.01}$ | $< 65$ | $23.1^{+3.2}_{-3.1}$ | $94^{+13}_{-13}$ $[9^{+1}_{-1}]$ | 253.4/3 | $> 99.99$ |
| | | broad(G) | $6.41^{+0.12}_{-0.09}$ | $262^{+142}_{-109}$ | $20.5^{+6.4}_{-5.8}$ | $84^{+26}_{-24}$ | 23.1/3 | $> 99.99$ |
| PDS 456$^{\diamond}$ | 701056010 | blend? | $7.04^{+0.17}_{-0.15}$ | $238^{+214}_{-126}$ | $3.2^{+1.7}_{-1.5}$ | $72^{+32}_{-32}$ | 12.8/3 | $> 99.22$ |
| PG 1211+143 | 700009010 | Fe K$\alpha[\beta]$ | $6.37^{+0.04}_{-0.04}$ | $10^{*}$ | $3.2^{+1.1}_{-1.1}$ | $59^{+20}_{-20}$ $[10^{+3}_{-3}]$ | 20.2/2 | $> 99.99$ |
| | | Fe XXV | $6.64^{+0.03}_{-0.04}$ | $93^{+46}_{-46}$ | $6.9^{+1.8}_{-1.7}$ | $130^{+34}_{-32}$ | 50.7/3 | $> 99.99$ |
| SW J2127.4+5654$^{\diamond}$ | 702122010 | Fe K$\alpha[\beta]$ | $6.40^{+0.07}_{-0.07}$ | $10^{*}$ | $6.0^{+4.3}_{-4.3}$ | $16^{+11}_{-11}$ $[3^{+2}_{-2}]$ | 10.8/2 | $> 99.99$ |
| | | broad(G) | $6.22^{+0.14}_{-0.16}$ | $496^{+175}_{-131}$ | $39.1^{+12.9}_{-12.1}$ | $100^{+33}_{-30}$ | 23.6/3 | $> 99.99$ |

$^{*}$ Indicates a parameter was tied during spectral fitting;
$^{f}$ Indicates a parameter was frozen during spectral fitting;
$^{\diamond}$ Indicates that a highly-ionised outflow is detected in this source.

# Publications

## Reviewed

1. *"Discovery of Ultra-fast Outflows in a Sample of Broad-line Radio Galaxies Observed with Suzaku"*; Tombesi, F., Sambruna, R. M., Reeves, J. N., Braito, V., Ballo, L., **Gofford, J.**, Cappi, M., Mushotzky, R. F., 2010, ApJ, 719, 700

2. *"Chandra High-resolution Spectroscopy of the Circumnuclear Matter in the Broad-line Radio Galaxy 3C 445"*; Reeves, J. N., **Gofford, J.**, Braito, V., Sambruna, R., 2010, MNRAS, 725, 803

3. *"Evidence for a circumnuclear and ionized absorber in the X-ray obscured broad-line radio galaxy 3C 445"*; Braito, V., Reeves, J. N., Sambruna, R. M., **Gofford, J.**, 2011, MNRAS, 414, 2139

4. *"A broad-band X-ray view of the warm absorber in radio-quiet quasar MR 2251-178"*; **Gofford, J.**, Reeves, J. N., Turner, T. J., Tombesi, F., Braito, V., Porquet, D., Miller, L., Kraemer, S. B., Fukazawa, Y., 2011, MNRAS, 414, 3307

5. *"The Suzaku view of highly ionized outflows in AGN - I. Statistical detection and global absorber properties"*; **Gofford, J.**, Reeves, J. N., Tombesi, F., Braito, V., Turner, T. J., Miller, L., Cappi, M., 2013, MNRAS, 430, 60

## In proceedings

6. *"The Suzaku View of Highly-ionized Outflows in AGN"*; **Gofford, J.**, Reeves, J. N., Braito, V., Tombesi, F., 2012, ASPC, 460, 18

# Bibliography

Aller M. C., Richstone D. O., 2007, ApJ, 665, 120

Antonucci R., 1993, Annu. Rev. Astron. Astrophys., 31, 473

Antonucci R. R. J., Miller J. S., 1985, ApJ, 297, 621

Arav N., 1996, ApJ, 465, 617

Arav N., Korista K. T., Barlow T. A., Begelman, 1995, Nature, 376, 576

Arav N., Li Z.-Y., Begelman M. C., 1994, ApJ, 432, 62

Arnaud K., Smith R., Siemiginowska A., 2011, Handbook of X-ray Astronomy, Cambridge Observing Handbooks for Research Astronomers. Cambridge University Press

Arnaud K. A., 1996, in Astronomical Society of the Pacific Conference Series, Vol. 101, Astronomical Data Analysis Software and Systems V, Jacoby G. H., Barnes J., eds., p. 17

Avni Y., 1976, ApJ, 210, 642

Balbus S. A., Hawley J. F., 1991, ApJ, 376, 214

Balbus S. A., Hawley J. F., 1998, Reviews of Modern Physics, 70, 1

Barai P., Martel H., Germain J., 2011, ApJ, 727, 54

Barger A. J., Cowie L. L., Mushotzky R. F., Yang Y., Wang W.-H., Steffen A. T., Capak P., 2005, AJ, 129, 578

Barthelmy S. D. et al., 2005, SSRv, 120, 143

Baumgartner W. H., Tueller J., Markwardt C., Skinner G., 2010, in Bulletin of the American Astronomical Society, Vol. 42, AAS/High Energy Astrophysics Division #11, p. 675

Beckmann V., Shrader C., 2012, Active Galactic Nuclei, Physics textbook. Wiley

Behar E., Kaspi S., Reeves J., Turner T. J., Mushotzky R., O'Brien P. T., 2010, ApJ, 712, 26

Behar E., Netzer H., 2002, ApJ, 570, 165

Behar E., Sako M., Kahn S. M., 2001, ApJ, 563, 497

Bennert V. N., Auger M. W., Treu T., Woo J.-H., Malkan M. A., 2011, ApJ, 742, 107

Bentz M. C., Peterson B. M., Pogge R. W., Vestergaard M., 2009a, ApJL, 694, L166

Bentz M. C. et al., 2009b, ApJ, 705, 199

Bergeron J., Dennefeld M., Boksenberg A., Tarenghi M., 1983, MNRAS, 202, 125

Blandford R. D., Begelman M. C., 1999, MNRAS, 303, L1

Blandford R. D., Payne D. G., 1982, MNRAS, 199, 883

Blandford R. D., Znajek R. L., 1977, MNRAS, 179, 433

Blustin A. J., Page M. J., Fuerst S. V., Branduardi-Raymont G., Ashton C. E., 2005, A&A, 431, 111

Boldt E., 1987, in IAU Symposium, Vol. 124, Observational Cosmology, Hewitt A., Burbidge G., Fang L. Z., eds., pp. 611–615

Boroson T. A., 2002, ApJ, 565, 78

Bottorff M., Korista K. T., Shlosman I., Blandford R. D., 1997, ApJ, 479, 200

Bower R. G., Benson A. J., Malbon R., Helly J. C., Frenk C. S., Baugh C. M., Cole S., Lacey C. G., 2006, MNRAS, 370, 645

Braito V., Reeves J. N., Sambruna R. M., Gofford J., 2011, MNRAS, 414, 2739

Brenneman L. W. et al., 2011, ApJ, 736, 103

Brinkman A. C. et al., 2000, ApJL, 530, L111

Burrows D. N. et al., 2000, in Society of Photo-Optical Instrumentation Engineers (SPIE) Conference Series, Vol. 4140, Society of Photo-Optical Instrumentation Engineers (SPIE) Conference Series, Flanagan K. A., Siegmund O. H., eds., pp. 64–75

Canizares C. R. et al., 2005, PASP, 117, 1144

Canizares C. R., McClintock J. E., Ricker G. R., 1978, ApJL, 226, L1

Cappi M. et al., 2009, A&A, 504, 401

Cash W., 1979, ApJ, 228, 939

Castor J. I., Abbott D. C., Klein R. I., 1975, ApJ, 195, 157

Castor J. L., 1974, MNRAS, 169, 279

Chartas G., Brandt W. N., Gallagher S. C., Garmire G. P., 2002, ApJ, 579, 169

Chartas G., Eracleous M., Dai X., Agol E., Gallagher S., 2007, ApJ, 661, 678

Chartas G., Kochanek C. S., Dai X., Poindexter S., Garmire G., 2009, ApJ, 693, 174

Chatterjee R. et al., 2011, ApJ, 734, 43

Chelouche D., Netzer H., 2003, MNRAS, 344, 223

Chelouche D., Netzer H., 2005, ApJ, 625, 95

Chevallier L., Collin S., Dumont A.-M., Czerny B., Mouchet M., Gonçalves A. C., Goosmann R., 2006, A&A, 449, 493

Ciotti L., Ostriker J. P., 2001, ApJ, 551, 131

Ciotti L., Ostriker J. P., Proga D., 2009, ApJ, 699, 89

Contopoulos J., Lovelace R. V. E., 1994, ApJ, 429, 139

Cooke B. A. et al., 1978, MNRAS, 182, 489

Coppi P. S., 1999, in Astronomical Society of the Pacific Conference Series, Vol. 161, High Energy Processes in Accreting Black Holes, Poutanen J., Svensson R., eds., p. 375

Crenshaw D. M., Kraemer S. B., 2007, ApJ, 659, 250

Crenshaw D. M., Kraemer S. B., 2012, ApJ, 753, 75

Crenshaw D. M., Kraemer S. B., Boggess A., Maran S. P., Mushotzky R. F., Wu C.-C., 1999, ApJ, 516, 750

Crenshaw D. M., Kraemer S. B., George I. M., 2003a, Annu. Rev. Astron. Astrophys., 41, 117

Crenshaw D. M., Kraemer S. B., George I. M., 2003b, Annu. Rev. Astron. Astrophys., 41, 117

Croton D. J. et al., 2006, MNRAS, 365, 11

Crummy J., Fabian A. C., Gallo L., Ross R. R., 2006, MNRAS, 365, 1067

Czerny B., Elvis M., 1987, ApJ, 321, 305

Czerny B., Nikołajuk M., Piasecki M., Kuraszkiewicz J., 2001, MNRAS, 325, 865

Czerny B., Nikołajuk M., Różańska A., Dumont A.-M., Loska Z., Zycki P. T., 2003, A&A, 412, 317

Dadina M., 2008, A&A, 485, 417

Dai X., Kochanek C. S., Chartas G., Kozłowski S., Morgan C. W., Garmire G., Agol E., 2010, ApJ, 709, 278

Davis J. E., 2001, ApJ, 562, 575

den Herder J. W. et al., 2001, A&A, 365, L7

Denney K. D., 2012, ApJ, 759, 44

Dewangan G. C., Griffiths R. E., Dasgupta S., Rao A. R., 2007, ApJ, 671, 1284

Di Matteo T., Springel V., Hernquist L., 2005, Nature, 433, 604

Done C., 2010, ArXiv e-prints

Done C., Davis S. W., Jin C., Blaes O., Ward M., 2012, MNRAS, 420, 1848

Done C., Nayakshin S., 2007, MNRAS, 377, L59

Dunn J. P., Crenshaw D. M., Kraemer S. B., Trippe M. L., 2008, AJ, 136, 1201

Edri H., Rafter S. E., Chelouche D., Kaspi S., Behar E., 2012, ApJ, 756, 73

Egami E., Neugebauer G., Soifer B. T., Matthews K., Ressler M., Becklin E. E., Murphy, Jr. T. W., Dale D. A., 2000, ApJ, 535, 561

Elvis M. et al., 1994, ApJS, 95, 1

Emmering R. T., Blandford R. D., Shlosman I., 1992, ApJ, 385, 460

Everett J. E., 2005, ApJ, 631, 689

Fabian A. C., 1999, MNRAS, 308, L39

Fabian A. C., Iwasawa K., Reynolds C. S., Young A. J., 2000a, PASP, 112, 1145

Fabian A. C. et al., 2000b, MNRAS, 318, L65

Fabian A. C., Sanders J. S., Taylor G. B., Allen S. W., Crawford C. S., Johnstone R. M., Iwasawa K., 2006, MNRAS, 366, 417

Fabian A. C. et al., 2002, MNRAS, 335, L1

Fanaroff B. L., Riley J. M., 1974, MNRAS, 167, 31P

Feng H., Soria R., 2011, nar, 55, 166

Ferrarese L., Ford H., 2005, SSRv, 116, 523

Ferrarese L., Merritt D., 2000, ApJL, 539, L9

Foltz C. B., Weymann R. J., Morris S. L., Turnshek D. A., 1987, ApJ, 317, 450

Frank J., King A., Raine D., 2002, Accretion Power in Astrophysics. Cambridge University Press

Freeman P., Doe S., Siemiginowska A., 2001, in Society of Photo-Optical Instrumentation Engineers (SPIE) Conference Series, Vol. 4477, Society of Photo-Optical Instrumentation Engineers (SPIE) Conference Series, Starck J.-L., Murtagh F. D., eds., pp. 76–87

Fruscione A. et al., 2006, in Society of Photo-Optical Instrumentation Engineers (SPIE) Conference Series, Vol. 6270, Society of Photo-Optical Instrumentation Engineers (SPIE) Conference Series

Fukazawa Y. et al., 2011, ApJ, 727, 19

Fukumura K., Kazanas D., Contopoulos I., Behar E., 2010a, ApJ, 715, 636

Fukumura K., Kazanas D., Contopoulos I., Behar E., 2010b, ApJL, 723, L228

Gallagher S. C., Brandt W. N., Wills B. J., Charlton J. C., Chartas G., Laor A., 2004, ApJ, 603, 425

Gallagher S. C., Everett J. E., 2007, in Astronomical Society of the Pacific Conference Series, Vol. 373, The Central Engine of Active Galactic Nuclei, Ho L. C., Wang J.-W., eds., p. 305

Ganguly R., Brotherton M. S., 2008, ApJ, 672, 102

Ganguly R., Charlton J. C., Eracleous M., 2001, ApJL, 556, L7

García J., Kallman T. R., 2010, ApJ, 718, 695

Garmire G. P., Bautz M. W., Ford P. G., Nousek J. A., Ricker, Jr. G. R., 2003, in Society of Photo-Optical Instrumentation Engineers (SPIE) Conference Series, Vol. 4851, Society of Photo-Optical Instrumentation Engineers (SPIE) Conference Series, Truemper J. E., Tananbaum H. D., eds., pp. 28–44

Gebhardt K. et al., 2000, ApJL, 539, L13

Genzel R., Thatte N., Krabbe A., Kroker H., Tacconi-Garman L. E., 1996, ApJ, 472, 153

George I. M., Fabian A. C., 1991, MNRAS, 249, 352

Germain J., Barai P., Martel H., 2009, ApJ, 704, 1002

Ghez A. M. et al., 2008, ApJ, 689, 1044

Gibson R. R. et al., 2009, ApJ, 692, 758

Gibson R. R., Marshall H. L., Canizares C. R., Lee J. C., 2005, ApJ, 627, 83

Gierliński M., Done C., 2004, MNRAS, 349, L7

Gillessen S., Eisenhauer F., Trippe S., Alexander T., Genzel R., Martins F., Ott T., 2009, ApJ, 692, 1075

Giustini M. et al., 2011, A&A, 536, A49

Goodrich R. W., 1989, ApJ, 342, 224

Grevesse N., Sauval A. J., 1998, SSRv, 85, 161

Grupe D., Wills B. J., Leighly K. M., Meusinger H., 2004, AJ, 127, 156

Guilbert P. W., Rees M. J., 1988, MNRAS, 233, 475

Gültekin K. et al., 2009, ApJ, 698, 198

Haardt F., Maraschi L., 1991, ApJL, 380, L51

Haardt F., Maraschi L., 1993, ApJ, 413, 507

Halpern J. P., 1984, ApJ, 281, 90

Hamann F., Korista K. T., Morris S. L., 1993, ApJ, 415, 541

Häring N., Rix H.-W., 2004, ApJL, 604, L89

Hawley J. F., Gammie C. F., Balbus S. A., 1995, ApJ, 440, 742

Heisler C. A., Lumsden S. L., Bailey J. A., 1997, Nature, 385, 700

Hewett P. C., Foltz C. B., 2003, AJ, 125, 1784

Hopkins P. F., Elvis M., 2010, MNRAS, 401, 7

Hopkins P. F., Hernquist L., Cox T. J., Di Matteo T., Robertson B., Springel V., 2006, ApJS, 163, 1

Hopkins P. F., Richards G. T., Hernquist L., 2007, ApJ, 654, 731

Houck J. C., Denicola L. A., 2000, in Astronomical Society of the Pacific Conference Series, Vol. 216, Astronomical Data Analysis Software and Systems IX, Manset N., Veillet C., Crabtree D., eds., p. 591

Inoue H., Matsumoto C., 2003, PASJ, 55, 625

Iwasawa K., Taniguchi Y., 1993, ApJL, 413, L15

Jansen F. et al., 2001, A&A, 365, L1

Jiang P., Wang J. X., Wang T. G., 2006, ApJ, 644, 725

Jin C., Ward M., Done C., 2012a, MNRAS, 422, 3268

Jin C., Ward M., Done C., 2012b, MNRAS, 425, 907

Jin C., Ward M., Done C., Gelbord J., 2012, MNRAS, 420, 1825

Junkkarinen V. T., 1983, ApJ, 265, 73

Kaastra J. S. et al., 2012, A&A, 539, A117

Kaastra J. S., Mewe R., Nieuwenhuijzen H., 1996, in UV and X-ray Spectroscopy of Astrophysical and Laboratory Plasmas, Yamashita K., Watanabe T., eds., pp. 411–414

Kalberla P. M. W., Burton W. B., Hartmann D., Arnal E. M., Bajaja E., Morras R., Pöppel W. G. L., 2005, A&A, 440, 775

Kallman T. R., McCray R., 1982, ApJS, 50, 263

Kallman T. R., Palmeri P., Bautista M. A., Mendoza C., Krolik J. H., 2004, ApJS, 155, 675

Kaspi S., Brandt W. N., Maoz D., Netzer H., Schneider D. P., Shemmer O., 2007, ApJ, 659, 997

Kaspi S., Maoz D., Netzer H., Peterson B. M., Vestergaard M., Jannuzi B. T., 2005, ApJ, 629, 61

Kaspi S., Netzer H., Chelouche D., George I. M., Nandra K., Turner T. J., 2004, ApJ, 611, 68

Kaspi S., Smith P. S., Netzer H., Maoz D., Jannuzi B. T., Giveon U., 2000, ApJ, 533, 631

Kataoka J. et al., 2007, PASJ, 59, 279

Kazanas D., Fukumura K., Behar E., Contopoulos I., Shrader C., 2012, The Astronomical Review, 7, 030000

Kellermann K. I., Sramek R., Schmidt M., Shaffer D. B., Green R., 1989, AJ, 98, 1195

Kelley R. L. et al., 2007, PASJ, 59, 77

Khachikian E. Y., Weedman D. W., 1974, ApJ, 192, 581

Khorunzhev G. A., Sazonov S. Y., Burenin R. A., Tkachenko A. Y., 2012, Astronomy Letters, 38, 475

King A., 2005, ApJL, 635, L121

King A. L. et al., 2013, ApJ, 762, 103

King A. R., 2010, MNRAS, 402, 1516

King A. R., Pounds K. A., 2003, MNRAS, 345, 657

Kokubun M. et al., 2007, PASJ, 59, 53

Kollmeier J. A. et al., 2006, ApJ, 648, 128

Konigl A., Kartje J. F., 1994, ApJ, 434, 446

Kormendy J., Gebhardt K., 2001, in American Institute of Physics Conference Series, Vol. 586, 20th Texas Symposium on relativistic astrophysics, Wheeler J. C., Martel H., eds., pp. 363–381

Kormendy J., Richstone D., 1995, Annu. Rev. Astron. Astrophys., 33, 581

Koyama K. et al., 2007, PASJ, 59, 23

Kraemer S. B. et al., 2012, ApJ, 751, 84

Kraemer S. B. et al., 2005, ApJ, 633, 693

Kriss G. A., 2002, in Astronomical Society of the Pacific Conference Series, Vol. 255, Mass Outflow in Active Galactic Nuclei: New Perspectives, Crenshaw D. M., Kraemer S. B., George I. M., eds., p. 69

Kriss G. A., 2004, in IAU Symposium, Vol. 222, The Interplay Among Black Holes, Stars and ISM in Galactic Nuclei, Storchi-Bergmann T., Ho L. C., Schmitt H. R., eds., pp. 223–228

Kriss G. A., 2006, in Astronomical Society of the Pacific Conference Series, Vol. 348, Astrophysics in the Far Ultraviolet: Five Years of Discovery with FUSE, Sonneborn G., Moos H. W., Andersson B.-G., eds., p. 499

Krolik J., 1999, Active Galactic Nuclei: From the Central Black Hole to the Galactic Environment, Princeton Series in Astrophysics. Princeton University Press

Krolik J. H., Hawley J. F., Hirose S., 2005, ApJ, 622, 1008

Krolik J. H., Kriss G. A., 1995, ApJ, 447, 512

Krolik J. H., Kriss G. A., 2001, ApJ, 561, 684

Krongold Y., Nicastro F., Elvis M., Brickhouse N., Binette L., Mathur S., Jiménez-Bailón E., 2007, ApJ, 659, 1022

Kurosawa R., Proga D., 2009, MNRAS, 397, 1791

Laor A., Brandt W. N., 2002, ApJ, 569, 641

Lewis G. F., Chapman S. C., Ibata R. A., Irwin M. J., Totten E. J., 1998, ApJL, 505, L1

Lightman A. P., White T. R., 1988, ApJ, 335, 57

Lobban A. P., Reeves J. N., Miller L., Turner T. J., Braito V., Kraemer S. B., Crenshaw D. M., 2011, MNRAS, 414, 1965

Lusso E. et al., 2010, A&A, 512, A34

Lynden-Bell D., 1969, Nature, 223, 690

Lynds C. R., 1967, ApJ, 147, 396

Macchetto F., Colina L., Golombek D., Perryman M. A. C., di Serego Alighieri S., 1990, ApJ, 356, 389

Magdziarz P., Zdziarski A. A., 1995, MNRAS, 273, 837

Magorrian J. et al., 1998, AJ, 115, 2285

Maiolino R. et al., 2010, A&A, 517, A47

Malizia A. et al., 2008, MNRAS, 389, 1360

Marconi A., Hunt L. K., 2003, ApJL, 589, L21

Marconi A., Risaliti G., Gilli R., Hunt L. K., Maiolino R., Salvati M., 2004, MNRAS, 351, 169

Marinucci A., Bianchi S., Nicastro F., Matt G., Goulding A. D., 2012, ApJ, 748, 130

Markowitz A., Reeves J. N., Braito V., 2006, ApJ, 646, 783

Martínez-Sansigre A., Rawlings S., Lacy M., Fadda D., Jarvis M. J., Marleau F. R., Simpson C., Willott C. J., 2006, MNRAS, 370, 1479

Mason K. O. et al., 2001, A&A, 365, L36

Mathur S., 1994, ApJL, 431, L75

Mathur S., Elvis M., Wilkes B., 1995, ApJ, 452, 230

Mathur S., Wilkes B., Elvis M., Fiore F., 1994, ApJ, 434, 493

Matt G., 2002, MNRAS, 337, 147

Matt G., Perola G. C., Piro L., 1991, A&A, 247, 25

McHardy I. M., Gunn K. F., Uttley P., Goad M. R., 2005, MNRAS, 359, 1469

McKernan B., Yaqoob T., Reynolds C. S., 2007, MNRAS, 379, 1359

McQuillin R. C., McLaughlin D. E., 2012, MNRAS, 423, 2162

McQuillin R. C., McLaughlin D. E., 2013, ArXiv e-prints

Mehdipour M. et al., 2011, A&A, 534, A39

Meier D. L., 2002, New Astron. Rev., 46, 247

Merritt D., Ferrarese L., 2001, ApJ, 547, 140

Middleton M., Done C., Gierliński M., 2007, MNRAS, 381, 1426

Miller J. M., Raymond J., Fabian A., Steeghs D., Homan J., Reynolds C., van der Klis M., Wijnands R., 2006, Nature, 441, 953

Miller J. M., Raymond J., Reynolds C. S., Fabian A. C., Kallman T. R., Homan J., 2008, ApJ, 680, 1359

Miller L., Turner T. J., 2013, ArXiv e-prints

Miller L., Turner T. J., Reeves J. N., 2008, A&A, 483, 437

Miller L., Turner T. J., Reeves J. N., 2009, MNRAS, 399, L69

Miller L., Turner T. J., Reeves J. N., Braito V., 2010, MNRAS, 408, 1928

Miller L., Turner T. J., Reeves J. N., George I. M., Kraemer S. B., Wingert B., 2007, A&A, 463, 131

Mineo T., Stewart G. C., 1993, MNRAS, 262, 817

Miniutti G., Fabian A. C., 2004, MNRAS, 349, 1435

Miniutti G., Fabian A. C., 2006, MNRAS, 366, 115

Misawa T., Charlton J. C., Eracleous M., Ganguly R., Tytler D., Kirkman D., Suzuki N., Lubin D., 2007, ApJS, 171, 1

Mitsuda K. et al., 2007, PASJ, 59, 1

Mitsuda K. et al., 1984, PASJ, 36, 741

Miyakawa T., Ebisawa K., Inoue H., 2012, PASJ, 64, 140

Monier E. M., Mathur S., Wilkes B., Elvis M., 2001, ApJ, 559, 675

Morgan C. W., Kochanek C. S., Dai X., Morgan N. D., Falco E. E., 2008, ApJ, 689, 755

Morris S. L., 1988, ApJL, 330, L83

Morrison R., McCammon D., 1983, ApJ, 270, 119

Mortlock D. J. et al., 2011, Nature, 474, 616

Mullaney J. R. et al., 2012, ApJL, 753, L30

Murphy K. D., Yaqoob T., 2009, MNRAS, 397, 1549

Murray N., Chiang J., 1995, ApJL, 454, L105

Murray S. S. et al., 2000, in Society of Photo-Optical Instrumentation Engineers (SPIE) Conference Series, Vol. 4012, Society of Photo-Optical Instrumentation Engineers (SPIE) Conference Series, Truemper J. E., Aschenbach B., eds., pp. 68–80

Mushotzky R. F., 1982, ApJ, 256, 92

Nandra K., O'Neill P. M., George I. M., Reeves J. N., 2007, MNRAS, 382, 194

Nandra K., Pounds K. A., 1994, MNRAS, 268, 405

Narayan R., McClintock J. E., 2012, MNRAS, 419, L69

Narayan R., SÄ dowski A., Penna R. F., Kulkarni A. K., 2012, MNRAS, 426, 3241

Nardini E., Fabian A. C., Reis R. C., Walton D. J., 2011, MNRAS, 410, 1251

Nardini E., Fabian A. C., Walton D. J., 2012, MNRAS, 3068

Nardini E., Risaliti G., 2011, MNRAS, 417, 2571

Nayakshin S., 2001, Advances in Space Research, 28, 425

Nayakshin S., Kazanas D., Kallman T. R., 2000, ApJ, 537, 833

Neilsen J., Homan J., 2012, ApJ, 750, 27

Netzer H., 2004, ApJ, 604, 551

Nikołajuk M., Czerny B., Gurynowicz P., 2009, MNRAS, 394, 2141

Norman C. et al., 2002, ApJ, 571, 218

Novikov I. D., Thorne K. S., 1973, in Black Holes (Les Astres Occlus), Dewitt C., Dewitt B. S., eds., pp. 343–450

Ohsuga K., 2012, in Astronomical Society of the Pacific Conference Series, Vol. 460, AGN Winds in Charleston, Chartas G., Hamann F., Leighly K. M., eds., p. 176

Ohsuga K., Mineshige S., 2011, ApJ, 736, 2

Ohsuga K., Mineshige S., Mori M., Kato Y., 2009, PASJ, 61, L7

Orr A., Barr P., Guainazzi M., Parmar A. N., Young A. J., 2001, A&A, 376, 413

Osterbrock D. E., 1981, ApJ, 249, 462

Osterbrock D. E., Pogge R. W., 1985, ApJ, 297, 166

Osterbrock D. E., Pogge R. W., 1987, ApJ, 323, 108

Page K. L., O'Brien P. T., Reeves J. N., Turner M. J. L., 2004, MNRAS, 347, 316

Pan H. C., Stewart G. C., Pounds K. A., 1990, MNRAS, 242, 177

Papadakis I. E., 2004, MNRAS, 348, 207

Patrick A. R., Reeves J. N., Lobban A. P., Porquet D., Markowitz A. G., 2011a, MNRAS, 416, 2725

Patrick A. R., Reeves J. N., Porquet D., Markowitz A. G., Braito V., Lobban A. P., 2012, MNRAS, 426, 2522

Patrick A. R., Reeves J. N., Porquet D., Markowitz A. G., Lobban A. P., Terashima Y., 2011b, MNRAS, 411, 2353

Perola G. C., Matt G., Cappi M., Fiore F., Guainazzi M., Maraschi L., Petrucci P. O., Piro L., 2002, A&A, 389, 802

Peterson B., 1997, An Introduction to Active Galactic Nuclei. Cambridge University Press

Peterson B. M. et al., 2004, ApJ, 613, 682

Phillips M. M., 1980, ApJL, 236, L45

Phillips M. M., Feldman F. R., Marshall F. E., Wamsteker W., 1979, A&A, 76, L14

Ponti G., Fender R. P., Begelman M. C., Dunn R. J. H., Neilsen J., Coriat M., 2012, MNRAS, 422, L11

Porquet D., Dubau J., 2000, A&AS, 143, 495

Porquet D., Dubau J., Grosso N., 2010, SSRv, 157, 103

Porquet D., Mewe R., Dubau J., Raassen A. J. J., Kaastra J. S., 2001, A&A, 376, 1113

Porquet D., Reeves J. N., O'Brien P., Brinkmann W., 2004a, A&A, 422, 85

Porquet D., Reeves J. N., O'Brien P., Brinkmann W., 2004b, A&A, 422, 85

Porquet D., Reeves J. N., Uttley P., Turner T. J., 2004c, A&A, 427, 101

Pounds K. A., Nandra K., Stewart G. C., George I. M., Fabian A. C., 1990, Nature, 344, 132

Pounds K. A., Reeves J. N., 2009, MNRAS, 397, 249

Pounds K. A., Reeves J. N., King A. R., Page K. L., O'Brien P. T., Turner M. J. L., 2003a, MNRAS, 345, 705

Pounds K. A., Reeves J. N., Page K. L., Wynn G. A., O'Brien P. T., 2003b, MNRAS, 342, 1147

Proga D., 2003, ApJ, 585, 406

Proga D., 2005, ApJL, 630, L9

Proga D., 2007, in Astronomical Society of the Pacific Conference Series, Vol. 373, The Central Engine of Active Galactic Nuclei, Ho L. C., Wang J.-W., eds., p. 267

Proga D., Kallman T. R., 2004, ApJ, 616, 688

Proga D., Stone J. M., Kallman T. R., 2000, ApJ, 543, 686

Protassov R., van Dyk D. A., Connors A., Kashyap V. L., Siemiginowska A., 2002, ApJ, 571, 545

Punsly B., Coroniti F. V., 1990, ApJ, 350, 518

Ramírez J. M., Komossa S., Burwitz V., Mathur S., 2008, ApJ, 681, 965

Rees M. J., 1984, Annu. Rev. Astron. Astrophys., 22, 471

Reeves J., Done C., Pounds K., Terashima Y., Hayashida K., Anabuki N., Uchino M., Turner M., 2008a, MNRAS, 385, L108

Reeves J., Done C., Pounds K., Terashima Y., Hayashida K., Anabuki N., Uchino M., Turner M., 2008b, MNRAS, 385, L108

Reeves J., Pounds K., 2012, in Astronomical Society of the Pacific Conference Series, Vol. 460, AGN Winds in Charleston, Chartas G., Hamann F., Leighly K. M., eds., p. 13

Reeves J. N., Gofford J., Braito V., Sambruna R., 2010, ApJ, 725, 803

Reeves J. N., Nandra K., George I. M., Pounds K. A., Turner T. J., Yaqoob T., 2004, ApJ, 602, 648

Reeves J. N. et al., 2009, ApJ, 701, 493

Reeves J. N., O'Brien P. T., Ward M. J., 2003, ApJL, 593, L65

Reeves J. N., Turner M. J. L., 2000, MNRAS, 316, 234

Reynolds C. S., 1997, MNRAS, 286, 513

Reynolds C. S., Brenneman L. W., Lohfink A. M., Trippe M. L., Miller J. M., Reis R. C., Nowak M. A., Fabian A. C., 2012, in American Institute of Physics Conference Series, Vol. 1427, American Institute of Physics Conference Series, Petre R., Mitsuda K., Angelini L., eds., pp. 157–164

Ricker G. R., Clark G. W., Doxsey R. E., Dower R. G., Jernigan J. G., Delvaille J. P., MacAlpine G. M., Hjellming R. M., 1978, Nature, 271, 35

Riechers D. A., Walter F., Carilli C. L., Lewis G. F., 2009, ApJ, 690, 463

Risaliti G., Bianchi S., Matt G., Baldi A., Elvis M., Fabbiano G., Zezas A., 2005, ApJL, 630, L129

Risaliti G. et al., 2009, ApJL, 705, L1

Risaliti G., Elvis M., Fabbiano G., Baldi A., Zezas A., Salvati M., 2007, ApJL, 659, L111

Risaliti G., Maiolino R., Salvati M., 1999, ApJ, 522, 157

Risaliti G., Nardini E., Salvati M., Elvis M., Fabbiano G., Maiolino R., Pietrini P., Torricelli-Ciamponi G., 2011, MNRAS, 410, 1027

Rivers E., Markowitz A., Rothschild R., 2011, ApJ, 732, 36

Ross R. R., Fabian A. C., 2005a, MNRAS, 358, 211

Ross R. R., Fabian A. C., 2005b, MNRAS, 358, 211

Saez C., Chartas G., 2011, ApJ, 737, 91

Saez C., Chartas G., Brandt W. N., 2009, ApJ, 697, 194

Sako M. et al., 2001, A&A, 365, L168

Salpeter E. E., 1964, ApJ, 140, 796

Sanders J. S., Fabian A. C., Taylor G. B., 2009, MNRAS, 396, 1449

Sazonov S. Y., Ostriker J. P., Ciotti L., Sunyaev R. A., 2005, MNRAS, 358, 168

Scannapieco E., Silk J., Bouwens R., 2005, ApJL, 635, L13

Schmidt M., Green R. F., 1983, ApJ, 269, 352

Schödel R. et al., 2002, Nature, 419, 694

Schurch N. J., Done C., 2007, MNRAS, 381, 1413

Schurch N. J., Done C., Proga D., 2009, ApJ, 694, 1

Serlemitsos P. J. et al., 2007, PASJ, 59, 9

Severgnini P. et al., 2006, A&A, 451, 859

Shakura N. I., Sunyaev R. A., 1973, A&A, 24, 337

Shen Y., Greene J. E., Strauss M. A., Richards G. T., Schneider D. P., 2008, ApJ, 680, 169

Shu X. W., Yaqoob T., Wang J. X., 2010, ApJS, 187, 581

Silk J., Rees M. J., 1998, A&A, 331, L1

Sim S. A., Long K. S., Miller L., Turner T. J., 2008, MNRAS, 388, 611

Sim S. A., Proga D., Miller L., Long K. S., Turner T. J., 2010, MNRAS, 408, 1396

Singh K. P., Rao A. R., Vahia M. N., 1992, ApJ, 385, 132

Sobolewska M. A., Done C., 2007, MNRAS, 374, 150

Spiegel M., Lipschutz S., Liu J., 2008, Schaum's Outline of Mathematical Handbook of Formulas and Tables, 3ed, Schaum's Outline Series. McGraw-Hill Education

Stern D. et al., 2002, ApJ, 568, 71

Stevens I. R., Kallman T. R., 1990, ApJ, 365, 321

Strüder L. et al., 2001, A&A, 365, L18

Surdej J., Hutsemekers D., 1987, A&A, 177, 42

Takahashi T. et al., 2007, PASJ, 59, 35

Tamura T., Baba H., Matsuzaki K., Miura A., Shinohara I., Nagase F., Fukushi M., Uchida K., 2004, in Astronomical Society of the Pacific Conference Series, Vol. 314, Astronomical Data Analysis Software and Systems (ADASS) XIII, F. Ochsenbein, M. G. Allen, & D. Egret, ed., p. 22

Tarter C. B., Tucker W. H., Salpeter E. E., 1969, ApJ, 156, 943

Tatum M. M., Turner T. J., Miller L., Reeves J. N., 2013, ApJ, 762, 80

Tatum M. M., Turner T. J., Sim S. A., Miller L., Reeves J. N., Patrick A. R., Long K. S., 2012, ApJ, 752, 94

Thorne K. S., 1974, ApJ, 191, 507

Titarchuk L., 1994, ApJ, 434, 570

Tombesi F., Cappi M., Reeves J. N., Braito V., 2012a, MNRAS, 422, L1

Tombesi F., Cappi M., Reeves J. N., Nemmen R. S., Braito V., Gaspari M., Reynolds C. S., 2013, MNRAS, 430, 1102

Tombesi F., Cappi M., Reeves J. N., Palumbo G. G. C., Braito V., Dadina M., 2011a, ApJ, 742, 44

Tombesi F., Cappi M., Reeves J. N., Palumbo G. G. C., Yaqoob T., Braito V., Dadina M., 2010a, A&A, 521, A57

Tombesi F., Sambruna R. M., Marscher A. P., Jorstad S. G., Reynolds C. S., Markowitz A., 2012b, MNRAS, 424, 754

Tombesi F., Sambruna R. M., Reeves J. N., Braito V., Ballo L., Gofford J., Cappi M., Mushotzky R. F., 2010b, ApJ, 719, 700

Tombesi F., Sambruna R. M., Reeves J. N., Reynolds C. S., Braito V., 2011b, MNRAS, 418, L89

Tran H. D., 1995a, ApJ, 440, 565

Tran H. D., 1995b, ApJ, 440, 597

Tremaine S. et al., 2002, ApJ, 574, 740

Turner M. J. L. et al., 2001, A&A, 365, L27

Turner T. J., Miller L., Kraemer S. B., Reeves J. N., 2011, ApJ, 733, 48

Turner T. J., Miller L., Kraemer S. B., Reeves J. N., Pounds K. A., 2009, ApJ, 698, 99

Turner T. J., Miller L., Reeves J. N., Kraemer S. B., 2007, A&A, 475, 121

Turner T. J., Miller L., Tatum M., 2012, in American Institute of Physics Conference Series, Vol. 1427, American Institute of Physics Conference Series, Petre R., Mitsuda K., Angelini L., eds., pp. 165–172

Turner T. J., Pounds K. A., 1988, MNRAS, 232, 463

Turner T. J., Reeves J. N., Kraemer S. B., Miller L., 2008, A&A, 483, 161

Turnshek D. A., 1984, ApJ, 280, 51

Urry C. M., Padovani P., 1995, PASP, 107, 803

Vasudevan R. V., Fabian A. C., 2007, MNRAS, 381, 1235

Vasudevan R. V., Fabian A. C., 2009, MNRAS, 392, 1124

Vasudevan R. V., Fabian A. C., Gandhi P., Winter L. M., Mushotzky R. F., 2010, MNRAS, 402, 1081

Vaughan S., Fabian A. C., 2004, MNRAS, 348, 1415

Vaughan S., Reeves J., Warwick R., Edelson R., 1999, MNRAS, 309, 113

Vaughan S., Uttley P., 2008, MNRAS, 390, 421

Vaughan S., Uttley P., Pounds K. A., Nandra K., Strohmayer T. E., 2011, MNRAS, 413, 2489

Véron-Cetty M.-P., Véron P., 2010, A&A, 518, A10

Vestergaard M., Fan X., Tremonti C. A., Osmer P. S., Richards G. T., 2008, ApJL, 674, L1

Vestergaard M., Peterson B. M., 2006, ApJ, 641, 689

Wagner A. Y., Umemura M., Bicknell G. V., 2013, ApJL, 763, L18

Walter R., Fink H. H., 1993, A&A, 274, 105

Wang J.-G. et al., 2009, ApJ, 707, 1334

Wang J.-M., Netzer H., 2003, A&A, 398, 927

Wang Y. P., Biermann P. L., Wandel A., 2000, A&A, 361, 550

Warwick R. S., Pounds K. A., Turner T. J., 1988, MNRAS, 231, 1145

Weisskopf M. C., Tananbaum H. D., Van Speybroeck L. P., O'Dell S. L., 2000, in Society of Photo-Optical Instrumentation Engineers (SPIE) Conference Series, Vol. 4012, Society of Photo-Optical Instrumentation Engineers (SPIE) Conference Series, Truemper J. E., Aschenbach B., eds., pp. 2–16

Weymann R. J., Morris S. L., Foltz C. B., Hewett P. C., 1991, ApJ, 373, 23

Willis A. G., Strom R. G., Wilson A. S., 1974, Nature, 250, 625

Winkler H., 1992, MNRAS, 257, 677

Woo J.-H., Urry C. M., 2002, ApJ, 579, 530

Yamaoka K. et al., 2006, in Society of Photo-Optical Instrumentation Engineers (SPIE) Conference Series, Vol. 6266, Society of Photo-Optical Instrumentation Engineers (SPIE) Conference Series

Yaqoob T., Murphy K. D., 2011, MNRAS, 412, 277

Yaqoob T., Murphy K. D., Miller L., Turner T. J., 2010, MNRAS, 401, 411

Young A. J., Lee J. C., Fabian A. C., Reynolds C. S., Gibson R. R., Canizares C. R., 2005, ApJ, 631, 733

Zhou X.-L., Zhao Y.-H., 2010, ApJL, 720, L206

Zubovas K., King A., 2012a, ApJL, 745, L34

Zubovas K., King A., 2013, ApJ, 769, 51

Zubovas K., King A. R., 2012b, MNRAS, 426, 2751